Aus der Medizinischen Klinik und Poliklinik IV
Klinikum der Ludwig-Maximilian-Universität München

Different roles of Regnase3 in resident macrophages and tubular epithelial cells in kidney disease

Dissertation
zum Erwerb des Doktorgrades der Humanbiologie
an der Medizinischen Fakultät der
Ludwig-Maximilians-Universität München

vorgelegt von
Chenyu Li
Aus Qingdao, China
2023

Mit Genehmigung der Medizinischen Fakultät
der Ludwig-Maximilians-Universität zu München

Erster Gutachter:	Prof. Dr. med. Hans-Joachim Anders
Zweiter Gutachter:	Prof. Dr. Christian Schulz
Dritter Gutachter:	Prof. Dr. Clemens Cohen
ggf. weitere Gutachter:	
Mitbetreuung durch den promovierten Mitarbeiter:	Dr. Julian Aurelio Marschner
Dekan:	Prof. Dr. med. Thomas Gudermann
Tag der mündlichen Prüfung:	27.07.2023

Zusammenfassung

Akutes Nierenversagen (ANV) ist eine häufige, jedoch schwere Erkrankung, die v.a. in klinischen Einrichtungen auftritt. ANV ist durch einen plötzlichen Rückgang der Nierenfunktion gekennzeichnet und wird durch den Anstieg des Serum-Kreatinin-Spiegels und die Abnahme der Urinausscheidung oder beides angezeigt. Die Prognose von ANV ist selbst für Überlebende schlecht, da viele Patienten nach einem schweren ANV eine chronische Niereninsuffizienz entwickeln können, was den Einsatz von Nierenersatzverfahren nowendig macht. Dies beeinträchtigt nicht nur die Lebensqualität der Patienten, sondern erhöht auch die Belastung für pflegende Angehörige und medizinische Kosten. Derzeit gibt es keine pharmazeutisch wirksamen präventiven oder therapeutischen Maßnahmen für ANV, es stehen lediglich Dialyse und unterstützende medizinische Versorgung zur Verfügung.

Ribonukleinsäure (Ribonucleic acid, RNA)-bindende Proteine (RBPs) sind eine Klasse von Proteinen, die eine entscheidende Rolle bei der Regulation der Genexpression spielen und bei einer Vielzahl von Erkrankungen beteiligt sind. Diese Proteine besitzen die Fähigkeit, unterschiedliche Transkripte zu binden und dadurch komplexe regulative Netzwerke zu bilden, die für die Erhaltung der Zellintegrität von entscheidender Bedeutung sind. Neuere Studien haben gezeigt, dass eine Reihe von RBPs an ANV beteiligt sind, darunter das kälteinduzierbare RNA-bindende Protein, humanes Antigen R, Pumilio und Y-Box-bindendes Protein. Regnase 3 ist ein Mitglied der Regnase RBP Familie und fördert Entzündungen, indem es die Expression vonTumor Nekrose Faktor (TNF) in Makrophagen erhöht und Interleukin 6 (IL6) in plasmazytoiden dendritischen Zellen unterdrückt. Trotz dieses Wissens ist die Bedeutung der Rolle, die Regnase 3 in renalen Tubuluszellen spielt, unbekannt. Wir haben die Hypothese aufgestellt, dass Regnase 3 sowohl in Makrophagen als auch in renalen Tubuluszellen eine Rolle spielt und Entzündungen und Tubulusreparatur in ANV beeinflusst.

Um die mögliche Rolle von Regnase 3 bei Nierenschädigungen zu untersuchen, wurden eine Reihe von genetisch veränderten Mäusen im Hintergrund C57BL/6J hergestellt. Diese Mauslinien umfassten paired box gene 8 (Pax8)-reverse tetracycline transactivator (rTtA, Pax8rTtA), tetracycline resistance protein (TetO)-Cre (TetOCre), transgenic receptor activator of nuclear factor kappa-B (Rank)-Cre (RankCre), and Regnase 3 floxed (Regnase3fl/fl) Mäuse. Diese genetisch veränderten Mäuse haben wir in einer Reihe von experimentellen Tiermodellen eingesetzt, um die Auswirkungen von Regnase 3 auf Nierenschädigung zu untersuchen, darunter ein unilaterales Nierenischämie-Reperfusionsmodel mit oder ohne Nephrektomie und ein Nephrocalcinose-induziertes Nierenschädigungsmodel. Zusätzlich haben wir in vitro-Modelle mit

primären Nieren- und Entzündungszellen verwendet, um die Auswirkungen von Regnase 3 auf der Zellenebene zu studieren. Darüber hinaus haben wir single cell und bulk RNA-Sequenzierung durchgeführt, um die zugrundeliegenden Mechanismen der Funktion von Regnase 3 zu untersuchen.

Wir entdeckten, dass Regnase 3 in renalen Makrophagen nach ANV hoch exprimiert ist. Wir beobachteten, dass die Regnase 3-Expression positiv mit Phagozytose, Chemokinenproduktion und Monozytenreifung korrelieren. Darüber hinaus litten Rank-Regnase 3 Mäuse nach ANV aufgrund der Zunahme der CCR2-positiven Zellinfiltration im Vergleich zur Wildtyp-Kontrollgruppe mehr an Entzündung und Nierenschädigung. In vitro-Experimente zeigten, dass Regnase 3 an der Modulation der Makrophagenfunktion beteiligt ist, indem es die Polarisation von Makrophagen zu einem M1- und M2-Phänotyp bewirkt und die Zellmigration beeinflusst. Diese Ergebnisse deuten darauf hin, dass Regnase 3 bei der Makrophagenmigration und -infiltration nach ANV eine entscheidende Rolle spielt, die sowohl zur frühen Entzündungsphase nach ANV als auch der Progression zur chronischem Nierenversagen beiträgt.

Im nächsten Schritt wollten wir die Rolle von Regnase 3 im Kontext von Nierentubulusschädigung untersuchen. Wir beobachteten, dass Regnase 3 in gesunden Nierentubuli hoch exprimiert ist, aber die Expression nach Verletzung deutlich reduziert ist. Mittels in vivo- und in vitro-Experimenten fanden wir heraus, dass Regnase 3 eine entscheidende Rolle bei der Regulierung der frühen Apoptose, Zelltod, Proliferation und Wundheilung von tubulären Epithelzellen spielt. Diese Auswirkungen tragen zur Nierenverletzung bei postischemischen Nieren bei. Darüber hinaus entdeckten wir, dass Regnase 3-Defizienz Schutz vor ischämischem ANV bietet. Unsere Daten belegen, dass Regnase 3 prä-RNA erkennt und alternatives Splicing durch die Erhöhung des Anteils an gezielt übersprungenen Exonen und die Verringerung der Wahrscheinlichkeit gezielter behaltener Introne moduliert. Insgesamt deuten unsere Ergebnisse darauf hin, dass Regnase 3 eine wichtige Rolle bei ANV spielt und möglicherweise ein potenzielles Ziel für therapeutische Interventionen sein könnte.

Zusammenfassend zeigen unsere Ergebnisse, dass Regnase3 eine wichtige Rolle in der Entwicklung von Nierenschäden in postischemischen Nieren spielt und somit ein potenzielles therapeutisches Ziel für die Behandlung von renalen IRI darstellt. Der Einfluss von Regnase3 auf Nierenschäden ist jedoch von der spezifischen Zelllinie abhängig. Unsere Forschung zeigt, dass das Löschen von Rank-Regnase3 zu einer Verschlimmerung von Nierenschäden durch eine Erhöhung der Makrophagenrekrutierung führt, während das

Löschen von Pax8-Regnase3 zu einer Verbesserung von Nierenschäden durch seine Auswirkungen auf Zelltod und Wundheilungsfähigkeit von tubulären Epithelzellen führt und somit einen Schutz gegen ischämische ANV bietet. Daher ist die Rolle von Regnase3 in Nierenschäden stark von Standort und Zelllinie abhängig, was letztendlich den schädlichen oder nutzbringenden Einfluss auf Nierenschäden bestimmt.

Summary

Acute kidney injury (AKI) is a prevalent yet severe condition that occurs in clinical settings. It is characterized by a sudden decline in kidney function, as indicated by an increase in serum creatinine (Scr) levels and a decrease in urine output, or both. The prognosis for AKI is poor, with many patients progressing to acute kidney disease, chronic kidney disease (CKD), and even end-stage kidney disease especially in those who were admitted to the intensive care unit. This not only negatively impacts patients' quality of life but also increases the burden on family caregivers and medical costs. Despite this, there are currently no effective preventive or therapeutic measures for AKI, with only dialysis and supportive medical care being available.

Ribonucleic acid (RNA)-binding proteins (RBPs) are a class of proteins that play a vital role in regulating gene expression and have been implicated in a wide range of diseases. These proteins possess the ability to bind and target multiple transcripts, forming intricate regulatory networks that are crucial for maintaining cellular integrity. Recent studies have revealed that a number of RBPs are involved in AKI, including the cold inducible RNA binding protein, human antigen R, Pumilio, and Y-box binding protein. Regnase3 is a member of the Regnase RBPs family and has been shown to promote inflammation by simultaneously increasing TNF in macrophages and repressing IL6 in plasmacytoid dendritic cells. Despite this knowledge, the full extent of the role played by Regnase3 in AKI remains largely unknown. Therefore, we hypothesized that Regnase3 plays a role in both macrophages and tubular epithelial cells, influencing inflammation and tubular repair in AKI.

In order to investigate the potential role of Regnase3 in kidney injury, a series of genetically-modified mice were developed on the C57BL/6J genetic background. These mice included the paired box gene 8 (Pax8)-reverse tetracycline transactivator (rTtA, Pax8rTtA), tetracycline resistance protein (TetO)-Cre (TetOCre), transgenic receptor activator of nuclear factor kappa-B (Rank)-Cre (RankCre), and Regnase3 floxed (Regnase3fl/fl) mice. Using these genetically modified mice, we applied a range of experimental animal models to study the effects of Regnase3 on kidney injury, including unilateral kidney ischemia-reperfusion surgery with or without nephrectomy and nephrocalcinosis-related kidney injury. Additionally, we employed in vitro models utilizing primary cells to study Regnase3 on the cellular level. Furthermore, we utilized scRNA-seq and RNA-seq to investigate the underlying mechanisms of Regnase3's function.

We conducted a thorough investigation and discovered that the Regnase3 is highly expressed in macrophages located within the kidney after AKI. We observed that the expression levels of Regnase3 positively correlated with the functions of phagocytosis, chemokines, and monocyte maturation. Furthermore, Rank-Regnase3 mice suffered from more inflammation and kidney injury after AKI, characterized by an increase in CCR2 positive leukocyte infiltration when compared to the wildtype control group. Additionally, in vitro experiments revealed that Regnase3 is involved in modulating macrophage behavior, acting as a regulator of macrophage polarization towards an M1 and M2 phenotype and influencing the capacity of cell migration. These findings indicate that Regnase3 is essential in the migration of macrophages after AKI, which contribute to both early phase inflammation and progression towards AKI-CKD.

Next, we aimed to examine the role of Regnase3 in the context of kidney and renal tubule injury. We observed that Regnase3 is highly expressed in healthy renal tubules, but its expression is significantly reduced following injury. Through in vivo and in vitro experiments, we found that Regnase3 controls early apoptosis, cell death, proliferation, and wound healing capability of tubular epithelial cells. These effects contribute to kidney injury in postischemic kidneys. Additionally, we discovered that the deletion of Regnase3 provides protection against ischemic AKI. Mechanistically, Regnase3 targets pre-RNA and modulates alternative splicing by increasing the proportion of targeted skipped exon events and decreasing the probability of targeted retained intron events. Overall, our findings indicate that Regnase3 plays a vital role in tubular epithelial cells in the response to kidney injury by regulating alternative splicing.

In summary, our findings indicate that Regnase3 contributes to kidney injury in postischemic kidneys. However, the impact of Regnase3 on kidney injury is contingent upon the specific cell lineage in question. Our research demonstrates that the deletion of Rank-Regnase3 leads to an exacerbation of kidney injury by increasing macrophage recruitment, whereas the deletion of Pax8-Regnase3 leads to an improvement in kidney injury through its effects on cell death and wound healing capability of tubular epithelial cells, providing protection against ischemic AKI. Therefore, the role of Regnase3 in kidney injury is highly dependent on the cell lineage, which ultimately determines the detrimental or beneficial impact on kidney injury.

1. Introduction

1.1 Acute Kidney Injury

Acute kidney injury (AKI) is a prevalent yet severe condition, which characterized by a rapid kidney function decline, with the urine output decrease and levels of serum creatinine (Scr) increase, or both[1]. AKI-related mortality is higher than that of heart failure or breast cancer, with an estimated number of deaths worldwide reaching 2 million every year[2]. Also the prognosis for AKI survivors is poor, with many patients progressing to acute kidney disease (AKD), chronic kidney disease (CKD), and even end-stage kidney disease (ESKD) especially in those who hospitalized in intensive care unit (ICU)[3]. The survivors of AKI with a complete recovery of kidney function enjoy a better long-term prognosis, while they may experience irreversible nephron loss, leading to CKD and the need for dialysis later in life [3-7]. In 2010, there are approximately 2.62 million patients undergoing dialysis globally, and epidemiologists expect the number will double by 2030[8]. Dialysis not only negatively impacts on patients' quality of life but also increases the burden on family caregivers and medical costs. However, there are currently no effective preventive or therapeutic measures for AKI, with only dialysis and supportive medical care being available.

1.1.1 History and Definition

AKI can be traced back to literature published during World War II in 1941 by Beall et al.[9]. They described a rapidly progressive kidney function insufficiency in patients with dark urine, edema, elevated potassium levels, and disorientation. In 1946, the first definition of AKI was established by Lucké, who depicted the histopathological change now known as acute tubular necrosis (ATN)[10, 11]. Two years later, Bywaters et al performed the first hemodialysis to treat AKI[12]. Despite efforts by clinicians to prevent and intervene in AKI, there remained a lack of generally recognized criteria for AKI diagnosis for decades. The concept of kidney function insufficiency gradually shifted to become acute renal failure (ARF), which represented a clinical syndrome rather than the histopathologic finding. In 2000, the Acute Dialysis Quality Initiative group (ADQI) was established by nephrologists and critical care physicians, with the goal of defining AKI. The group reached a consensus on AKI at a conference in Italy and later in 2004, launched an AKI multilevel classification system called RIFLE, which stands for Risk, Injury, Failure, Loss and ESKD[13]. The RIFLE (Table 1) was based on Scr levels and patient's urine output which was widely validated in several inpatients' settings to assessing the AKI incidence and prognostic stratification[14-17]. However, it has several important limitations, such as difficulty in estimating the baseline Scr, evaluating AKI on CKD, and not taking into account the etiology of AKI[18].

The term of "acute kidney injury" first emerged at the AKI network (AKIN) meeting in 2006[19], which replaced the term "ARF" following a consensus that even slight Scr changes could lead to significant changes in outcome. The AKIN classifications proposed diagnostic and staging criteria for AKI, but both the AKIN and RIFLE classifications are based only on Scr or urine output, and the worst of these parameters is utilized to assess the disease staging, which cannot handle the complexity of AKI, especially in non-ICU wards[1]. In 2012, the guideline from Kidney Disease: Improving Global Outcomes (KDIGO) set the latest diagnostic criteria for AKI. KDIGO covers both the AKIN and RIFLE criteria, considering Scr changes within 48 hours or a glomerular filtration rate (GFR) decline over 7 days[20]. The 2012 KDIGO criteria for AKI are comprehensive in predicting the need for dialysis and early mortality[20], but given the good reversibility of pre- and post-renal AKI compared to AKI related to ATN, the KDIGO matrix is less useful in predicting long-term outcomes[21]. On November 8, 2015, the 16th AQDI council defined the criteria for AKD, which is an acutely impaired kidney function for longer than 7 days[2]. It should be noted that all three criteria operate using the same laboratory indicators and urine output measurements to diagnose and stratify pre-established kidney injury stages. Therefore, the accuracy of the values will be affected by any bias that may change the baseline, thus reducing efficiency and accuracy of these criteria[22].

1.1.2 AKI epidemiology and prognosis

The global annual incidence of AKI is approximately 2,100 per million, with 9-15% of hospitalized patients and around 40% of critically ill patients affected[23]. The mortality rate for patients requiring dialysis is over 40%[6, 24]. A meta-analysis of more than 150 studies using 2012 KDIGO AKI classification included 3,585,911 participants and found that 8.3% developed community-acquired AKI and 20-32% AKI in various in-hospital settings[25]. The incidence and prevalence of AKI varies greatly depending on the level of development and economy of the patient's country of residence. In developed countries, AKI is commonly found in ICUs and is often a complication of severe medical conditions that carry a high mortality rate. It is mostly a single disease's complication with hypotension and shock, and its incidence is around 21% which changed in parallel with aging in last decades[1 26]. In contrast, in developing countries, dehydration is the most common risk factor for AKI, with 70% of cases being community-acquired while the proportion is 50% in developed countries[26]. In this case, AKI is largely preventable through public health initiatives in developing countries, but this increases the healthcare burden as cost for severe AKI patients becomes unaffordable[27].

Table 1 Criteria for acute kidney injury*

	RIFLE[13]	AKIN[19]	KDIGO[20]
Diagnostic criteria			
		Scr↑ ⩾0.3 mg/dL or ⩾ 50% within 48 hours or UO <0.5 mL/kg/hour for >6 hours	Scr↑ ⩾0.3 mg/dL within 48 hours or ⩾50% within 7 days or UO <0.5 mL/kg/hour for >6 hours
Staging criteria			
Risk (RIFLE) or stage 1 (AKIN/ KDIGO)	Scr↑ to 1.5 times baseline or UO <0.5 mL/kg/hour for 6 to 12 hours	Scr↑ ⩾0.3 mg/dL or to 150~200% baseline or UO <0.5 mL/kg/hour for 6 to 12 hours	Scr↑ ⩾0.3 mg/dL or to 1.5~1.9 times baseline or UO <0.5 mL/kg/hour for 6 to 12 hours
Injury (RIFLE) or stage 2 (AKIN/ KDIGO)	Scr↑ to 2 times baseline or UO <0.5 mL/kg/hour for 12 to 24 hours	Scr↑ to 200~300% baseline or UO <0.5 mL/kg/hour for 12 to 24 hours	Scr↑ to 2~2.9 times baseline or UO <0.5 mL/kg/hour for 12 to 24 hours
Failure (RIFLE) or stage 3 (AKIN/ KDIGO)	Scr↑ to 3 times baseline or >0.5 mg/dL to >4 mg/dL or UO <0.3 mL/kg/hour for >24 hours or anuria for >12 hours or need KRT	Scr↑ to >300% baseline or >0.5 mg/dL to ⩾4 mg/dL or UO <0.3 mL/kg/hour for >24 hours or anuria for >12 hours or need KRT	Scr↑ to ⩾3 times baseline or ⩾0.3 mg/dL to ⩾4 mg/dL or UO <0.3 mL/kg/hour for ⩾24 hours or anuria for ⩾12 hours or need KRT
Loss (RIFLE)	KRT > 4 weeks		
End stage (RIFLE)	KRT > 3 months		

* UO, urine output; Scr, serum creatinine; KRT, kidney replacement therapy.

Damage to the kidneys caused by AKI is often irreversible and many AKI survivors develop AKD and CKD[3]. The severity of AKI determines the extent of irreversible loss of nephrons, leading to a reduction in kidney lifespan and post-AKI CKD, with varying degrees of damage ranging from minor to significant[2, 28]. Indeed, 20-50% of AKI patients will progress to CKD, while 3-15% will develop ESKD.[29]. Moreover, increasing evidence suggests that AKI is not only a risk for CKD, but also a risk factor for the progression of precedent CKD. Several recent clinical studies confirmed that even patients with complete recovery of GFR after AKI still have an increased risk of persistent kidney function decline and progression to ESKD[30, 31]. Even patients with AKI stages 1 and 2 are at risk of advancing to CKD or uremia, and a 3-9 times increased risk of mortality compared to those without AKI. A recent meta-analysis of 82 studies, which included 2,017,437 participants, showed that AKI patients had a very high risk of progression to CKD (hazard ratio 2.67), ESKD (hazard ratio 4.81) or mortality (hazard ratio 1.80)[32]. Comorbidities such as pre-existing diabetes mellitus and coronary heart disease also negatively impact on long-term outcomes after AKI. This study identified the adverse effects

of AKI on long-term prognosis and highlights the significance of the severity of kidney injury and the patient's comorbidities on prognosis after AKI[32].

AKI survivors following hospitalization have a significantly higher risk of death from cardiovascular disease and kidney cancer, with mortality rates nearly eight times higher than the general population[33]. Moreover, AKI following partial nephrectomy increases the risk of kidney cancer recurrence, potentially due to DNA damage leading to clonal expansion of mutated cells during repair[34]. Therefore, the regeneration of renal tubular epithelial cells (TEC) in response to ischemic ATN may result in the progenitor cells transformation into tumor stem cells, potentially resulting in the development of papillary renal cell adenoma-carcinoma[35]. Additionally, injuries to other segments of the kidneys may also contribute to the development of various types of kidney cancer[36]. Thus, while short-term survival may be supported, it comes at the cost of long-term trade-offs related to the regeneration of the kidneys.

1.2 Pathophysiology of AKI

The kidneys are essential organs that play a critical role in maintaining homeostasis by excreting metabolic waste products and regulating water and electrolyte balance. AKI is a complex condition that results from a variety of physiological and pathological processes, including acute injury phase, necroinflammation, resolution of inflammation and repair or progressive scarring. Although there is an increasing knowledge about the contribution of various cell types in AKI, the mechanisms behind the AKI-CKD progression are still not well comprehended. While numerous therapeutic approaches have shown efficacy in animal models, there is a scarcity of evidence regarding their ability to prevent AKI or decrease the mortality and chronicity consequences of AKI-CKD. Thus, studies are needed to fully investigate the mechanisms of chronic AKI progression in order to develop new therapeutic targets and more effective treatment plans for promoting rapid repair of kidney injury.

1.2.1 Mechanisms of kidney injury and recovery

1.2.1.1 Common causes for the AKI

AKI can be caused by various factors such as reduced ejection fraction in heart failure, hemorrhagic shock, and volume depletion. Volume depletion to the kidneys happens when blood perfusion is decreased due to dehydration, blood loss, or other conditions. Hemorrhagic shock is characterized by severe blood loss, while reduced ejection fraction heart failure occurs when the heart is not able to pump blood efficiently[37]. AKI can

also be caused by medical conditions such as hepatorenal syndrome, venous congestion, or hypercalcemia, which can reduce GFR by decreasing kidney perfusion. Furthermore, ischemic injuries can lead to persistent inflammation, promoting tubule necrosis[38, 39]. AKI in hospitalized patients can be caused by nephrotoxic drugs and radiocontrast agents through several mechanisms[40]. Certain drugs, including cisplatin and antimicrobials, have direct chemical nephrotoxicity, while others like vancomycin can accumulate in the body due to decreased kidney function, leading to increased toxicity[41]. Some drugs, like checkpoint inhibitors, can cause allergic tubulointerstitial nephritis through immune-mediated mechanisms[42]. ACEIs/ARBs can also decrease GFR by affecting the hemodynamics within the kidney[43]. There are also drugs that crystallize inside the kidney tubules, leading to obstruction of urinary flow and kidney damage.

1.2.1.2 Tubule necrosis

The kidney's most common cell type is proximal TEC (PTEC), which account for reabsorbing around 65% of the filtered load and most filtered solutes, glucose, amino acids, and low molecular weight proteins. PTEC have high metabolic activity but receive low levels of oxygen from capillaries[44], making them susceptible to ischemia, which can lead to a depletion of adenosine triphosphate (ATP), an increase in reactive oxygen species, and eventually were vulnerable cell death[45]. Various factors contribute to cell death and damage to the structure of the tubules[46, 47]. PTEC can undergo both necrosis and apoptosis, which can lead to the separation and loss of functional PTECs into the tubular lumen. This results in an area of S3 segment denudation, which causes tubular failure, physical obstruction of flow, and activation of tubule glomerular feedback due to the solute-rich fluid in distal delivery. Furthermore, this feedback reduces glomerular filtration. Immature progenitor cells surviving ischemia have the capacity to proliferate, and reconstitute tubules, thus playing an vital part in the adaptive repair process to restore kidney function[48]. However, in the case that under severe ischemic event combined with persistent inflammation, surviving renal tubular epithelial cells suffer from DNA damage[49] that can trigger further cell necrosis. ATN is an active process, in which specific forms of regulated cell death, such as necroptosis and ferroptosis, contribute significantly to the progressive loss of tubular epithelial cells and tubule atrophy. These forms of necrosis lead to the synchronization of tubular cell death along the entire tubule segments, while sparing the glomeruli[50, 51], which further amplifies inflammation and interstitial fibrosis (Figure 1)[52].

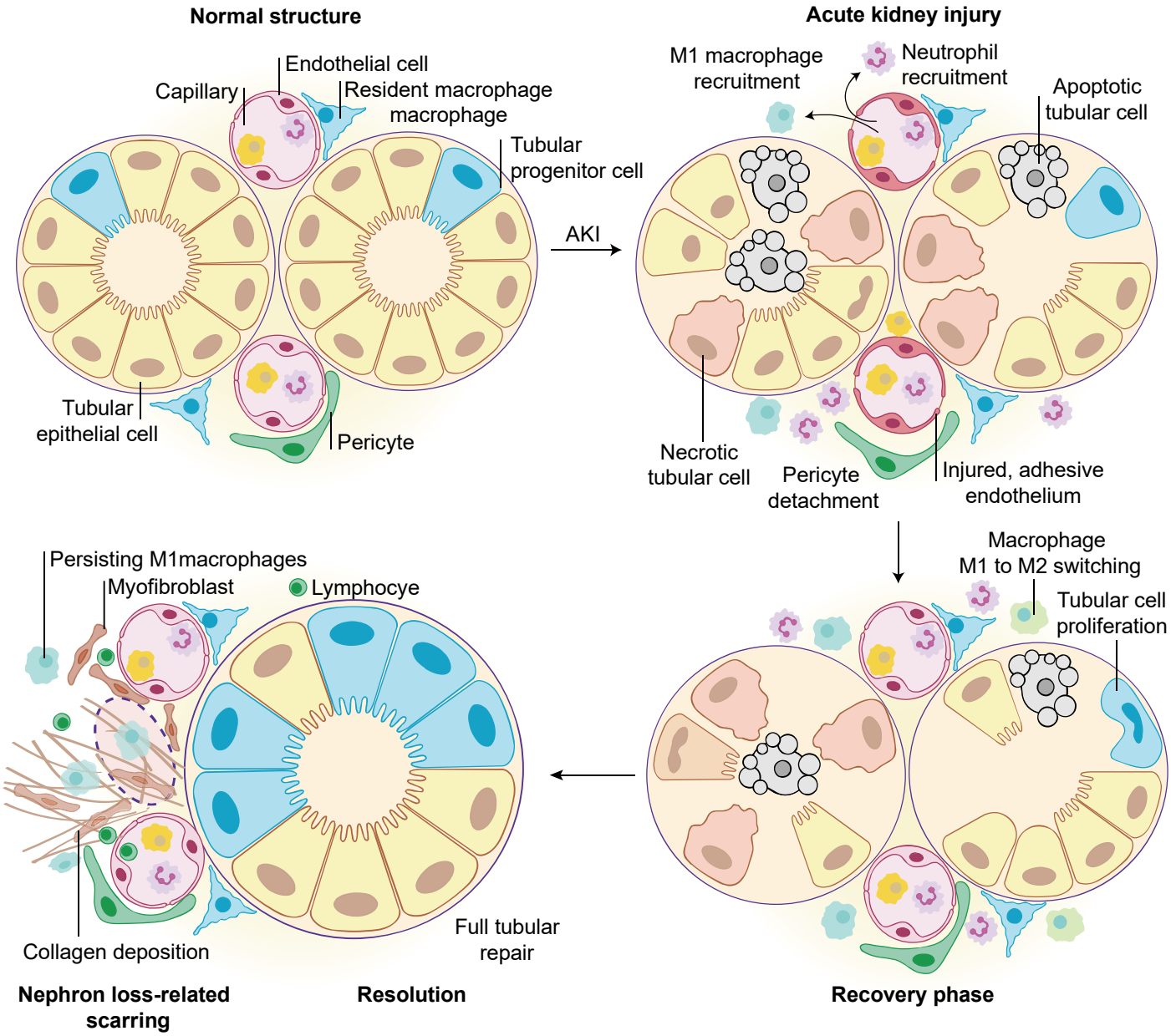

Figure 1. The evolution of acute kidney injury and repair after AKI. When the kidney injury is mild, the kidney can often recover its regular function and normal structure without any permanent cellular adjustments. In such cases, there is minimal to no loss or necrosis of tubular cells, and the number of nephrons remains the unchanged. In contrast, severe AKI cases with significant tubular necrosis can have a considerable impact on nephron number. The injured tubular cells are permanently lost during the acute necroinflammation, ant the recovery of them in nephrons is only possible with surviving progenitor cells. Furthermore, the surviving differentiated tubular cells and entire nephrons increase in size to adapt to filter and metabolic demands. However, the remaining nephrons may struggle to keep up with the increased workload, and this can surpass the ability of podocytes to compensate for the increased filtration surface (not shown). As a result, secondary focal segmental glomerulosclerosis may occur, which can lead to the loss of remaining nephrons and the development of progressive chronic kidney disease.

1.2.1.3 Tubule regeneration

It was previously thought that all PTECs that survive ischemic or nephrotoxic injury undergo cell division in order to generate new cells that can replace damaged tissue and repair the structure of the tubules[53-55]. The S3 segment of the PTECs is particularly susceptible to injury during ischemic AKI and is also the area that

displays the greatest proliferative response throughout the entire cortex[37]. Furthermore, all PTECs, not just those in the S3 segment, are associated with the repair process post-AKI, as even proximal tubular cells located far from the site of injury enter the cell cycle and exhibit high expression of cell cycle markers[48, 56]. However, this idea that all PTECs have the capacity to proliferate and fully restore the kidney from injury is incompatible with the fact that AKI survivors often develop CKD. To address this discrepancy, Lazzeri et al. conducted a batch of in vivo studies utilizing Confetti mice, which revealed the presence of a scattered population of specialized intratubular kidney progenitor cells that due to their immature status are still able to proliferate and regenerate injured tubules, rather than the proliferation of (formerly) differentiated PTECs[57].The data obtained from the Confetti mouse experiments clearly disprove the idea of dedifferentiation of mature tubular cells as part of the repair process. Therefore, the adult kidney has a limited capacity to restore lost TECs, as this ability bound by a specialized group of immature cells called kidney progenitor.

The role of kidney progenitors in the regeneration of nephrons following AKI is a topic of ongoing research and debate. These cells are located throughout the nephron and can replace individual epithelial cells, and sometimes even regenerate entire tubule segments[57-59]. However, if these progenitors are lost, nephron regeneration may be hindered, resulting in permanent loss. Assessing nephron loss accurately in clinical practice is challenging since kidney function may recover to some extent even after persistent AKI[60]. However, it is crucial to recognize that functional recovery does not certainly signify regeneration, since functionality can also be increased through TECs becoming polyploidized in unaffected nephrons[57]. This mechanism allows for an increase in functional output in kidney with limited turnover of cells. Activities such as mitotic events and dedifferentiation, which do not affect functional performance, are not suitable for maintaining kidney function during the critical phase required for survival in injured kidneys. In cases of severe ATN, polyploidization and progenitor proliferation are inadequate to maintain residual function[61]. Severe ATN can be fatal without kidney replacement therapy to bridge the period until a kidney function level that can sustain life is restored.

1.2.2 Cellular immune response in AKI

The study of the pathophysiology of AKI is a complex endeavor, with multiple factors participating in the injury and recovery process. One particularly crucial aspect of this process is the innate immune system with various leukocytes playing a prominent role as initiators of inflammation, regulators of cell apoptosis and necrosis, and facilitators of repair in PTECs. Immune cells are a key component in the development and

progression of AKI, and thus a deeper understanding of the processes by which these cells contribute to the injury and recovery process is of great significance in the field of nephrology[45, 62].

1.2.2.1 Neutrophils

In the context of experimental ischemia/reperfusion injury (IRI), the early infiltration of neutrophils into the kidney interstitium has been well documented as a key factor in the crescendo phase of necroinflammation. As the primary mediators of inflammation, neutrophils release cytokines such as interleukin (IL)-1 and -17, causing downstream immune activation[63-65]. Neutrophil extracellular traps are structures comprised of chromatin, nuclear, granular, and cytoplasmic proteins expelled by neutrophils in response to both pathogenic infections and sterile inflammation[66]. During the early phase of reperfusion, the formation of neutrophil extracellular traps can amplify kidney injury and exacerbate remote organ damage after neutrophils migrate to the kidney endothelium and start inflammation-mediated tissue injury[67]. However, the impact of neutrophils on kidney injury remains controversy, as various efforts to inhibit or deplete their function have produced inconsistent results, with some studies reporting protection[68, 69], while others have found a lack of protection[70, 71], depending on the method used and species studied.

1.2.2.2 Macrophages

Macrophages present in the kidney can be roughly categorized into two distinct subtypes, namely resident macrophages, and infiltrated macrophages. Resident macrophages originate from embryonic tissue and are capable of self-renewal, while bone marrow-derived macrophages (BMDM) are recruited to the injury tissue during the inflammatory response[72]. With age, the embryo-derived resident macrophages are gradually replaced by BMDM and shifts in surface marker expression can occur under conditions of inflammation or stress[73]. Macrophages are highly adaptable and can adopt various phenotypes upon exposure to internal and external stimuli, particularly immunomodulatory transcription factors that regulated by cytokines from injury cells, which explains their different phenotypes in different tissue environments. Studies have shown that the source of macrophages can influence their function, with transcriptional studies demonstrating that resident macrophages exhibit specific functions and characteristics across different tissues[74]. Usually, the infiltrated macrophages play a pro-inflammatory role in tissues in the early phase following injury, while resident macrophages can exhibit anti-inflammatory ability and support the subsequent restoration of kidney structure[75].

During the early stages of AKI, monocytes enter the kidney interstitial compartment and polarize into the classic pro-inflammatory type M1 macrophages upon exposure to damage-associated molecular patterns and lipopolysaccharides. These M1 macrophages then act as a source of cytokines and chemokines, recruiting more immune cells and further releasing inflammatory mediators that expand the inflammation and exacerbate tissue damage. During the repair phase, however, M1/0 macrophages undergo a phenotype switch into alternatively-activated type M2 macrophages, capable of supporting tissue repair and mitigate inflammation through the secretion of factors such as TGF-β, fibronectin, Wnt-7b, IL22, and IL1 receptor antagonists, which aid in the repair of renal tubular epithelial cells[2, 76, 77]. The presence of colony-stimulating factor induces the classical M2-phenotype macrophages, which promotes kidney tissue repair through the cytokines production, such as TGF-β, IL10, insulin-like growth factor, and hepatocyte growth factor[78]. These cytokines have the ability to suppress T-cells and macrophages, thereby alleviating kidney inflammation.[79] This concept is further supported by macrophage depletion studies at different timepoints during AKI. Deletion prior to AKI lowers the level of kidney inflammation and damage, however, deleting macrophages three days after surgery results in a delay in the repair of tubules[76]. Nevertheless, over-activation of M2 macrophages may lead to increased production of TGF-β and Galectin-3, which directly contribute to kidney interstitial fibrosis[80]. This is due to the ongoing injury that follows AKI, which help the development of CKD by perpetuating inflammation and fibrosis through the activation of macrophages in the kidney interstitium[81], i.e., AKI-CKD transition. In these instances, blocking the CX3C motif chemokine receptor 1 on macrophages can alleviate interstitial fibrosis[82] and the deletion of macrophages using sodium chlorophosphite significantly reduce kidney tissue damage and fibrosis after ischemia-reperfusion[83]. Therefore, the recovery from AKI is associated with the infiltration of renal macrophages and their continuous activation, which leads to late kidney interstitial fibrosis[76, 84, 85].

1.2.2.3 Lymphocytes

The presence of lymphocytes in the kidneys is not substantial even in AKI. Nevertheless, lymphocytes do play a role in AKI[86]. Firstly, T cell recruitment occurs during AKI in both the early injury and recovery stages, and a significant raise in CD4 cells number were detected in the early stages[87]. Mice that lack either B cells or T cells are less vulnerable to AKI. However, Rag1-knockout mice, which absence both of mature B and T cells within tiny lymphoid organs, show no change in response to injury[88, 89]. The protective effect can be restored in these mice by introducing either B or T lymphocytes, but not both, indicating the injury outcome is influenced by intricate interactions among different lymphocyte populations[90].Forkhead box $P3^+$, $CD25^+$ regulatory T cells have been documented to counteract tissue injury, as a deficiency in these cells leads to an

increase in inflammation and tissue damage after IRI[91].A study using B-cell deficient mice indicated that chimeric animals exhibited a quicker recovery than wild type mice, suggesting that B cells are participating in tissue restoration[92]. Another study reported that the introduction of lymphocytes from animals that had been previously exposed to severe IRI into naive recipients resulted in the induction of albuminuria, implying that immunological memory contributes to the proteinuria development and could play a role in facilitating the onset of CKD after AKI[93]. However, the precise role of lymphocytes in tissue repair remains unclear.

1.3 RNA-binding proteins (RBPs) and Regnase3

RBPs are crucial regulators of gene expression and have been studied in many diseases like neurological disorders (e.g., amyotrophic lateral sclerosis)[94], genetic disorders[96], muscle atrophies, and cancer[95]. These proteins can recognize and bind multiple transcripts, forming wide regulatory networks that maintain cellular integrity. Bioinformatics studies disclosed that there are more than 1,500 potential RBPs, accounting over 7% of all gene that coding protein in the human genome. Additionally, there is mounting evidence suggesting that RBPs is substantial in various kidney diseases, such as diabetic kidney disease and glomerular diseases[97]. Targeting RNA-protein binding presents a promising therapeutic opportunity for these conditions.

1.3.1 RNA-binding proteins functions

RBPs control gene expression by attaching to RNAs via specific domains known as RNA-binding domains (RBDs). These domains consist of the widely observed RNA recognition motif, the zinc-finger domains, DEAD box helicase domain, and other atypical domains[98]. Moreover, numerous RBPs have mononucleotide and dinucleotide binding domains or disordered regions that interact directly with RNA[99-102]. RBPs can interact with variety of RNA molecules including both coding and non-coding RNA, as 38% is predicted to bind messenger RNA (mRNA), 12% transfer RNA and 14% ribosomal RNA. These RNAs share similarities through which these interactions regulate numerous processes[103-105] such as modulating long non-coding RNA, small nuclear RNA, microRNA, small nucleolar RNA, PIWI-interacting RNA, and even extrinsic RNAs like viral RNAs (Figure 2)[98]. This highlights the importance of RBPs in the gene expression regulation and the potential for targeting RBPs as a therapeutic strategy.

RBPs exert a fundamental contribution in the gene expression regulation through their influence on the various stages of nuclear processing of pre-mRNA, including splicing pre-mRNAs, 5' capping, 3' polyadenylation, mRNAs exporting, mRNAs stability, and protein translation[106]. This process commences with RNA

transcription and is carried out through large and complex ribonucleoprotein machineries[107]. Once the pre-mRNA has been modified with a 5' cap and its introns have been removed, it is polyadenylated and packaged to mRNA-protein complexes, and then transported to the cytoplasm[108], with the entire process being tightly regulated by RBP binding[109]. RBPs also regulate mRNA decay, by removing the 5' capping and the 3' poly-A-tail and providing access to exonucleases. Some RBPs also degrade mRNA transcripts through binding to specific recognition motifs.

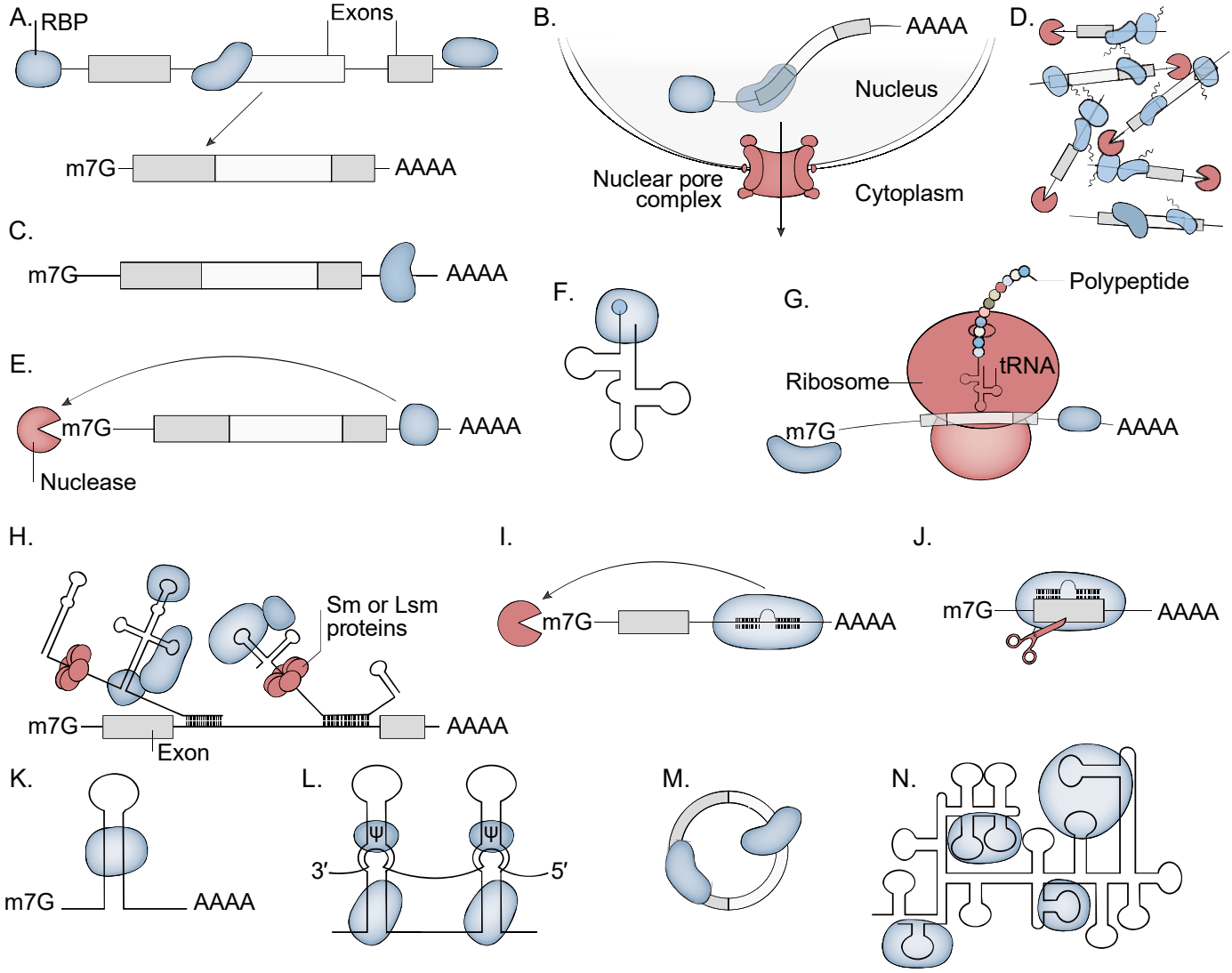

Figure 2. RNA-RBP interactions and biological functions. RBPs are important for the A. pre-mRNA processing, B. assembling and disassembling of ribonucleoprotein complexes for transporting mRNA, C. Influencing mRNA stability, D. Participating the formation of membraneless organelles, E. Handling mRNA decay, F. Binding with tRNA, G. Regulating translational initiation, and interactions with H. small nuclear RNA, I. MicroRNA, J. Short-interfering RNA or Piwi-interacting RNA, K. long non-coding RNA, L. Small Cajal body-specific RNA and Small nucleolar RNA and M. Circular RNA, N. Ribosomal RNA. Information and figure adopted and modified from Ref.[97].

The interaction between RBPs and other proteins, including the regulation on RNA-binding partners that are associated with RNAs through the non-RBPs mediator, has significant impact on cellular processes. One

example of this is the direct interaction among the poly(A)-binding protein 1, the ATP-dependent DEAD-Box helicase 3 X-linked protein and non-RBP translation initiation factors. This interaction is essential for the mRNA's regulation, which impact their expression and further modulates the cell cycle[110]. Additionally, RBP heterogeneous nuclear ribonucleoprotein M and RBP fox-1 homologue 2 have a very close RNA targets binding site's location. These two RBPs functionally cooperate with one another, implying that there is general coordination between them[111].

1.3.2 RNA-binding proteins and acute kidney injury

RBPs regulate RNA processing and function in a tissue-specific manner, e.g., through cell-type specific expression of RBPs and their regulatory partners. The formation of RBPs cell-specific complexes can be influenced by various factors, such as the interaction of interacting partners, the RNA local sequence or structure, and post-translational modifications[101, 112-114]. It is worth noting that RNA-binding to RBPs doesn't always result in regulatory effects. While RBPs targets bind with huge number of RNA, only a subset of these may be modulated in specific contexts. These sets of RNAs controlled by an RBP in response to a certain stimulus are referred to as RNA regulons[100, 115]. RBPs create wide-ranging networks with their RNA targets and other proteins that involve feedback and feed-forward control mechanisms, resulting in varying levels of buffering in different cell types. Thus, RBPs can bring about tissue-specific regulation, especially in specific disease scenarios.

The studies by Seufert et al. employed the RNA interactome capture technology to examine the regulation of RNA-protein interaction patterns in tubular epithelial cells subjected to hypoxia signaling in both CKD and AKI[97]. They found over 50 differential RNA-binding capacities of RBPs in these cells under hypoxia conditions[116, 117]. Certain RBPs have been shown to significantly contribute to AKI, including cold inducible RNA binding protein (CIRBP)[118], human antigen R (HuR)[104, 119, 120], Pumilio 2[121], and Y-box binding protein 1[122]. HuR, in particular, has been extensively studied in relation to kidney disease and is believed to play a protective effect for AKI. HuR is present in both the nucleus and cytoplasm and can be translocated in response to various stimuli, such as hypoxia or chemotherapy, to stabilize RNA[123]. The over-expression of HuR protects against ATP depletion-induced apoptosis, while its knockdown decreased the expression levels of cell survival genes such as the 70 kilodalton heat shock proteins and B-cell lymphoma 2[124]. One study demonstrated that kidney injury induced by IRI leads to the direct nucleocytoplasmic shuttling of HuR in PTEC, however, this was not observed in other cell types[124]. In vitro experiments showed that HuR can regulate the expression of

growth factor receptor-bound protein 10 (GRB10), which is crucial for AKT activation and pro-survival signaling. Additionally, the interaction between GRB10 and protein kinase B has been shown to upregulate HuR expression, leading to a positive feedback loop that is active in PTEC under normal conditions and is further enhanced upon ATP depletion[120]. CIRBP is another well-studied RBP that plays a significant role in AKI. It is equipped with an N-terminal RNA-binding motif domain, which enables it to regulate RNA stability and translation through its interaction with 3′UTRs. This protein is capable of translocating from the nucleus to the cytoplasm and influencing various cellular processes in response to cellular stress[97]. Studies conducted on CIRBP$^{-/-}$ mice have revealed that the absence of CIRBP leads to a significant decrease in the levels of inflammatory mediators like IL6, nitrotyrosine, cyclooxygenase-2 and a reduction in the activity of caspase-3. These observations were accompanied by an improvement in renal outcomes after IRI[125]. Furthermore, evidences suggest that administration of CIRBP antibodies and antagonists can enhance kidney function, as evidenced by a reduction in blood urea nitrogen levels after IRI[126], and mitigate septic shock in mouse models[127].

1.3.3 The roles of Regnase family members in AKI

The Regnase family consists of four members, Regnase1 to Regnase4, which are categorized as Cys–Cys–Cys–His-type (CCCH) Zinc Finger proteins thus, Regnase1 to 4 is also referred to as Zinc Finger CCCH Domain-Containing Protein 12 A-D (ZC3H12A-D)[128]. These proteins are also known as Monocyte Chemoattractant Protein-Induced Protein 1-4 (MCPIP1-4). All members of the Regnase family possess two conserved functional domains, a Pilt-N-terminus (PIN)-like domain and the zinc finger domain and that enables the recognition and binding of RNA (Figure 3)[128-131]. There is growing evidence indicating the involvement of the Regnase family in widespread diseases, including sterile inflammation and autoimmune diseases that affect various organs[129, 132, 133].

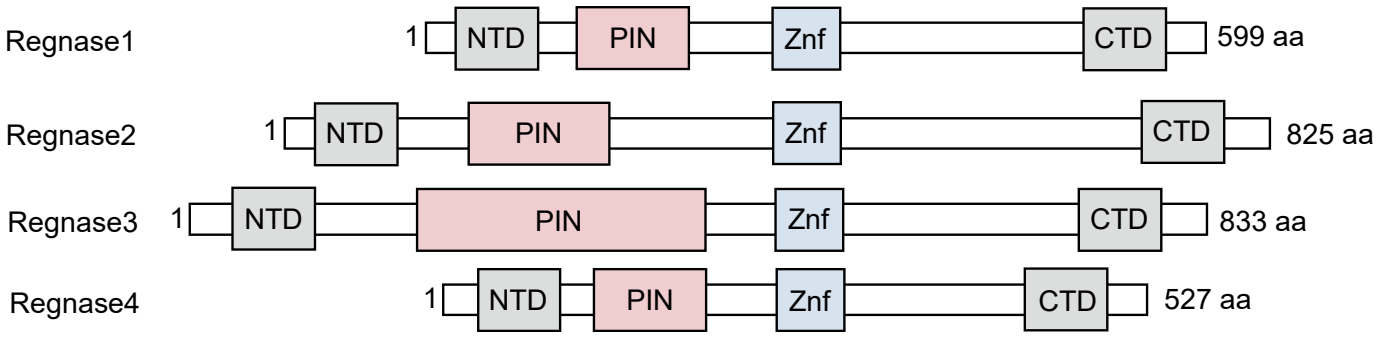

Figure 3. Schematic of Regnase family members. This family contain 4 members, from Regnase 1 to 4. All these proteins hold 4 conserved functional domains as C-terminal domain (CTD), CCCH-type zinc finger domain (ZF), PinT N-terminus domain (PIN) and N-terminal domain (NTD). aa, amino acids.

1.3.3.1 Regnase1

Regnase1 is a well-studied member of the Regnase family, with distinctive characteristics and functions. The global deficiency of Regnase1 in mice has been shown to result in premature death and the development of severe autoimmune responses, including anemia, elevated levels of immunoglobulins in the serum, and the production of autoantibodies[134]. Regnase1 has been recognized as a negative regulator of macrophage activation[131] and its conditional knockout in myeloid cells is associated with spontaneous autoimmunity and autoinflammation[135-138]. The absence of Regnase1 in macrophages resulted in overexpression of Il6 and Il12b under presence of Toll-like receptors (TLR) ligand but with no alteration in the activation of the TLR pathway[134]. The overactivation of Regnase1 promoted degradation the mRNA of Il6 and regulation of additional targets such as the mRNA of Il12b and calcitonin receptor, suggesting that Regnase1 is necessary in regulating inflammation and immunity in macrophages and granulocytes[134]. Furthermore, Regnase1 serves not only as an immunomodulator, but also directly participates in the defense against positive- and negative-sense RNA viruses and DNA viruses[139, 140].

The IKK complex exerts a regulating effect on Regnase1 by controlling its phosphorylation, and when Regnase1 is phosphorylated, it loses capability of mRNA degradation and released into the cytosol from the endoplasmic reticulum [141]. Consequently, the degradation of mRNA through Regnase1 might be contingent upon the function of the IκB kinase complex[142]. Regnase1 also displays post-translational activity by deubiquitination, specifically in promoting the elimination of ubiquitin from TNF receptor-associated factors and further regulating the c-Jun N-terminal kinases (JNK) and downstream NF-kB[143]. Furthermore, Regnase1 was confirmed to negatively regulate sterile inflammation and limit the occurrence of AKI induced by IRI in Regnase1 knockout mice[144]. This observation highlights the potential regulatory function of macrophage-specific Regnase1 during the AKI-to-CKD transition phase, when large numbers of macrophages are present in the tubulointerstitium of the injured kidney. This is in line with previous studies that showed that Regnase1 knockdown exacerbates liver IRI in mice[145], indicating that Regnase1 operates as a negative regulator of immune responses in the kidney[146-148].

1.3.3.2 Regnase2 and Regnase4

Despite being a member of the Regnase family of RBP and having been proven to be involved in immunomodulation[128], Regnase2 and Regnase4's functions have remained largely unknown. Regnase2 is

unique in comparison to other Regnase family members, as it is not induced by stimulation with lipopolysaccharide (LPS) and interferon gamma (IFNg), unlike Regnase1 and Regnase3[149]. Although it has been demonstrated that Regnase2 shares some messenger RNA targets with Regnase1[149] and interacts with IL6 mRNA, the underlying mechanism remains a mystery.

Regnase4 is highly expressed in the spleen, lung, and lymph nodes, but relatively low expressed in other organs such as the liver, heart, intestine, thymus, and kidney[150]. Absence of Regnase4 does not significantly affect lymphopoiesis, as there were no observed changes in the physiological profiles of lymphocytes in the blood, spleen, and lymph nodes[151]. However, a notable raise in the T cells number and cytokines upregulation, such as TNF, IL6, IL2, and IL10, was observed and confirmed to be degraded by Regnase4[152]. In macrophages, Regnase4 expression can be stimulated by TLR ligands via the JNK and NF-kB signaling pathways. Regnase4 overactivation has been shown to inhibit macrophage inflammation and downregulate the activation of TLR2 and TLR4, as well as the associated JNK, and NF-kB signaling. Additionally, Regnase4 has been shown to decrease global cellular ubiquitination, similar to Regnase1[128]. The interaction between Regnase4 and Regnase1 in developing a complex that play a necessary role in mRNA decay. This complex has been shown to co-localize and express with Regnase1 in processing complex, which promotes degradation of mRNA[153]. Despite these findings, the relationship between the Regnase family is still controversial and requires further study, and the functions of Regnase4 in inflammatory remain to be fully understood.

1.3.4 Regnase3 in ischemia-reperfusion kidney injury

Data on Regnase3 (Figure 4) are scarce. A first study suggested that Regnase3 may contribute to regulate cell migration genes in both colorectal cancer and endothelial cells[154]. Regnase3 contributes to the promotion of inflammation by increasing TNF levels in macrophages and suppressing IL6 levels in plasmacytoid dendritic cells. Macrophages that lack Regnase3 produce less TNF and IL12, while plasmacytoid dendritic cells lacking Regnase3 exhibit higher secretion levels of IL6, potentially mitigating imiquimod-induced inflammation[155]. Regnase3 directly degrades mRNAs of IL6, Regnase1, and IκBζ[155]. Additionally, a study examining LPS-stimulated macrophages revealed that LPS upregulates Regnase1 and Regnase3, which aligns with the upregulation of expression patterns of cytokines like TNF, CCL2, IL1β, and IL6 in macrophages[131]. Gamm et al. showed that Regnase3 is important in maintaining immune balance even though unlike Regnase1, its deficiency does not lead to spontaneous systemic autoimmunity or inflammation. Furthermore, Regnase3 expression is elevated in macrophages following activation by TLR3 and is regulated by interferon regulatory

factors 3 and 7. Additionally, absence of Regnase3 resulted in increased expression of C-C chemokine receptors (CCR) 2 and 5, which may contribute to the development of fibrosis[156, 157]. Collectively, these findings suggest that Regnase3 potentially regulate the behavior of macrophages.

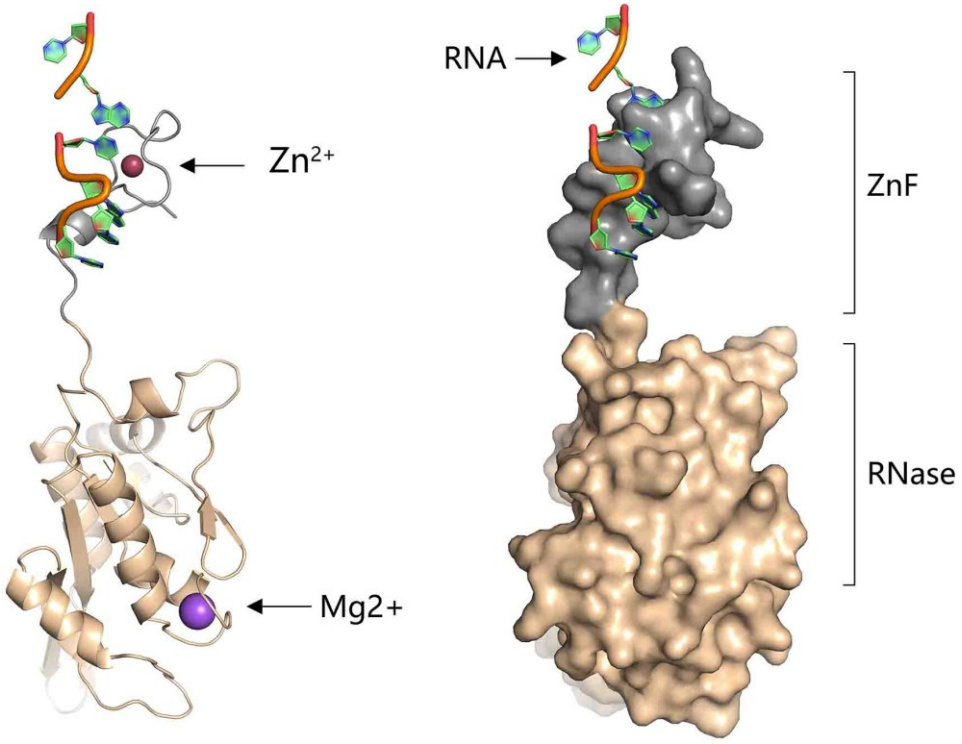

Figure 4. ZC3H12C Pilt-N-terminus-CCCH-type ZnF domain in RNA recognition. (A) Molecular interactions in cartoon and (B) surface representation between RNA and ZnF (grey)/ PIN domain (orange). Adopt from https://www.rcsb.org/structure/7ndj.

In summary, Regnase3 as a member of the Regnase family, has been the subject of investigation in recent years. It has been demonstrated to be involved in the control of various cellular processes, and its ablation has been shown to result in increased inflammation and dysfunction of macrophages. The exact mechanism of Regnase3 function is still under investigation, but it is thought to impact the genes expression regulation through the binding to specific mRNAs and altering their stability or translation into protein. Further research is necessary to fully study the Regnase3 function and its potential therapeutic applications.

2. Research hypotheses

Based on the available information, the central hypothesis of this thesis can be stated as follows:

1. Deletion of Regnase3 from resident macrophages has a detrimental effect on kidney function following ischemic injury. We assume that Regnase3 acts as a negative regulator of macrophage polarization towards a pro-inflammatory phenotype and therefore modulates the early necroinflammation phase of AKI as well as the progression of AKI to CKD.

2. In TECs, Regnase3 is involved in post-ischemic kidney injury. We assume that depletion of Regnase3 in tubular epithelial cells ameliorates cell death upon injury and promotes tubular proliferation and repair upon AKI.

The objectives of the thesis are as follows:

1. To establish animal models that mimic AKI and AKI-CKD transition, and to create mice that allow the conditional Regnase3 depletion selectively in resident macrophages and tubular epithelial cells.

2. To create an in vitro model to study the function of Regnase3 in macrophages under hypoxic damage, with the aim of understanding its role in modulating immunity in the context of AKI and AKI-CKD transition.

3. To establish an in vitro model for investigating the function of Regnase3 in tubular epithelial cells, which will provide insight into the functions of Regnase3 on the cell death and proliferation capacity of these cells following injury.

4. To explore the potential mechanism of Regnase3, which is hypothesized to degrade certain pre-RNAs in order to limit the pro-inflammatory cytokines/chemokines expression and chemokine receptors during kidney necrosis.

3. Material and Methods

3.1 Instruments and reagents

The instruments and reagents used in this study are listed in the Appendix 1 and Appendix 2

3.2 Transgenic mice

To study the role of Regnase3 in the kidney injury, a series of genetically modified C57BL/6J background mice were developed. These included the paired box gene 8 (Pax8)-reverse tetracycline transactivator (rTtA, Pax8rTtA), tetracycline resistance protein (TetO)-Cre (TetOCre), transgenic receptor activator of nuclear factor kappa-B-Cre (RankCre), and Regnase3 floxed (Regnase3$^{fl/fl}$) mice.

The Regnase3fl/fl mice were obtained from Prof. Dr. Christian Schulz at the Ludwig-Maximilians-Universität München, Munich, Germany. These mice carry a targeting vector in intron between exon 3 and exon 4 with a selection cassette flanked by flippase recognition targeting sites, while exon 4 is flanked by loxP-site. The splice acceptor together with a poly-A signal leads to a mature and spliced fusion mRNA of β-galactosidase (lacZ) gene sequence in Exon 3. The poly-A signal causes a premature transcriptional stop and consequently a truncated gene product. These mice were crossed with mice expressing FLP recombinase with a general promotor, which generates offspring that have lost major parts of the inserted cassette including the premature poly-A signal but remain two loxP sites within the introns flanking Exon 4 (Figure 5). These Regnase3-floxed mice (Regnase3$^{fl/fl}$) could be further crossbred with mice expressing a site-specific Cre recombinase to obtain conditional deletion of Regnase3.

Transgenic RankCre Regnase3 mice were developed by crossing-breeding RankCre mice and homozygous floxed Regnase3 mice. The RankCre mice[158] were received from Prof. Dr. Christian Schulz, Ludwig-Maximilians-Universität München, Munich, Germany. As described before[159], RankCre mice were generated by inserting the recombinant Cre gene into the promotor of Rank. We set up the mice strain with the Regnase3 deletion in Rank positive cells after crossing with Rank Cre mice. Only male littermates of 8-12week-old were used for experimentation. Mice without the RankCre but homozygous of the floxed Regnase3 gene were considered as wildtype and those with heterozygous RankCre and the homozygous of the floxed Regnase3 were considered as Regnase3 knockout (Rank-Regnase3cKO, Figure 5).

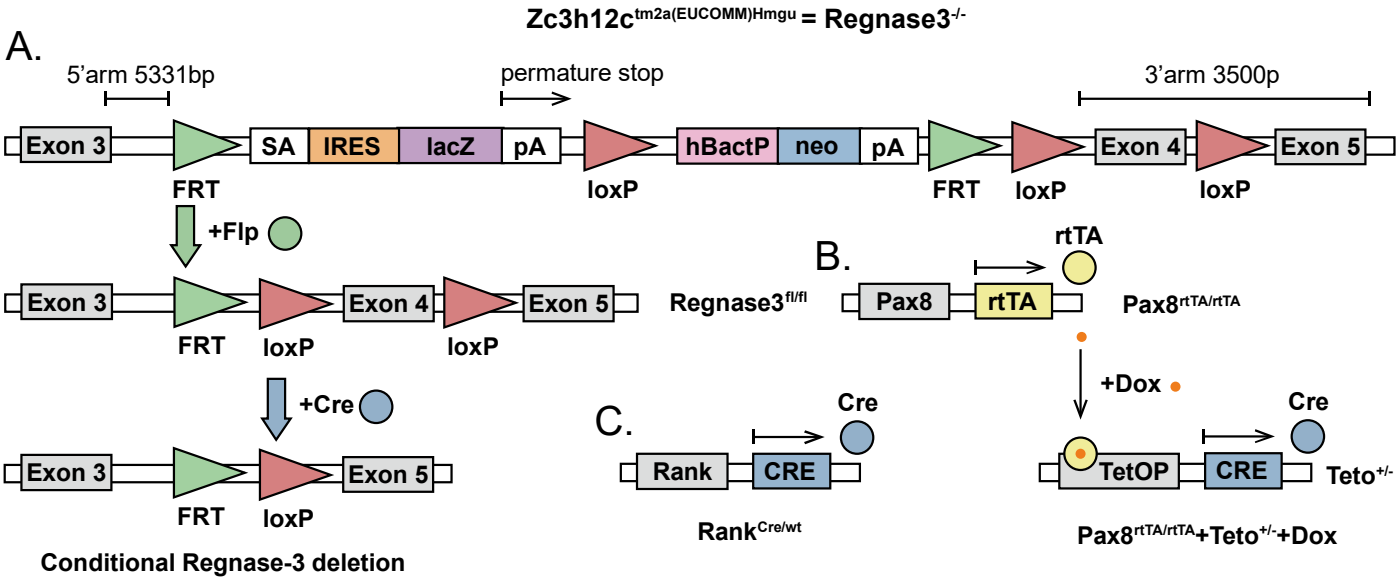

Figure 5. Schematic representation of the targeting strategy for Regnase3 conditional knockout mice. (A) Targeting vector for Zc3h12c$^{tm2a(EUCOMM)Hmgu}$ mice. Breeding strategies with promotor-driven FLP recombinases and to obtain mice with a floxed Zc3h12c (Regnase3) allele and then mice with a conditional deletion of Exon 4 in the Zc3h12c gene locus upon the Cre recombinases present. (B) The Pax8 gene promoter was modified with the transactivator rTtA, and the Pax8rTtA promoter controlled the TetOCre recombinase. Upon Doxycycline induction, the rTtA transgene was activated, leading to the activation of the TetOCre recombinase. The recombinase then cut the loxP site of Regnase3. (C) Cre recombinases insert into the Rank promotor. Flippase, FRT; FLP recombinase target, FRT; splice acceptor, SA; human beta-actin promoter, hBactP; internal ribosome entry site, IRES; β-galactosidase, lacZ; poly-A, pA; mycin resistance gene neo, Neo.

Pax8rTtA-TetOCre mice were generated through crossing the B6.Cg-Tg (TetO-Cre)1Jaw/J with Tg (Pax8-rtTA2S*M2)1Koes. These strains were received from the Jackson Laboratory. Transgene recombination of Pax8rTtA, TetOCre, and Regnase3$^{fl/fl}$ was induced by 5% D (+)-saccharose water with 2 g/l of doxycycline hyclate (refreshed every 2 days) for a minimum of two weeks to the littermates. This process was intended to stimulate recombinant Cre expression and cutting of the Regnase3 flox cassette in Pax8 positive cells, resulting in an inducible Regnase3 deletion. The experiments were performed on 8-12 weeks old male mice. The control group for the study was composed of mice with no recombinase Cre but only homozygous floxed Regnase3, referred to as wildtype (Pax8-Regnase3WT, Figure 5). Mice with both heterozygous Pax8rTtA and heterozygous TetOCre, and the homozygous of floxed Regnase3 gene were used as Pax8-Regnase3cKO in this study.

3.3 Animal studies

All mice were housed under specific-pathogen-free conditions under a 12-h light and dark cycle with the temperature of 22 ± 2°C. All necessary materials including mice cages, diet, drinking water and nesting

materials were thoroughly sterile through autoclaving prior to usage. During the duration of the experiments, mice were provided with standard chow diet (Ssniff, Soest, Germany) and access to water ad libitum. It is important to note that all mice models were conducted in adherence to German animal care legislation, the EU Directive 2010/63/EU, and were permitted by local government authority (Regierung von Oberbayern).

Table 2. Receipts for the Narcosis, Antagonist and Analgesia

Application	Drug	Administration Method	Conc. (mg/kg)	Cat.	Company
Narcosis	Medetomidine	i.p. once prior to surgery	0.5	7725752	Zoetis
	Midazolam		5	4921530	Ratiopharm
	Fentanyl		0.05	2084366	Janssen-Cilag
Antagonist	Atipamezole	s.c. once after the surgery	5	8-00732	CP-Pharma
	Flumazenil		0.1	4470990	Hexal
Analgesia	Buprenorphine	i.p. 30 min before antagonization, t.i.d. after the surgery for 3 days	0.1	1498870	Bayer Vital
	Metamizole	p.o. 5min before narcosis induction	200	731672	Sanofi-Aventis

* i.p., Intraperitoneal injection; s.c., subcutaneous; p.o. oral administration

3.3.1 Unilateral kidney ischemia-reperfusion surgery

Kidney unilateral IRI with or without nephrectomy of the contralateral kidney was conducted as described before[160]. In order to conduct the procedure in an ethical and controlled manner, mice preemptively received the analgesic Metamizol, followed by anesthetization in accordance with the established protocol (Table 2). During the surgical procedure, measures were taken to maintain the core body temperature of the mice within the recommended range of 36.5°C to 38.5°C[160]. An online rectal temperature monitoring system was utilized to continuously monitor the body temperature of the mice until the wound closure process was completed[160]. To maintain the mice's body temperature stability during the perioperative period, they were kept in an incubator set at 37°C. Additionally, the surgical procedure was performed on an operating table maintained at a constant temperature of 41°C to further ensure the mice's temperature. The experimental group underwent nephrectomy (NX) on the right kidney, followed by one week later, the left renal pedicle was clamped for 16 or 17 minutes using a microaneurysm clamp (Medicon, Tuttlingen, Germany). To avoid dehydration or contraction of the uncovered kidney, two drops of physiological saline at a temperature of 37°C were administered to all mice. After removal of the clamp, the kidney recovery was confirmed through observation of blood reperfusion and the return of the kidney to its original color. Then, the muscular layer was sutured using Vicryl while Ethibond was used for the cutaneous layer for the wound closure process. Buprenorphine was given as analgesia 30 minutes before ending the anesthesia. The same operation was conducted on sham

group mice, except for the renal pedicle clamping step. The pain management regimen following surgery includes the administration of buprenorphine every 8 hours for the first three days followed by every 8 hours for the fourth day and every 12 hours for the three days.

3.3.2 Calcium oxalate (CaOx) model

Male mice of eight weeks old were housed in filter-top cages in groups of five, with unrestricted access to food and water. The mice were fed the oxalate-rich diet (Ssniff, Soest, Germany) to produce nephrocalcinosis-related kidney injury, which involved supplementing the calcium-free standard diet with 50 μmol/g of sodium oxalate, as previously described[161, 162].

3.4 Blood sampling

Before sacrifice, blood sample was obtained through retro-orbital bleeding approach under anesthesia by 20% oxygen isoflurane. The sample was collected in 1.5 ml tubes with heparin and centrifuged for 10 minutes at 800 revolutions per minute, subsequently the plasma supernatant was collected and stored at -80°C for future use.

3.5 Creatinine measurement

To measure creatinine levels in plasma samples, a standardized protocol was implemented utilizing a commercial creatinine assay kit. Standard solutions were created with varying concentrations to establish a standard curve for reference. The working reagent mix (R1:R2 = 4:1) was prepared according to the instructions of kit. A 10μl plasma aliquot was placed onto the 96-well plate and mixed with the reagent immediately prior to measurement. The absorbance was then read at 492 nm at specific time intervals (60, 120, 180 seconds, and 20 minutes) after the plasma-reagent mixture was formed. The adjusted absorbance was normalized by subtracting the blank reading. The final creatinine concentration in the plasma sample was then fitted by applying the adjusted absorbance value to the standard curve.

3.6 Measurement of glomerular filtration rate (GFR)

We measured GFR by assessing sinistrin clearance using a transdermal registration method according to the protocol[163]. A sinistrin compound conjugated with fluorescein-isothiocyanate (FITC) was utilized as an exogenous GFR tracer to determine the excretion kinetics. The FITC-sinistrin solution was prepared in 30 mg/ml in physiological saline. The mice were first anesthetized by 20% oxygen isoflurane before the GFR

device (Medibeacon, Germany) with the battery was mounted to the shaved neck of the mice via a patch (Medibeacon, Germany), with one side of the patch attaching to the GFR device with the battery and the other side attaching to the mice. The device was then secured in place with hypoallergenic silk tape. The device begins recording data after a light-emitting diode flashes. To acquire the baseline signal, the device was left running for approximately 10 minutes. Subsequently, the FITC-sinistrin was administered to the mice via intravenous injection at a dose of 0.15 mg/g. The measurement period is approximately 1.5 hours. The GFR device data were read and processed using the MPD Lab software (Medibeacon, Germany).

3.7 Immunohistochemistry

Kidney tissue samples were harvested and fixed in a 4% formalin solution for 24 hours. The samples were then processed using a tissue processor (Leica) to produce paraffin-embedded blocks. These blocks were subsequently sliced to obtain paraffin sections, which underwent a process of de-paraffinization by being exposed to xylene for three cycles of 5 minutes each. The sections were then rehydrated by immersing them in a series of ethanol solutions, starting with 3 minutes absolute ethanol for 3 cycles, followed by 2 cycles 95% ethanol for 3 minutes, and 3 minutes with 70% ethanol. This was followed by rinsing the sections with PBS for 3 cycles of 5 minutes.

To suppress endogenous peroxidase, tissue sections were treated in a solution consisting of methanol and 3% hydrogen peroxide for a duration of 20 minutes in dark. Subsequently, the sections were thoroughly washed with PBS 3 times for 5 min each. The process of antigen unmasking was then performed by immersing the tissue sections in an antigen unmask reagent and put them in the microwave for steaming 10 min. To further block endogenous biotin, the sections were further incubated with Avidin (Vector) for 15 minutes, followed by an additional 15 minutes with biotin (Vector). The tissue sections were incubated 12 hours at a temperature of 4°C with primary antibodies of Lotus tetragonolobus lectin (LTL) or Tamm-Horsfall protein (THP-1). After that, biotinylated secondary antibodies were applied to the sections for 30 minutes, followed by PBS washing. The sections were then treated with substrate reagent (ABC solution, Vector) for 30 minutes, washed by PBS, rinsed by 5 minutes Tris, and subjected to DAB staining. Methyl-green (Fluka) was used as a counterstain for the sections. Excess stain was removed by washing the sections with 96% alcohol, followed by treatment with xylene. Finally, the sections were mounted with VectaMount (Vector) after drying. Python and OpenCV[164] were utilized for quantifying the THP-1 and LTL, by determining the proportion of the THP-1 positive area in the kidney medulla and the proportion of the LTL positive area in the kidney cortex.

3.8 Periodic acid Schiff (PAS) and Sirius red staining

PAS staining. The sections that had been rehydrated were initially treated with 2% periodic acid for 5 minutes and then rinsed with double-distilled water. Subsequently, they were stained with for 20 minutes Schiff solution and rinsed with tap water. Hematoxylin solution was used to counterstain the sections for 2 minutes and then washed with tap water. After drying, the sections were dipped in 90% alcohol and covered with slips. The injury extent of tubular was measured by assessing the corticomedullary junction proportion that demonstrated indications of brush border loss, tubular dilatation and cast formation. A scoring system ranging from 0 to 2 was used to quantify the severity of injury, with 0 indicating no injury and 2 indicating 100% injury. The overall PAS score was graded on a scale of 0 to 8.

Sirius red staining. The Weigert's hematoxylin was first used to stain the rehydrated sections for 8 minutes and then washed with double-distilled water. Picro-sirius red was applied for 60 minutes, and then rinse the sections with tap water. Following that, the sections were dipped in 90% ethanol and covered with slips after drying. The extent of kidney fibrosis was determined by calculating the percentage of collagen (Red) in the tissue sections using python and OpenCV[164].

3.9 TdT-mediated dUTP-biotinnick end labeling (TUNEL)

TUNEL Assay Kit-FITC (ab66108) was utilized to identify dead cells in the kidney. The slides were evaluated and subsequently photographed by fluorescence microscope.

3.10 RNA isolation and polymerase chain reaction (PCR)

3.10.1 RNA isolation

The tissue samples were carefully and delicately transferred to a container with 2 milliliters of lysis buffer, which contains 1% 2-mercaptoethanol, using forceps. The samples were always kept on the ice to ensure preservation of the RNA integrity. The samples were homogenized for 20 seconds at a level 4 setting on the Ultra-Turrax machine. The homogenized samples were then centrifuged at 6,000g for 5 minutes to separate the supernatant from the pellet. The supernatant was saved and transferred to a new, RNase-free tube. Subsequently, 700 microliters of the supernatant were added to an equal amount of 70% ethanol, and the mixture was thoroughly mixed. The rest of the RNA isolation procedure was carried out by following the

Qiagen mRNA extraction kit instructions. The RNA samples were subsequently put in storage at -80°C for long-term preservation.

3.10.2 Reverse transcription for RNA

The purified RNA was subjected to a denaturation process by incubating it at 65°C for 10 minutes to breakdown the secondary structures of the RNA. This reaction was subsequently halted by placing the RNA at 4°C. Each sample's RNA was prepared at a final concentration of 2µg in 22.45µl of a pre-prepared master mix (as outlined in Table. 3). The resulting mixture was then kept at 42°C for 2 hours followed by an 85°C for 5 minutes to generate cDNA. The cDNA was then deposited at -20°C for future use.

Table. 3 RNA reverse transcription master mix

Master mix	Concentration	Volume (µl)
Taq buffer	5x	4.5
DTT	0.1M	1
dNTPs	25 mM	0.45
Rnasin and ribonuclease inhibitor	40 u/µl	0.5
Acrylamide	15 µg/ml	0.25
Hexanucleotide Mix	10x	0.25
Superscript II	200 u/µl	0.5
Sample	2 µg	15
Total		22.45

Table 4. Master mix for the quantitative real-time PCR

Master mix	Concentration	Volume (µl)
Mix SybrGreen		10
Taq polymerase	5000 u/ml	0.16
Reverse primer	10 µM	0.6
Forward primer	10 µM	0.6
cDNA		0.2
ddH2O		8.44
Total		20

3.10.3 Quantitative Real-time PCR (qPCR)

The SYBR-Green was utilized as fluorescent dye for qPCR. The cDNA samples were first diluted at a ratio of 1:100 and then mixed with SYBR-Green, Taq polymerase (Table 4), and primers (as outlined in the Appendix 3). The mixture was run on a Light Cycler 480 instrument with the following setting: 5-minute pre-incubation at 95°C, 15-second amplification at 95°C, 60°C for 15-second, and 68°C for 20-second, with 40 cycles total. A melting curve as also performed at 95°C for 5-second, 65°C for 60-second. The samples were

then cooled to 40°C for 30-second. The cycle threshold values were analyzed using the Light Cycler 480 instrument. For statistical analysis and plotting, the mRNA relative expression was determined using the cycle threshold values normalized by 18s rRNA.

Table 5. Primers for the genotype

Primers	Sequence	Product
Rank Cre		
Rank-ORF#1618_fw	TCAAGGGTGACATCATCGTGGT	506 bp
Rank-Cre_PGKNeo_fw	GTAACTTCTCCATGGTAGCCTC	251 bp
Rank-ORF#2321_rev	CTCAATAATGCAGGACACCAACG	
Pax8 rTta		
M_Pax8_rTta_FWD	CCATGTCTAGACTGGACAAGA	
M_Pax8_rTta_REV	CTCCAGGCCACATATGATTAG	
TetO Cre		
M_TetO_Cre_FWD	TCGCTGCATTACCGGTCGATGC	
M_TetO_Cre_REV	CCATGAGTGAACGAACCTGGTCG	
Regnase3 flox		303 bp
gRegnase3_WT+KO_#3_F	GGAAGAAGTTCATAGATGAGCGG	
gRegnase3_KO_#2_R	GAACTGATGGCGAGCTCAGAC	
Regnase3 wild type		401 bp
gRegnase3_WT_#1_F	CTGGCTGACAGAAATATCTGTC	
gRegnase3_WT_#1_R	GGTGCTCAGACTTCAACCT	

3.11 Transgenic mice genotype

3.11.1 Pax8rtTA, TetOCre genotyping

The qPCR primers for Pax8rtTA and TetOCre genotyping are listed Table 5. A master mix was prepared according to the protocols outlined in Table 4, and the samples were incubated in the Light Cycler 480 instrument with the following settings. The pre-incubation step was conducted at 95°C for 10-minute, followed by 15-second amplification at 95°C, 45-second at 60°C, and 60-second at 72°C, with a total of 40-cycle. A melting curve analysis was then conducted at 95°C for 10-second and 65°C for 60-second, followed by cooling at 40°C for 30-second. The cycle threshold values were analyzed using the Light Cycler 480 instrument. The mRNA relative expression was determined using the cycle threshold values normalized by 18s rRNA.

3.11.2 Endpoint PCR for Rank Cre and Regnase3 transgene

The primers for genotyping are specified in Table 5. A master mix was prepared for both Rank-Cre and Regnase3-Flox, as outlined in Table 6 and Table 7. The DNA samples were then amplified using an Eppendorf

PCR cycler in the following conditions: for Regnase3, 3-minute pre-denaturation at 95°C followed by 35-cycle of 20-second 95°C denaturation, 30-second 62°C annealing, and 40-second extension at 72°C, with a final 5-minute extension at 72°C. The samples were then deposited at 4°C. For Rank-Cre, 3-minute pre-denaturation at 95°C followed by 10-cycle of 15-second denaturation at 95°C, 30-second annealing at 65°C, and 30-second extension at 68°C, then 28 cycles of 15-second denaturation at 95°C, 30-second annealing at 61°C, and 30-second extension at 72°C, with a final 5-minute extension at 72°C. The resulting sample was stored at 4°C, and then subjected to 2% agarose gel electrophoresis (Figure 6).

Table 6. Reaction components for the Rank genotype

Master mix	Stock Conc.	Volume (µl)
H_2O		18.3
PCR Buffer	10x ′	2.5
dNTP`s	10mM	0.5
Rank-ORF#1618_fw	10µM	0.5
Rank-Cre_PGKNeo_fw	10µM	0.5
Rank-ORF#2321_rev	10µM	0.5
Taq polymerase	5U/µl	0.2
DNA		2.0
Total		25.0

Table 7. Reaction components for the Regnase3 genotype

Master mix	Stock Conc.	Volume (µl)
H_2O		17.8
PCR Buffer	10x	2.5
dNTP`s	10mM	0.5
g Regnase3_WT+KO_#3_F	10µM	0.5
g Regnase3_KO_#2_R	10µM	0.5
g Regnase3_WT_#1_F	10µM	0.5
g Regnase3_WT_#1_R	10µM	0.5
Taq polymerase	5U/µl	0.2
DNA		2.0
Total		25.0

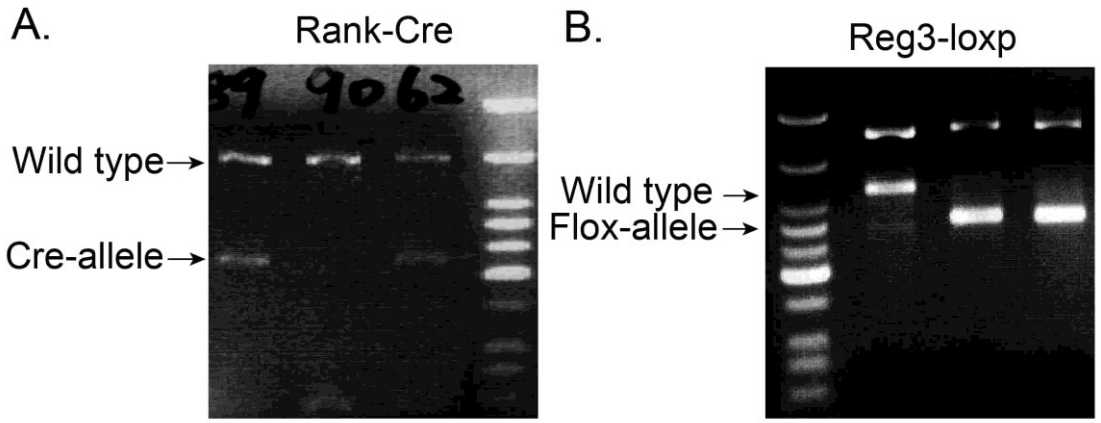

Figure 6. Agarose gel electrophoresis for Rank-Cre and Regnase3-flox. (A) products from Rank-Cre mice: 506 bp for WT band, 251 bp for knock-in band. (B) products from Regnase3-flox mice: 401 bp for WT band and 303 bp for flox band.

3.12 In vitro model

3.12.1 Bone marrow mononuclear cell (BMDM) isolation

After obtaining femurs and tibiae from mice -sacrificed mice by cervical dislocation, the bones were immersed in 75% ethanol for 1 minute before being stored in PBS. Removing the residual tissue from the bones, and the tibiae were separated from the femurs by gently breaking the knee joint. Then removing the terminal caps of the bones by sterile scissors and putting marrow cavity into the cavity to flush the bone marrow with PBS until the bone appeared white. The bone marrow was centrifuged 5-minute at 1,200 rpm for. Then 0.155 M NH_4Cl was used to resuspend the pellet to lyse erythrocytes for 10 minutes on ice, passed through a 70μM strainer, and centrifuged 5-minute at 1,200 rpm. L929-conditioned Dulbecco's Modified Eagle Medium (DMEM, Table 8) was used to suspend the pellet was and cells were grown in culture dishes in an incubator with 37°C, 5% CO_2, and humidity control. Every 3 day the fresh medium added to the dishes, and after 7 days the cells were harvested for further experiment.

Table 8. Recipes for L929-conditioned DMEM medium*

Conditioned medium	Volume
DMEM medium	64 ml
L929-supernatant	20 ml
FCS	10 ml
House serum	5 ml
PS	1 ml
Total	100 ml

*DMEM: Dulbecco's Modified Eagle Medium; FCS: fetal calf serum; PS: Penicillin-streptomycin.

3.12.2 Murine renal tubules isolation

The isolation of renal tubules from mouse was performed using a modified protocol previously published[165]. In brief, the process involved the collection of mice kidneys, which were then decapsulated and smashed and placed in a 2ml tube containing incubation solution (1.3 mM Ca-gluconate, 1 mM a-ketoglutarate, 10 mM $CH_3COONa \times 3\ H_2O$, 1 mM $MgSO_4 \times 7H_2O$, 1.6 mM $K_2HPO_4 \times 3H_2O$, 0.4 mM KH_2PO_4, 140 mM NaCl, 25 mg/l DNAse I and 48 mg/l trypsin inhibitor) with 2 mg/ml of collagenase type II. The mixture was incubated 5-minute at 37°C and centrifuged 5-minutes at 850 rpm. The pellet was loaded with an additional collagenase type II and digested again for 5 minutes under the same conditions. Add 1 ml 10% fetal calf serum (FCS) DMEM medium to the supernatant in a 2 ml tube on ice and wait the renal tubule precipitation. Then remove the supernatant and washed the tubules twice with medium.

3.12.3 Renal primary murine tubule isolation and TEC culture

The process of isolating primary murine TEC followed the same initial steps as that for isolation of fresh murine tubules. Then 2 ml cold PBS was used to load the samples and added onto the surface of 10 ml 31% Percoll. The mixture was centrifuged 20-minutes at 3,000 rpm in 4°C without any brakes and the pellet was collected, washed twice with PBS and suspended by culture medium consisting of DMEM supplemented with1% Penicillin-Streptomycin, 25 ng/ml epithelial growth factor , 5 mg insulin transferrin-sodium selenite supplement, 1% hormone mix (Table 9), 2.5% Hepes (1 M, potential of hydrogen, PH=7.55), and 10% FCS. The cells were kept in an incubation r with 5% CO_2, 37°C, and humidity control.

Table 9. Recipes for the Hormone mix

Hormone mix	Stock Conc.	Volume (µl)
Hanks' Balanced Salt Solution		50 ml
Prostaglandin E1	125 ng/ml	12.5
Triiodothyronine,	3.4 ng/ml	50
Hydrocortisone	1.8 µg/ml	0.5 ml

3.13 Nephrotoxic serum preparation

The nephrotoxic serum was obtained by harvesting 10 million primary murine TEC in 1 ml PBS, which was then subjected to a freezing-thawing process repeated five times. The samples were then centrifuged 5-minute at 500g, and the supernatant was collected as the necrotic protein solution for stimulation. The necrotic protein solution was mixed to the medium and incubated with cells for one day in a ratio of 1:1 for necrotic tubular TEC to stimulated cells.

3.14 Flow cytometry

3.14.1 Kidney mononuclear cell preparation

Anesthetize mice by 20 % oxygen isoflurane and collect the kidney. Then the kidney was processed by removing its capsule and smashing it onto a 6-well plate containing a solution of 2 ml DMEM mixed with40 U DNAse I and 1.5 mg/ml collagenase A and for digestion. The plate was then kept at 37°C while being agitated 45-minute at 120 rpm. The homogenization of the kidney was achieved by squeezing it through a 10 ml syringe with a sterile plunger and passing it through a 70 μm filter. The homogenate subjected to centrifugation 5-minute at 1,200 rpm in 4°C and the resulting pellets were rinsed by fluorescence-activated cell sorting (FACS) buffer (0.1% NaN_3, 1% FCS, 500 ml PBS). In preparation for differential centrifugation, 40% and 70% Percoll solutions were prepared. The sample was then loaded with 8 ml of 40% Percoll and gently overlaid with 70% Percoll in 3 ml before being centrifuged for 30 minutes at 2,000 rpm with brake off in room temperature. Collect the cells from the interface layer between the 40% and 70% Percoll, wash them by FACS buffer and centrifuged. In order to further purify the leukocyte, the sample was subjected to magnetic bead-based depletion using CD45 microbeads (Miltenyibiotec, Germany) and LD columns (Miltenyibiotec, Germany).

Table 10. Antibodies for flow cytometry

Antibody	Clone	Fluorescent dyes	Company
anti-mouse F4/80	BM8	APC	Biolegend
anti-mouse CD192 (CCR2)	SA203G11	FITC	
anti-mouse CD206 (MMR)	C068C2	FITC	
anti-mouse Ly-6C	HK1.4	PerCP/Cyanine5.5	
anti-mouse CD86	GL-1	PerCP	
anti-mouse/human CD11b	M1/70	PE/Cyanine7	

3.14.2 Cell staining

Following the washing step with the FACS buffer, the sample underwent treatment with an Fc blocker to eliminate any non-specific binding to the Fc receptors. The sample was then exposed to an antibody conjugated with a fluorochrome, as specified in Table 10, for a duration of 30 minutes in the absence of light at 4°C. After this step, the sample underwent another washing phase with FACS buffer, followed by centrifugation. Resuspend the pellet in FACS buffer in preparation for flow cytometry analysis.

3.15 Cell viability and cytotoxicity assay

Cell viability activity: The cells were cultivated on 96-well plate, with each well containing $1x10^4$ cells, and a 100 µl volume of cell culture medium with a 2.5% FCS concentration. The cells were allowed to adhere overnight and prior to stimulation, all medium was replaced. The positive group was subjected to 2% Tween stimulation for a duration of 30 minutes. Subsequently, the old medium was aspirated and 100 µl 3-(4,5-Dimethylthiazol-2-yl)-2,5-Diphenyltetrazolium Bromide (MTT, CT01, Sigma-Aldrich) was put onto the well and incubated for 4 hours to facilitate the reaction. Afterwards, add 100 µl stop solution onto well and the plate was stored overnight in a humid environment. The samples were analyzed using an enzyme-linked immunosorbent assay (ELISA) reader with absorbance read at 570 nm. The reference wavelength was required to be greater than 650 nm.

Cell cytotoxicity: The cells were seeded onto the 96-well plate at $1x10^4$ cell/well in 100 µl 2.5% FCS medium and left overnight for the cell adhesion. Prior to stimulation, all the medium was replaced. The positive control group was subjected to 2% Tween for 30 minutes. After the stimulation, 50 µl supernatant was transferred onto a new plate. According to the protocol (4744934001, Roche), 50 µl of lactate dehydrogenase (LDH) reagent from the kit was put into well, and immediately read the absorbance at 450 nm was using the ELISA reader at 5-minute intervals. The reference wavelength was required to be greater than 650 nm.

3.16 Transwell migration assay

The Transwell migration assay was carried out utilizing 8-micrometer pore size inserts (designated as catalog CLS3464-48EA, supplied by Corning® Costar® Transwell® cell culture inserts) as previously described in reference[166]. In accordance with sterile conditions, the bone marrow-derived macrophages (BMDMs) were seeded on the transwell insert, with 2×10^5 cells loaded in 200 µl DMEM, and 700 µl DMEM was put into the bottom well. The plate was placed at 5% CO_2 and 37°C and for 12 hours prior to the initiation of the assay. The bottom surface of the insert was swabbed to remove cells that had migrated through the membrane. Then, add 10ng/ml of Ccl2 to the bottom well and further incubate for 12 hours. After incubation, the Transwell inserts were collected, and 4% paraformaldehyde was used to fix the cells for 5 minutes. The inserts were then washed twice with PBS and 0.1% crystal violet (Invitrogen) was used to stain the cell for 15 minutes. Carefully remove the cells with a cotton swab which remaining on the top surface of the e insert membrane. Imaging of the insert membrane was performed using the 10x objective lens at Nikon Eclipse Ti2 microscope.

3.17 Time-lapse imaging

The primary murine tubular and passaged TEC were subjected to treatment with hydrogen peroxide (H_2O_2) in a 96-well plate and were then imaged at 30-minute intervals. To visualize the permeabilized cells, an additional 500ng/mL of propidium iodide stain was applied. The imaging process was carried out using a 10x objective lens on Nikon Eclipse Ti2 microscope and involved the utilization of transmitted light and fluorescence.

3.18 Phagocytosis of monocyte-derived macrophages

The fluorescent latex beads (green-labeled,1-μm diameter, L4655 Sigma)[167] and a latex beads-rabbit IgG-FITC Phagocytosis Assay Kit (catalog number 500290 from Cayman)[168] was used to quantify the cell's phagocytic activity. To measure the phagocytosis, cells were seeded onto the 96-well plate with $1x10^4$ per well and incubated at 5% CO and 37°CO_2 overnight to allow the cells to adhere. Cytochalasin D (1 μg/mL) was added 45 minutes prior to the bead's incubation, and the beads were then incubated for further analysis.

3.18.1 Phagocytosis assay bead on fluorescent latex beads

The pre-incubation of latex beads was conducted at a concentration of 50 μg/ml at 37°C for 30 minutes in the conditioned medium. Subsequently, 5 μg/ml latex beads were incubated with cells for 3 hours in a 5% CO_2 and 37°C incubator. The 96-well plate was then washed with warm PBS for three times. Images were acquired using the Nikon DS-Qi2 camera with both transmitted light and fluorescence. For quantitative analysis, the CellPose[169] Neural Convolutional Network was employed to detect the cells and create masks for cell location, followed by counting the cell number and calculate the positive area within the cell.

3.18.2 Phagocytosis assay bead on latex beads-rabbit lgG-FITC

In accordance with the instructions provided by the Phagocytosis Assay Kit, the latex beads-rabbit lgG-FITC complex was diluted to a 1:100 with pre-warmed culture medium. The complex was then incubated with cells for a period of 3 hours in a controlled 5% CO_2 and 37°C environment. The 96-well plate was subsequently rinsed three times with warm PBS. In order to differentiate between cells that have internalized the beads and those with beads attached to their surface, the cells were subjected to the trypan blue quenching solution incubation for 2 minutes and wash with FACS buffer. Then the cells were detached from the plate and resuspended in FACS buffer, which ready to undergo flow cytometry analysis[170].

3.19 Cell-substrate impedance sensor (ECIS) system

The impedance of primary murine renal tubule cells (TEC) was analyzed in real-time by seeding 105 cells onto 8W10E+ 8 well arrays (manufactured by Applied BioPhysics)[171]. The arrays were placed in 5% CO_2 with 37°C to facilitate cell adherence and reach full confluency on the sensors. Following incubation, H_2O_2 was added to the medium and further incubate for 24 hours. Afterwards, replace the medium was with fresh one to remove the H_2O_2. The resistance changes were measured at 8,000 Hz by ECIS technology (Applied BioPhysics)[172]. The data obtained was imputed and smoothed utilizing a restricted cubic splines algorithm.

3.20 Single cell RNA-seq (scRNA-seq)

The raw data or count matrices were obtained from several publicly available databases (as indicated in Table 11). The scRNA-seq data was processed using the Scanpy[173] pipeline, which facilitated the integration and merging of different batches of data. Quality control was performed by utilizing the threshold values as reported in the original article (Table 11). The normalization of the data was conducted using the scran[174] package, which included assuming equal size factors, normalizing the library size to counts per million, and log-transforming the count data. The 3000 most variable genes were used for the principal component analysis w. To eliminate technical differences and preserve biological differences, the harmony integration pipeline was employed, which reduces data dimensions and removes batch effects[175]. The reduction of data dimensions and Uniform Manifold Approximation and Projection (UMAP) was applied for unsupervised clustering based on the first 50 integrated principal components. The resolution of clustering was determined accordingly. The gene enrichment score was evaluated by "scanpy.tl.score_genes()" functions.[176]

3.21 RNA-Sequencing

The library construction and sequencing process was carried out by Beijing Genomics Institute utilizing the DNBSEQ (G400) platform. The RNA samples were subjected to 100-base-pair paired-end sequencing. The bioinformatics workflow, which included data filtering, mapped transcript prediction, analysis of differential gene expression and gene ontology, was carried out in accordance with the protocols of hisat2[184], samtools[185], FeatureCounts[191]/ eisaR[186], clusterProfiler[192].

Table 11. The public datasets used in this thesis

Description	Setting	Sequencing type	Sp. *	GEO/EBI deposit	Software
$CD11b^+$ sorted cell from kidney, blood and bone marrow[177]	1 and 3 days after bilateral IRI	scRNA-seq	M	GSE174324	Scanpy[173], scran[174], harmonypy[175]
$CD45^+TCRb^-CD19^-$ $NK1.1^-Gr\text{-}1^-$ $CD11b^{INT}F4/80^{HI}$ cell from kidney[178]	0, 1, 6, 28 days after bilateral IRI	scRNA-seq	M	GSE200115	Scanpy[173], scran[174], harmonypy[175]
Mixed cell from kidney[179]	4, 12 hours, 2, 14 days and 6 weeks after IRI	snRNA-seq	M	GSE139107	Scanpy[173], scran[174], harmonypy[175]
Urinary single cell in human acute kidney injury[180]	40 urine samples from 32 patients with AKI	scRNA-seq	H	GSE199321	Scanpy[173], scran[174], harmonypy[175]
Binding specificities of human RNA-binding proteins[183]	86 RBPs and their RNA-binding domains sequencing	RNA-SELEX	H	PRJEB25907	Autoseed[181], FIMO[182]
Regnase3 knockout alveolar macrophages[188]	Cells from the $Regnase3^{+/+}$ and $Regnase3^{-/-}$ mice	bulk RNA-seq	M	GSE129325	hisat2[184], samtools[185], eisaR[186], DESeq2[187]
Murine ischemia reperfusion injury model for 12 months post injury[189]	Kidney tissue 2, 4 hours; 1, 2, 3 days; 1, 2, 4 weeks; and 6, 12 months after IRI	bulk RNA-seq	M	GSE98622	eisaR[186], DESeq2[187]
Translating ribosome affinity purification of mRNA populations[190]	Endothelial, Interstitial, Macrophage and Nephron from kidney after IRI	bulk RNA-seq	M	GSE52004	eisaR[186], DESeq2[187]

* Sp., species ;H, Homo sapiens; M, Mus musculus.

3.22 Statistics

For pairwise comparison, continuous variables were subjected to t-test for normal distributed variables or the Mann-Whitney U test for non-normal distributed, and categorical variables subjected to $\chi 2$ test or Fisher's exact test. For multiple comparisons, continuous variables were subjected to one-way analysis of variance (ANOVA) followed by Tukey Post-hoc-Test. The restricted cubic splines were used for data interpolation and curve fitting. All data are presented as mean ± standard deviation (SD). A P-value that lower than 0.05 was considered to be statistical significance. Python or R was used for all figures preparation and statistical analyses.

3.23 Software

The Software involved in this thesis are summarized in the Table 12 and the Session information is described in the Appendix 4.

Table 12. Software used

Software	Version	Developer
Adobe Illustrator®	25.4.1	Adobe
Adobe Photoshop®	22.5.1	Adobe
BD FACSDIVA™	8.0.1	BD Biosciences
CaseViewer	2.4	CaseViewer
DASYLab	12.00.01	National Instruments Ireland Resources Ldt.
DESeq2	1.32.0	Michael I. Love and Simon Anders et al
eisaR	1.4.0	Michael Stadler
featureCounts	2.0.3	Shi Lab
FlowJo	10.8.1	Tree Star, Inc.
GPT	3	OpenAI
hisat2	2.2.1	UTsouthwestern
LightCycler® 480 Software	1.5.0	Roche Life Science
MPD-Lab Application	1	Mannheim Pharma & Diagnostics
NIS-Elements Viewer	5.21	Nikon
Python	3.9.7	Python Software Foundation
R	4.1.1	R Foundation
samtools	1.16.1	John Marshall and Petr Danecek et al
Scanpy	1.8.2	Helmholtz Munich
Visual Studio Code	1.74.3	Microsoft

4. Results

4.1 Bioinformatics analysis on Regnase3

A comprehensive data mining analysis was performed on the dataset obtained from GSE129325, which consists of 6 samples, including 3 Regnase3 knockout and 3 wildtype macrophages. Results showed that there were 137 differentially expressed genes that were related to Regnase3 (Figure 7). Gene ontology suggested that the Regnase3 involved in the oxidative stress, inflammatory response, and positive regulation of monocyte chemo taxis (Table 13).

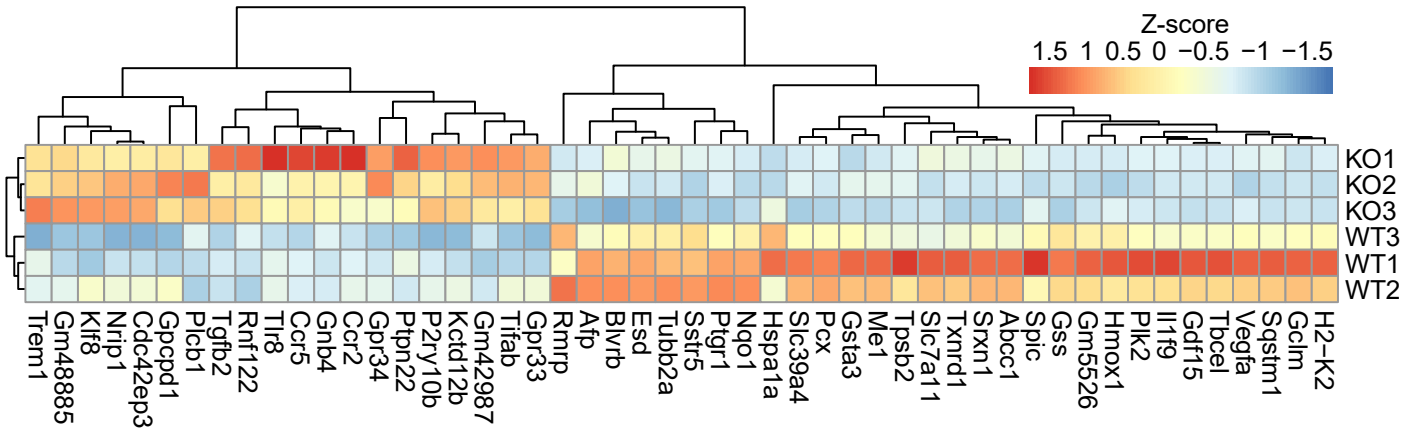

Figure 7. Heatmap of RNA-seq for significantly change genes in Regnase3$^{-/-}$ macrophage. A plot displaying a heatmap of the most significantly different genes between Regnase3 knockout and wild type groups, with the genes filtered by their fold change. The pattern of gene expression reveals two separate groups with distinct expression patterns, according to the unsupervised hierarchical clustering analysis. The colors red and blue are used to indicate high and low expression levels of the genes, respectively. Adopted from GSE129325.

Table 13. GO analysis of Regnase3$^{-/-}$ macrophages

Terms	Count	%	P-Value	adjust P-value
response to oxidative stress	6	16.7	4.7E-06	0.0015
inflammatory response	5	13.9	0.0038	0.46
negative regulation of myoblast fusion	2	5.6	0.0056	0.46
oxidation-reduction process	6	16.7	0.0082	0.49
regulation of cell proliferation	4	11.1	0.0088	0.44
positive regulation of monocyte chemo taxis	2	5.6	0.026	0.76
cellular zinc ion homeostasis	2	5.6	0.033	0.79
negative regulation of myoblast differentiation	2	5.6	0.048	0.86

The dataset series GSE52004[190] analyzed transcriptome from four different cell types (endothelial cells, interstitial cells, macrophages and TECs) taken from mice with bilateral I/R kidney injury. The data showed that Regnase3 was highly expressed in macrophages and poorly expressed in TECs at 24 hours post injury (Figure 8). This indicate that Regnase3 has a cell-specific expression pattern in response to hypoxia injury. The long-term transcriptome analysis of IRI AKI (GSE98622)[189] showed that the mRNA expression of

Regnase3 was low at 24 hours after injury and remained low for 28 days (Figure 9), suggesting a potential association between Regnase3 and AKI repair and fibrosis. A comparison of 139 differentially expressed genes in Regnase3-deficient macrophages and 3,240 differentially expressed genes in I/R macrophages revealed 44 common genes (Figure 10), with gene ontology analysis indicating that these genes were primarily involved in oxidative stress. Specifically, the downregulation of the genes from pathways of E2-related-factor-2/heme oxygenase-1 (such as Hmox1 and Nqo1, Table 13) in Regnase3-deficient macrophages suggests that Regnase3 may involve in hypoxia signaling and further exacerbate oxidative stress in AKI (Table 14).

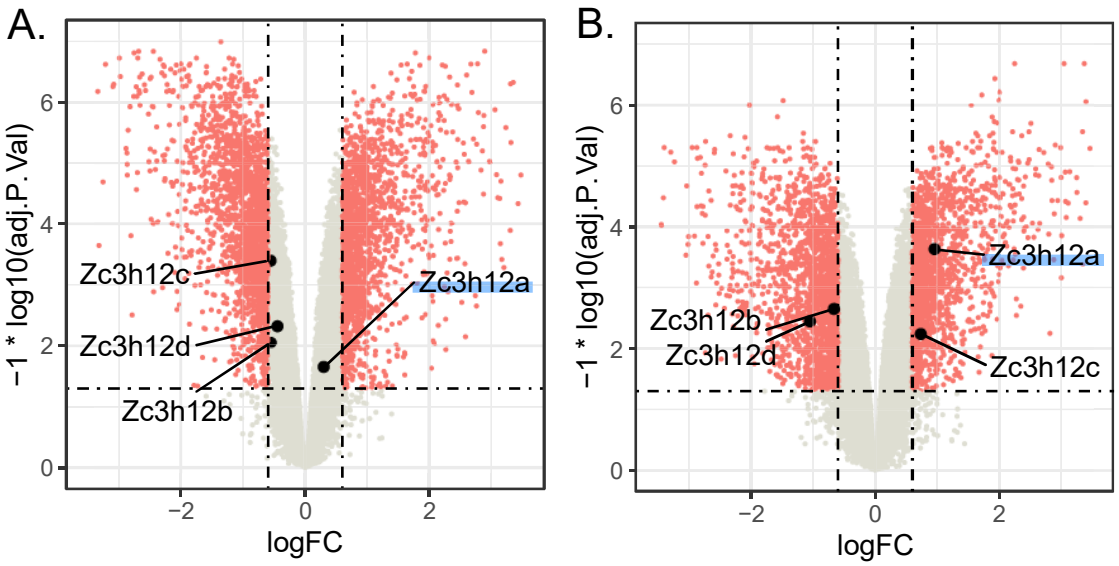

Figure 8. Expression of Regnase3 mRNA in (A) TEC and (B) macrophages. The cutoff for 1.5-fold change (FC) is shown by the vertical dashed lines, while the cutoff for the adjusted p-value of 0.05 is indicated by the horizontal dashed line. Adopted from GSE52004.

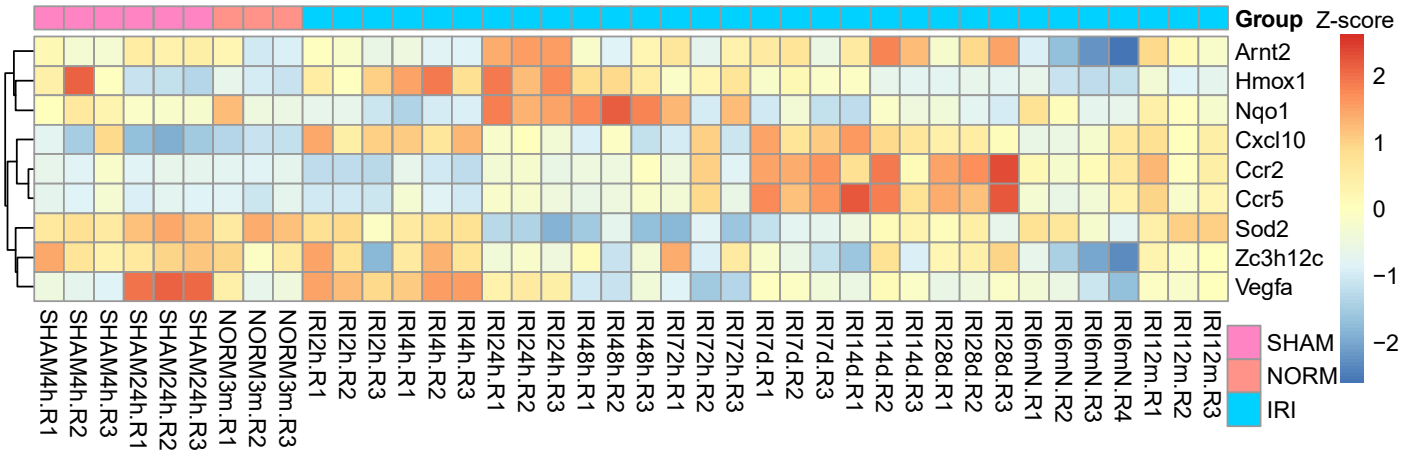

Figure 9. Heatmap of RNA-seq for significantly change genes after AKI. A plot displaying a heatmap of the most significantly different genes in long-term time course after ischemia reperfusion injury, with the genes filtered by their fold change. The left pattern of gene expression reveals a divergent expression pattern across all conditions, according to the unsupervised hierarchical clustering analysis. The colors red and blue are used to indicate high and low expression levels of the genes, respectively. Adopted from GSE98622.

Additionally, an investigation of the transcriptome from the GSE98622 revealed that the expression of CCR2/5 in the kidneys significantly increases from 7 days to 28 days post-AKI (Figure 9). This upregulation of CCR2/5 may be associated with the onset of fibrosis in the kidneys. Interestingly, a negative correlation has been observed between the expression of Regnase3 and CCR2/5, suggesting that there may be a connection between Regnase3, CCR2/5, and the development of kidney fibrosis after AKI. These findings further emphasize the Regnase3's role in AKI at early stages and in the repair process of the kidneys following AKI.

Table 14. Differentially expressed genes in Regnase3$^{-/-}$ macrophages and IRI kidney macrophages*

	Regnase3$^{-/-}$ macrophages (GSE129325)			**IRI kidney macrophages (GSE52004)**		
Genes	**logFC**	**P**	**adjust P**	**logFC**	**P**	**adjust P**
Hmox1	-1.248	4.00E-14	1.16E-10	1.545	6.55E-07	4.65E-05
Txnrd1	-0.707	2.32E-07	9.00E-05	1.290	1.09E-06	6.39E-05
Abcc1	-0.821	1.27E-08	6.74E-06	0.834	3.49E-07	3.25E-05
Nqo1	-1.101	1.85E-18	2.16E-14	0.918	0.003557	0.017853
Slc7a11	-1.399	3.21E-08	1.50E-05	4.937	8.33E-11	3.68E-07
Srxn1	-0.773	2.28E-09	1.66E-06	1.920	1.60E-09	1.91E-06

*GSE129325 consists of wildtype and Regnase3 deficiency alveolar macrophages. GSE52004 consists of kidney macrophages with or without ischemia reperfusion injury (IRI).

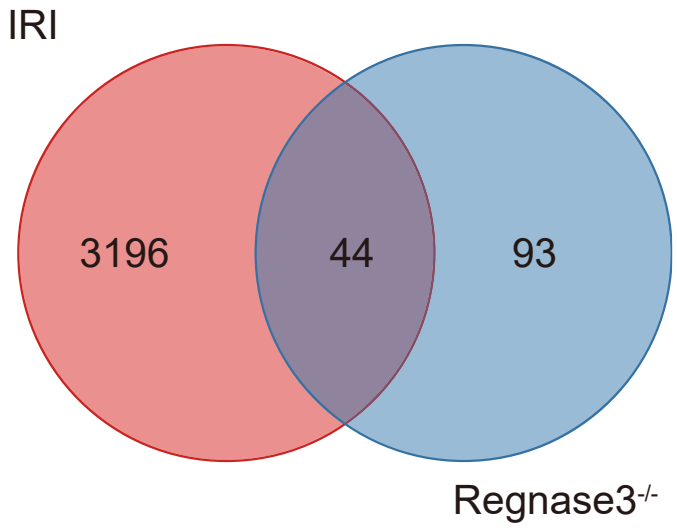

Figure 10. Venn diagram for differentially expressed genes (DEGs) in Regnase3$^{-/-}$ and I/R kidney macrophages. The number of DEGs associated to Regnase3 deficiency alveolar macrophages and the macrophages from the ischemia reperfusion injury (IRI) kidney are shown in the Venn diagram. In total, Regnase3 knockout regulated 137 DEGs and 3,240 DEGs in IRI macrophages.

4.2 Rank-Regnase3 in postischemic kidney injury

4.2.1 The scRNA-seq for mononuclear phagocytic cells (MPCs) in IRI

To study the character of MPCs and their mRNA expression in the context of AKI, we collected a scRNA-seq dataset from GSE174324. This dataset includes sorted leukocytes from blood by $CD11b^+$ $Ly6c^+$, kidney by $CD11b^+$ $F4/80^+$, and spleen by $CD11b^+$ of control mice and 1 and 3 days post-IRI. After performing quality control measures, a total of 81,154 cells were sequenced, with 29,999 of these cells defined as MPCs based on the representative MPC genes expression such as Clec9a, Cd209a, Itgax, Cx3cr1, Adgre1 and Cd68 (Figure 11). Our analysis showed that the MPCs highly expressed Rank (official symbol isTnfrsf11a), particularly those found in the kidney (Figure 12) instead of the blood (Figure 13).

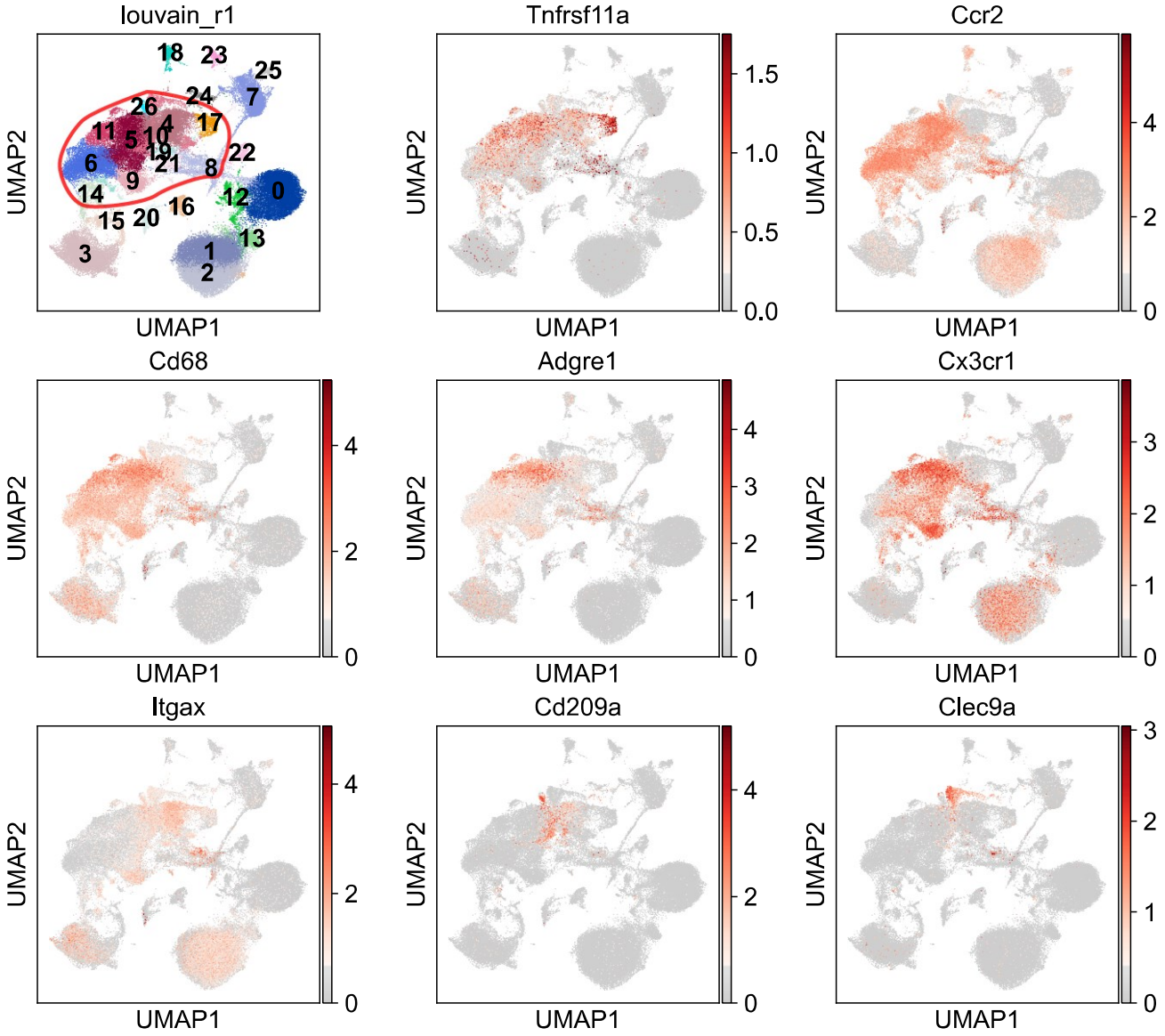

Figure 11. UMAP plot for sorted immune cells from blood, kidney, and spleen after IRI. The clusters were segmented by the Louvain algorithm with the resolution of 1. According to feature plots of markers (Cd68, Ccr2, Adgre1, Cx3cr1, Itgax, Cd209a, Clec9a), the clusters in the red circle represent different subsets of mononuclear phagocytes. Tnfrsf11a, TNF receptor superfamily member 11a = Rank, receptor activator of NF-κB. (Adopted from GSE174324)

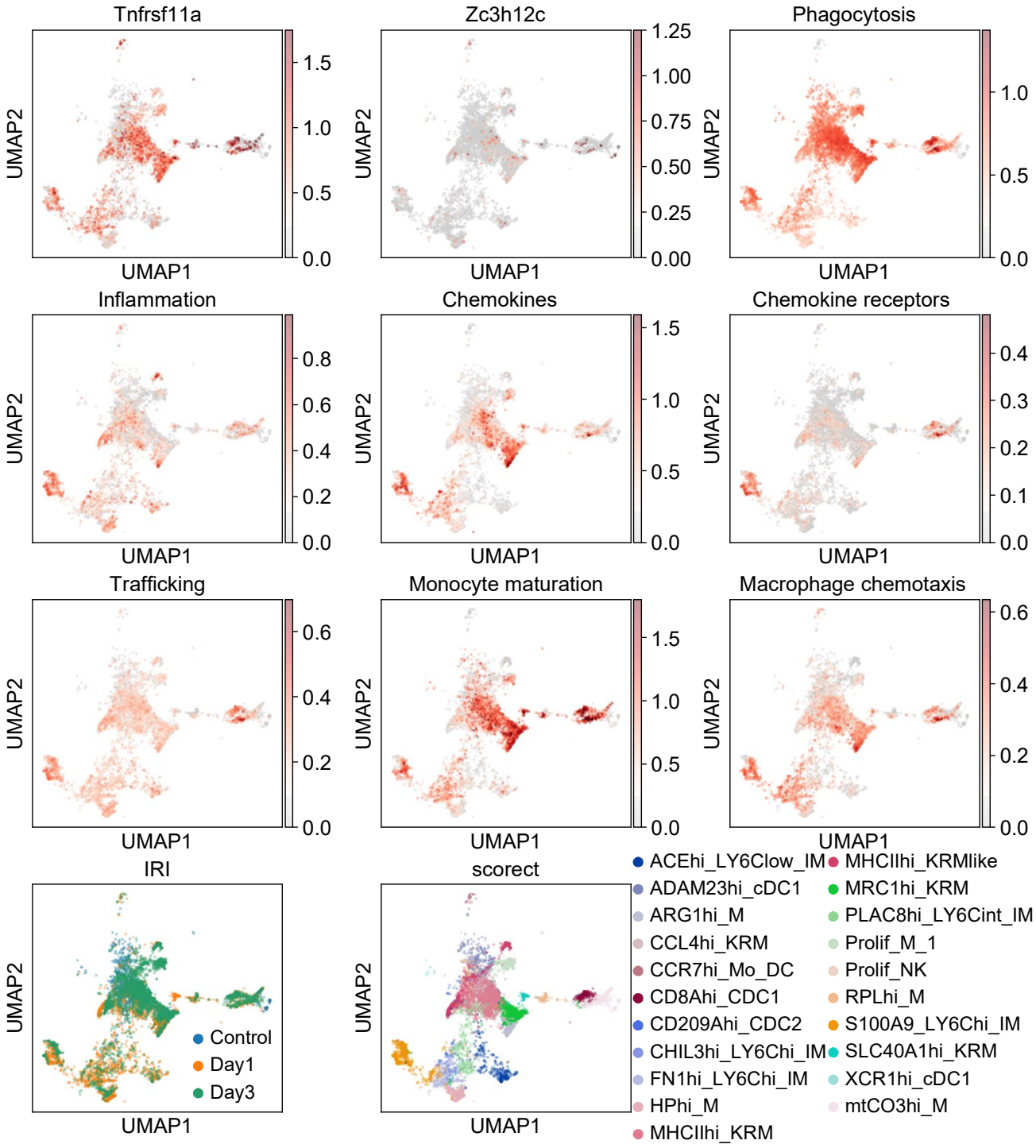

Figure 12. UMAP plot for mononuclear phagocytic cell from kidney after IRI. The monocyte/macrophage/dendritic were annotated based on cell markers from ImmGen mouse immune cell datasets. The activation of genes important for phagocytosis, inflammation, chemotaxis, trafficking and monocyte maturation were assessed based on the average expression of corresponding function. IM, infiltrating monocytes; DC, dendritic cells; M, Monocyte; KRM, kidney resident macrophage; Mo, macrophage; NK, natural killer cell; Tnfrs11a, TNF receptor superfamily member 11a = Rank, receptor activator of NF-κB. (Adopted from GSE174324)

We found a positive correlation between Rank mRNA levels and the gene enrichment of phagocytosis, chemokines, and monocyte maturation, particularly in the 1 and 3 days post-IRI groups (Figure 14). Additionally, the Rank is predominantly expressed in matured MPCs such as Arg1, Mrc, Slc40A1, and CCL4 positive cells, highlighting its potential role in the monocyte maturation response to kidney injury.

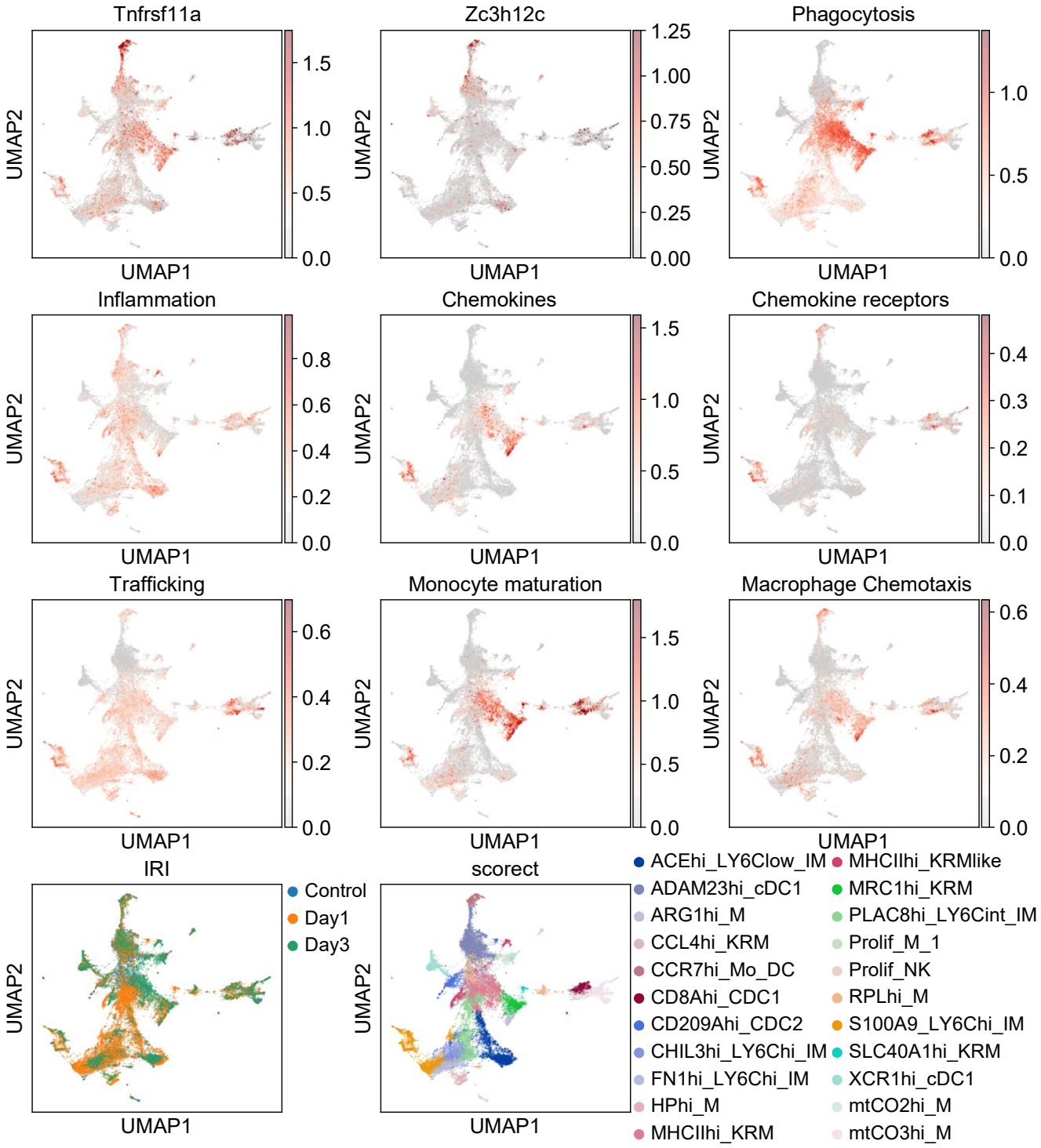

Figure 13. UMAP plot for mononuclear phagocytic cell from blood after IRI. The monocyte/macrophage/dendritic were annotated based on cell markers from ImmGen mouse immune cell datasets. The activations for phagocytosis, inflammation, chemokines and its receptors, trafficking and monocyte maturation were assessed based on the average expression of corresponding function. IM, infiltrating monocytes; DC, dendritic cells; M, Monocyte; KRM, kidney resident macrophage; Mo, macrophage; NK, natural killer cell; Tnfrs11a, TNF receptor superfamily member 11a = Rank, receptor activator of NF-κB (Adopted from GSE174324)

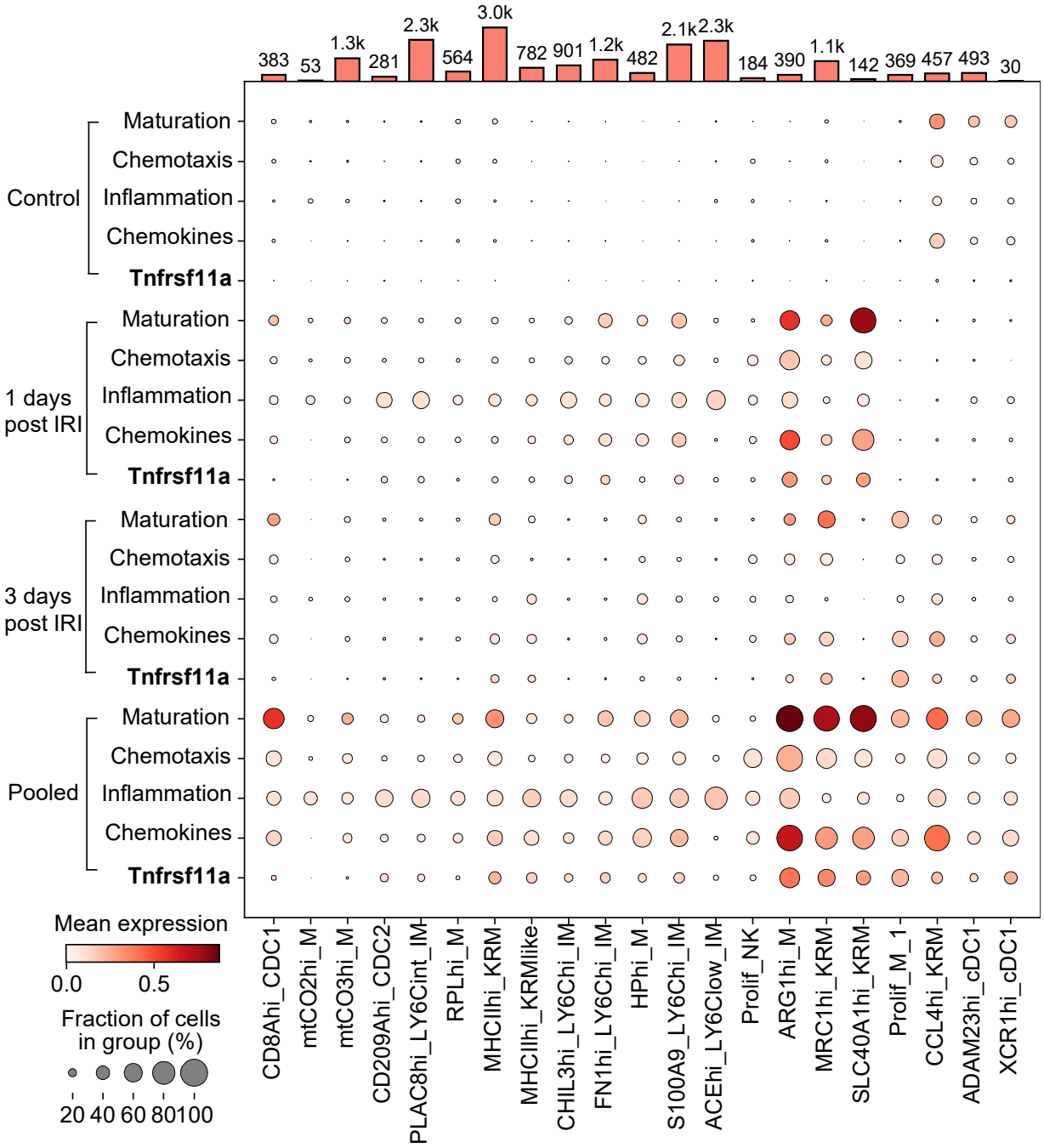

Figure 14. Dot plot for monocyte maturation and Rank expression in the kidney mononuclear phagocytic cell after IRI. The dot size represents the cells' proportion in the group and the color represent the mean expression. The bars plot on the top of the plot are the numbers of the cell in group. IM, infiltrating monocytes; DC, dendritic cells; M, Monocyte; KRM, kidney-resident macrophage; Mo, macrophage; NK, natural killer cell; Tnfrs11a, TNF receptor superfamily member 11a = Rank, receptor activator of NF-κB. (Adopted from GSE174324)

We further analyzed a dataset GSE200115 and examined the Rank expression in MPCs sorted by $CD45^{+}TCRb^{-}CD19^{-}NK1.1^{-}Gr\text{-}1^{-}CD11b^{INT}F4/80^{HI}$ from the kidney after 12 hours, 1, 6 and 28 days of IRI kidney. The results showed that Rank was highly expressed at 1 day after the IRI and expression of it positively correlated with the functions of phagocytosis, chemokines and monocyte maturation (Figure 15)., which is consistent with previous findings from GSE174324. The result from both datasets suggests that Rank involved in the maturation of macrophage in response to IRI-induced kidney injury. This is supported by the observation that

Rank is highly expressed in the protein levels of healthy kidney F4/80^{+} macrophages (Figure 16), making it a potential marker for generating conditional knockout mice in kidney macrophages.

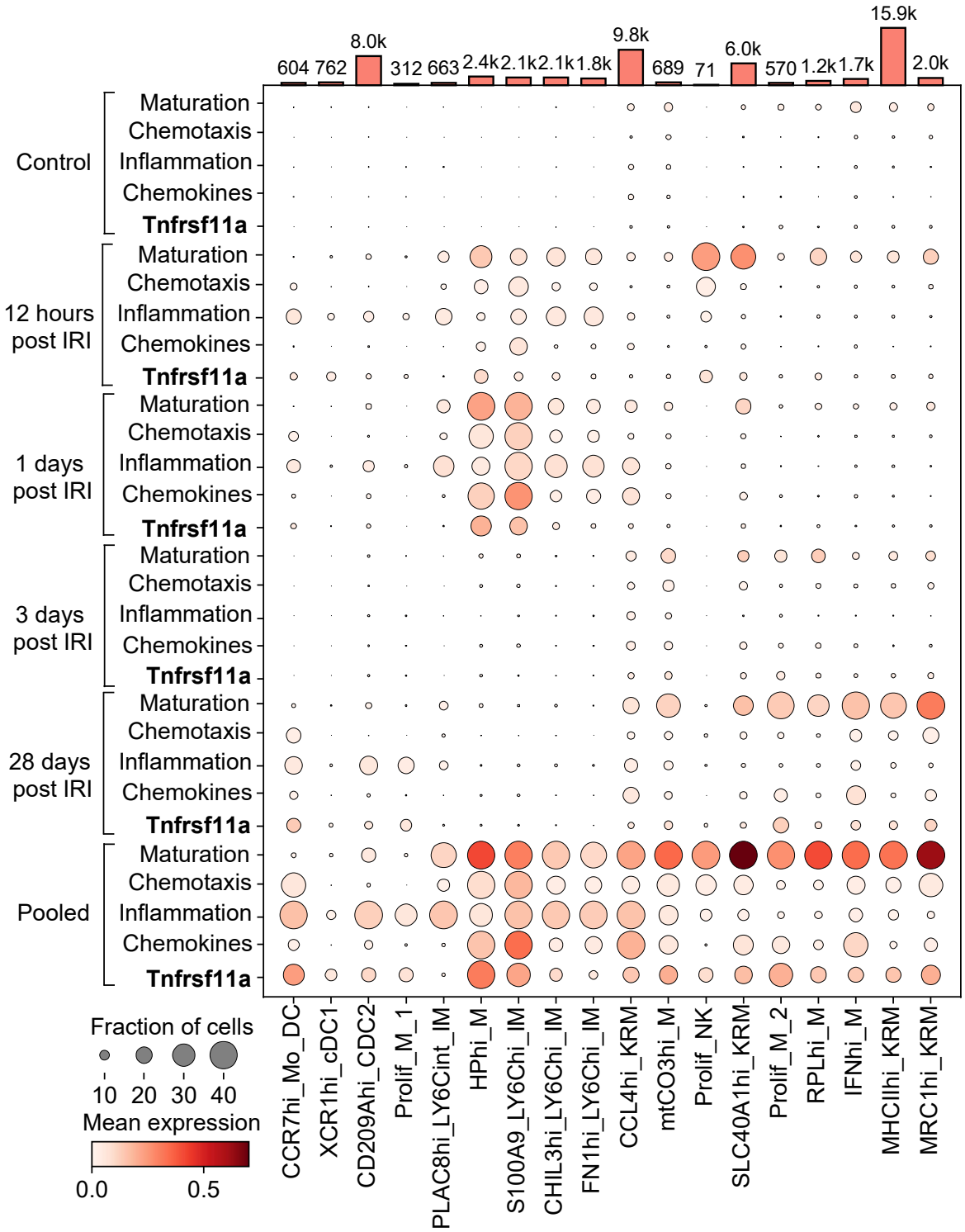

Figure 15. Dot plot for immune cell functions and Rank expression in CD45^{+}TCRb^{-}CD19^{-}NK1.1^{-}Gr-1^{-}CD11b^{INT}F4/80^{HI} mononuclear phagocytic cell from kidney after IRI. The dot size represents the cells' proportion in the group and the color represent the mean expression. The bars plot on the top of the plot are the numbers of the cell in group. IM, infiltrating monocytes; DC, dendritic cells; M, Monocyte; KRM, kidney-resident macrophage; Mo, macrophage; NK, natural killer cell; Tnfrs11a, TNF receptor superfamily member 11a = Rank, receptor activator of NF-κB. (Adopted from GSE200115)

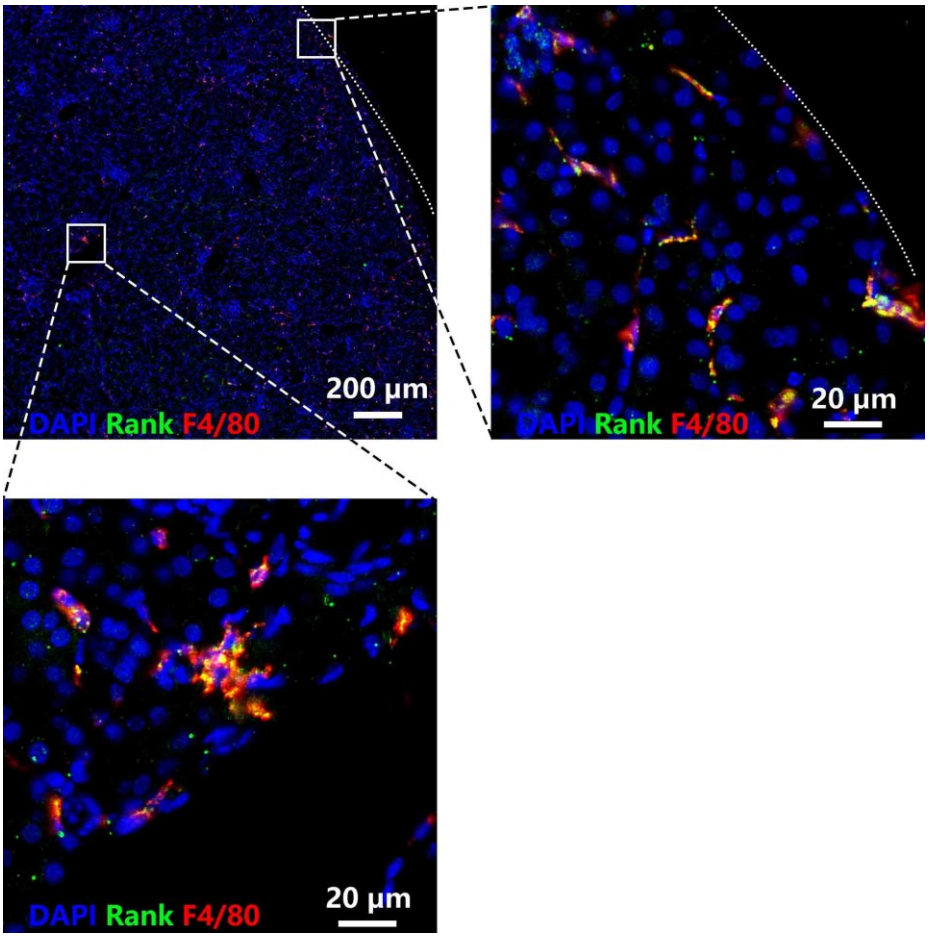

Figure 16. Immunofluorescence staining for Rank (green) and F4/80 (red) in healthy mouse kidney. The 4',6-diamidino-2-phenylindole (DAPI, blue) was used to stain the cell nuclei.

4.2.2 Selective Regnase3 deletion in Rank positive macrophage

To study the role of Regnase3 in kidney IRI, we established a transgenic mice line expressing the recombinant Cre and Regnase3-flox on Rank positive macrophage. To confirm the deletion of Regnase3 from these mice, we separated bone marrow derived mononuclear cells and treated them with L929 supernatant to induce them into BMDM, and dendritic cells which induced by granulocyte-macrophage colony-stimulating factor. Additionally, we isolated resident macrophages from the alveolar and peritoneal regions. Our results indicated that the Rank mRNA was highly expressed in BMDM than other type of the immune cells. Furthermore, we observed that the Regnase3 mRNA was lower expressed in Rank-positive cells, suggesting that the Rank-Cre effectively reduces Regnase3 mRNA levels (Figure 17). Additionally, RNA-seq results showed a clear deletion on the Regnase3 exon 4, while other exons remained unaffected (Figure 18), indicating that the Rank-Cre knockout was effective in reducing the levels of Regnase3 mRNA.

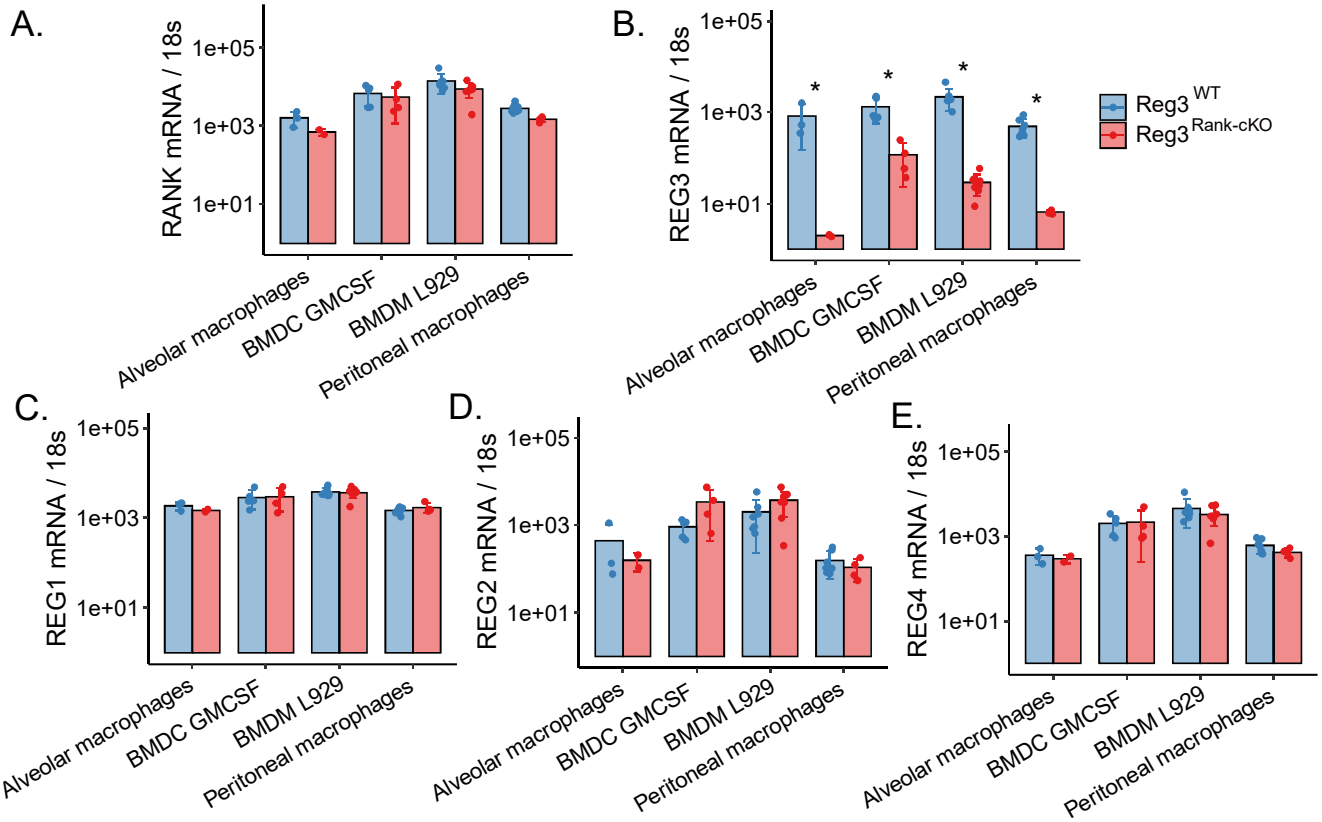

Figure 17. The mRNA level for Rank and Regnase family in mononuclear phagocytic cell. The mRNA for (A) Rank, (B-E) Regnase 1 to 4. All quantitative data are means ± SD. The two-way ANOVA was employed for the statistical examination. *P < 0.05 for comparison of Regnase3cKO and wild type. BMDM, Bone marrow derived macrophage; Reg, Regnase; GMCSF, granulocyte-macrophage colony-stimulating factor.

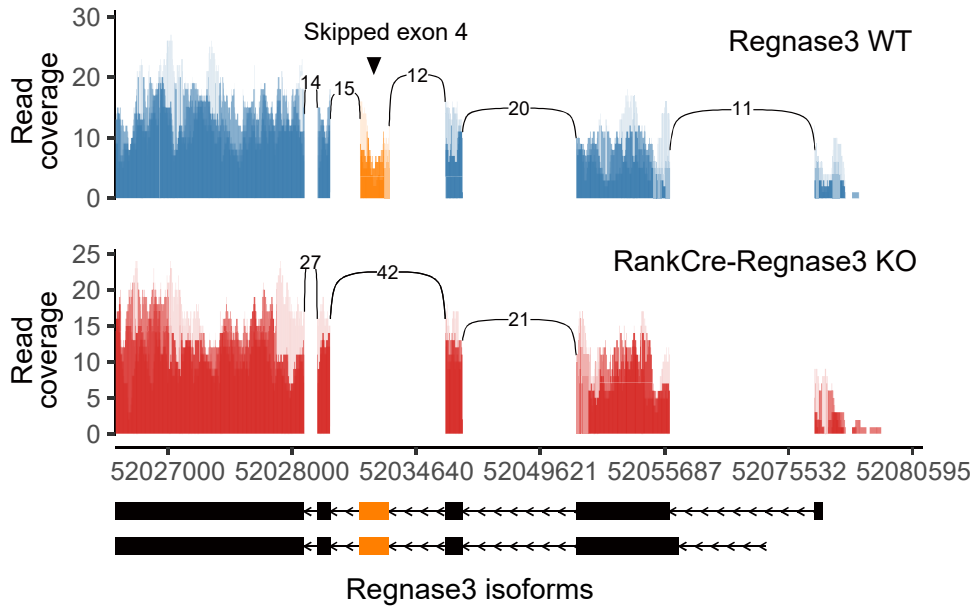

Figure 18. Sashimi plots for the Regnase3 chr9:52026580-52080668 in Rank-Regnase3 bone marrow derived macrophage. Rank-Regnase3cKO condition is shown in red plots, while the wildtype condition is depicted in blue. The X-axis shows the genomic locations, while the Y-axis indicates the transcription intensity. The plots show a "sashimi-like" region, which is a heavily transcribed region of exon, and the blank intronic regions between exon. The line crossing exonic regions represent the reads of junction and the count number is indicated on it. The exonic structure of the Regnase3 transcripts NM_001368810.1 and NM_001162921.2 is displayed below Sashimi plot, with the exonic region marked in yellow being the target that was inserted by flox and then deleted by recombinant Rank-Cre.

4.2.3 Rank-Regnase3cKO aggravating 20 mins IRI without NX kidney injury

To investigate if Regnase3 in macrophage associate in AKI after ischemia, a study was conducted using 8-12 weeks old Rank-Regnase3 mice. The mice were treated with 20 minutes of unilateral IRI without NX. After the procedure, it was observed that there was a significant drop in GFR in both the wildtype and Rank-Regnase3cKO mice one day post-IRI. However, the kidney function of the Rank-Regnase3cKO mice failed to fully recover as compared to the wildtype mice, as indicated by the GFR at day 21 post-IRI (Figure 19). The IRI-affected kidney weight and size were found to be significantly smaller in the Rank-Regnase3cKO mice than in the WT mice. Additionally, serum creatinine levels, as well as kidney injury markers (intrarenal mRNA of KIM1, NGAL, TIMP2, and TNF, Figure 20), were also found to be higher in the Rank-Regnase3cKO mice, together with an increased kidney injury score, interstitial fibrosis and tubular atrophy (IFTA), and interstitial F4/80^{+} cell infiltrates (Figure 21). Furthermore, the Rank-Regnase3cKO mice IRI kidney expressed higher levels of mRNA for aSMA, Fibronectin (FN), TGF-β, TGF-β receptor, VCAM1, ICAM1, CCR2, CCR5, CCL2, CXCL1 and CXCL2(Figure 22), which all indicate more fibrosis, inflammation, and damage in the Rank-Regnase3cKO mice IRI-injured kidneys.

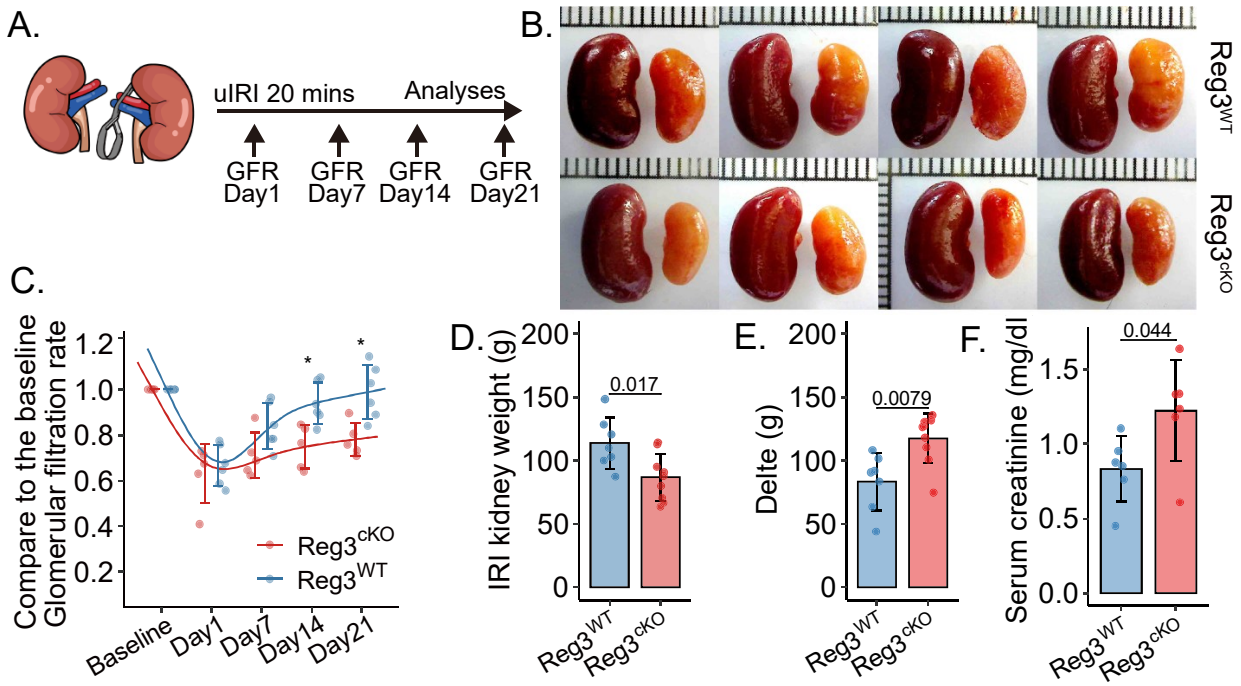

Figure 19. Rank-Regnase3cKO aggravate the 20 mins IRI without NX kidney injury. (A) A diagram illustrating the set-up of the experiment. Unilateral ischemia-reperfusion injury (IRI) was induced by clamping the kidney pedicle for 20 minutes. Organs were collected in two different states: healthy state and on day 21 following IRI. (B) Kidney appearance (C) The GFR normalized to baseline in response to the genotype. The curve is fitted using the cubic spline algorithm. (D) IRI kidney weight, (E) contralateral minus IRI kidney weight (Delta), (F) Serum creatinine level. All quantitative data are means ± SD. The t-test was employed for the statistical examination.

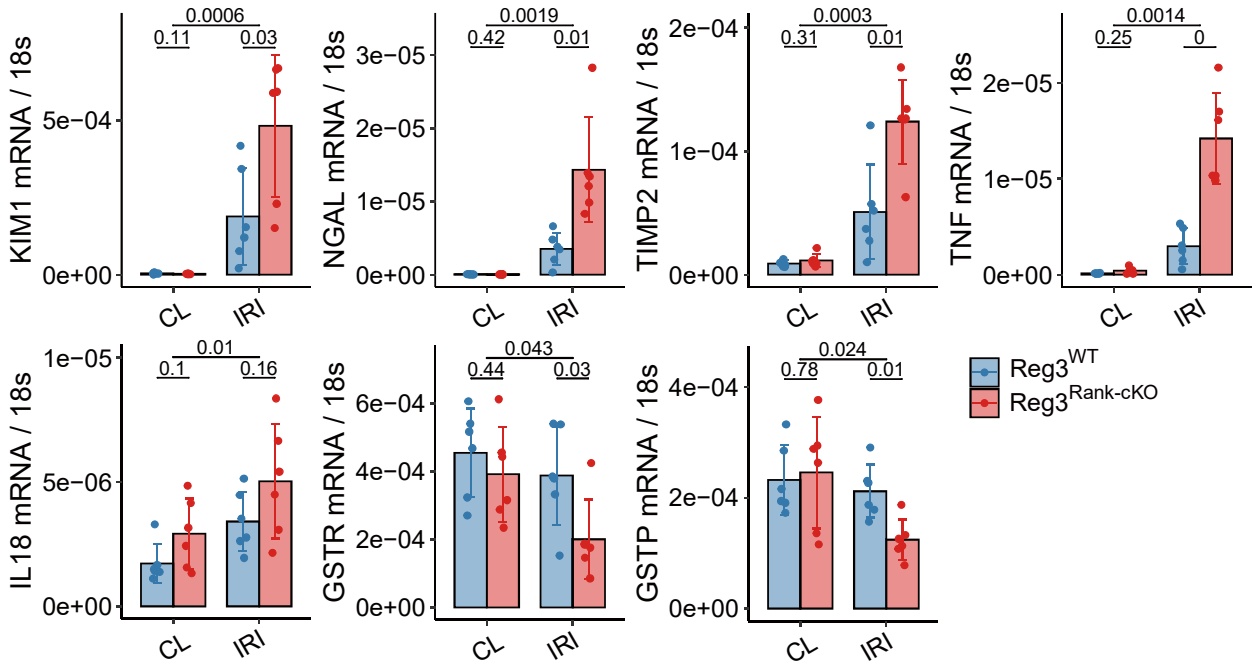

Figure 20. The qPCR for the kidney injury markers in Rank-Regnase3cKO 21 days after 20 mins IRI. The contralateral (CL) and IRI kidneys were harvest at day 21 after IRI. All quantitative data are means ± SD. The two-way ANOVA or t-test was employed for the statistical examination.

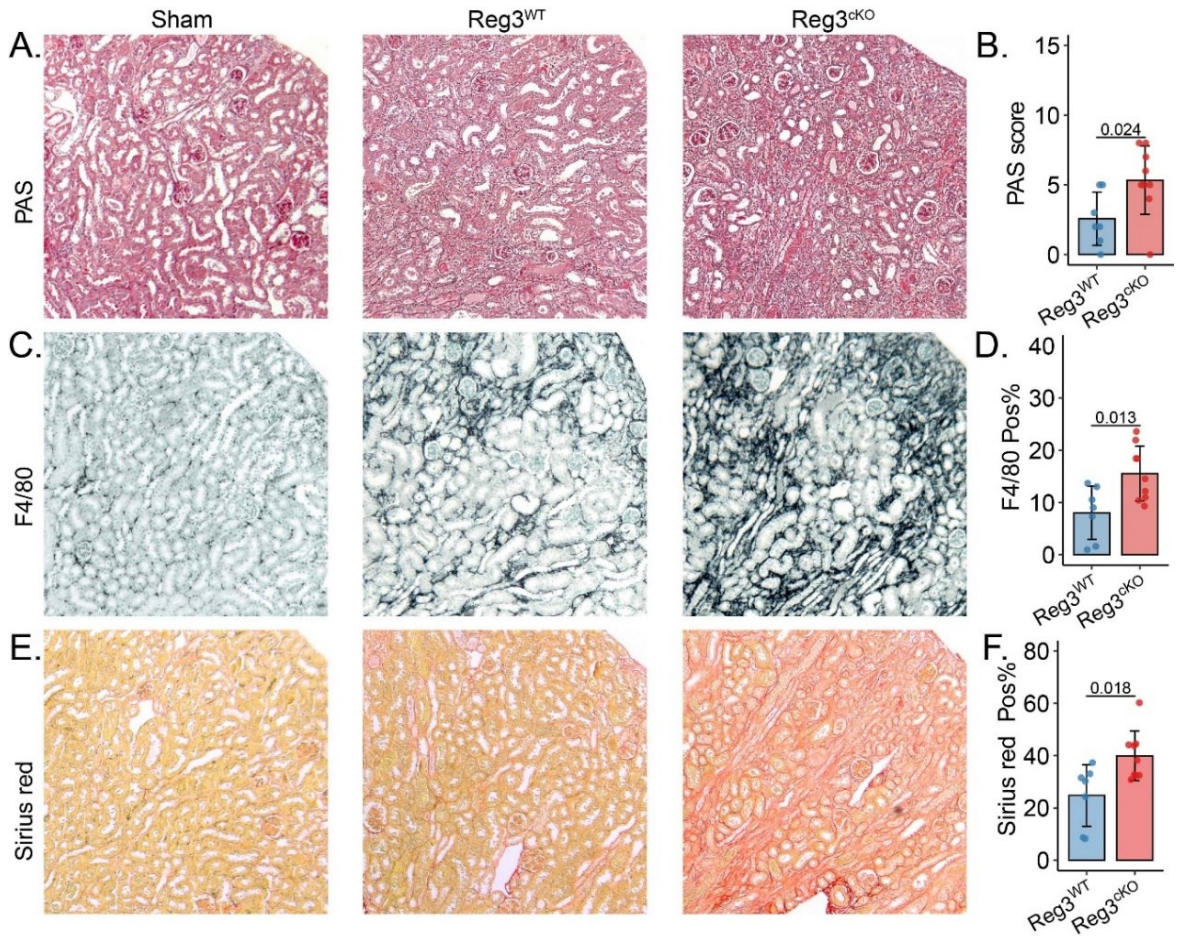

Figure 21. Pathological histology in Rank-Regnase3cKO 21 days after 20 mins IRI. (A) Renal tubular damage was quantified using Periodic acid-Schiff (PAS) staining. (B) Macrophage were visualized using F4/80 staining. (D) Collagen or fibrosis level was measured using Sirius red staining. The t-test was employed for the statistical examination. All quantitative data are means ± SD, and the images were magnified at 200x.

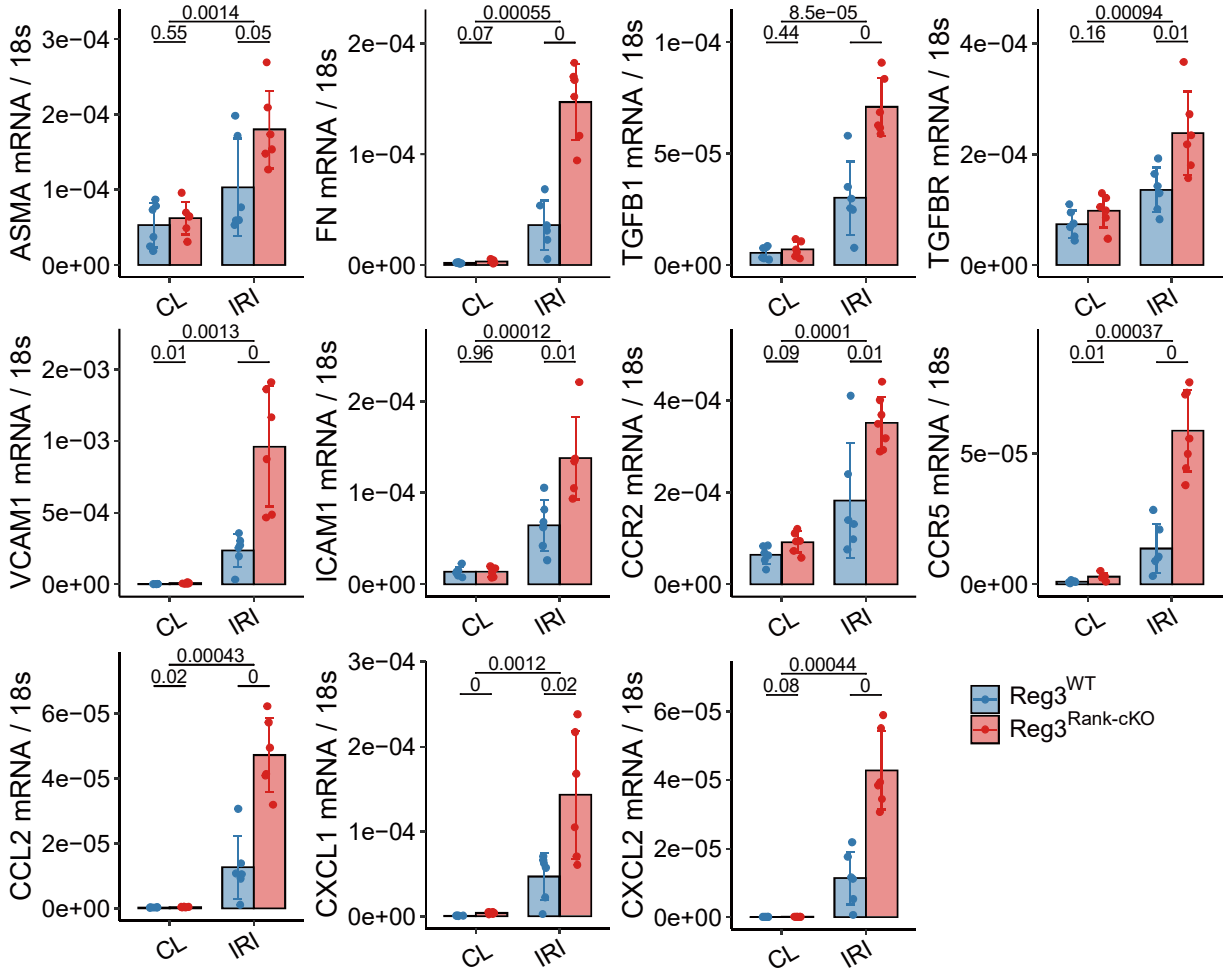

Figure 22. The qPCR for the fibrosis and inflammation markers in Rank-Regnase3cKO 21 days after 20 mins IRI. The contralateral (CL) and IRI kidneys were harvest at day 21 after IRI. All quantitative data are means ± SD. The two-way ANOVA or t-test was employed for the statistical examination.

4.2.4 CCR2$^+$ leukocytes accumulation in Rank-Regnase3cKO mice

To investigate the role of Regnase3 in macrophages, the first step was to identify leukocytes using CD45 as a marker. CD45 is commonly used to identify all hematopoietic cells, except mature erythrocytes and platelets. To achieve this, we employed the CD45 magnetic beads to purify leukocytes from the blood, bone marrow, and kidney. Our results showed that the CD45 magnetic beads were highly effective, particularly in terms of isolating immune cells from the kidney, as the purity of CD45$^+$ cells increased by 15% in the kidney and 11% in the bone marrow (Figure 23). Subsequent analysis revealed that one day following IRI, there was a substantial increase in the of CD45$^+$F4/80$^+$CD11b$^+$CCR2$^+$ mononuclear phagocytes proportion in both the bone marrow, blood, and kidney of Rank-Regnase3cKO mice (Figure 24).

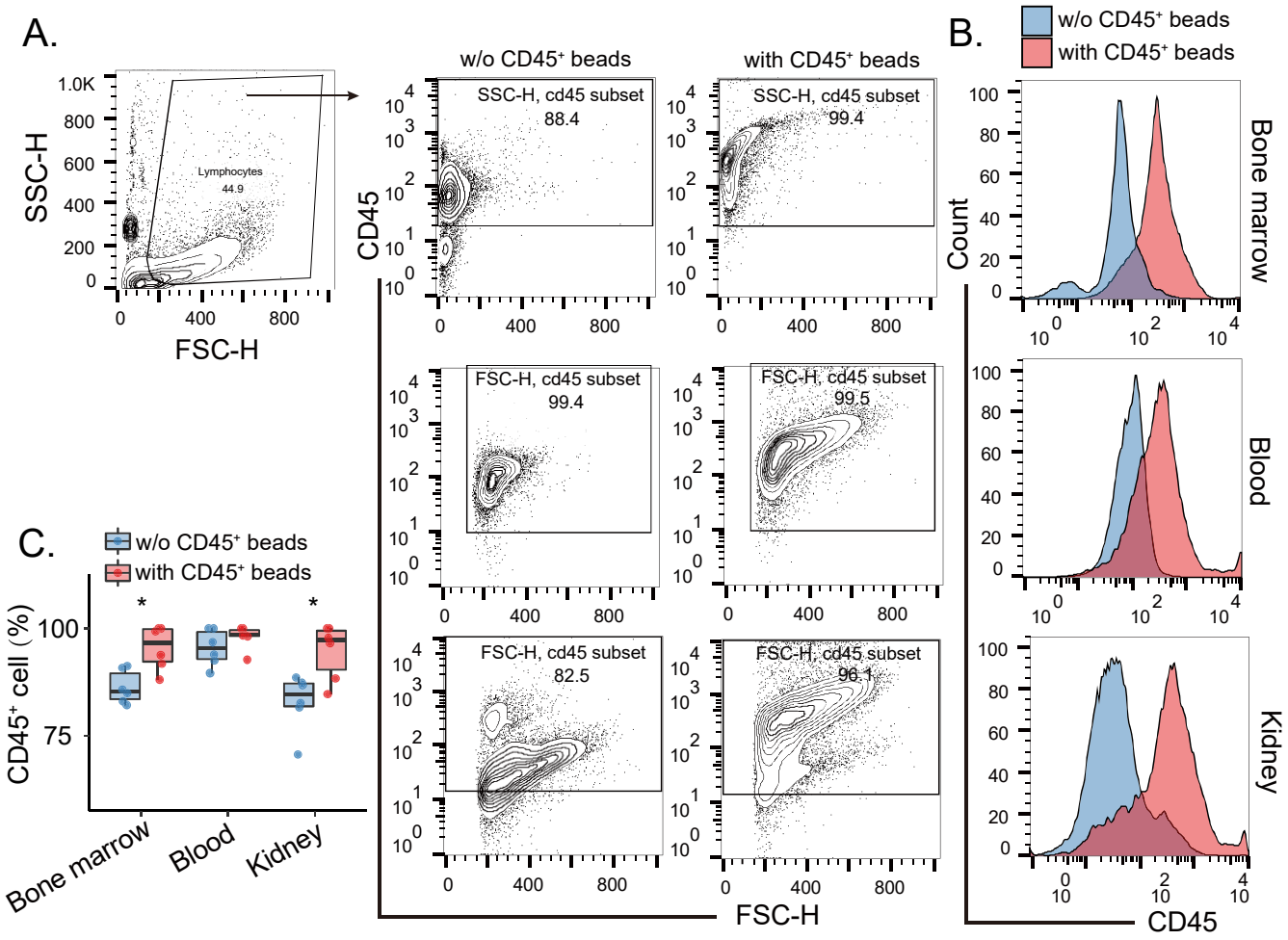

Figure 23. CD45 magnetic beads sorted the immune cell from the blood, bone marrow, and kidney. Gating strategy of $CD45^+$ cell and the histogram for the CD45 in (A) blood, (B) bone marrow, and (C) kidney with or without CD45 magnetic beads. All quantitative data are means ± SD. The t-test was employed for the statistical examination. *P-value lower than 0.05.

Additionally, we sorted $CD11b^+F4/80^+$ macrophages by M1 and M2 subsets based on the markers $CD86^+CCR2^+$ for the M1 and $Ly6C^-CD206^+$ for M2 polarization. While the M1 and M2 macrophages proportion were lesser in the Rank-Regnase3cKO mice kidney, the absolute number of these cells was found to be higher than in wildtype mice (Figure 25). These results imply that the macrophages in Rank-Regnase3cKO mice exhibit increased expression of the CCR2, which may enhance the migration of monocytes and promote more macrophage polarization towards the pro-inflammatory M1 phenotype.

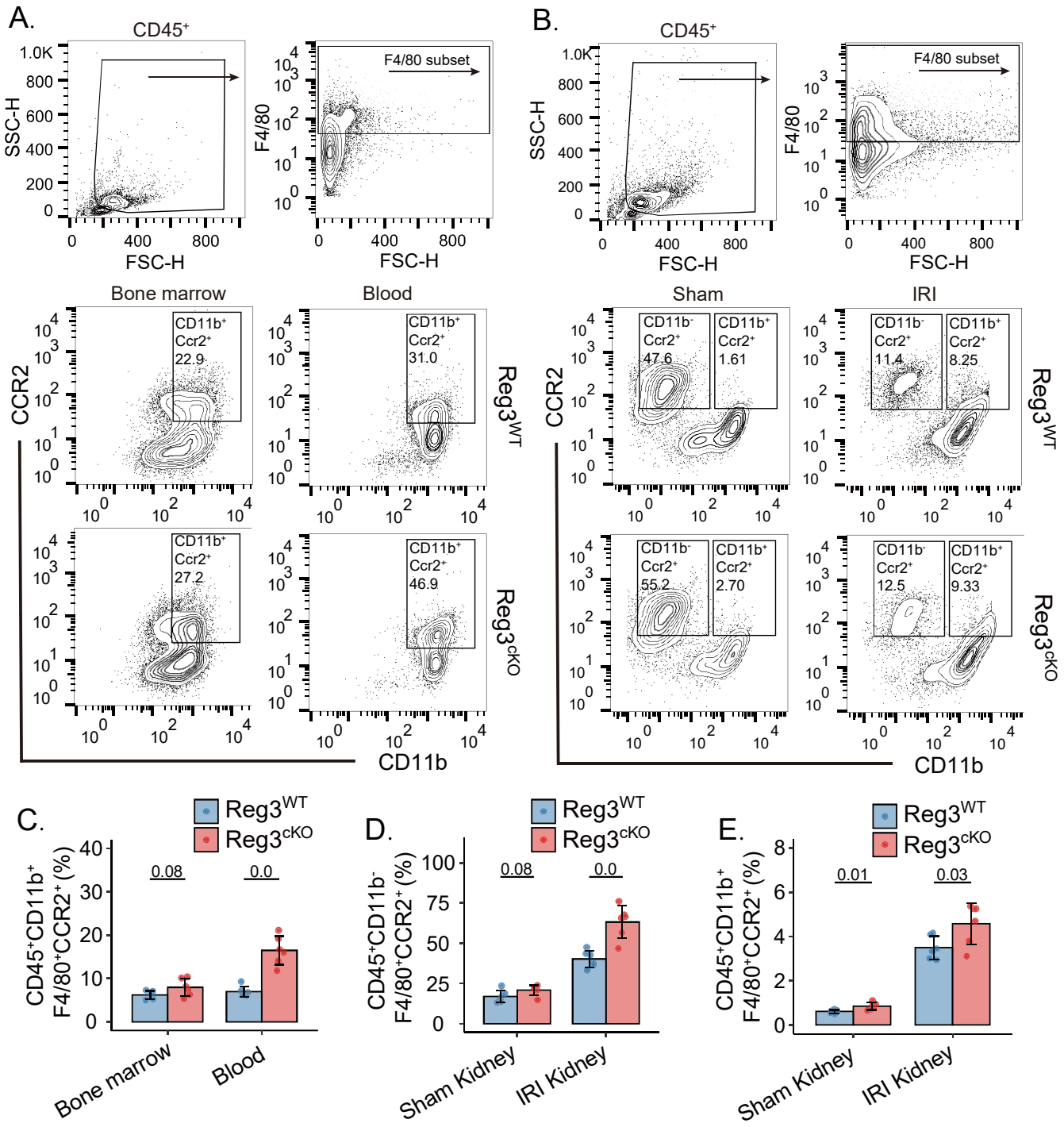

Figure 24. Accumulation of CD45$^+$F4/80$^+$CD11b$^+$CCR2$^+$ mononuclear phagocytes in blood and bone marrow and kidney of Rank-Regnase3cKO mice one day after IRI. (A) Gating strategy for CD45$^+$F4/80$^+$CD11b$^+$CCR2$^+$ cell from bone marrow, blood and (B) in kidney one day after IRI by flow cytometry. (C) Proportion for cells with CD45$^+$CD11b$^+$F4/80$^+$CCR2$^+$ in the bone marrow and blood, (D) CD45$^+$F4/80$^+$CD11b$^-$CCR2$^+$ and (E) cells with CD45$^+$CD11b$^+$F4/80$^+$CCR2$^+$ in sham and IRI kidney. All quantitative data are means ± SD. The t-test was employed for the statistical examination.

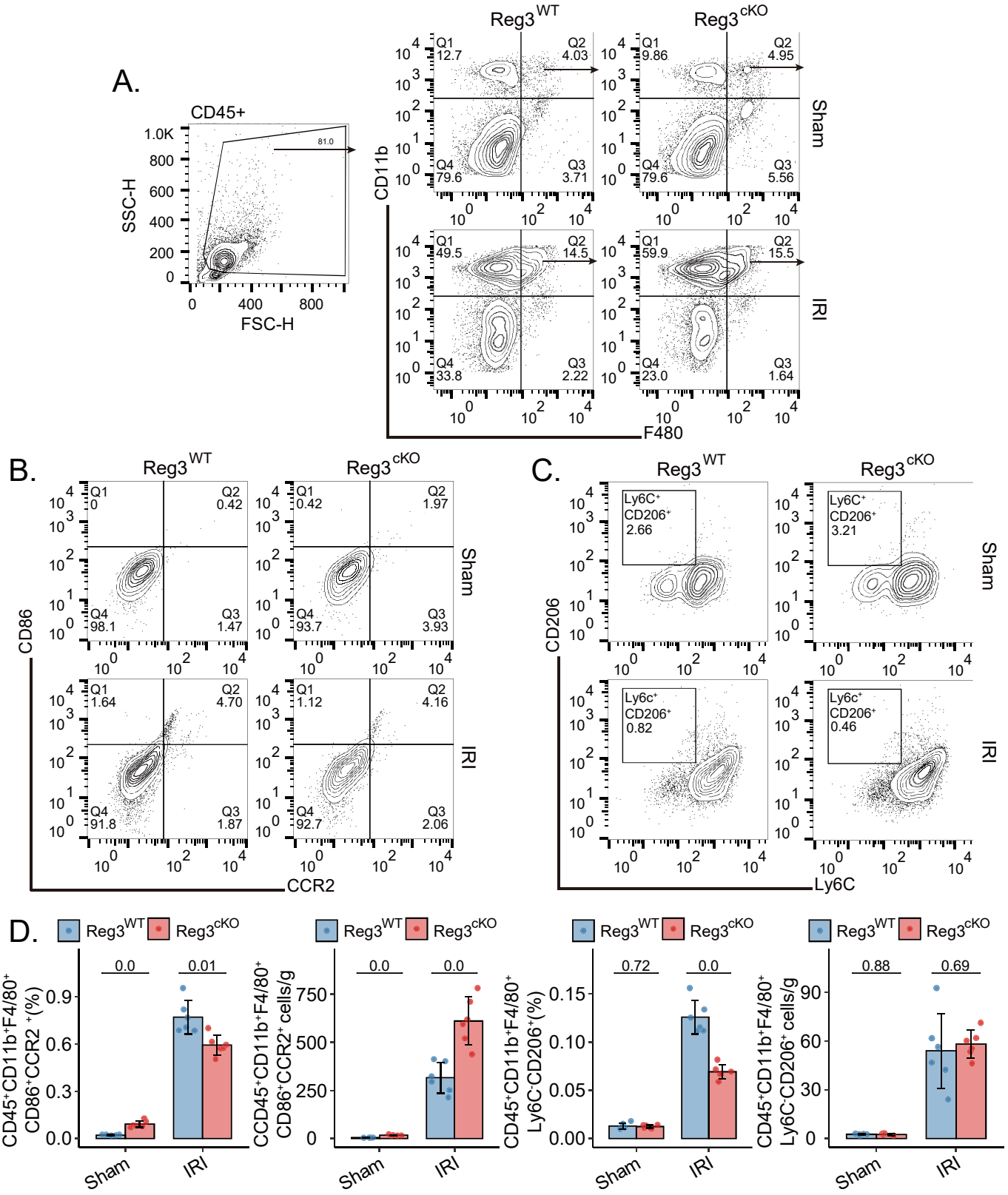

Figure 25. The kidney M1 and M2 macrophage in of Rank-Regnase3cKO mice one day after IRI. (A) Gating strategy for $CD45^+CD11b^+F4/80^+$, (B) $CD45^+CD11b^+F4/80^+$ $CD86^+CCR2^+$ and (C) $CD45^+CD11b^+F4/80^+Ly6C^-CD206^+$ cells in kidney one day post IRI by flow cytometry. (D) Proportion and absolute count for M1 and M2 macrophage in sham and IRI kidney. All quantitative data are means ± SD. The t-test was employed for the statistical examination.

4.2.5 Rank-Regnase3cKO aggravating 16 mins IRI with NX kidney injury

Given that IRI without NX is a model that simulates persistent post-AKI ischemia for kidney, we sought to study the function of Regnase3 in kidney injury by utilizing the 16 mins IRI with NX model, which mimics AKI with subsequent blood reperfusion of kidney. In IRI with NX model, analysis of GFR revealed that Rank-Regnase3cKO exhibited a delayed recovery of GFR, with only 30% of baseline GFR observed at day 3, compared to 50% in WT mice (Figure 26). Despite full recovery of GFR in both Regnase3cKO and wildtype mice 21day after IRI with NX, Rank-Regnase3cKO mice still displayed elevated levels of KIM1 and NGAL, along with increased IFTA and infiltration of $F4/80^{+}$ macrophage (Figure 27). Additionally, expression of mRNA for TGF-β, TGF-β receptor, CCR2 and CCR5 was found to be elevated in Rank-Regnase3cKO mice (Figure 28), consistent with increased fibrosis and inflammation post-AKI. These findings indicate that, even though kidney function is restored in mice with IRI with NX, Rank-Regnase3cKO mice still exhibit chronic inflammation in the kidney, persisting up to 21 days post-injury.

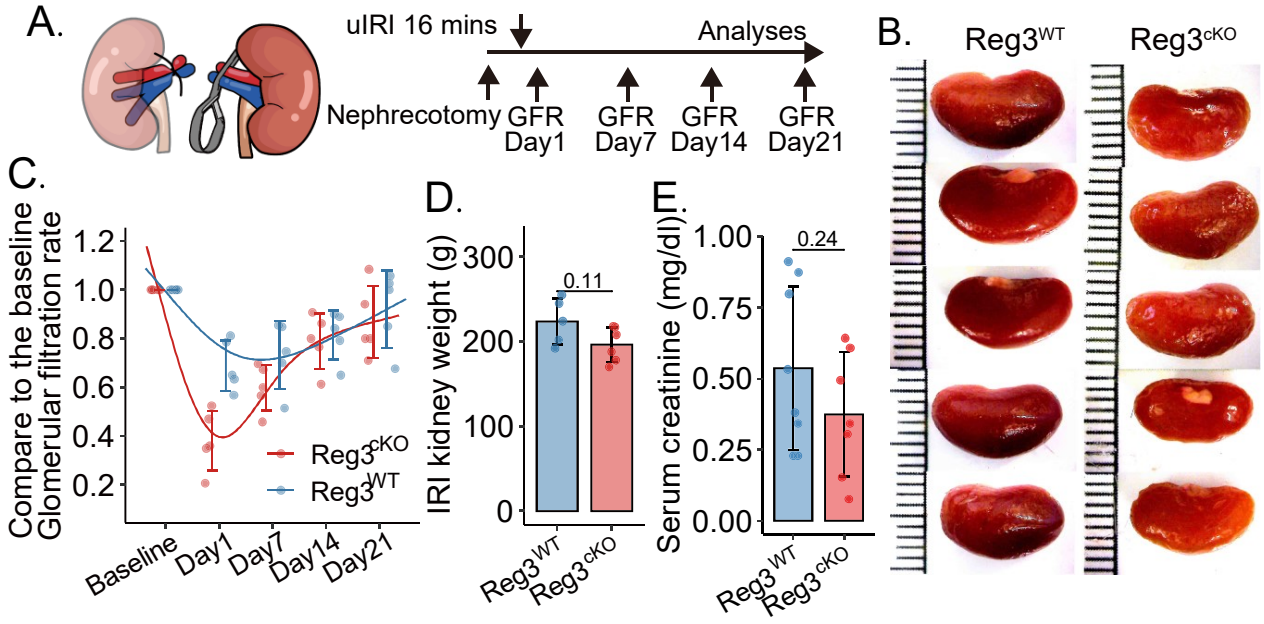

Figure 26. Rank-Regnase3cKO aggravate the 16 mins IRI with NX kidney injury with the nephrectomy. (A) A diagram illustrating the set-up of the experiment. Unilateral ischemia-reperfusion injury (IRI) was induced by clamping the kidney pedicle for 16 minutes. Organs were collected in two different states: healthy state and on day 21 following IRI. (B) Kidney appearance. (C) The GFR normalized to baseline in response to the genotype. The curve is fitted using the cubic spline algorithm. (D) IRI kidney weight, (F) serum creatinine level. The curve is fitted using the cubic spline algorithm. All quantitative data are means ± SD. The t-test was employed for the statistical examination.

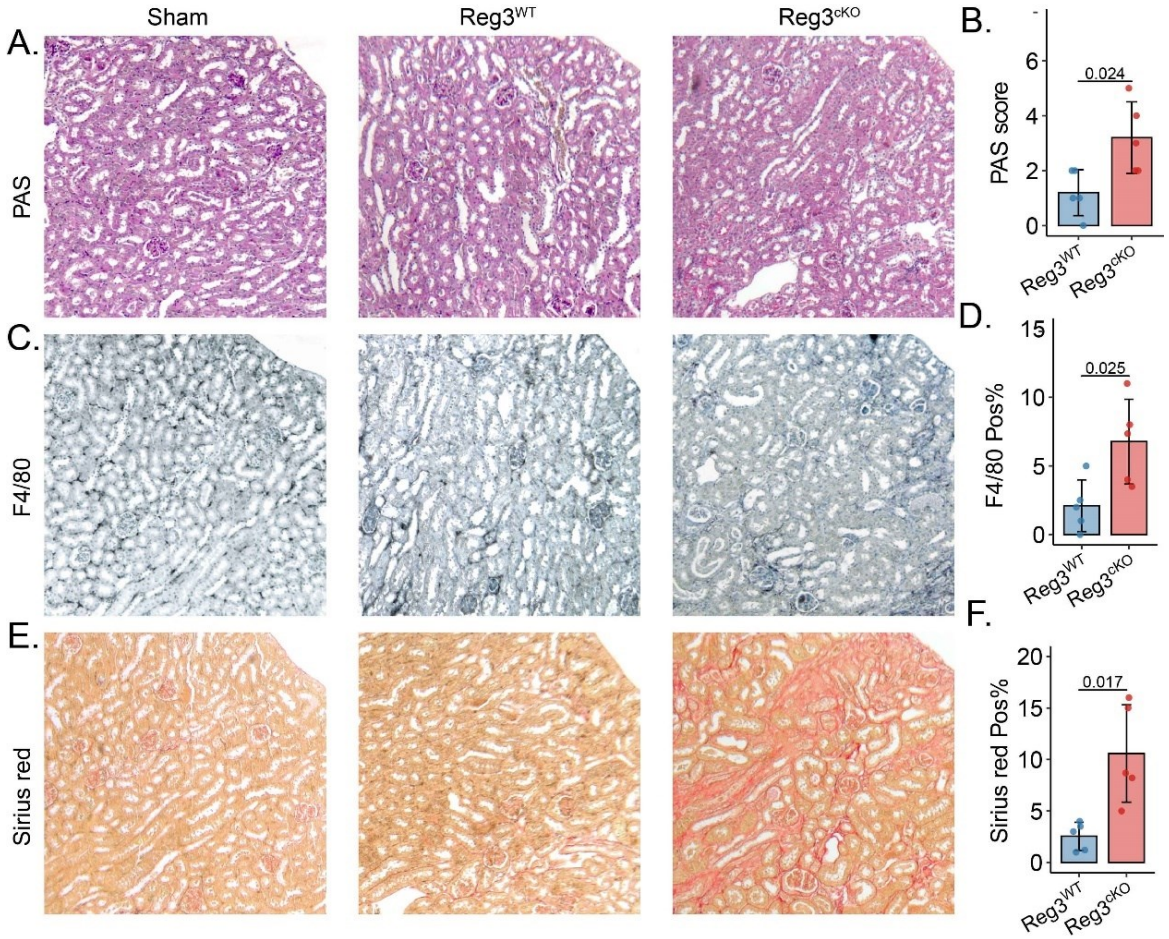

Figure 27. Pathological histology in Rank-Regnase3cKO 21 days after 16 mins IRI with NX kidney injury. (A, B) Renal tubular damage was quantified using Periodic acid-Schiff (PAS) staining. (C, D) Macrophage were visualized using F4/80 staining. (E, F) Collagen or fibrosis level was measured using Sirius red staining. The t-test was employed for the statistical examination. All quantitative data are means ± SD, and the images were magnified at 200x.

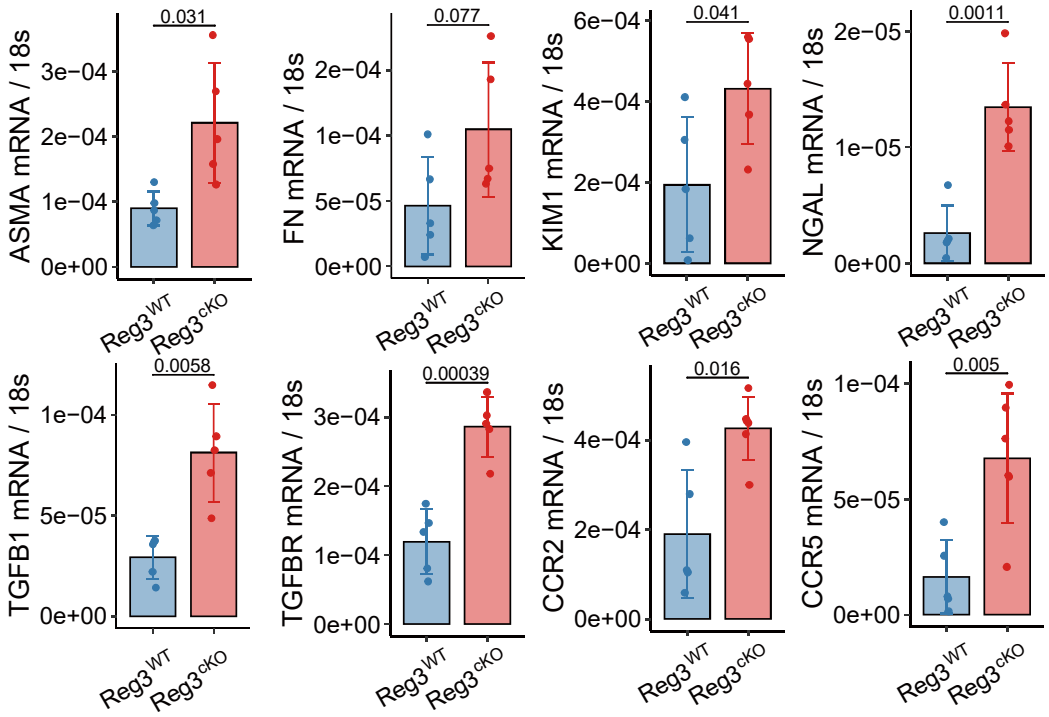

Figure 28 The qPCR for the fibrosis and inflammation markers in Rank-Regnase3cKO 21 days after 16 mins IRI with NX. IRI kidneys were harvest at day 21 after IRI. All quantitative data are means ± SD. The t-test was employed for the statistical examination.

4.2.6 Rank-Regnase3cKO aggravating CaOx kidney injury

To further study the role of Regnase3 in CKD, we employed the CaOx model, which utilizes an oxalate-rich diet to induce nephrocalcinosis-related CKD. Following the initiation of the dietary intervention, both wild-type and Rank-Regnase3cKO mice experienced a loss of body weight, with the latter group losing a significantly greater amount. As some Rank-Regnase3cKO mice lost more than 20% body weight for at least three consecutive days, the experiment had to be terminated at day 8 in compliance with animal welfare regulations. At the termination of the study, it was observed that the GFR had decreased by approximately 25% in wild-type mice and 15% in Rank-Regnase3cKO mice (Figure 29). This decline in GFR was consistent with the observed increase in Scr levels in the Rank-Regnase3cKO mice.

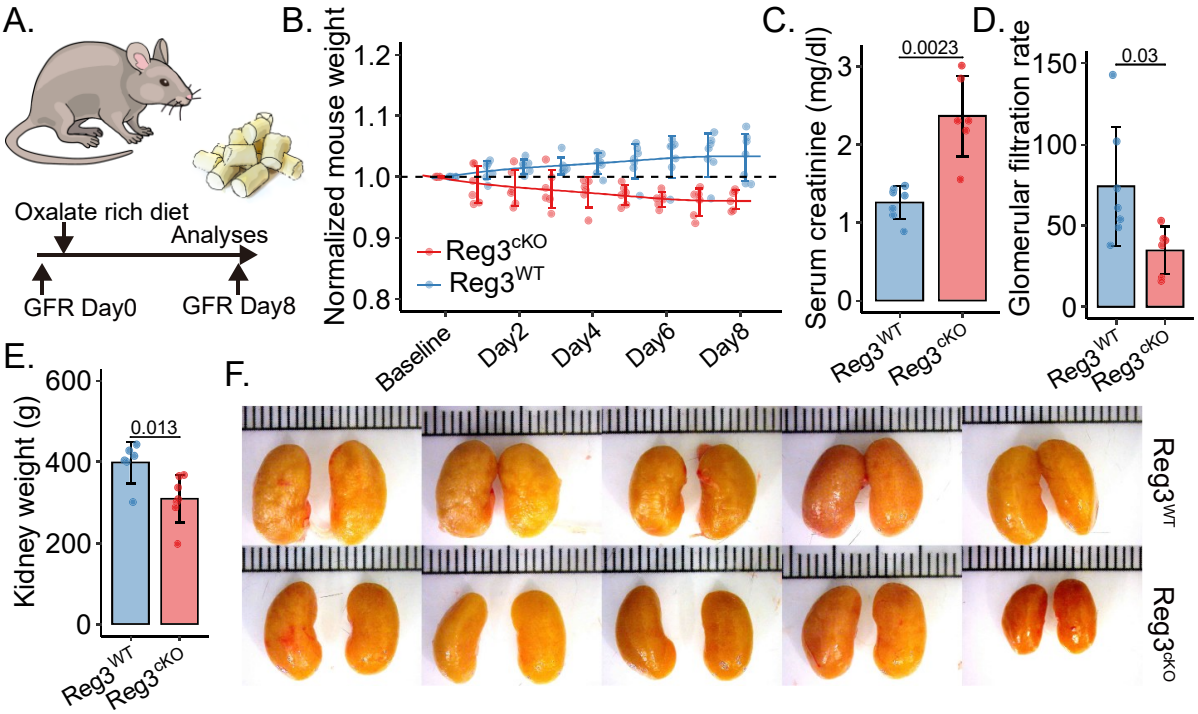

Figure 29. Rank-Regnase3cKO aggravate CaOx kidney injury. (A) Schematic of experimental set-up. Organ harvest was taken at day 8 after change the diet. (B) The mouse weight for each mouse after change the diet in response to the genotype. The curve is fitted using the cubic spline algorithm. (C) Serum creatinine level, (D) glomerular filtration rate (E) kidney weight at sacrifice, and (F) kidney appearance. All quantitative data are means ± SD. The t-test was employed for the statistical examination.

The histopathological results on of Rank-Regnase3cKO mice revealed that they were more susceptible to kidney injury as evidenced by the increased injury scores, greater fibrosis, and an elevated presence of F4/80 positive cells. However, the presence of CaOx crystal deposits was found to be less in the Rank-Regnase3cKO mice kidneys when compare to wild-type mice (Figure 30), which may be attributed to the increased phagocytic activity of macrophages. These results imply that while the Rank-Regnase3cKO mice displayed a

heightened susceptibility to injury in the CaOx-induced nephrocalcinosis model, they exhibited a reduced accumulation of CaOx crystals.

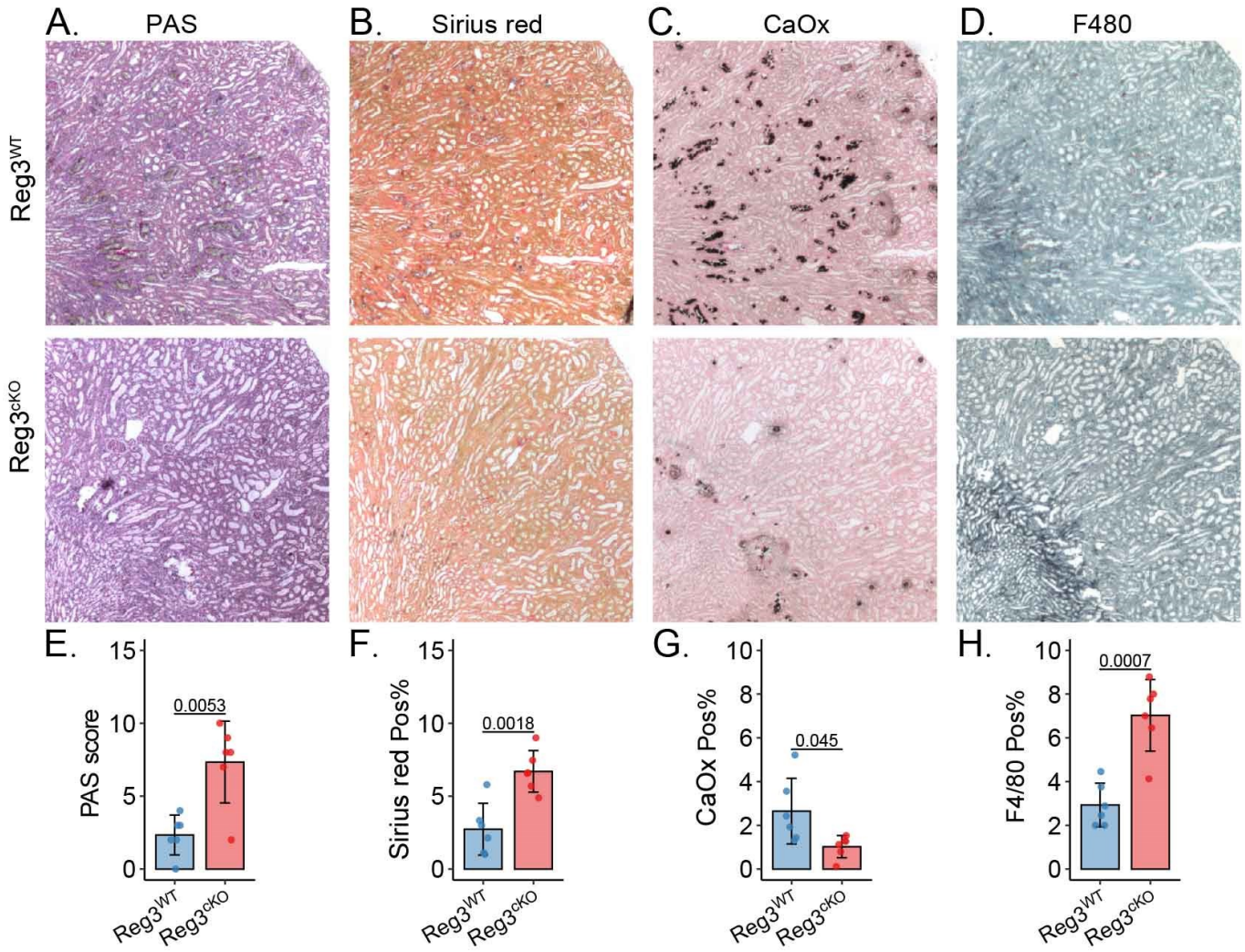

Figure 30. Pathological histology in Rank-Regnase3cKO 8 days after changed the CaOx diet. (A) Renal tubular damage was quantified using Periodic acid-Schiff (PAS) staining. (B) Collagen or fibrosis level was measured using Sirius red staining. (C) CaOx staining. (D) Macrophage were visualized using F4/80 staining. (E-H) quantitative analysis for the staining. The t-test was employed for the statistical examination. All quantitative data are means ± SD, and the images were magnified at 200x.

4.2.7 Regnase3 deletion in Rank-Cre BMDM

To further understand the role of Regnase3 in macrophage response to injury, an in vitro model was employed by isolating monocytes from the bone marrow using a well-established protocol and inducing them to differentiate into M0 macrophages by L929 supernatant. As demonstrated in Figure 17 and Figure 18, the Regnase3 is successfully deleted the exon 4 in the Rank-Regnase3cKO cells. To investigate the tolerance and metabolism of Rank-Regnase3cKO macrophages in response to injury, H_2O_2 was used to stimulate M0 macrophages and the levels of LDH and MTT were measured in both WT and Rank-Regnase3cKO. The results showed that Rank-Regnase3cKO macrophages exhibited higher metabolic activity following mild and

rapid H_2O_2 stimulation (1 hour), but the levels of LDH and MTT was no significant differences during severe H_2O_2 injury (Figure 31).

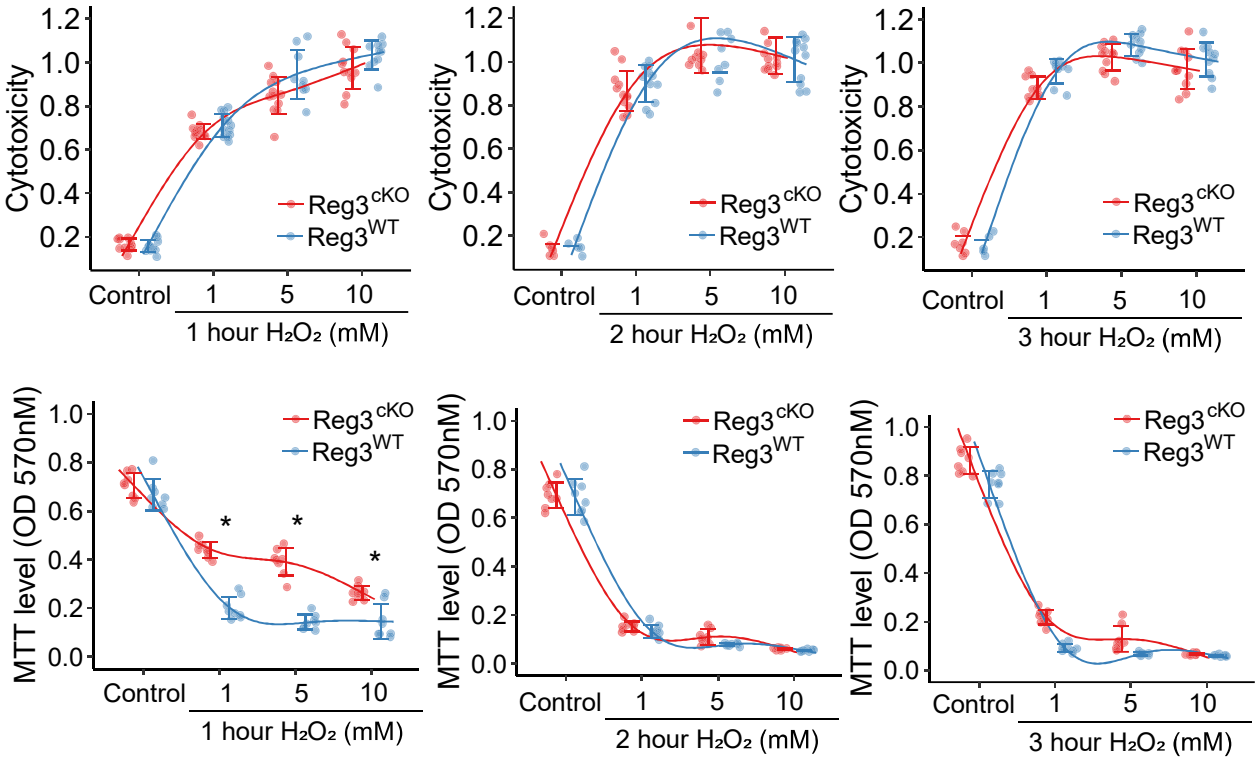

Figure 31. Cytotoxicity and metabolism on BMDM from Rank-Regnase3cKO mice after H_2O_2 incubation. The top three plots are the cytotoxicity (calculated by the LDH OD450) after 1,2- and 3-hour incubation with 1, 5 and 10 mM H_2O_2. The bottom three plots are the metabolism of the BMDM after with the corresponding concentration and incubation time of H_2O_2. The curve is fitted using the cubic spline algorithm. All quantitative data are means ± SD. The t-test was employed for the statistical examination.

The RNA-seq analysis results showed that the Regnase3 deletion in macrophages leads to significant changes in other gene expression. A total of 542 genes upregulated and 451 genes were downregulated at the exon level, while 206 genes were upregulated, and 57 genes were downregulated at the intron level. Additionally, the CCL2, CCR2, and TNF levels were found to be upregulated in the Rank-Regnase3cKO M0 macrophages, while VEGFa and TGF-β were downregulated. Gene set enrichment analysis (GSEA) showed that Rank-Regnase3cKO suppressed the immune response but promoted the DNA repair and cell cycle (Figure 32). The results obtained from the RNA-seq analysis give a clue that the ablation of Regnase3 results in the dysfunction of macrophages, as indicated by the raise in the mRNA levels which associated with inflammation and cell migration.

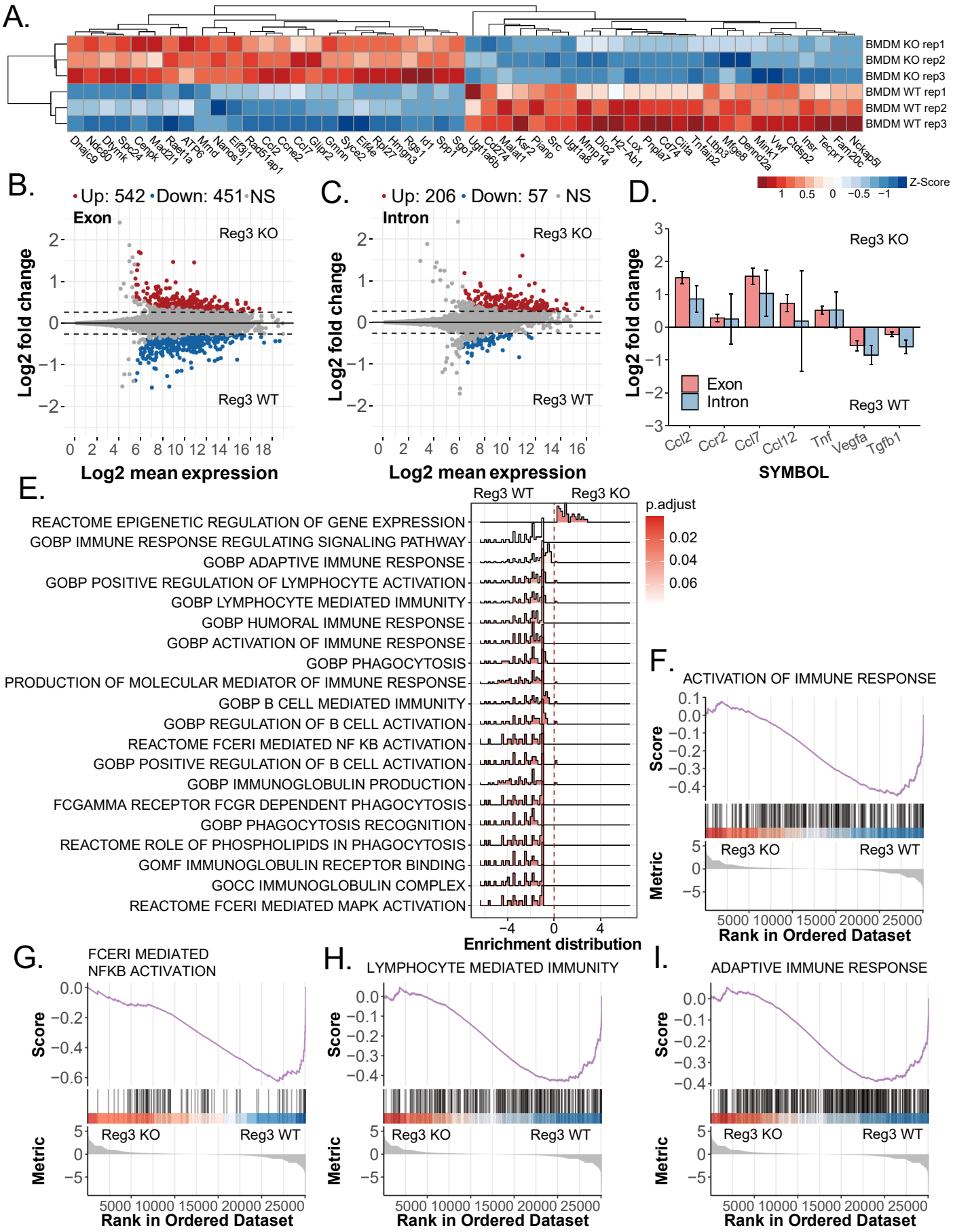

Figure 32. Bulk RNA-seq on Rank-Regnase3cKO and wild type M0 macrophage. Bulk RNA-seq on Rank-Regnase3cKO and wild type M0 macrophage. The M0 macrophages are derived from bone marrow monocyte from via L929 supernatant induction. (A) Heatmap of biological replicates of top differentially expressed genes in RankCre and wild type M0 macrophage. A heatmap and dendrogram were used to display the differentially expressed genes' z-scores of normalized counts. An MA plot was also created to display the shrink log2 fold change on exons (B) and introns(C)

between RankCre and wild type M0 macrophages. Genes that have undergone differential expression testing and have an adjusted p-value lower than 0.05 are identified by the colors red or blue. (D) Selected gene expression in exon and intron at two conditions. (E) Density ridges for the enriched gene sets. The expression distributions of core enriched genes for GSEA enriched gene sets are displayed through the density ridge plot, where the gradient color represents the adjusted p-values. (F-I) Selected enrichment plots from GSEA analysis based on the gene enrichment profiles of RankCre compared with wild type M0 macrophage. Enrichment is shown for transcriptional signatures related to immune response.

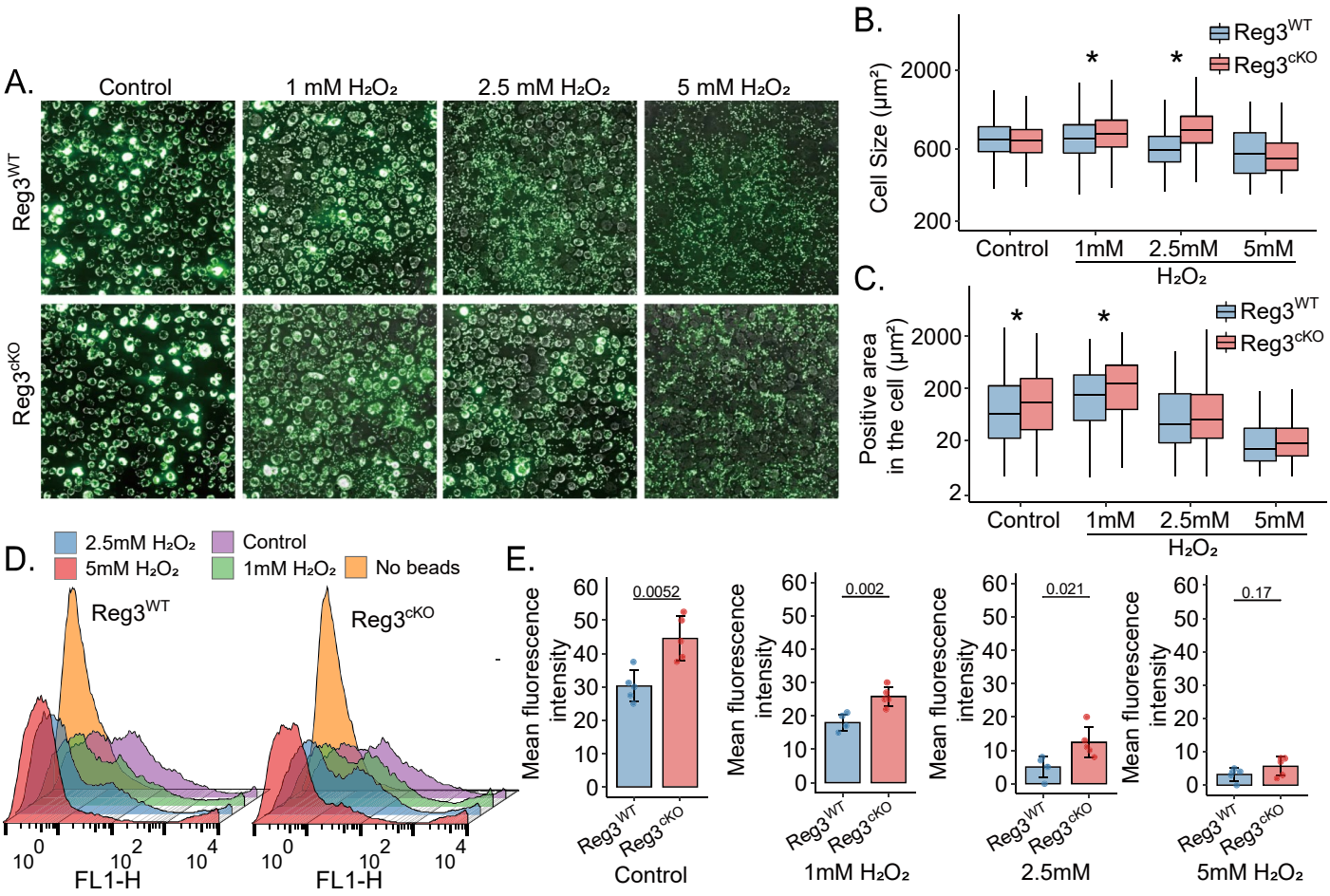

Figure 33. Phagocytic capacity on BMDM from Rank-Regnase3cKO mice after H_2O_2 The cells were first incubated with or without 0, 1 ,2.5 and 5 mM H_2O_2 for 1 hour, then change with the fresh medium with the fluorescent latex beads(A-C) and fluorescent latex rabbit lgG-FITC (D,E) beads. After incubation and the quenching, the cells and fluorescence intensity were detected by the (A) CellPose Neural Convolutional Network or (D)flow cytometry. (C) Positive area in the cell represents the fluorescent beads positive area in the (B) area of cell segmentation. (E) Quantitative analysis by flow cytometry. The t-test was employed for the statistical examination. All quantitative data are means ± SD.* P<0.05

Next, we found the phagocytic capacity of the Rank-Regnase3cKO macrophages were enhanced, with an ability to phagocytose more beads with or without of H_2O_2 injury (Figure 33). Furthermore, the Rank-Regnase3cKO macrophages showed an increased capability to migrate, even under the conditions of H_2O_2 injury, as demonstrated in the wound healing assay, and were found to be more sensitive to the cytokines CCL2 and nephrotoxic serum in the transwell assay (Figure 34). These findings imply that Regnase3 plays a

necessary role on the macrophage's survival and migration post-injury that facilitate inflammation. This could explain the heightened inflammation in the kidney observed in the Rank-Regnase3cKO mice after AKI.

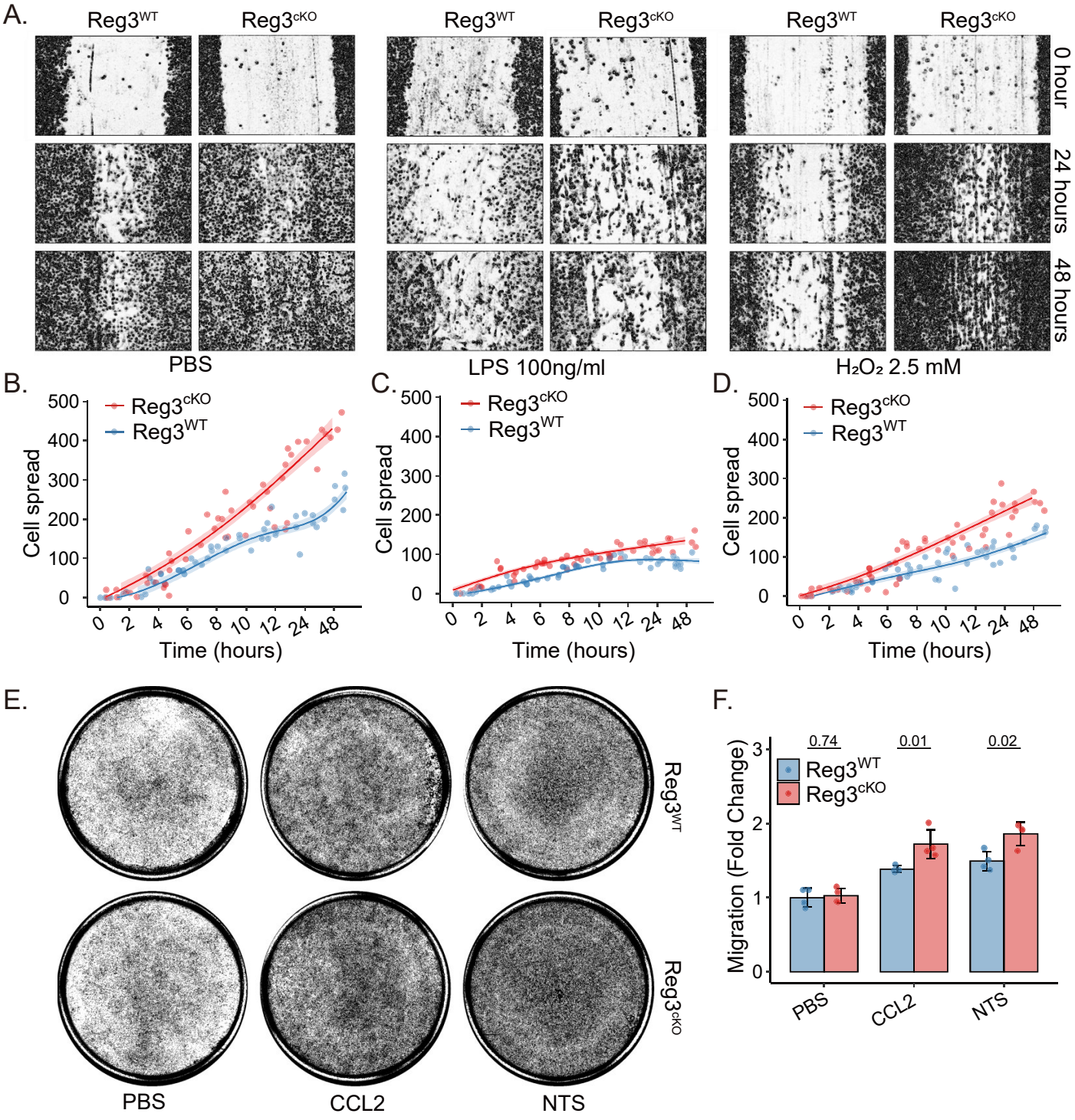

Figure 34. Migratory on L929 induced BMDM from Rank-Regnase3cKO mice after H_2O_2 and LPS incubation. (A) The images were token at the 0, 24 and 48 hours in control, 2.5mM H_2O_2 for 1 hours and 100ng/ml LPS for 25 hours incubation. Cell spread represents the cell number that migrate into the gap. The cells were detected by the (B-D) CellPose Neural Convolutional Network. The curve is fitted using the cubic spline algorithm. (E, F) Cell transwell assay on BMDM with cytokines CCL2 and nephrotoxic serum (NTS). All quantitative data are means ± SD. The t-test was employed for the statistical examination.

4.2.8 Regnase3 deletion in macrophage polarization

In order to study macrophage polarization, we employed an in vitro method by utilizing LPS and LPS+INFg for M1 polarization induction, and IL4 and IL10 for M2. The expression levels of Regnase1 and Regnase3 were found to be significantly upregulated in M1 macrophages ($P < 0.01$), while the expression of the remaining Regnases remained unchanged (Figure 35).

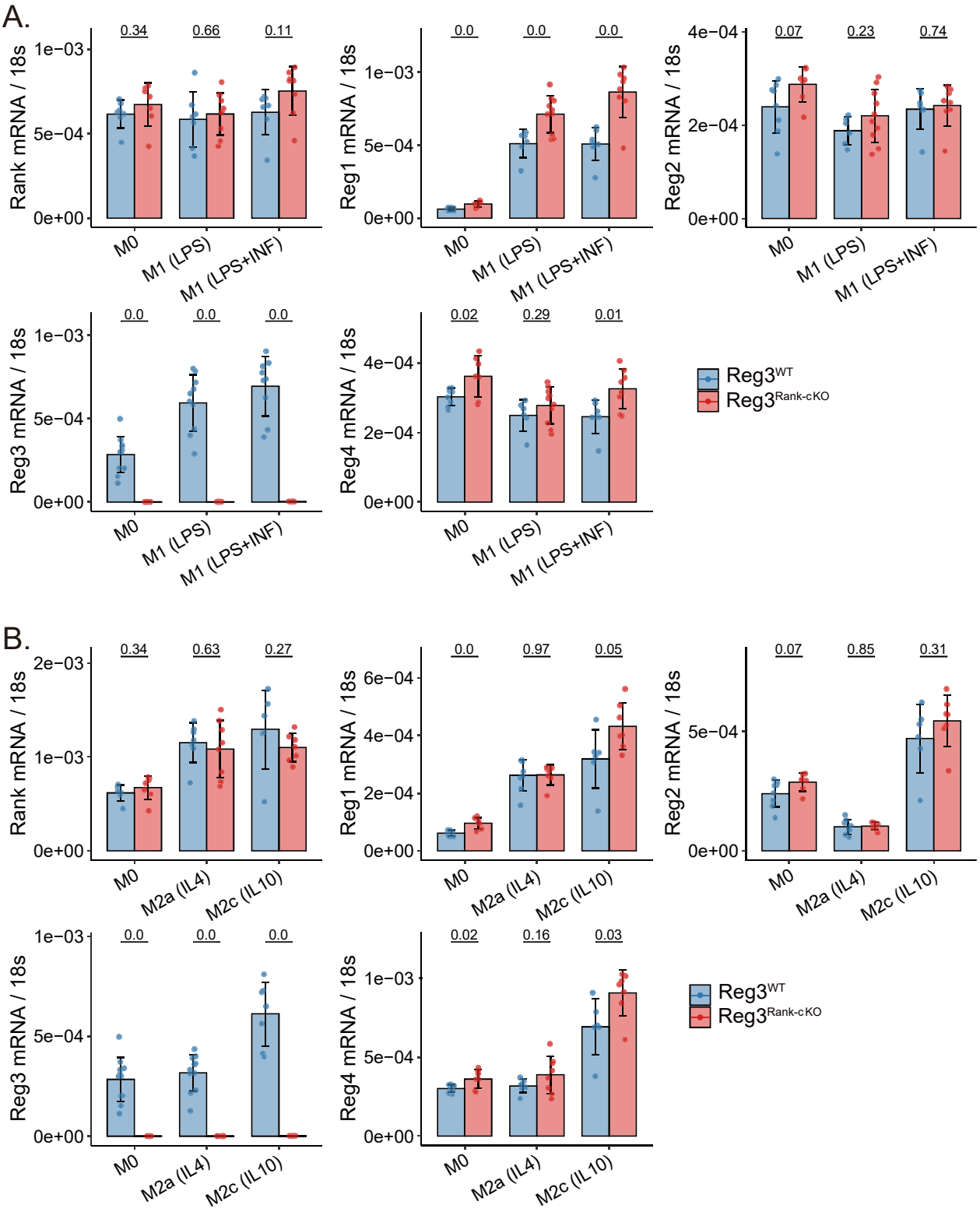

Figure 35. The mRNA level for Rank and Regnase family in M1 and M2 polarized macrophage. The mRNA for Rank and Regnase 1 to 4 in M0 and (A) LPS, LPS+INFg induced M1 and (B) IL4 and IL10 induced M2 macrophages. All quantitative data are means ± SD. The t-test was employed for the statistical examination.

In contrast, the expression of Regnase3 and Regnase4 was only observed to be responsive to the IL4 stimulus, while Regnase1 and Regnase2 were responsive to both stimuli (Figure 35). The deletion of exon4 of the M1 macrophage was successfully achieved in the Rank-Regnase3cKO as shown in Figure 36, which is consistent with the M0 macrophage results. Additionally, we observed a compensatory upregulation of Regnase1, 2, and 4 in the Rank-Regnase3cKO M1 macrophages.

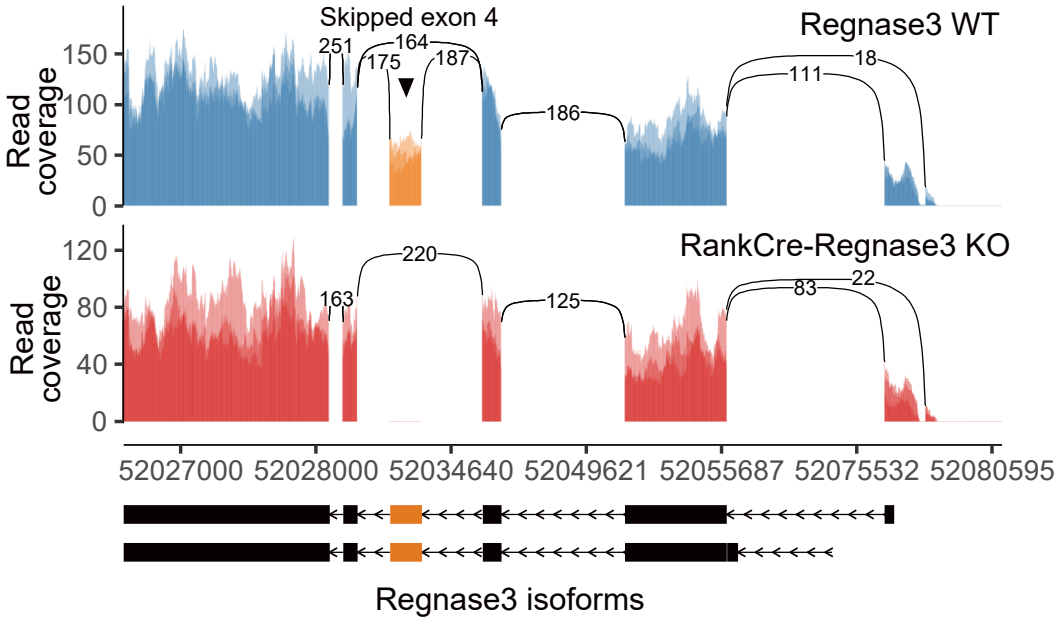

Figure 36. Sashimi plot for the Regnase3 chr9:52026580-52080668 in Rank-Regnase3cKO M1 BMDM. Rank-Regnase3cKO condition is shown in red plots, while the wildtype condition is depicted in blue. The X-axis shows the genomic locations, while the Y-axis indicates the transcription intensity. The plots show a "sashimi-like" region, which is a heavily transcribed region of exon, and the blank intronic regions between exons. The line crossing exonic regions represent the reads of junction and the count number is indicated on it. The exonic structure of the Regnase3 transcripts NM_001368810.1 and NM_001162921.2 is displayed below Sashimi plot, with the exonic region marked in yellow being the target that was inserted by flox and then deleted by recombinant Rank-Cre.

Our in vivo data indicates that the deletion of Regnase3 in the Rank-Regnase3cKO mice leads to a reduction in the proportion of M1 polarized macrophages, while simultaneously increasing the absolute number of these cells. In order to further investigate this phenomenon, we conducted an in vitro study. As results, the proportion of M1 polarized macrophages was decreased in Rank-Regnase3cKO macrophages compared to wild-type in combination stimulation of LPS or IFNg. Additionally, the ratio of M2 macrophages was also lower in the Rank-Regnase3cKO group, regardless of whether IL4 or IL10 was used (Figure 37). These results are consistent with the in vivo data as the Rank-Regnase3cKO leads to less M1 and M2 macrophage polarization. RNA-seq data indicated significant transcriptomic alterations in Rank-Regnase3cKO M1 macrophages, with 926 genes upregulated and 1,293 genes downregulated at the exon level, and 296 genes upregulated, and 541 genes downregulated at the intron level (Figure 38). GSEA revealed that the deletion of Regnase3 suppressed

the immune response, similar to the results observed in M0 macrophages. However, both RNA-seq and qPCR analysis revealed that pro-inflammatory genes, such as CCL2, CCR2/5, TNF, IL1b, ICAM1, and VCAM1, were overexpressed in Rank-Regnase3cKO M1 macrophages, particularly in the LPS+ IFNg M1 macrophages (Figure 39), but there were not many significant differences when comparing M2 polarization (Figure 40).

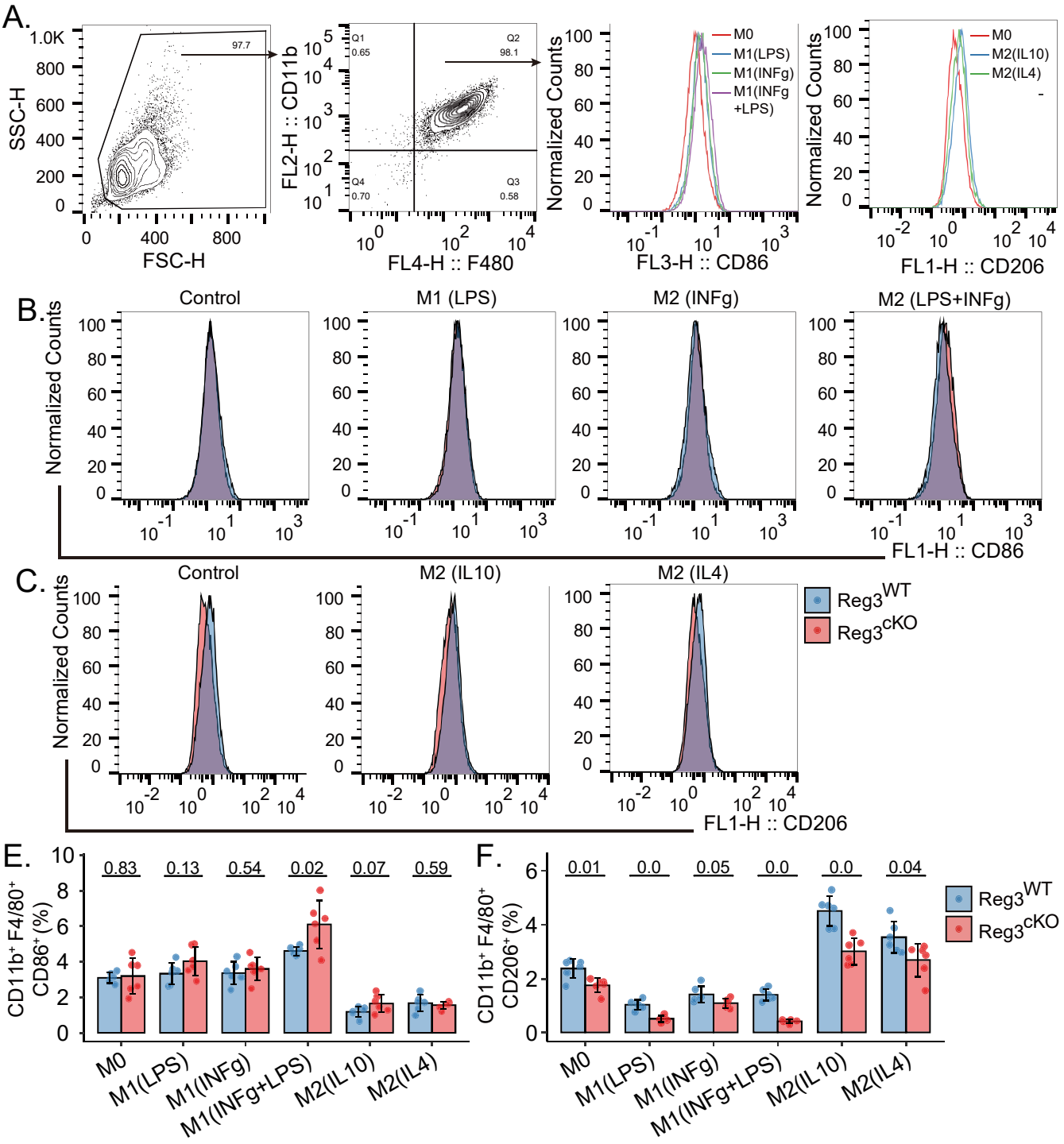

Figure 37. Rank-Regnase3cKO M1 and M2 Bone-marrow-derived macrophage. (A) Gating strategy for M1 and M2 cells macrophage. (B) Density plot for CD86 in LPS and INFg induced M1 macrophage. (C) Density plot for CD206 in IL10 and IL4 induced M2 macrophage. Proportion for M1 (E) and M2 cells (F). All quantitative data are means ± SD. The t-test was employed for the statistical examination.

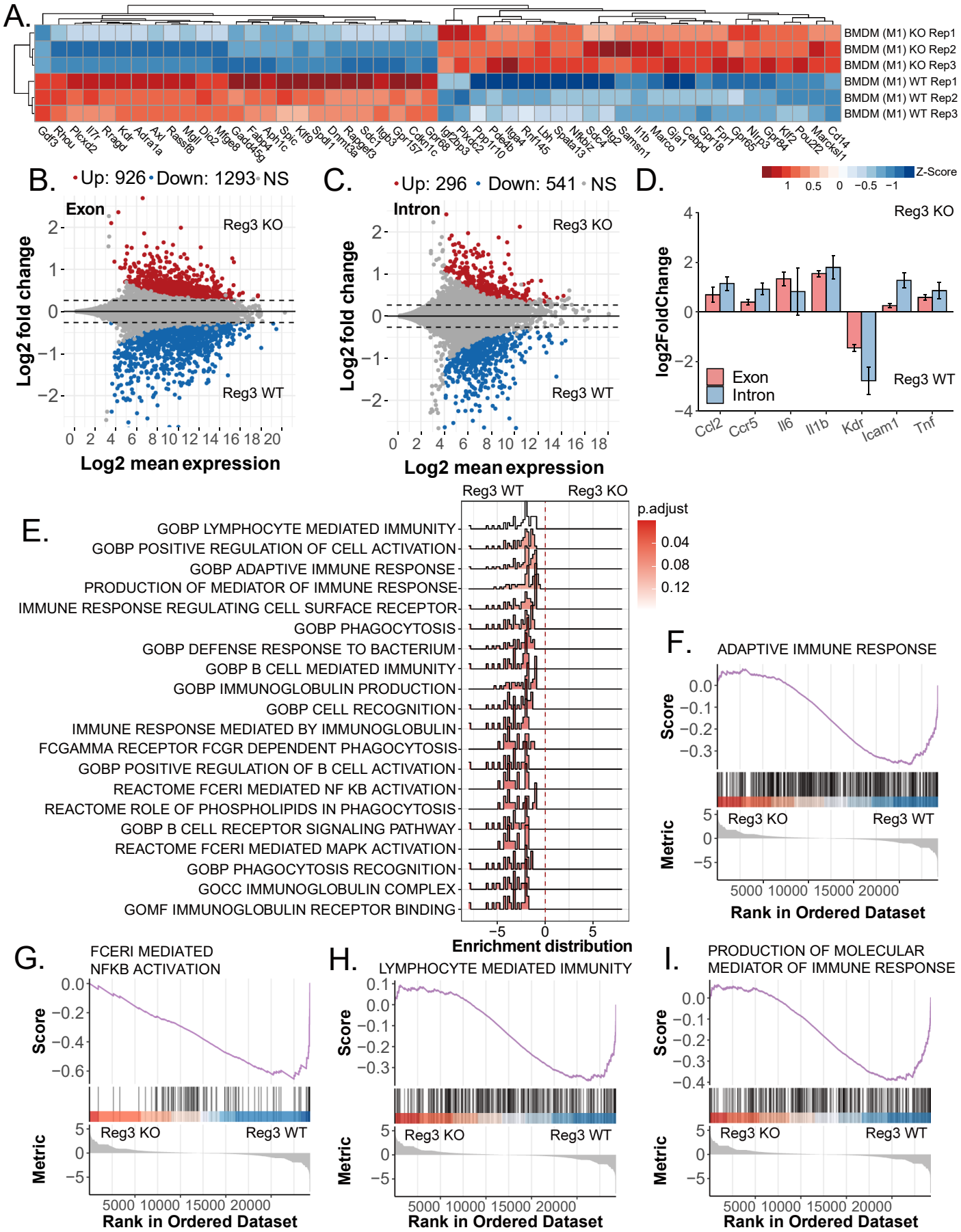

Figure 38. Bulk RNA-seq on Rank-Regnase3cKO and wild type M1 macrophage. The macrophages are derived from bone marrow monocyte from via L929 supernatant induction and then incubated with LPS plus INFg for 24 hour for M1. (A) Heatmap of biological replicates of top differentially expressed genes in RankCre and wildtype M1 macrophage. A heatmap and dendrogram were used to display the differentially expressed genes' z-scores of normalized counts. An MA plot was also created to display the shrink log2 fold change on exons (B) and introns(C) between

RankCre and wild type M1 macrophages. Genes that have undergone differential expression testing and have an adjusted p-value lower than 0.05 are identified by the colors red or blue. (D) Selected gene expression in exon and intron at two conditions. (E) Density ridges for the enriched gene sets. The expression distributions of core enriched genes for GSEA enriched gene sets are displayed through the density ridge plot, where the gradient color represents the adjusted p-values. (F-I) Selected enrichment plots from GSEA analysis based on the gene enrichment profiles of RankCre compared with wild type M1 macrophage. Enrichment is shown for transcriptional signatures related to immune response.

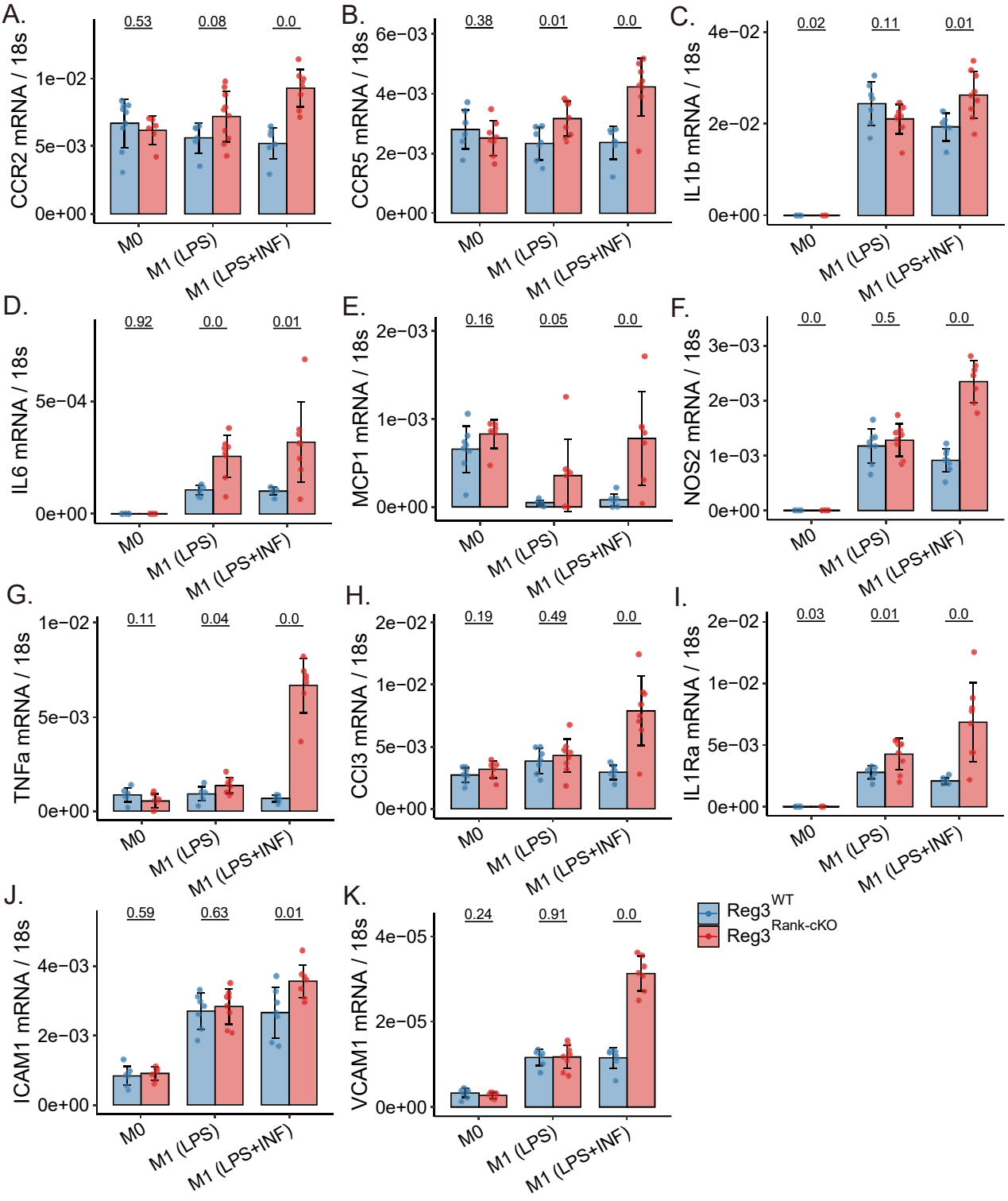

Figure 39. The mRNA level for pro-inflammatory genes in L929 induced BMDM from Rank-Regnase3cKO mice after M1 polarization induction(A-K). All quantitative data are means ± SD. The t-test was employed for the statistical examination.

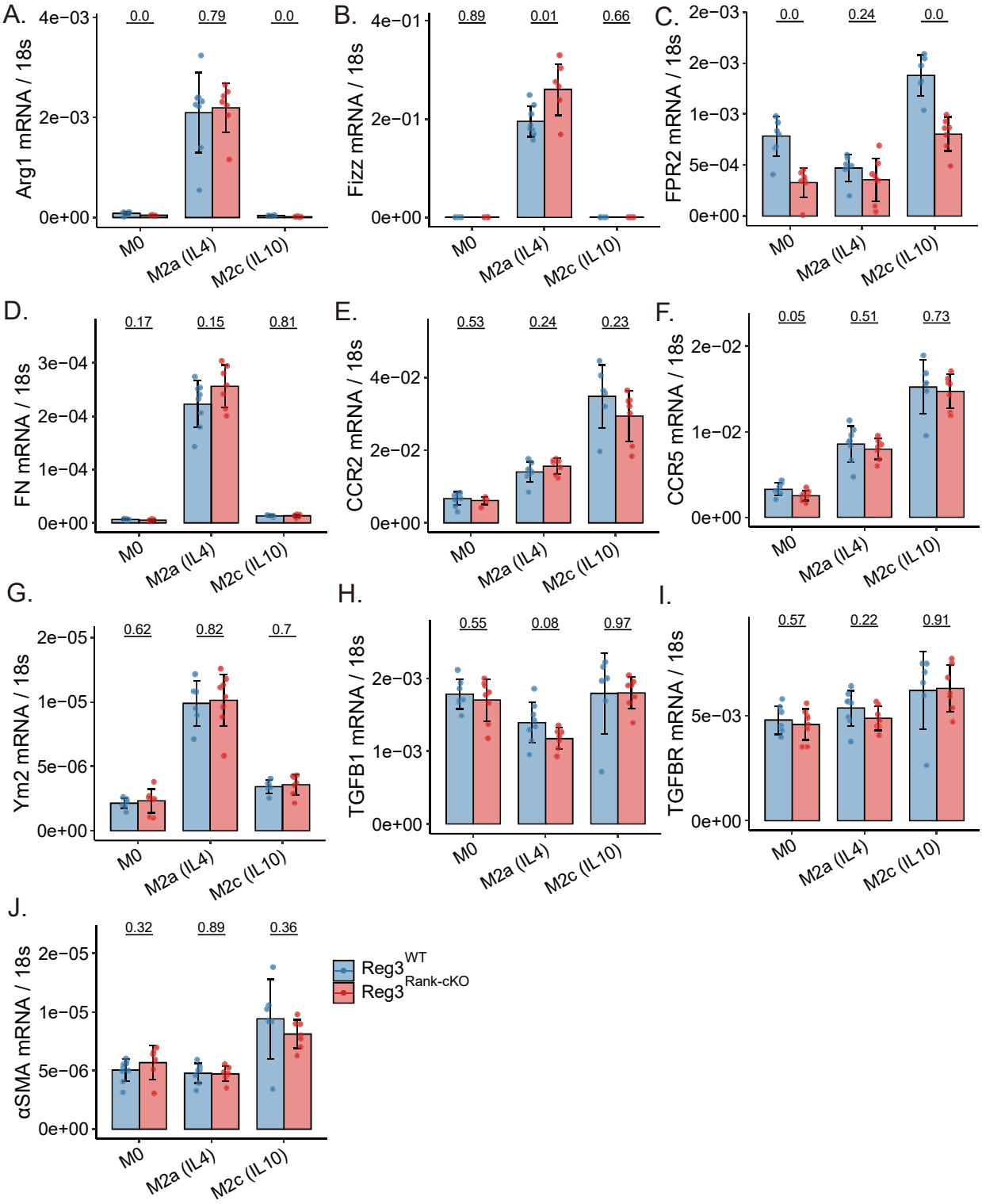

Figure 40. The mRNA level for genes in L929 induced BMDM from Rank-Regnase3cKO mice after M2 polarization induction (A-J). All quantitative data are means ± SD. The t-test was employed for the statistical examination.

The bulk RNA-seq for the alveolar macrophages showed the similar results, that the CCR2/5 are highly expressed in Rank-Regnase3cKO cells (Figure 41).Overall, our results suggest that Regnase3 acts as a vital part in macrophage polarization and that its deletion leads to immune disorders and the overexpression of inflammatory genes (Figure 42).

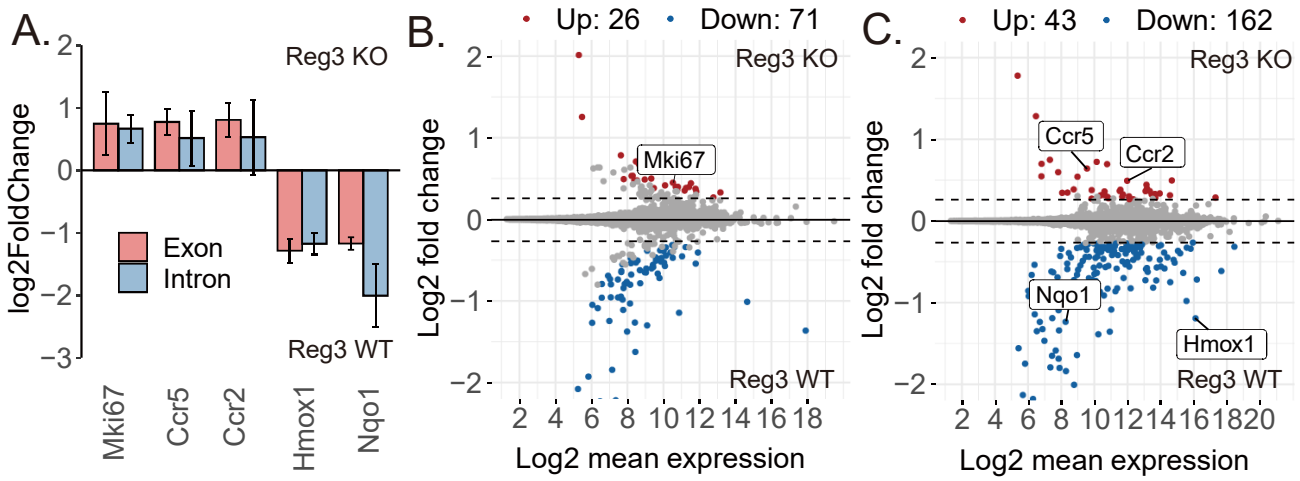

Figure 41. The bulk RNA-seq for the alveolar macrophages. (A) Regnase3 KO alveolar macrophage showed more expression of both intron and exon CCR5 and CCR2. An MA plot was also created to display the shrink log2 fold change on exons (B) and introns(C) between Regnase3 knockout and wild type macrophages. Genes that have undergone differential expression testing and have an adjusted p-value lower than 0.05 are identified by the colors red or blue.

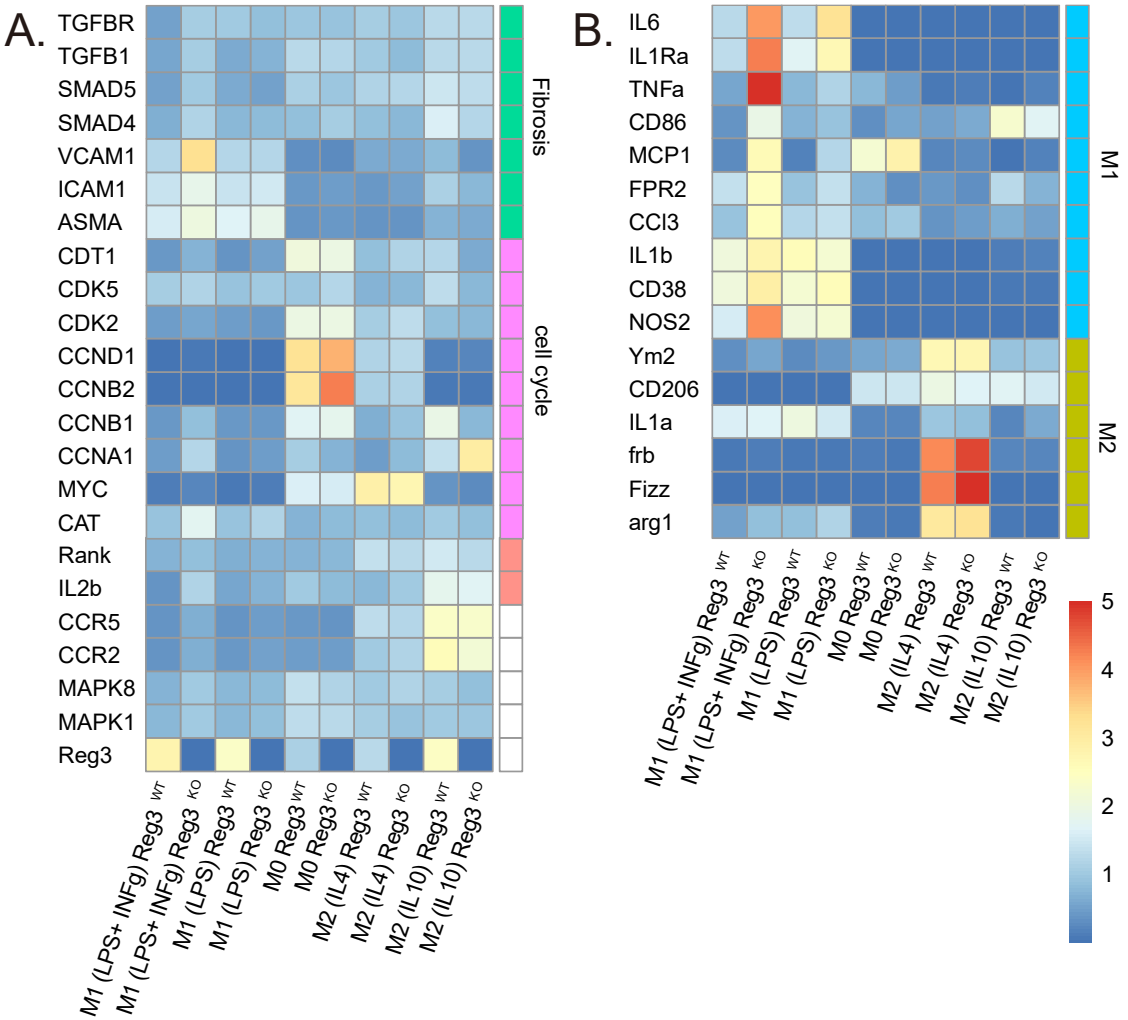

Figure 42. The mRNA level for genes in L929 induced BMDM from Rank-Regnase3cKO mice after M1 and M2 polarization induction. The M0 macrophages are derived from bone marrow monocyte from via L929 supernatant induction and then incubated with LPS, LPS+INFg, IL4 and IL10 24 hours for M1 and M2. Heatmap of mean values from 4 biological replicates of selected genes for (A) fibrosis, cell cycle (B) M1 and M2 markers in RankCre and wild type macrophage. The color on the heatmap representing z-scores of relative expressions on selected genes.

4.3 Pax8-Regnase3cKO in postischemic kidney injury

4.3.1 The scRNA-seq for renal proximal tubular cells in IRI

To further understand the Regnase3's role in kidney, we utilized scRNA-seq data from a published study (GSE139107) that analyzed kidney cells from mice at various time points post-IRI. After quality-control, there are 44,087 cells were sequenced, with 8,768 of them being identified as renal PTECs by expression of specific genes (Pax8, Lrp2, Slc5a12, Slc13a3, Havcr1, Cubn, Figure 43). The expression of the gene Regnase3 was found to be prevalent in the majority of PTECs. By utilizing markers outlined in the original study, the PTCs were further classified into healthy, repairing, failed repair, severely injured, and injured groups (Figure 44). It was observed that the Regnase3 was mostly expressed in healthy and repairing PTCs, but not in injured PTCs. According to the gene enrichment analysis results, Regnase3 was positively correlatied with programmed cell death and negatively correlated with immune cell chemotaxis. (Figure 45).

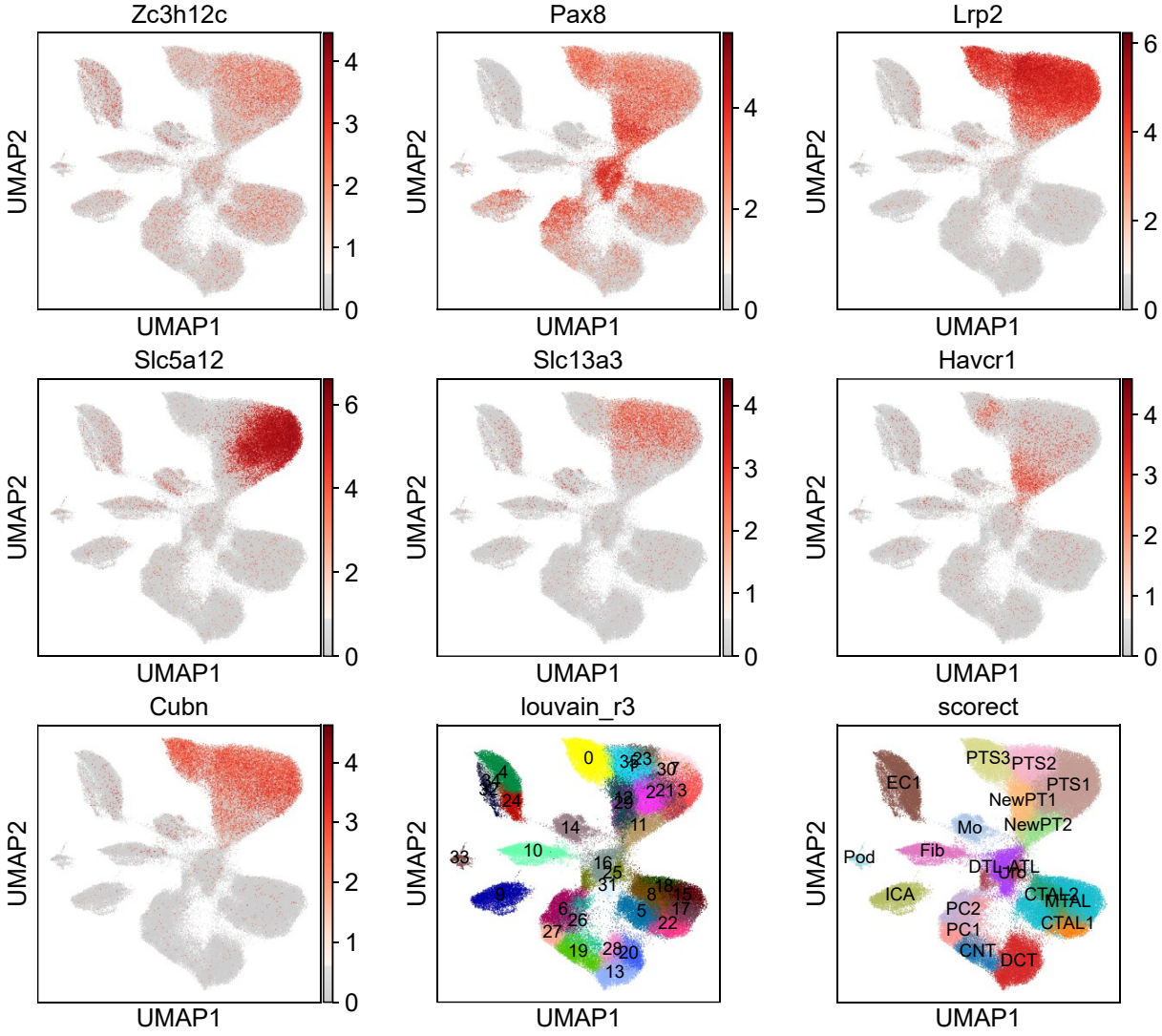

Figure 43. UMAP plot for mouse kidney cells after IRI. The clusters were segmented by the Louvain algorithm with the resolution of 3. According to feature plots of markers (Pax8, Lrp2, Slc5a12, Slc13a3, Havcr1, Cubn), the subclusters of 0, 1, 2 ,3 ,5, 35, 23, 30, 7, 29, 11, 13 were considered to be the proximal tubule cells. Regnase3=Zc3h12c, Zinc Finger CCCH-Type Containing 12C. All abbreviations are listed in the Appendix 5 and Appendix 6 (Adopted from GSE139107)

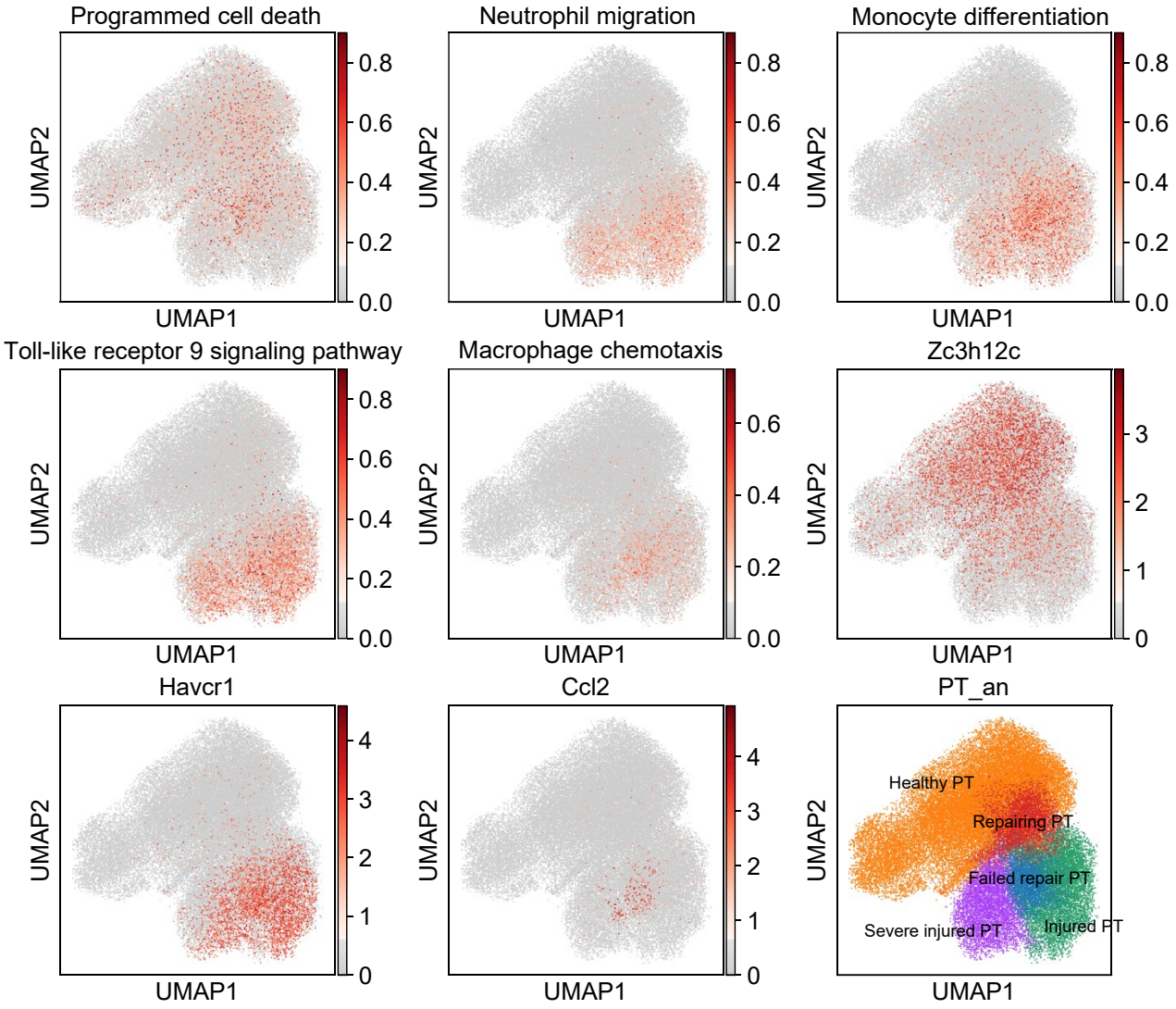

Figure 44. UMAP plot for gene enrichment scores and Regnase3 Zc3h12c expression in proximal tubule cells after IRI. The tubule cells were annotated based on cell markers from original article. The activations for regulation of programmed cell death, neutrophil migration, monocyte differentiation, toll-like receptor 9 signaling pathway, macrophage chemotaxis was assessed based on the average expression of corresponding function based on the MSigDB gene sets. UMAP, uniform manifold approximation and projection; Regnase3=Zc3h12c, Zinc Finger CCCH-Type Containing 12C; Havcr1, Hepatitis A virus cellular receptor 1; CCL2 CC-chemokine ligand 2; PT, proximal tubule. (Adopted from GSE139107)

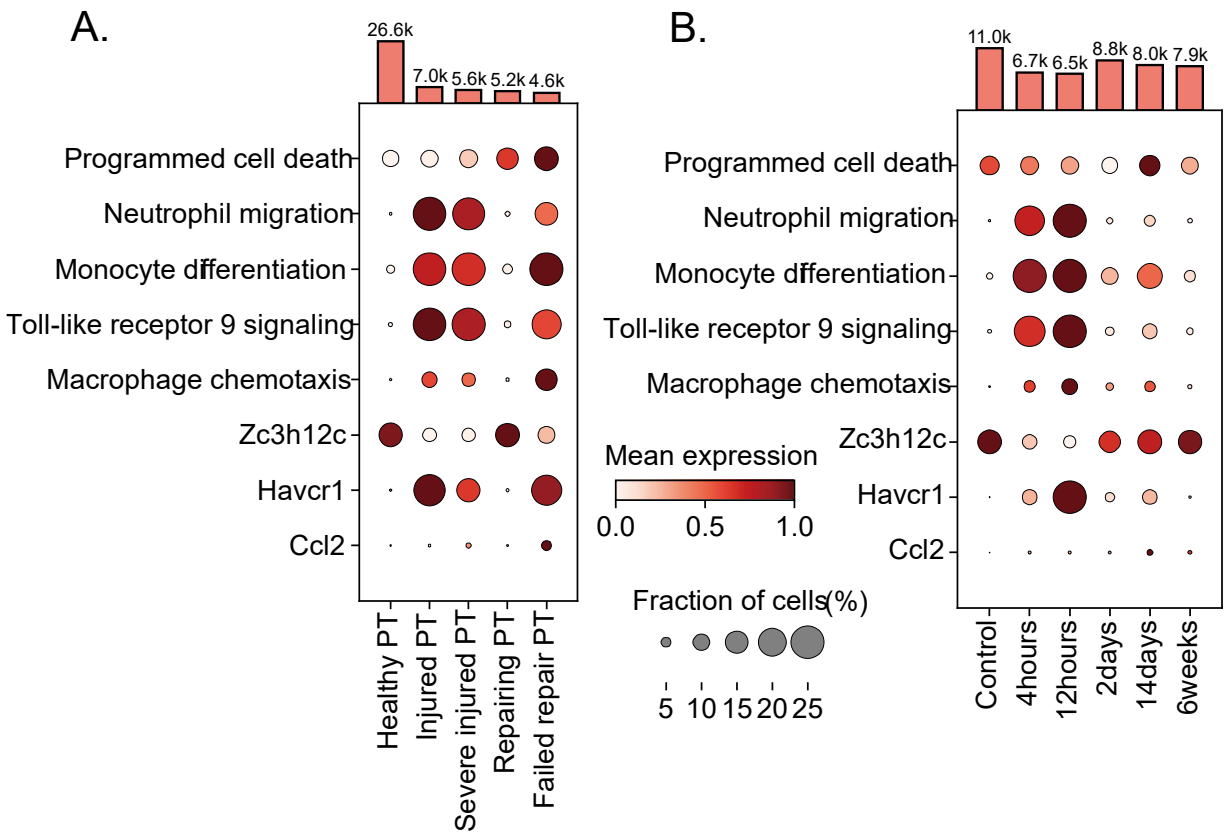

Figure 45. Dot plot for the gene enrichment scores and Regnase3 expression in proximal tubule cells after IRI. Annotation for the (A) subtype of proximal tubule cells and (B) sample after IRI. The dot size represents the cells' proportion in the group and the color represent the mean expression. The gene enrichment score are calculated based on the MSigDB gene sets. The bars plot on the top of the plot are the numbers of the cell in group. Regnase3=Zc3h12c, Zinc Finger CCCH-Type Containing 12C; Havcr1, Hepatitis A virus cellular receptor 1; CCL2 CC-chemokine ligand 2; PT, proximal tubule. (Adopted from GSE139107)

We further explored another scRNA-seq dataset (GSE199321) that analyzed the transcriptomes of single cell from 32 AKI patients' urine samples. After quality control, there are 44,087 cells were sequenced, with 11,181 cells identified as urinary renal tubular cells based on the annotation provided in the original study (Figure 46). Among the urinary cells, there were fewer cells that expressed Regnase3, which may be due to its low expression in injured cells. Additionally, the Regnase3 mRNA was negatively correlated with programmed cell death (Figure 47), consistent with the findings from the mouse IRI dataset. Thus, our analysis suggests that Regnase3 is highly expressed in healthy and repairing PTECs and performs a key function in both cell death at early stages of injury and the repair at later stages after the injury.

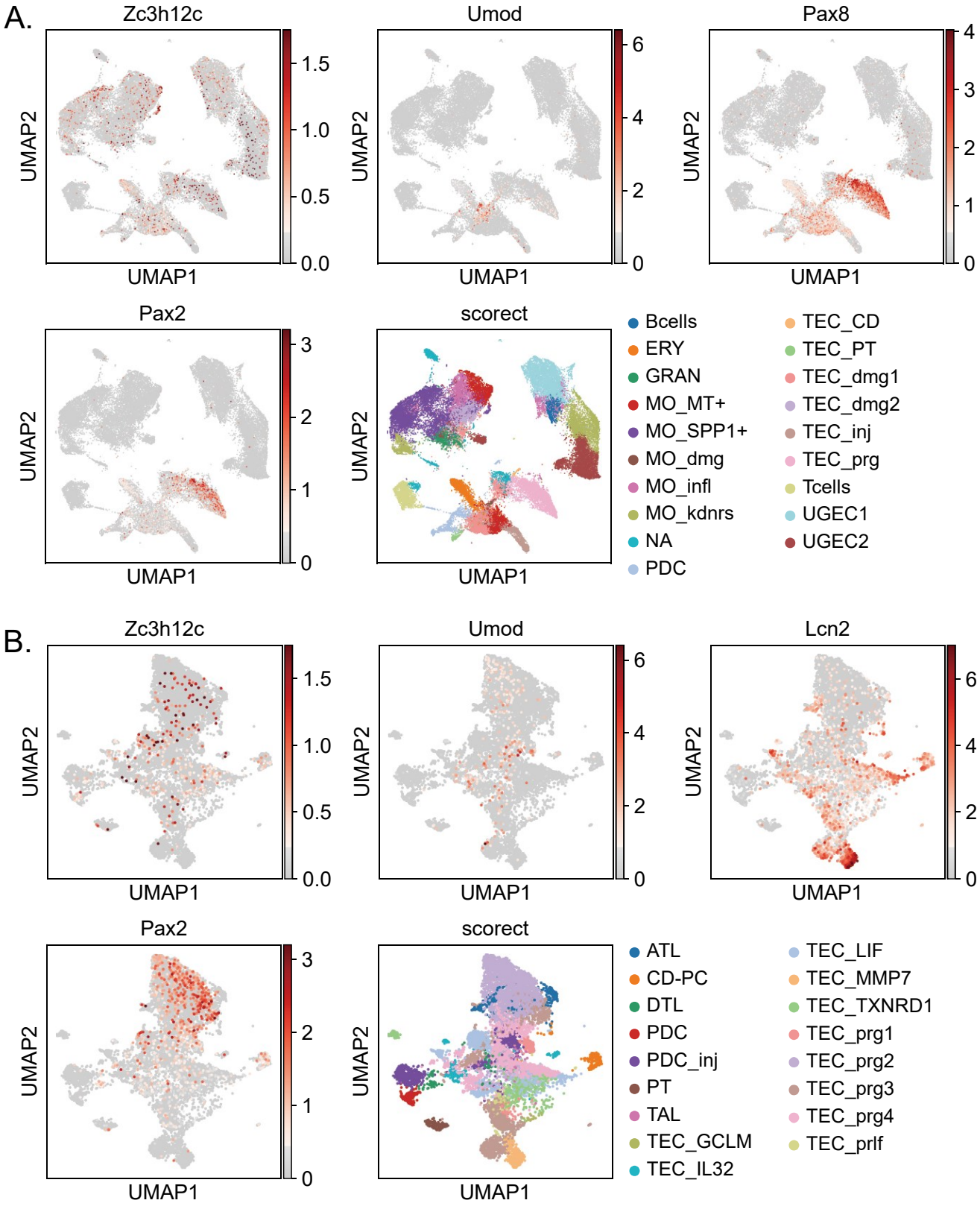

Figure 46. UMAP plot for gene expression in (A) urinary single cell and (B) TEC in human acute kidney injury. The TEC were annotated based on cell markers from Klocke J, et al. Kidney Int. All abbreviations are listed in the Appendix 5 and Appendix 6 (Adopted from GSE199321)

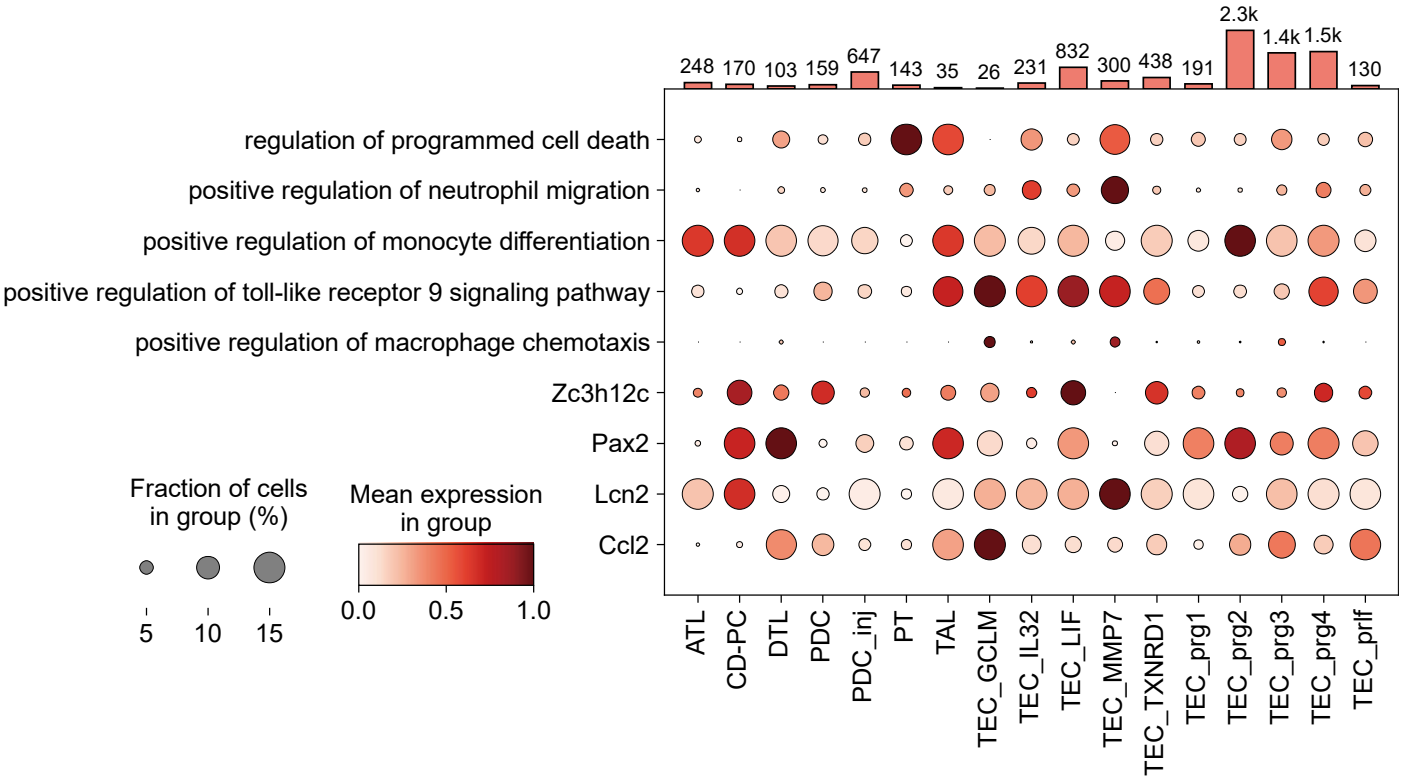

Figure 47. Dot plot for the gene enrichment scores and Zc3h12c expression in urinary TEC in human acute kidney injury. Annotation for the subtype of urinary renal tubule cell in acute kidney injury. The dot size represents the cells' proportion in the group and the color represent the mean expression. The bars plot on the top of the plot are the numbers of the cell in group. Regnase3=Zc3h12c, Zinc Finger CCCH-Type Containing 12C. All abbreviations are listed in the Appendix 5 and Appendix 6 (Adopted from GSE199321)

4.3.2 Selective Regnase3 deletion in Pax8 positive TEC

Since the scRNA-seq data suggests that Regnase3 is highly expressed in healthy TEC but is hardly expressed after injury, we sought to study if the expression pattern of Regnase3 protein follows a similar pattern in response to kidney injury in vivo. Our immunofluorescence staining results indicate that Regnase3 is highly expressed in TEC in healthy conditions, but low in the TEC following injury (Figure 48). This finding motivated us to further investigate the role of Regnase3 in renal TEC response to injury. To this end, we generated a transgenic Pax8-Regnase3 mouse line and confirmed the deletion of Regnase3 by qPCR and RNA-seq analysis. The RNA-seq analysis confirmed that there is a clear deletion of Regnase3 exon 4, while other exons remain unaffected (Figure 49). In vitro primary murine TEC express significantly lower levels of Regnase3, while Regnase1 and 4 are compensatory upregulated (Figure 50). This compensatory upregulation is also observed in Rank-Regnase3cKO macrophages. Therefore, we were able to successfully establish deletion of Regnase3 in Pax8-positive TEC.

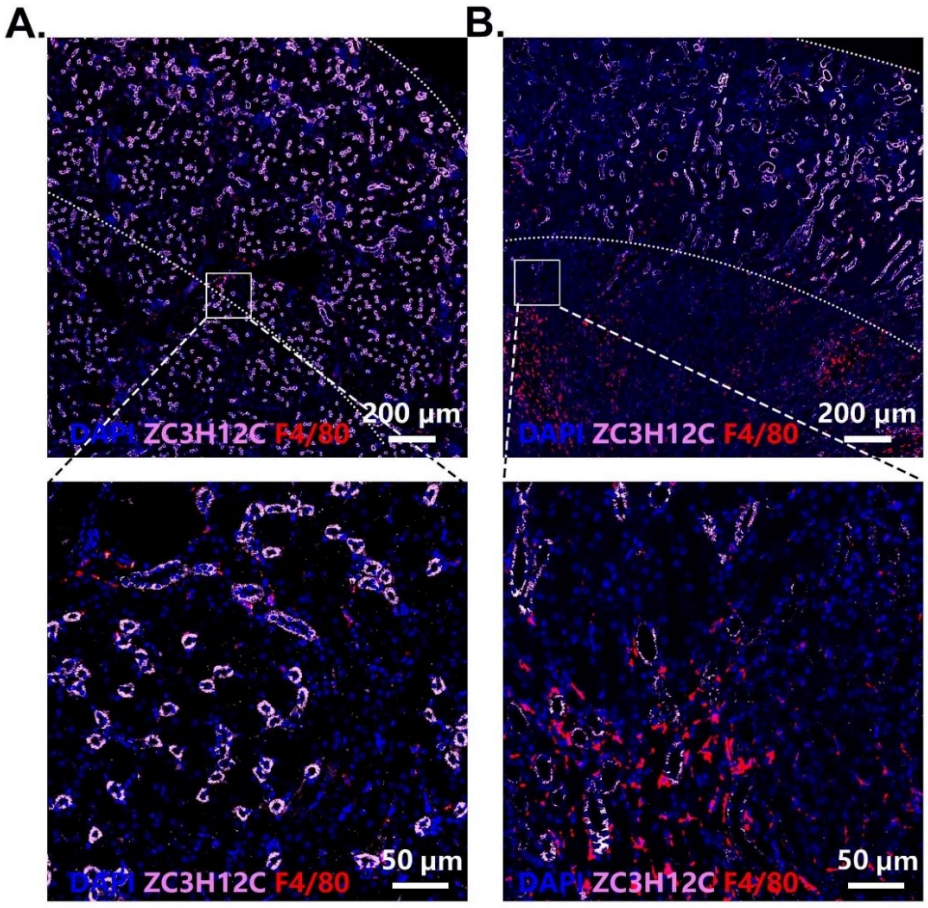

Figure 48. Immunofluorescence staining for Regnase3 (pink) and F4/80 (red) in (A) healthy and (B) IRI mouse kidney. Cell nuclei shows as blue by 4',6-diamidino-2-phenylindole (DAPI). Regnase3=Zc3h12c, Zinc Finger CCCH-Type

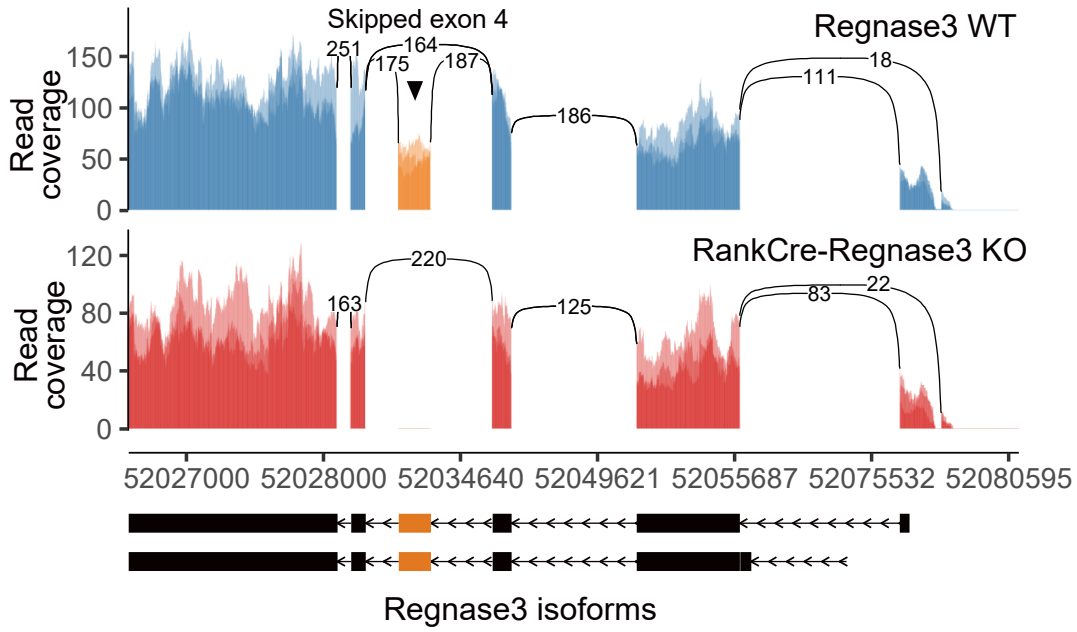

Figure 49. Sashimi plot for the Regnase3 chr9:52026580-52080668 in Pax8-Regnase3cKO renal tubular cell. Rank-Regnase3cKO condition is shown in red plots, while the wildtype condition is depicted in blue. The X-axis shows the genomic locations, while the Y-axis indicates the transcription intensity. The plots show a "sashimi-like" region, which is a heavily transcribed region of exon, and the blank intronic regions between exons. The line crossing exonic regions represent the reads of junction and the count number is indicated on it. The exonic structure of the Regnase3 transcripts NM_001368810.1 and NM_001162921.2 is displayed below Sashimi plot, with the exonic region marked in yellow being the target that was inserted by flox and then deleted by recombinant Rank-Cre.

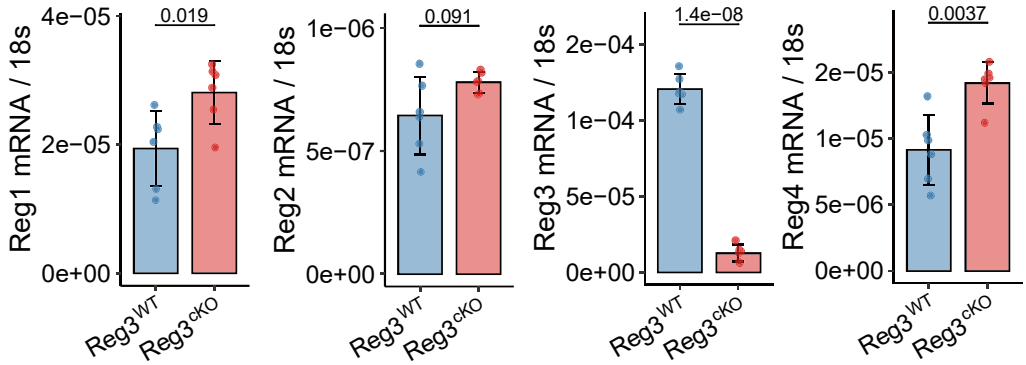

Figure 50. The mRNA level for Regnase family in renal primary murine tubular epithelial cells. The tubular epithelial cells were separated and cultured for one week. All quantitative data are means ± SD. The t-test was employed for the statistical examination.

4.3.3 Pax8-Regnase3cKO alleviating IRI without NX kidney injury

To study the role of TEC-derived Regnase3 in kidney following ischemia, mice with a deletion of Regnase3 in the Pax8-Regnase3cKO were subjected to 20 minutes of unilateral IRI without NX. As results, the GFR dropped significantly in both wildtype and Pax8-Regnase3cKO mice one day after IRI (Figure 51), but the deletion of Regnase3 in the TEC protected against injury and improved recovery from AKI. Specifically, at day 1 post-IRI , although GFR is not different in two group, histopathology examinations revealed that the Pax8-Regnase3cKO mice had less kidney injury score (P=0.068), less infiltration of F4/80 positive cells and more preservation of PTEC, as well as more Ki67-positive cells (Figure 52). Additionally, the Pax8-Regnase3cKO mice had a better recovery of kidney function as indicated by the GFR at day 7 till day 21 post-IRI. At day 21 post-IRI, the IRI kidney weight and size was also found to be larger in the Pax8-Regnase3cKO mice than the wildtype mice together with low kidney injury score, less IFTA and interstitial $F4/80^{+}$ cell infiltrates (Figure 53). The Scr levels and intrarenal levels of various injury markers such as Kim-1, NGAL, TIMP2, TNF and iNOS were found to be higher in wildtype mice (Figure 54). Moreover, the Pax8-Regnase3cKO mice had less expression in fibrosis, inflammation, and injury markers such as aSMA, Fibronectin, TGF-β, TGF-β receptor, VCAM1, ICAM1, CCR2, CCR5, CCL2, CXCL1 and CXCL2 (Figure 55). Overall, these results indicated that Regnase3 serves an integral role in TEC response to ischemia-reperfusion injury and its deletion can alleviate early injury and improve recovery from AKI.

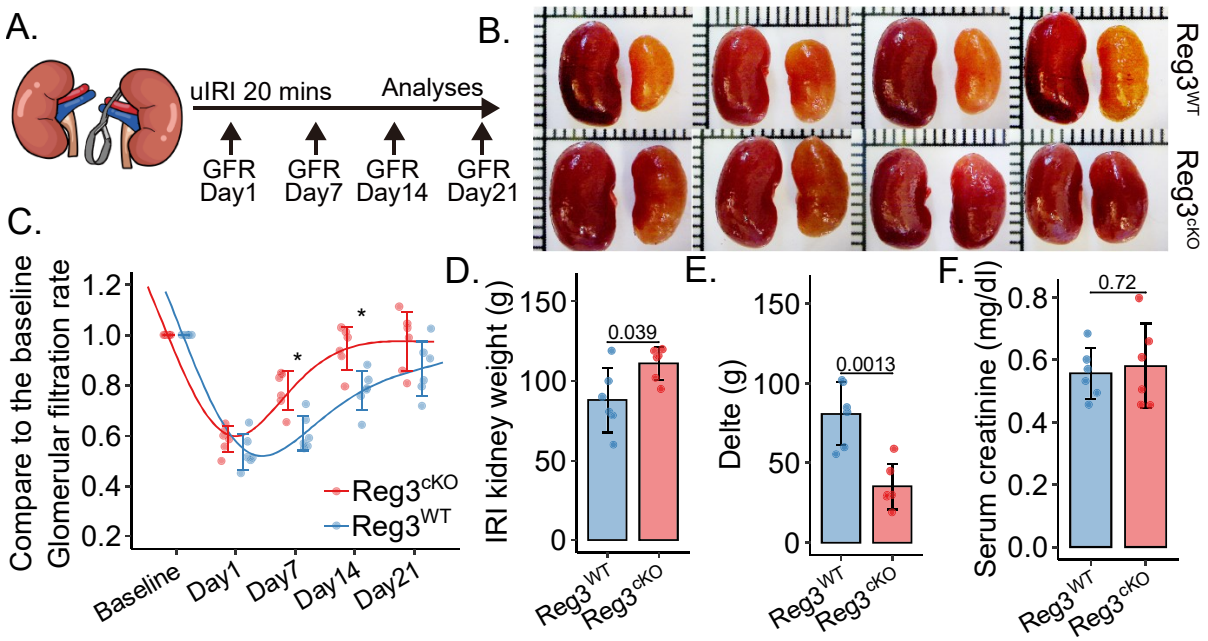

Figure 51. Pax8-Regnase3cKO alleviate the 20 mins IRI kidney injury. (A) A diagram illustrating the set-up of the experiment. Unilateral ischemia-reperfusion injury (IRI) was induced by clamping the kidney pedicle for 20 minutes. Organs were collected in two different states: healthy state and on day 21 following IRI. (B) Kidney appearance (C) The GFR normalized to baseline in response to the genotype. The curve is fitted using the cubic spline algorithm. (D) IRI kidney weight, (E) contralateral minus IRI kidney weight (Delta), (F) Serum creatinine level. All quantitative data are means ± SD. The t-test was used for the statistical analysis. *P<0.05.

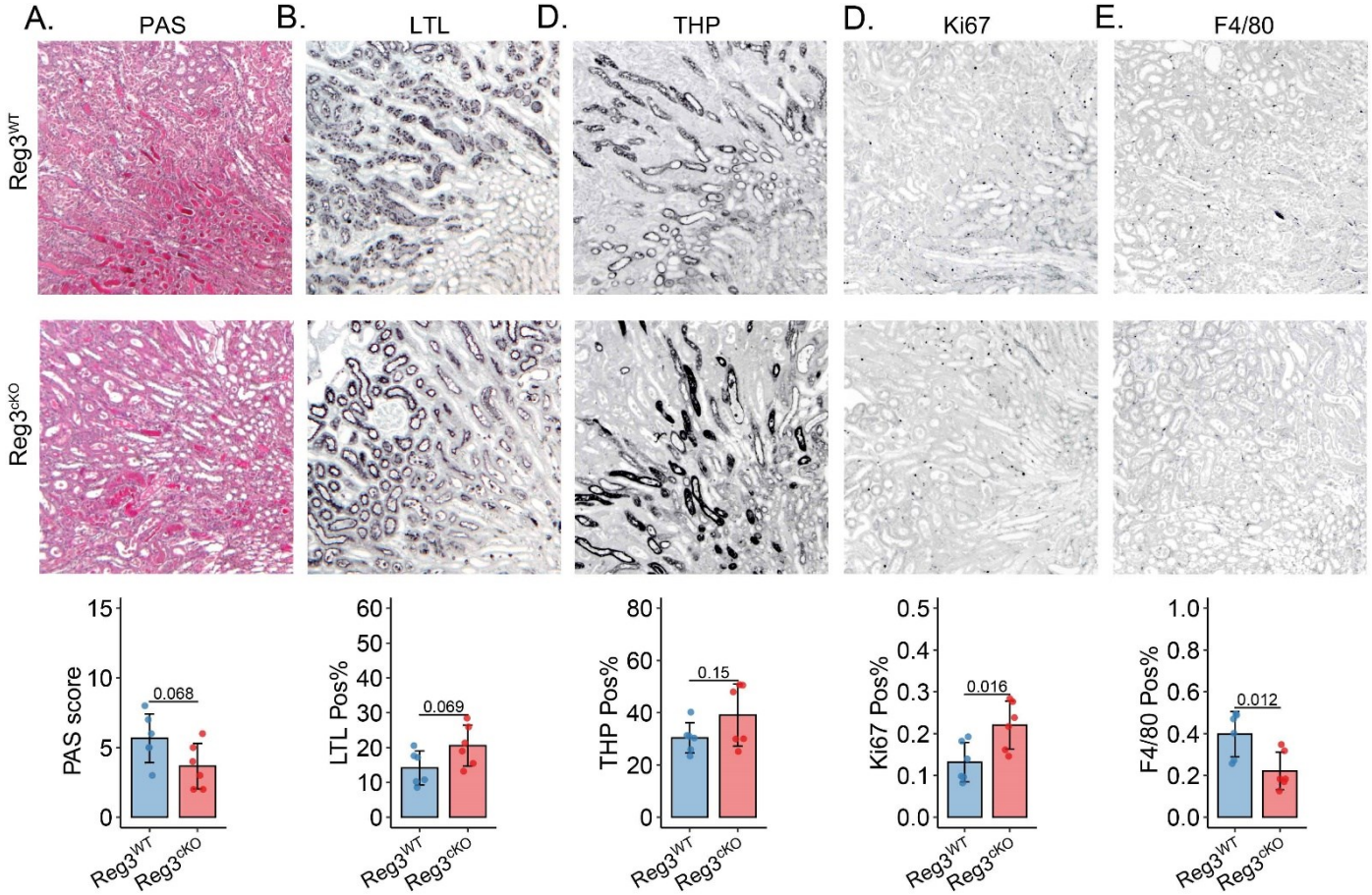

Figure 52. Pathological histology in Pax8-Regnase3cKO 1 days after 20 mins IRI without Nephrectomy. (A) Renal tubular damage was quantified using Periodic acid-Schiff (PAS) staining. (B) The renal distal tubules were visualized using Sirius red staining. (C)The renal proximal tubules were visualized using Lotus tetragonolobus lectin (LTL). (D) Ki67 staining. (E) F4/80 staining represents mononuclear phagocytic cell. The t-test was employed for the statistical examination. All quantitative data are means ± SD, and the images were magnified at 200x.

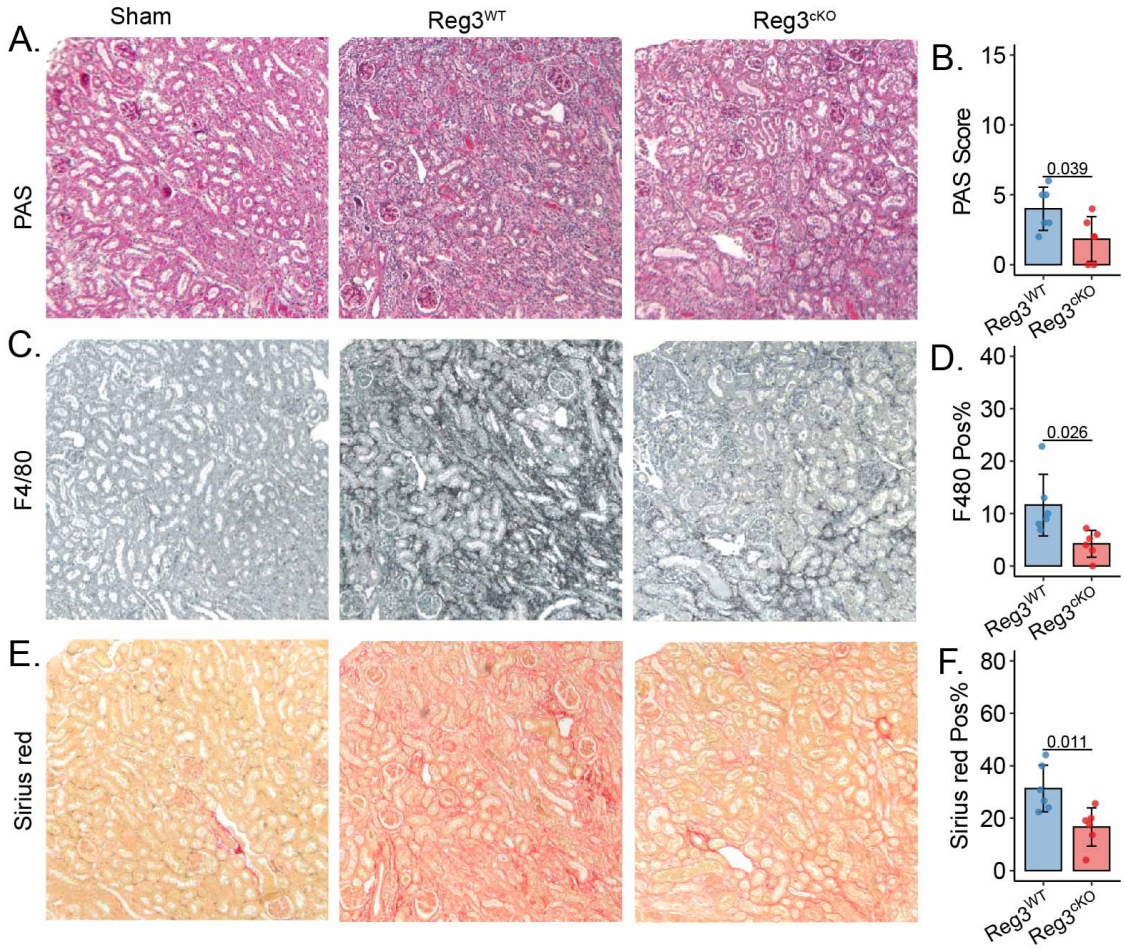

Figure 53. Pathological histology in Pax8-Regnase3cKO 21 days after 20 mins IRI kidney injury without Nephrectomy. (A, B) Renal tubular damage was quantified using Periodic acid-Schiff (PAS) staining. (C, D) Macrophage were visualized using F4/80 staining. (E, F) Collagen or fibrosis level was measured using Sirius red staining. The t-test was employed for the statistical examination. All quantitative data are means ± SD, and the images were magnified at 200x.

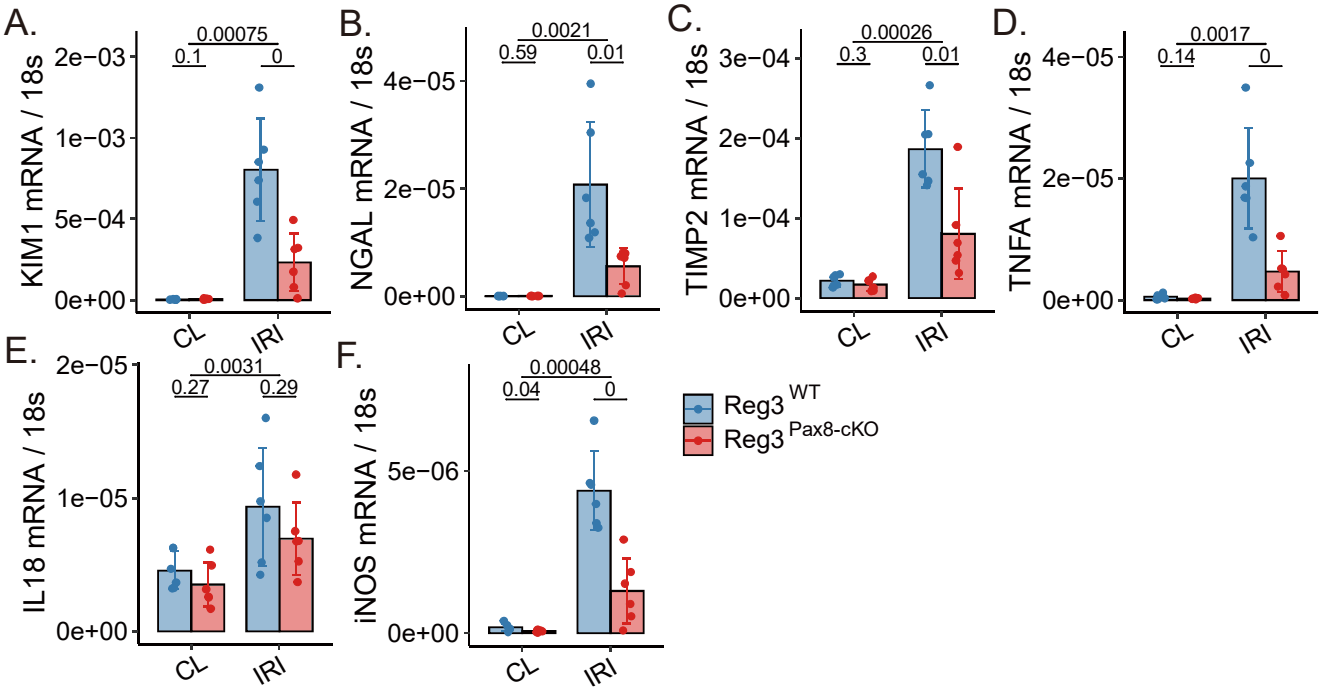

Figure 54. The qPCR for the kidney injury markers in Pax8-Regnase3cKO 21 days after 20 mins IRI. The contralateral (CL) and IRI kidneys were harvest at day 21 after IRI. All quantitative data are means ± SD. The t-test and ANOVA was employed for the statistical examination.

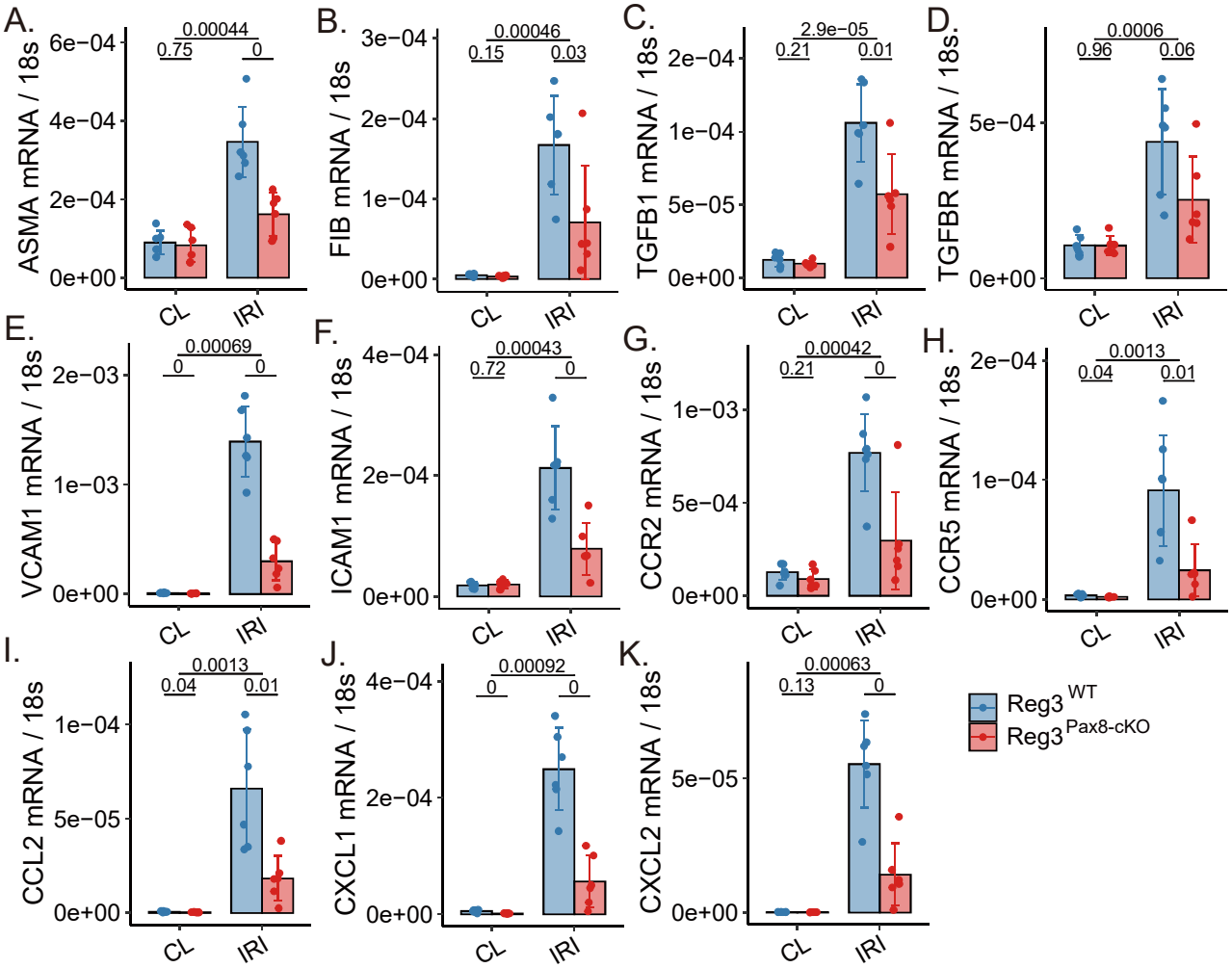

Figure 55. The qPCR for the fibrosis and inflammation markers in Pax8-Regnase3cKO 21 days after 20 mins IRI. The contralateral (CL) and IRI kidneys were harvest at day 21 after IRI. All quantitative data are means ± SD. The t-test and ANOVA was employed for the statistical examination.

4.3.4 Pax8-Regnase3cKO alleviating IRI with NX kidney injury

To further investigate the role of Regnase3 in TEC in response to ischemia, we used the Pax8-Regnase3cKO mice model in an IRI with NX model. A group of 8 to12 weeks old mice were subjected to 17 minutes of unilateral ischemia, followed by nephrectomy. Our results showed that at day 1 after IRI with NX, the GFR dropped by approximately 90% in wildtype mice, but only 80% in Pax8-Regnase3cKO mice (Figure 56). TUNEL staining showed there are less cell death in the Pax8-Regnase3cKO IRI kidney (Figure 57). By day 7, the GFR in the Regnase3cKO mice had recovered to 60%, while it remained at 40% in the WT mice. Despite full recovery of GFR by day 14 in both groups, levels of Kim-1, NGAL, TIMP2, TNF and iNOS remained elevated in the WT group 21 days after AKI (Figure 58). Additionally, WT mice expressed higher levels of mRNA for VCAM1 and ICAM1, as well as aSMA, Fn1, TGF-β1 and TGF-B receptor (Figure 59), indicating that Pax8-Regnase3cKO mice were less susceptible to fibrosis and inflammation post-AKI.

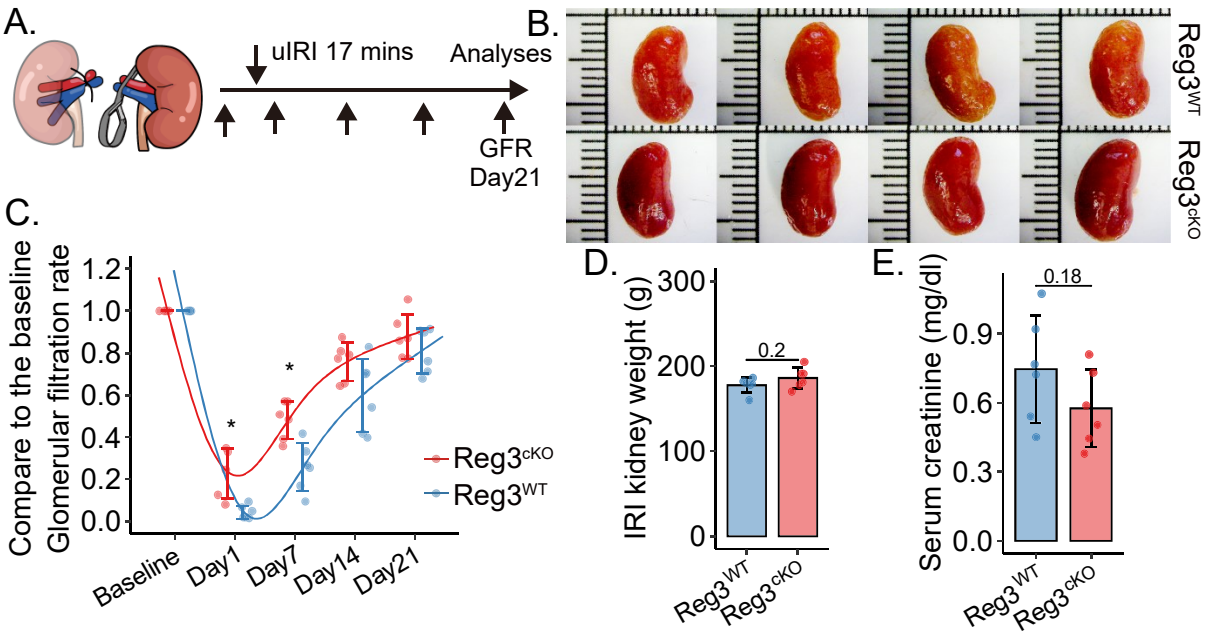

Figure 56. Pax8-Regnase3cKO alleviate 17 mins IRI kidney injury with the nephrectomy. (A) A diagram illustrating the set-up of the experiment. Unilateral ischemia-reperfusion injury (IRI) was induced by clamping the kidney pedicle for 17 minutes. Organs were collected in two different states: healthy state and on day 21 following IRI. (B) kidney appearance (C) The GFR normalized to baseline in response to the genotype. The curve is fitted using the cubic spline algorithm. (D) IRI kidney weight, (F) Serum creatinine level. All quantitative data are means ± SD. The t-test was used for the statistical analysis. *P<0.05.

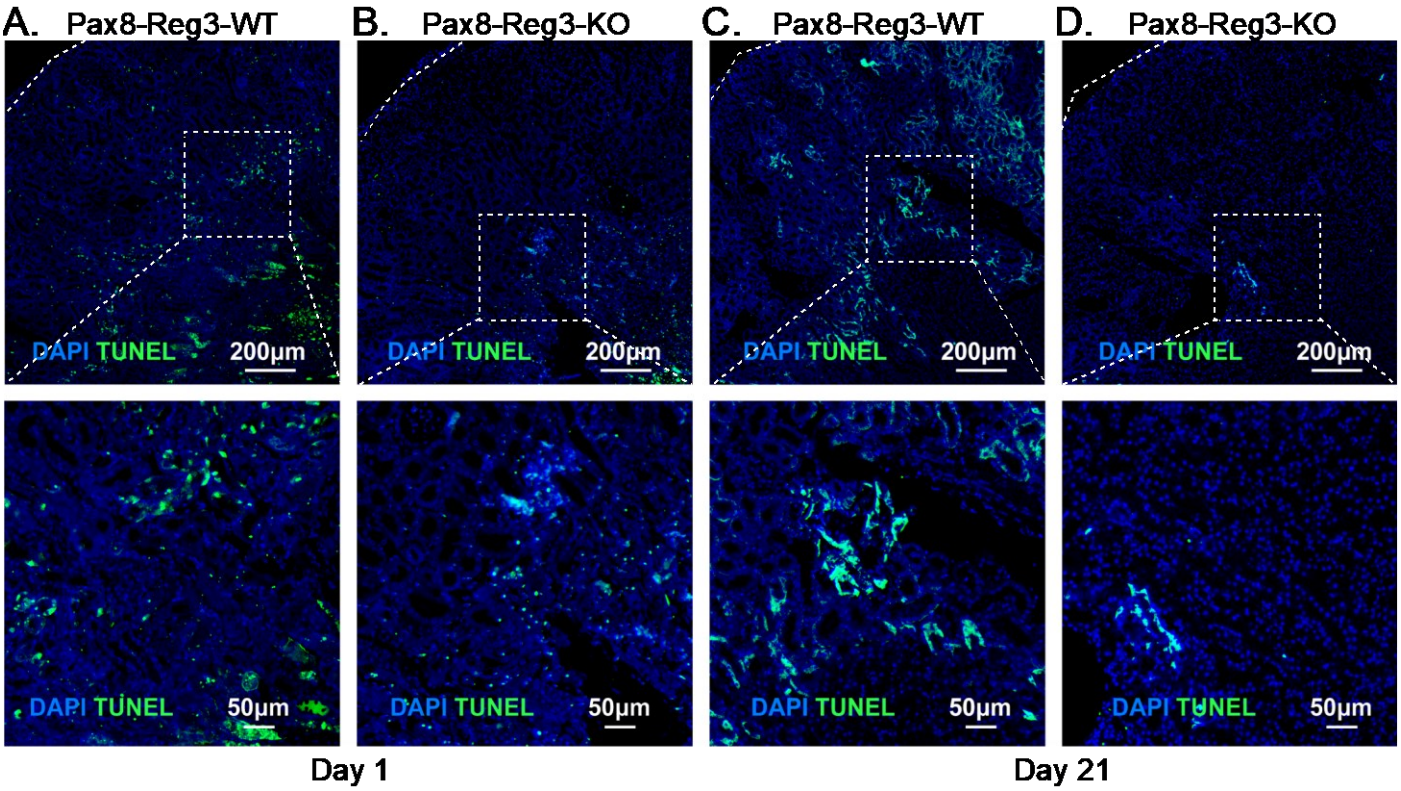

Figure 57. Immunofluorescence staining for TUNEL in Pax8-Regnase3cKO in IRI kidney 1 day and 21 days after IRI. Unilateral IRI was induced by 17 minutes ischemia time. Kidney was harvested at (A, B) 1 and (C, D) 21 days after IRI.

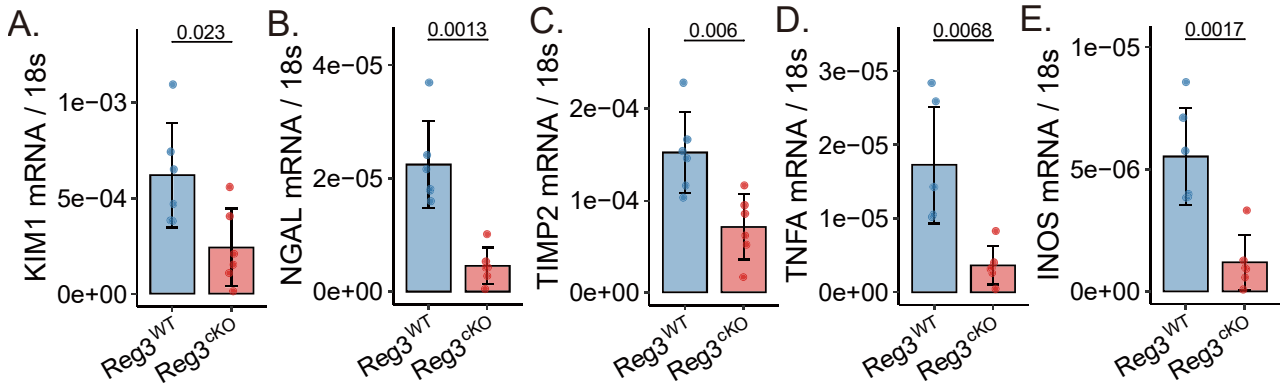

Figure 58. The qPCR for the kidney injury markers in Pax8-Regnase3cKO 21 days after 16 mins IRI with nephrectomy. All quantitative data are means ± SD. The t-test was employed for the statistical examination.

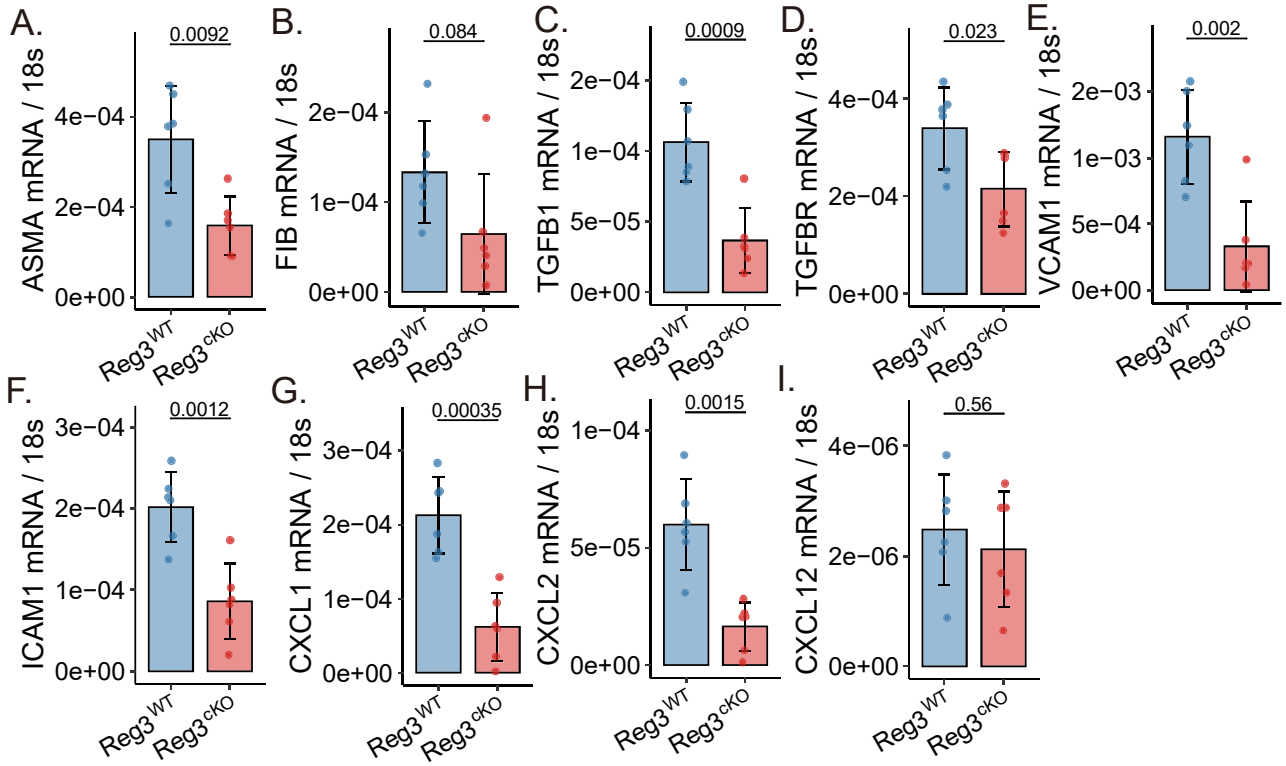

Figure 59. The qPCR for the fibrosis and inflammation markers in Pax8-Regnase3cKO 21 days after 16 mins IRI with nephrectomy. All quantitative data are means ± SD. The t-test was employed for the statistical examination.

4.3.5 Pax8-Regnase3cKO aggravating CaOx kidney injury

Next, we studied the role of Regnase3 on nephrocalcinosis-related CKD using the CaOx model. Following dietary intervention, both wildtype and Pax8-Regnase3cKO mice displayed weight loss, with the Pax8-Regnase3cKO mice losing significantly more weight than the wildtype mice. Like the previous models of Rank-Regnase3cKO, the Pax8-Regnase3cKO mice lost over 15~20% of their body weight for two days, resulting in the termination of the experiment at day 8 in compliance with animal welfare rules. At day 8, the GFR decreased by approximately 50% in wildtype and 75% in Pax8-Regnase3cKO mice (Figure 60). The levels of Scr were also consistent with the GFR, being higher in the Pax8-Regnase3cKO group. Histopathology results showed that the Pax8-Regnase3cKO group of mice suffered more kidney injury, with

higher injury scores, more calcium oxalate crystal deposits, but no significant differences in fibrosis positive areas (Figure 61). Additionally, the Pax8-Regnase3cKO mice showed an increased expression of Ki67, like what was observed in the IRI model. However, in contrast to the Rank-Regnase3cKO mice, the Pax8-Regnase3cKO mice had more calcium oxalate crystal.

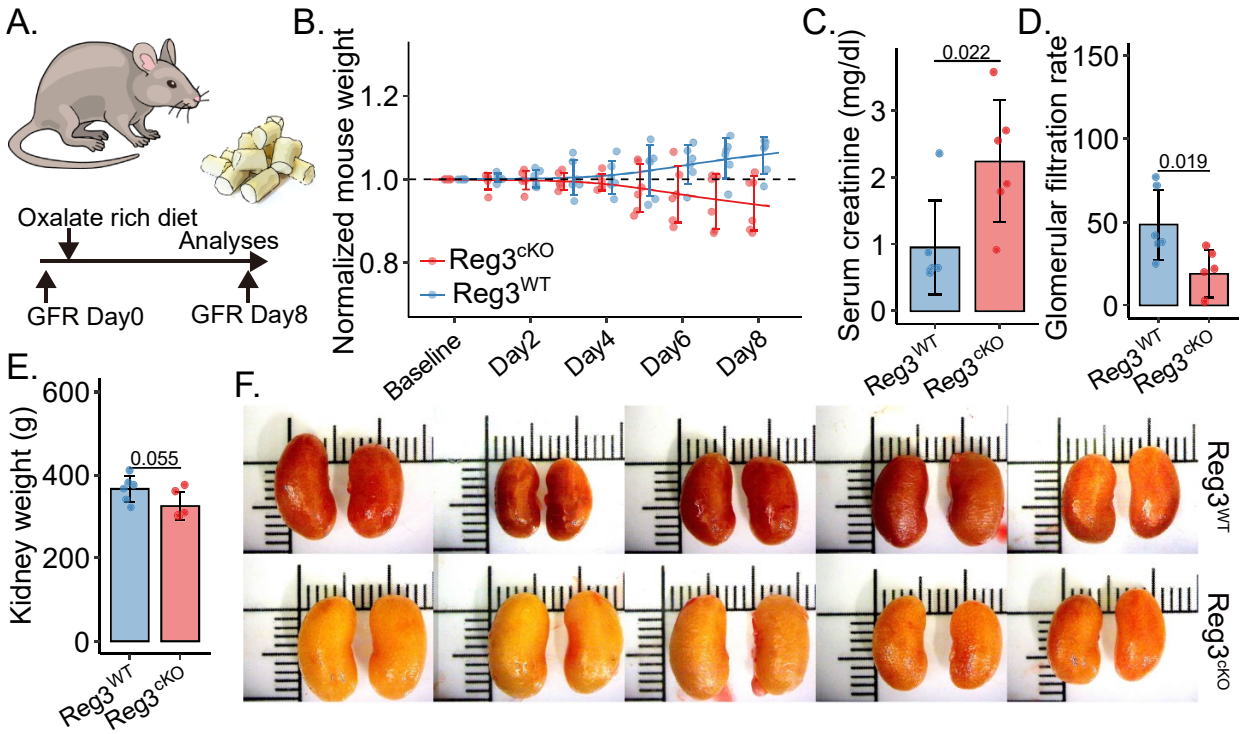

Figure 60. Pax8-Regnase3cKO aggravate CaOx kidney injury. (A) Schematic of experimental set-up. Organ harvest was taken at day 8 after change the diet. (B) kidney appearance (C) The mouse weight for each mouse after change the diet in response to the genotype. The curve is fitted using the cubic spline algorithm. (D) kidney weight, (E) Serum creatinine level, and (E) GFR. The curve is fitted using the cubic spline algorithm. All quantitative data are means ± SD. The t-test was employed for the statistical examination.

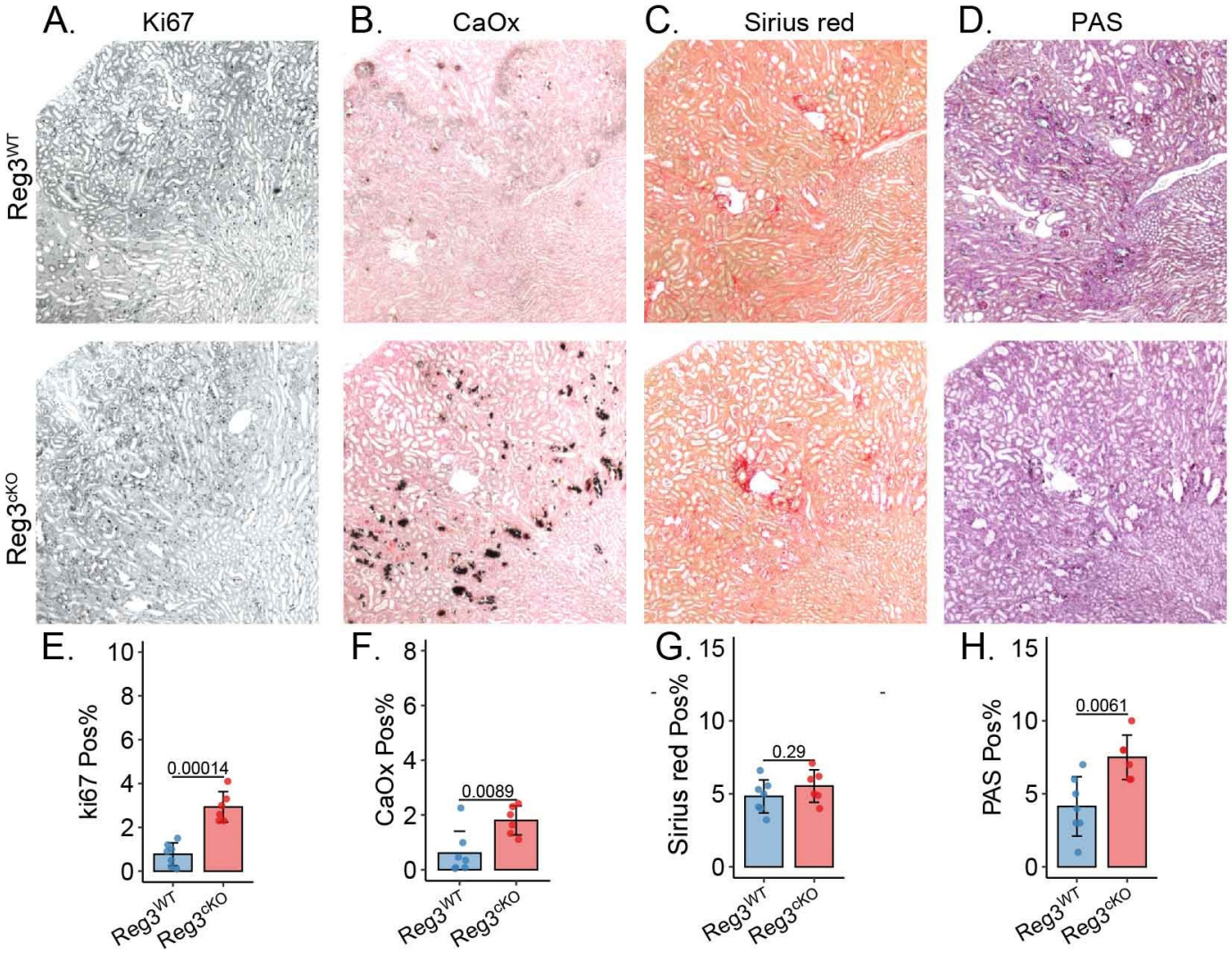

Figure 61. Pathological histology in Pax8-Regnase3cKO 8 days after changed the CaOx diet. (A) Renal tubular damage was quantified using Periodic acid-Schiff (PAS) staining. (B) Collagen or fibrosis level was measured using Sirius red staining. (C) CaOx staining. (D) Macrophage were visualized using F4/80 staining. (E-H) quantitative analysis for the staining. The t-test was employed for the statistical examination. All quantitative data are means ± SD, and the images were magnified at 200x.

4.3.6 Regnase3 deletion in primary murine TEC

To further investigate the Regnase3 in TEC, an in vitro model was established by isolating primary murine TEC from the kidney. Using this model, various stimuli were applied to the cells, including H_2O_2 at concentrations of 0.5 and 1 mM for 1 hour, 100 ng/ml LPS, and NTS for 24 hours. The results from qPCR analysis demonstrated that the deletion of Regnase3 was successful in the Pax8-Regnase3cKO cells, regardless of the presence of stimuli. Additionally, the results showed a compensatory upregulation of the remaining Regnase in the absence of Regnase3, as seen in Figure 62 and Figure 63.

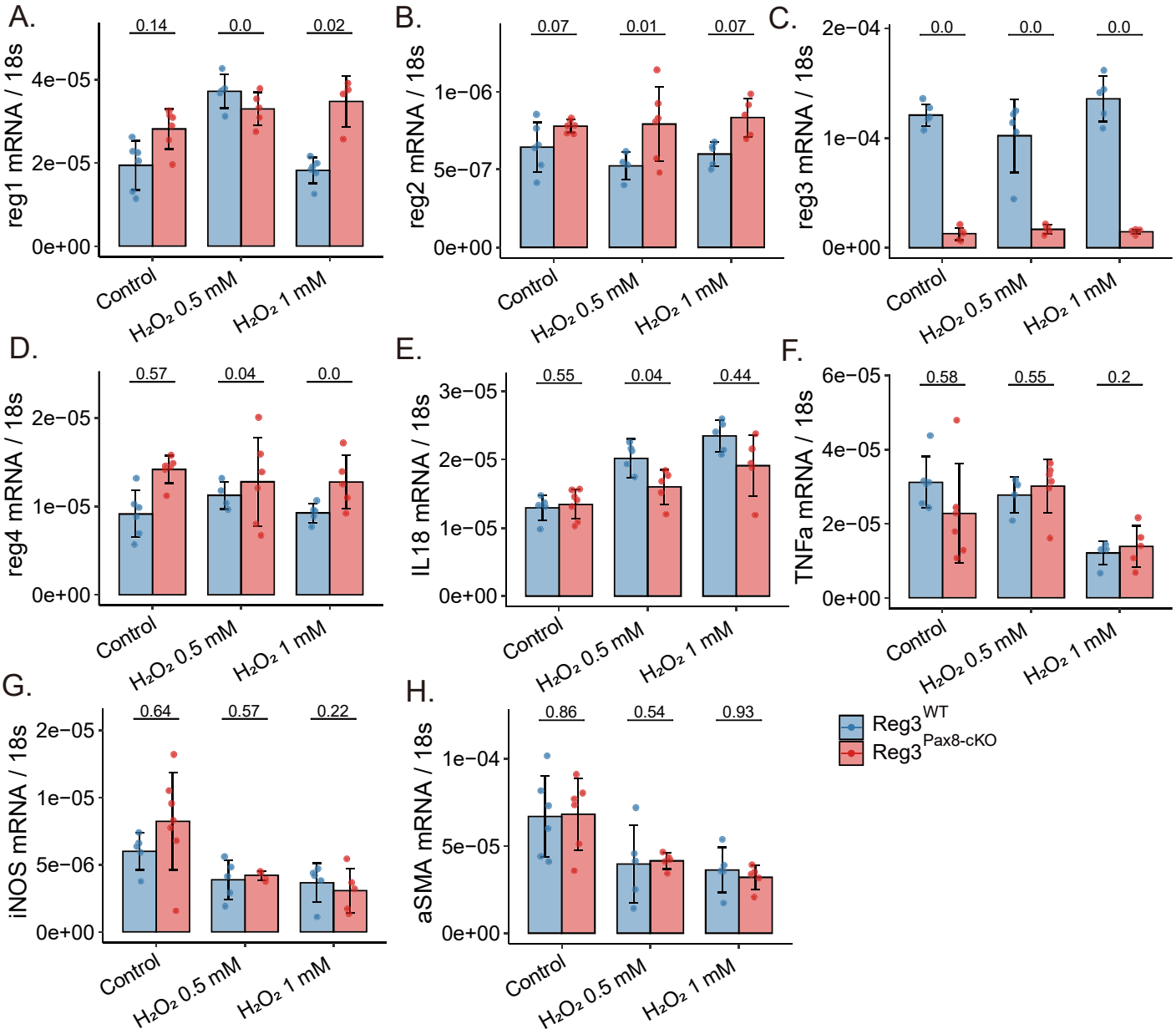

Figure 62. The mRNA level for genes in primary murine TEC response to the H_2O_2 injury (A-H). Primary TEC are isolated from the mice kidney. After the cell reached the 90% confluence, the cells are exposed to the H_2O_2 0.5 and 1mM for 1 hours. All quantitative data are means ± SD. The t-test was used for the statistical analysis.

We conducted an in vitro study utilizing primary murine renal tubule by isolating them from the kidneys of mice. Using time-lapse imaging, we recorded the tubule death in response to H_2O_2 injury. Our findings revealed that 20% of tubular cells underwent spontaneous death within the first day. However, a greater number of wild-type tubular cells died in comparison to the Pax8-Regnase3cKO tubular cells, which displayed a higher level of tolerance to injury when exposed to 0.1 mM H_2O_2 (Figure 64). Nonetheless, no significant difference was observed when the H_2O_2 concentration was higher than 1 mM. In addition, we employed the same approach to evaluate the impact of Regnase3 on primary murine TEC' response to H_2O_2 injury. As expected, the Pax8-Regnase3cKO primary murine TEC displayed lower cell death in both the 0.1 and 0.5 mM H_2O_2 groups but not in the 1 mM group (Figure 65). Furthermore, we conducted qPCR analysis to investigate

any differences in the acute phase of H_2O_2 injury (0.5 and 1 mM for 1 hour). Due to the short incubation time of the H_2O_2 and cells, most injury markers were not affected by the deletion of Regnase3, except for IL18 (Figure 62), which was expressed at lower levels in the Pax8-Regnase3cKO primary murine TEC.

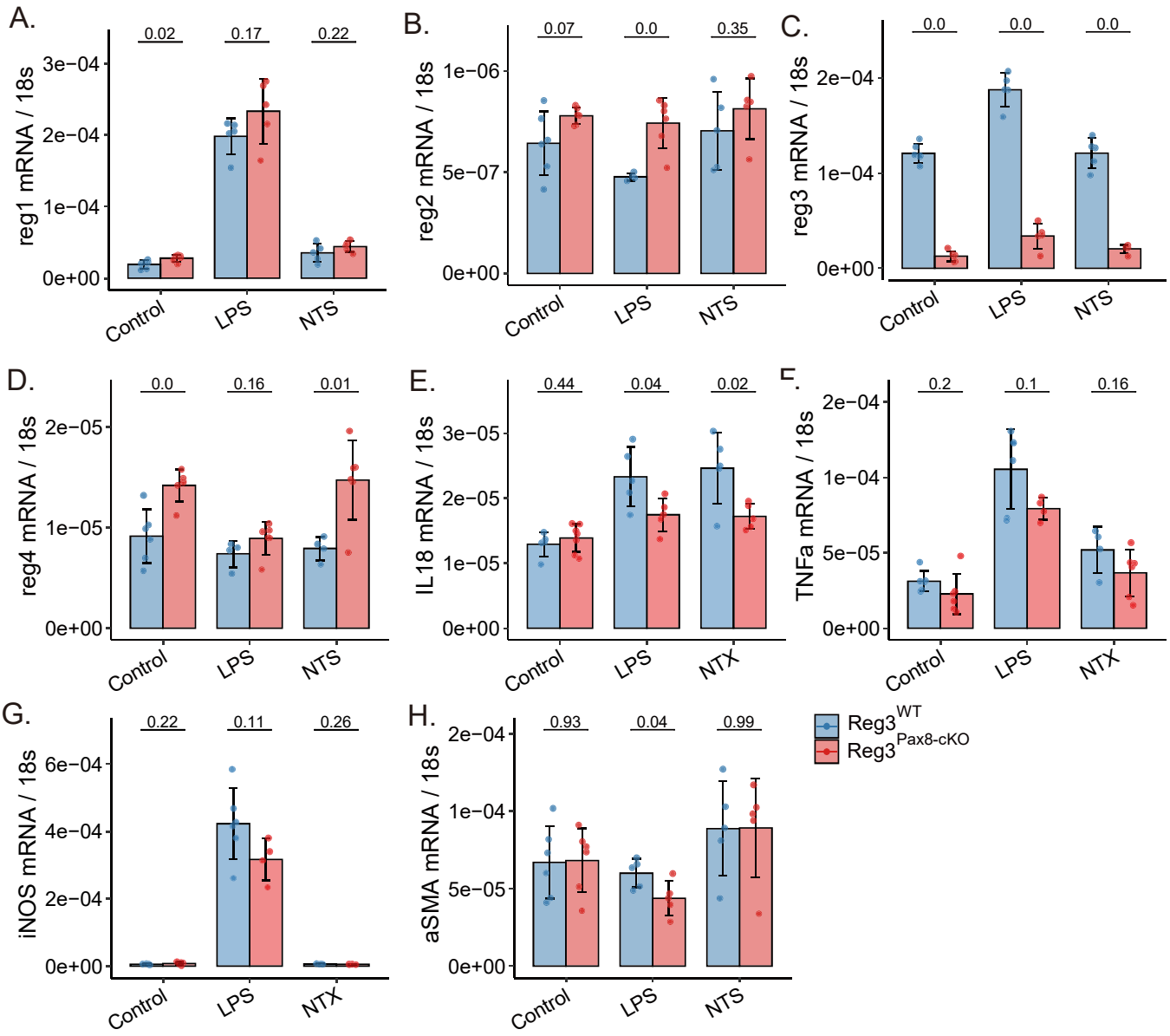

Figure 63. The mRNA level for genes in primary murine TEC response to the lipopolysaccharide (LPS) and nephrotoxic serum (NTS) injury. Primary TEC are isolated from the mice kidney. After the cell reached the 90% confluence, the cells are exposed to the 100 ng/ml 24 hours. All quantitative data are means ± SD. The t-test was used for the statistical analysis.

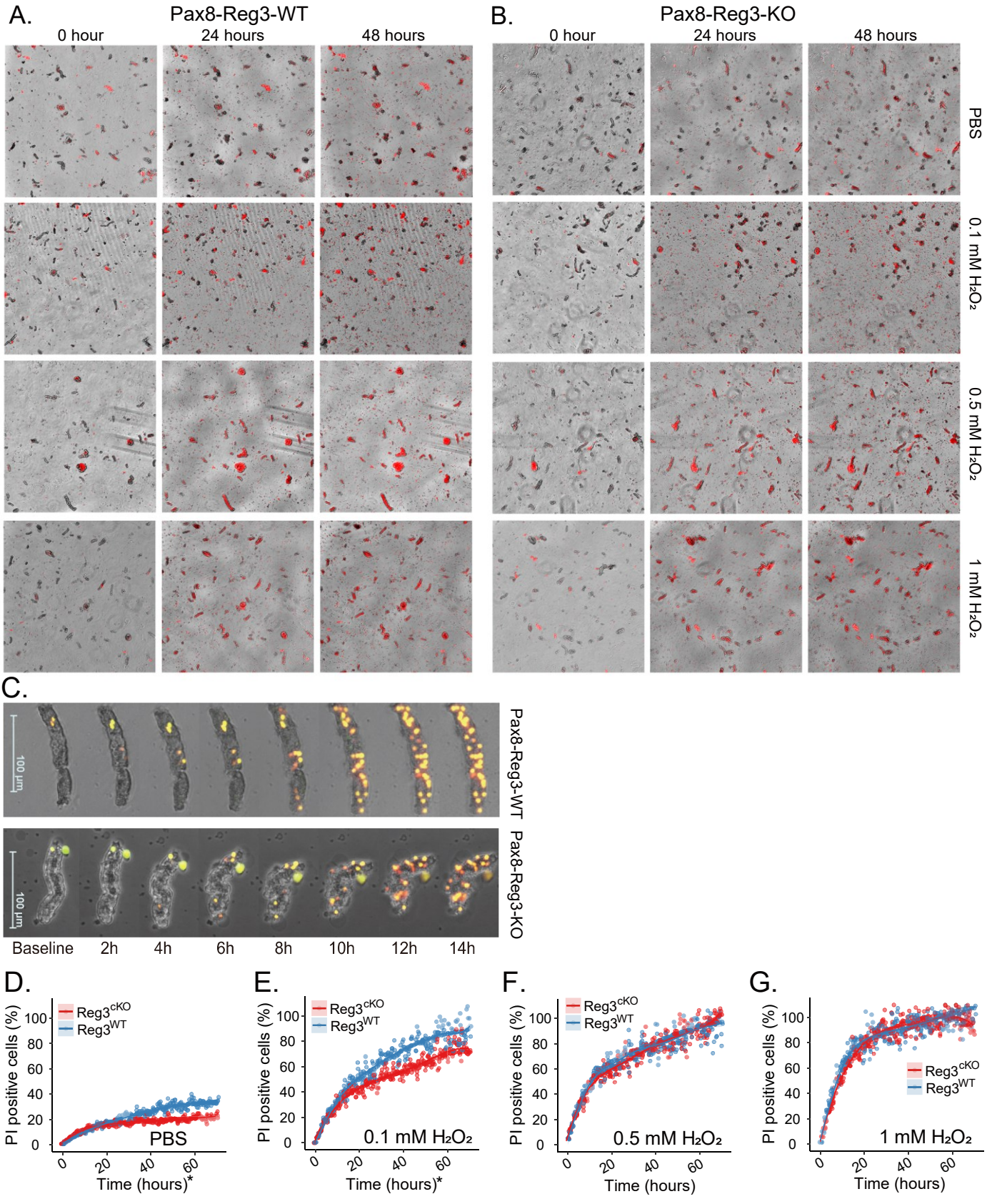

Figure 64. Time-lapse imaging on fresh tubule isolates. Freshly tubules were isolated from (A) wildtype and (B) Pax8-Regnase3cKO mice. Permeabilized (dead) cells were made visible by using a propidium iodide stain with a concentration of 500ng/ml. (C) High power field of view on co-staining with propidium iodide and 0.5μM Sytox green. Nikon Eclipse Ti2 microscopy was used to capture time-lapse images every half hour for a total of 72 hours on tubules with or without H_2O_2 (D-G). The curve is fitted using the cubic spline algorithm. All quantitative data are means ± SD. *P<0.05 for Chi-square test.

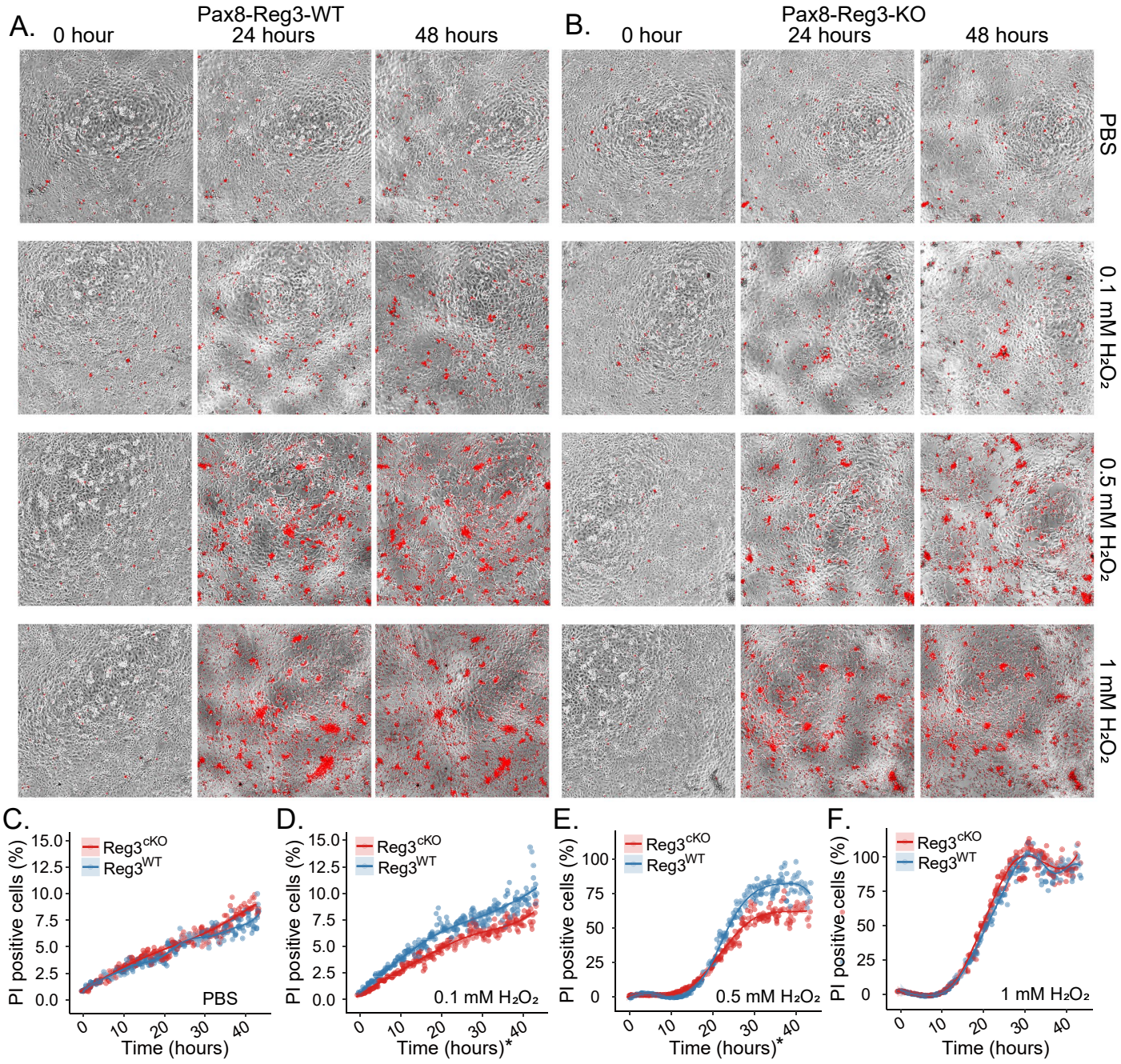

Figure 65. Time-lapse imaging cell death assay for in vitro primary murine TEC with H_2O_2 stimulation. Primary tubules were isolated from (A) wildtype and (B) Pax8-Regnase3cKO mice and cultured in vitro for at least one week till epithelial cells reached 100% confluency. Permeabilized (dead) cells were made visible by using a propidium iodide stain with a concentration of 500ng/mL. Nikon Eclipse Ti2 microscopy was to capture time-lapse images every half hour for a total of 72 hours on TEC with or without H_2O_2 (D-G). The curve is fitted using the cubic spline algorithm. All quantitative data are means ± SD. *P<0.05 for Chi-square test on data after 24 hours.

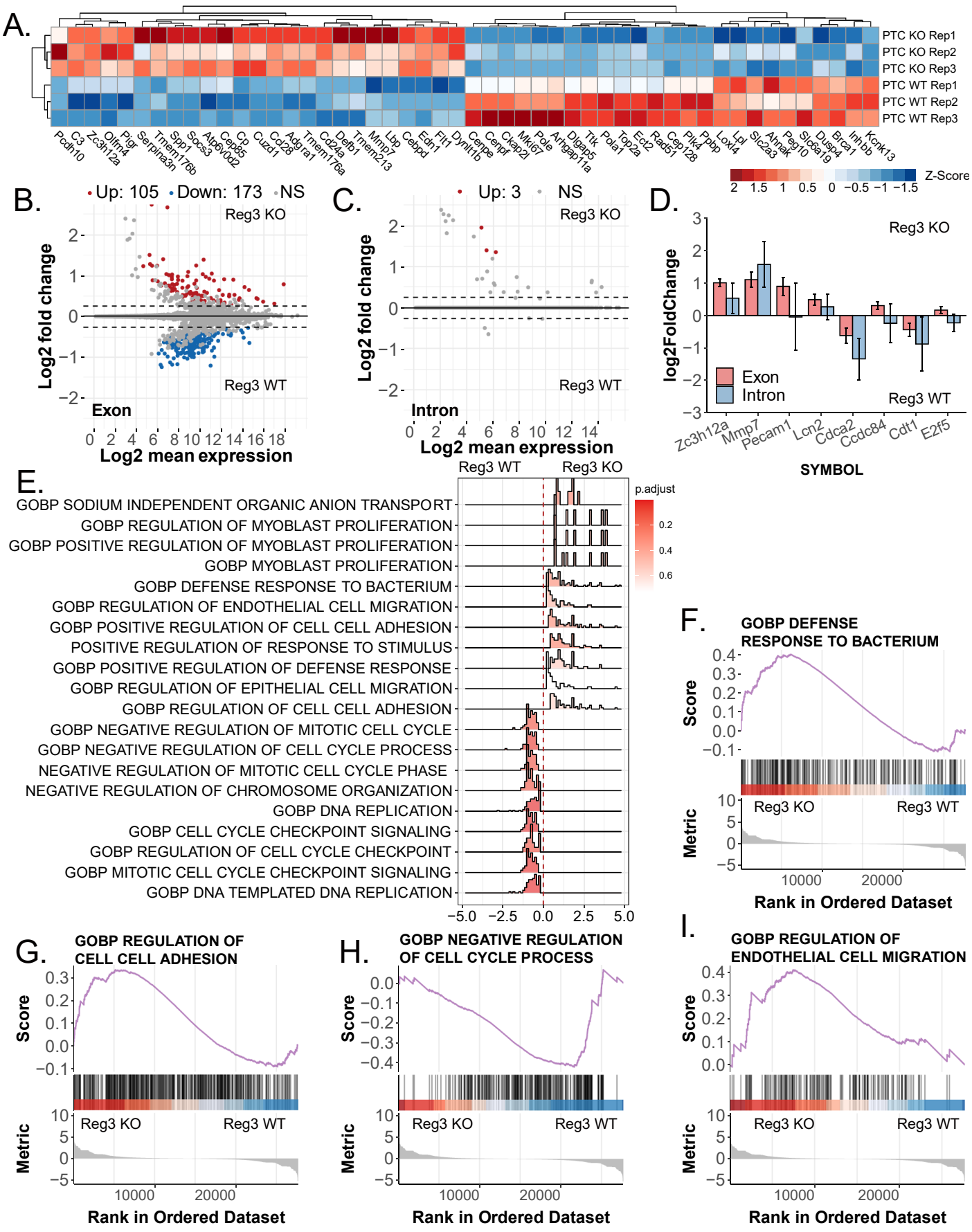

Figure 66. Bulk RNA-seq on Pax8-Regnase3cKO and wild type renal tubular cells. Primary murine tubular epithelial cells were isolated from wildtype and Pax8-Regnase3cKO mice kidneys and cultured in vitro for at least one week till they reach 100% confluency. (A) Heatmap of biological replicates of top differentially expressed genes in Pax8-rtTA/tetO-Cre-Regnase3 and wild type renal tubular cells. A heatmap and dendrogram were used to display the differentially expressed genes' z-scores of normalized counts. An MA plot was also created to display the shrink log2

fold change on exons (B) and introns(C) between RankCre and wild type M0 macrophages. Genes that have undergone differential expression testing and have an adjusted p-value lower than 0.05 are identified by the colors red or blue. (D) Selected gene expression in exon and intron at two conditions. (E) Density ridges for the enriched gene sets. The expression distributions of core enriched genes for GSEA enriched gene sets are displayed through the density ridge plot, where the gradient color represents the adjusted p-values. (F-I) Selected enrichment plots from GSEA analysis based on the gene enrichment profiles of Pax8-rtTA/tetO-Cre-Regnase3 compared with wild type renal tubular cells. Enrichment is shown for transcriptional signatures related to cell cycle and wound healing.

4.3.7 Regnase3 suppresses cell cycle-related genes

RNA-seq results revealed that the deletion of Regnase3 in primary murine TEC resulted in differential gene expression, with 105 genes being upregulated and 173 genes being downregulated at the exon level, but only 3 genes being upregulated at the intron level (Figure 66). Furthermore, the GSEA indicated that the deletion of Regnase3 promoted the processes of wound healing, cell migration, adhesion, and regulation of the nuclear division and cell cycle. Therefore, the presence of Regnase3 sustains negative regulators of the cell cycle and nuclear division, however, the cell cycle checkpoints remain active. Consequently, the absence of Regnase3 abrogates these negative effects on the cell cycle and hence promotes cell cycle activation and wound healing.

To validate these transcriptome results, a series of in vitro study was conducted to further investigate the connection between Regnase3 and cell cycle behavior. Using time-lapse imaging, we observed that both Pax8-Regnase3cKO and wildtype primary murine TEC exhibited similar initial proliferation rates (with double time of ~48 hours) before 6 days in culture. However, Pax8-Regnase3cKO cells continued to proliferate for an additional generation, ultimately resulting in a greater overall cell number than wildtype. Additionally, we observed that Pax8-Regnase3cKO cells were smaller in size than WT cells after 6 days in culture, because Pax8-Regnase3cKO cells were higher in number compared to WT cells (Figure 67.).

To further study the mechanisms underlying these observations, we performed flow cytometry analysis to examine the distribution of cells across different cell cycle stages. Our results revealed that a greater proportion of Pax8-Regnase3cKO cells were present in the S phase, while fewer were present in the G1/G2 phase, particularly in response to H_2O_2-induced injury. Furthermore, Annexin V and PI staining revealed that the Pax8-Regnase3cKO cells exhibited a lower rate of early apoptosis compared to WT cells (Figure 68).

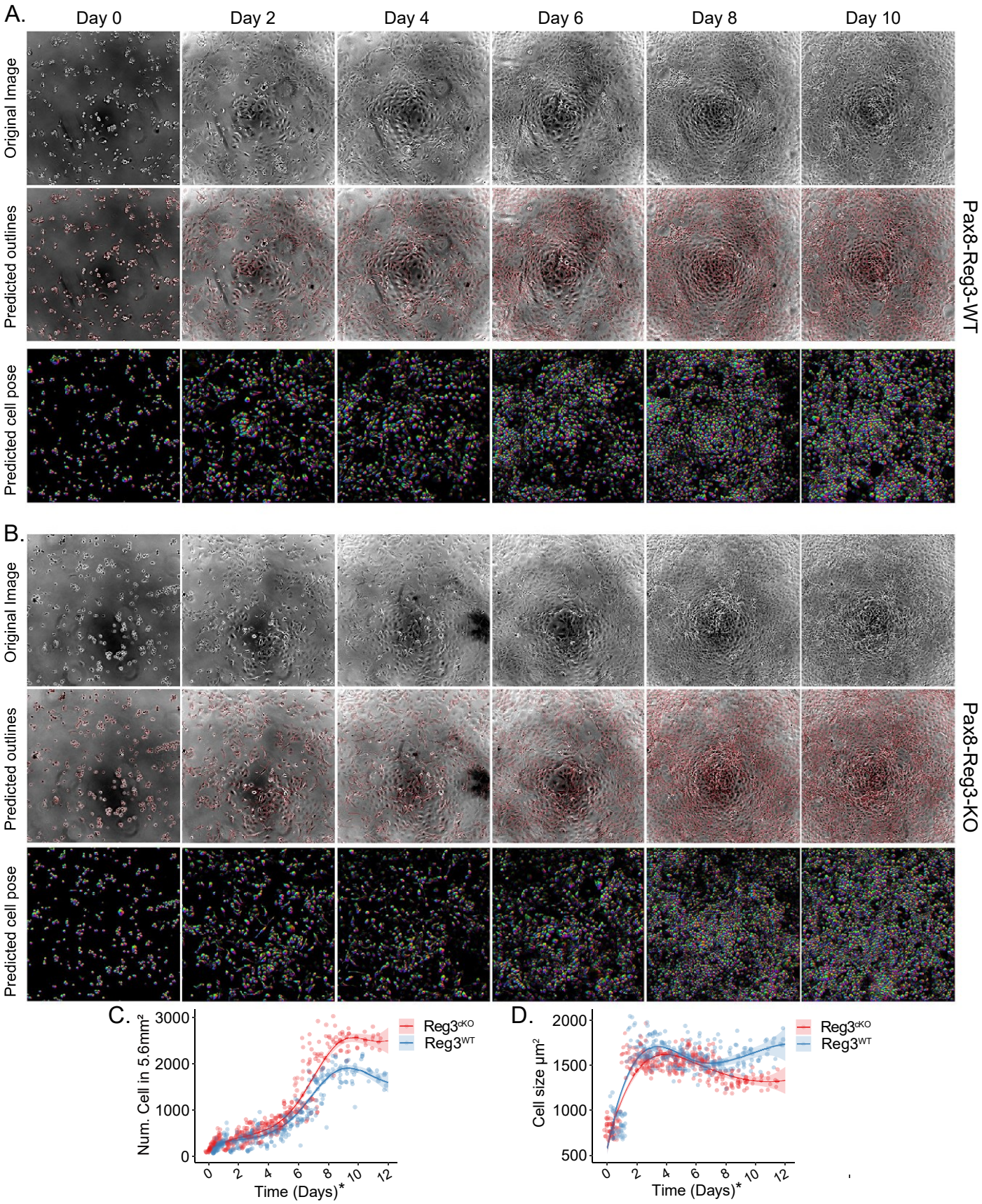

Figure 67. Time-lapse imaging cell proliferation assay for in vitro primary murine TEC. Murine tubular epithelial cells are separated from the mice kidney then cultured in vitro reach 80% confluency, then the cells were detached and reseed to a new plate. Nikon Eclipse Ti2 microscopy was used with 5% CO2, 37°C incubation, and humidity control to capture time-lapse images for a total of 12 days. The cell number and the size cell were counted and calculated by Cellpose software. The curve is fitted using the cubic spline algorithm. All quantitative data are means ± SD. *P<0.05 for Chi-square test on the data after 6 days.

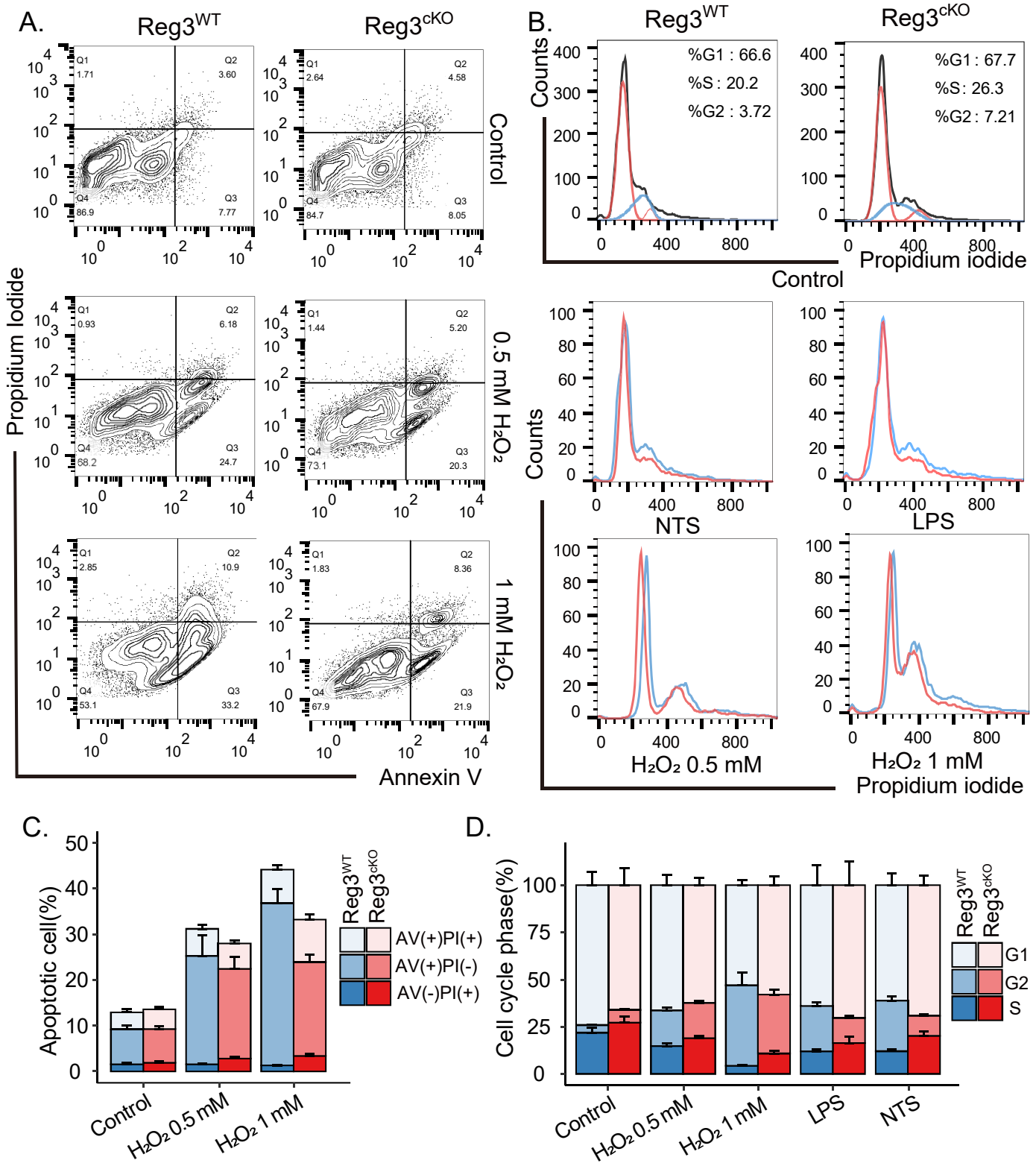

Figure 68. Cell cycle and apoptosis assay for in vitro renal tubular cells with H_2O_2 stimulation. Wildtype and Pax8-Regnase3cKO mice tubular epithelial cells were isolated and cultured in vitro for at least one week till they reach 80% confluency. Then the cells were treated with 0.5 and 1mM H_2O_2 for 1 day and changed with the fresh medium without the H_2O_2 and staining with the Propidium iodide (PI)and Annexin V (AV) according to the protocol which further measured by flow cytometry (A, B). quantitative analysis for (C) apoptotic cell and (D) cell cycle. All quantitative data are means ± SD. LPS = lipopolysaccharide, NTS = nephrotoxic serum

Finally, we utilized a scratch assay and ECIS assay to assess the wound healing capabilities of the Pax8-Regnase3cKO cells after H_2O_2-induced injury (24 hours incubation with H_2O_2 then change with fresh medium).

We found that the Regnase3cKO cells displayed a greater capacity for closing the gap of the wound, likely due to either increased proliferation or migration, which also confirmed by the ECIS assay (Figure 69). Taken together, these finding suggest that the absence of Regnase3 promotes cell proliferation and re-epithelialization/wound healing in primary murine TEC, while also reducing injury susceptibility.

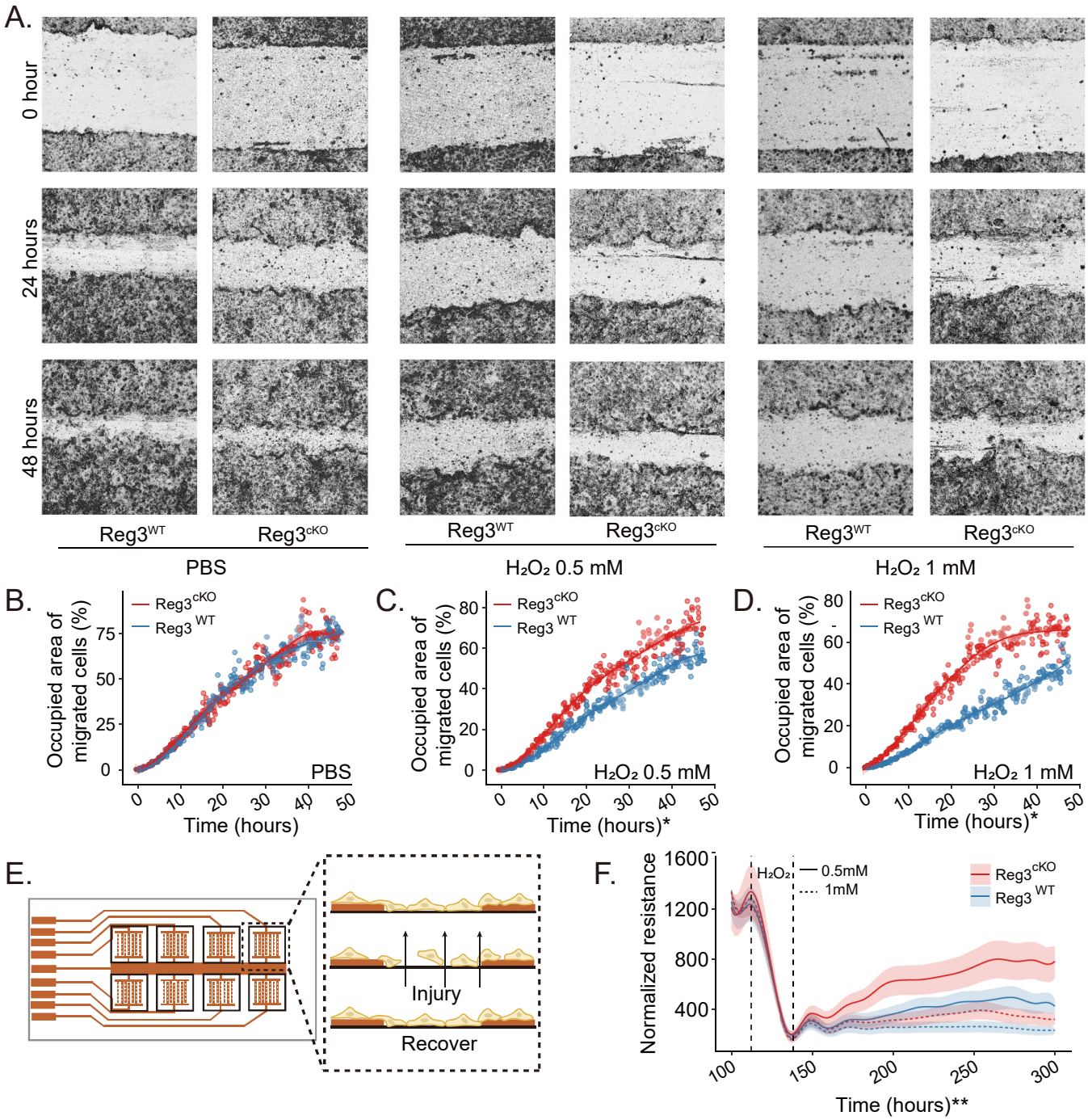

Figure 69. Electric cell-substrate impedance sensing assay and scratch assay for renal tubular cells with H_2O_2 stimulation. Primary tubules were isolated from wildtype and Pax8-Regnase3cKO mice and cultured in vitro for at least one week till epithelial cells reached 100% confluency. Then the cells were treated (A) without or with (B) 0.5 and (C) 1mM H_2O_2 for 24 hours and changed with the fresh medium without the H_2O_2. (B-D) The curve is fitted using the cubic spline algorithm. (E) Schematic diagram and (F) resistance analysis for electric cell-substrate impedance sensing assay. All quantitative data are means ± SD. *P<0.05 for χ2 test on the data after 12 hours. **P<0.05 for χ2 test for 0.5mM H_2O_2 group data after 180 hours.

4.4 Regnase3 regulates alternative splicing

To further understand the mechanism by which Regnase3 as a regulator for both cell cycle and immune response, we studied into the data from our RNA-seq analysis and proposed the hypothesis that Regnase3 modulates protein expression by alternative splicing of RNA. Using RNA-SELEX, the primary and secondary motifs of Regnase3 were identified as 3'-GCAGGUAAGUGCG-5' and 3'-ACGAUGGCUGACC-5' respectively (Figure 70A). The primary motif was found to target 50,545 introns and 13,466 exons, which are associated with 8,632 transcripts of 2,455 genes (Figure 70B-D). Similarly, the secondary motif targeted 6,937 introns and 6,628 exons, which are associated with 2,009 transcripts of 1,464 gene (Figure 70B, C, E).

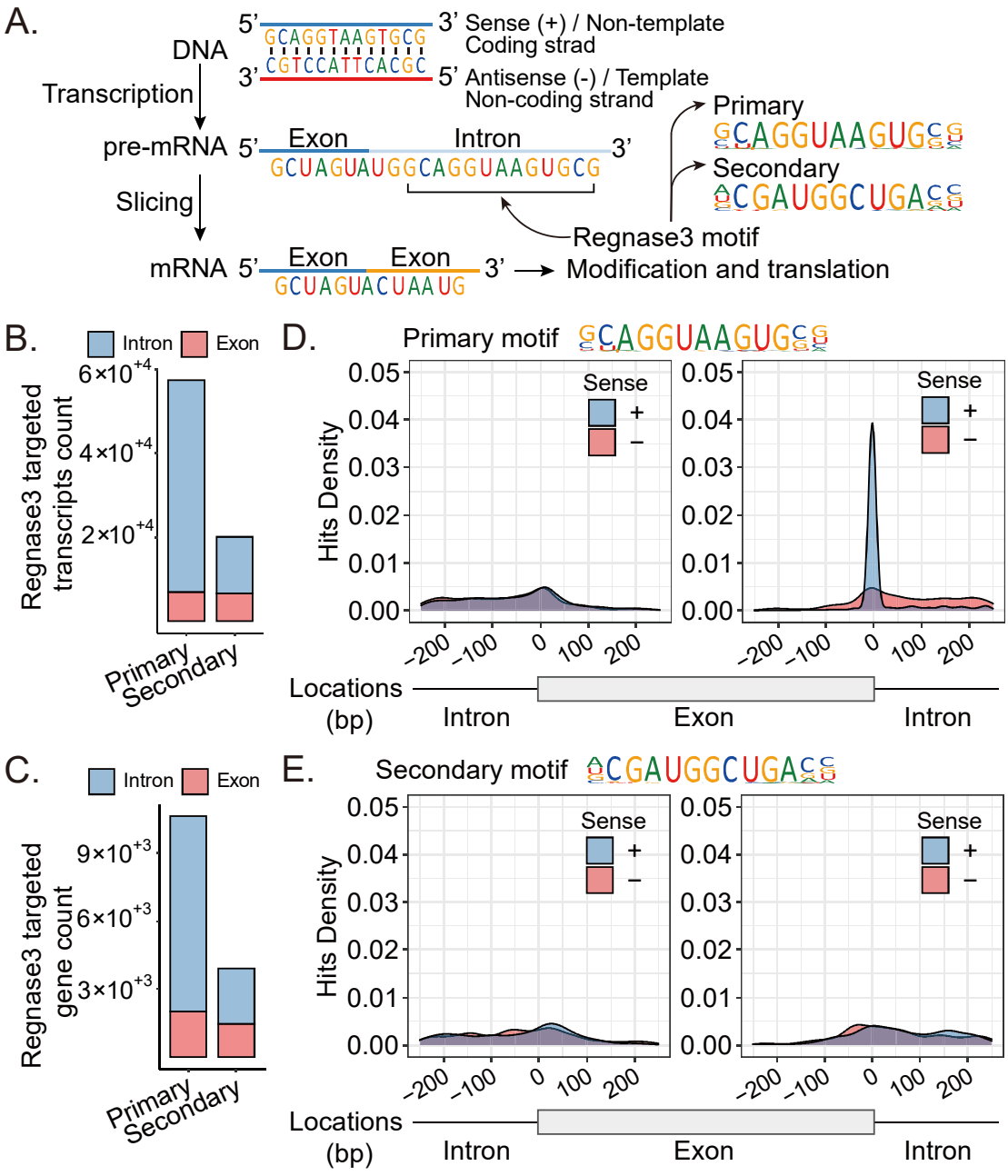

Figure 70. Regnase3' motif analysis. (A) Primary and secondary sense strand motif of Regnase3. (B) The numbers of motifs hit on the transcripts (B) of genes (C), illustrated for introns and exons. Regnase3's primary (D) and secondary (E) motif mostly bind introns, while the primary motif specifically targeting the junction between intron and exon.

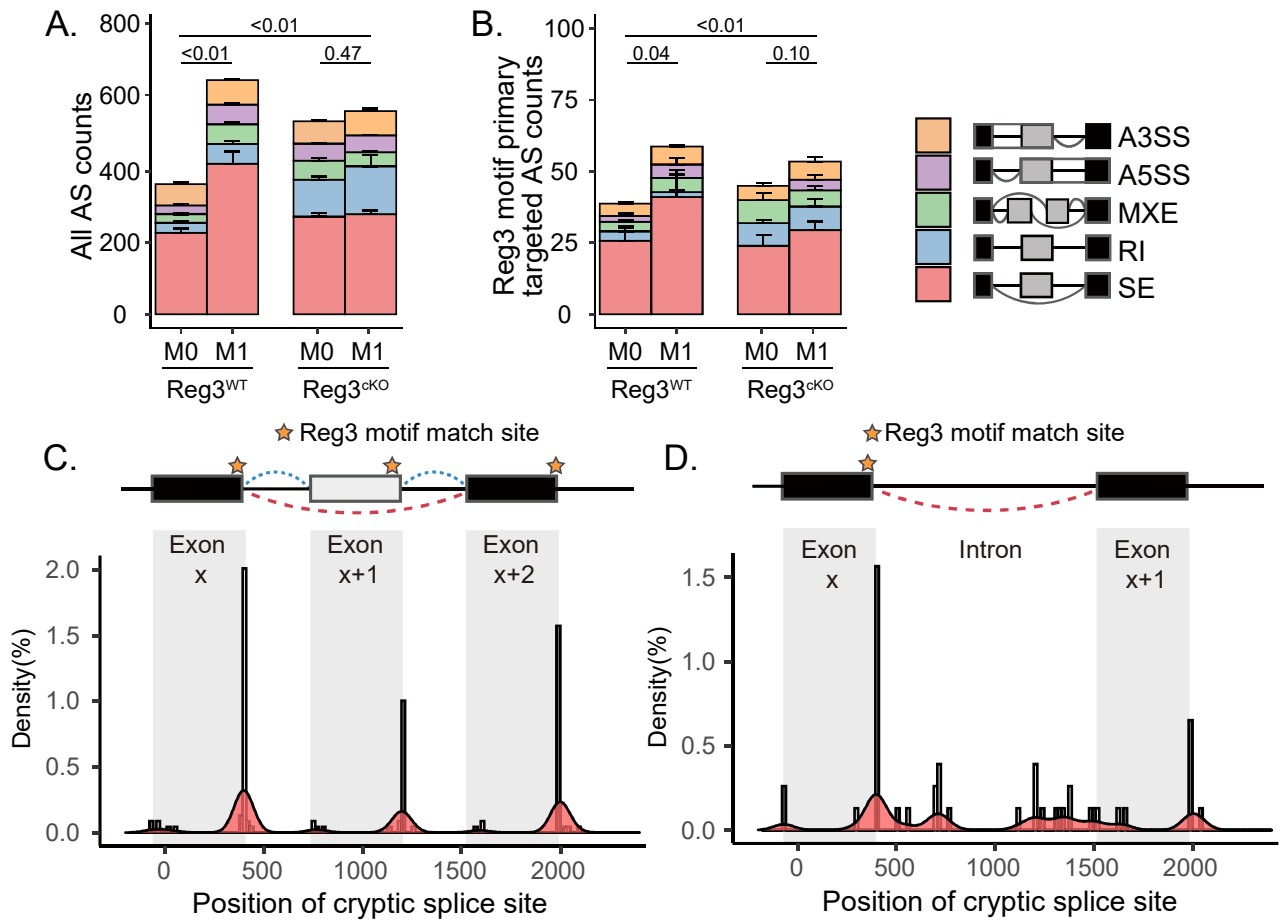

Figure 71. Alternative splicing (AS) analysis in Regnase3KO. The plots of the counts of (A) alternative splicing events and (B) Regnase3 motif targeted alternative splicing in the Regnase3KO and wild type M0 and M1 macropahge. Density plot for the Regnase3 motif targeted location on the (C) skipped exon and (D) retained intron. The p-value evaluates the distinction between two groups skipped exon (SE) number. MXE, mutually exclusive exon; RI, retained intron; A3(5)SS, alternative 3(5)'-splice sitee.

Given the evidence that Regnase3 primarily targets intron, in particular its primary motif targeting the exon-intron-junction, which is a location for pre-RNA splicing, we sought to study the role of Regnase3 on alternative splicing. Through the examination of the events of both skipped exon and retained intron regarding M0 and M1 macrophages, we found a significant difference in the events number of skipped exon and retained intron between Regnase3cKO and wildtype cells. Specifically, M1 macrophages exhibited a higher number of skipped exon and retained intron events upon activation compared to M0 (Figure 71A). However, Regnase3cKO cells displayed similar numbers of skipped exon events in M0 and M1 polarization (P=0.46), indicating that the presence of Regnase3 leads to more skipped exon events upon activation. Conversely, when Regnase3 was absent, a higher events number of retained intron were observed (P<0.01), regardless of whether the macrophages were activated (P=0.15). We further examined the alternative splicing events specifically targeted by the Regnase3 primary motif (Figure 71A) and found that wildtype macrophages had more Regnase3-targeted skipped exon events upon activation. On the other hand, Regnase3cKO macrophages had

less Regnase3-targeted skipped exon events and more retained intron events (P<0.01) compared to wildtype macrophages (Figure 71B). These findings indicate that Regnase3 regulates alternative splicing by increasing the occurrence of targeted skipped exon events upon macrophage activation while reducing the likelihood of targeted retained intron events.

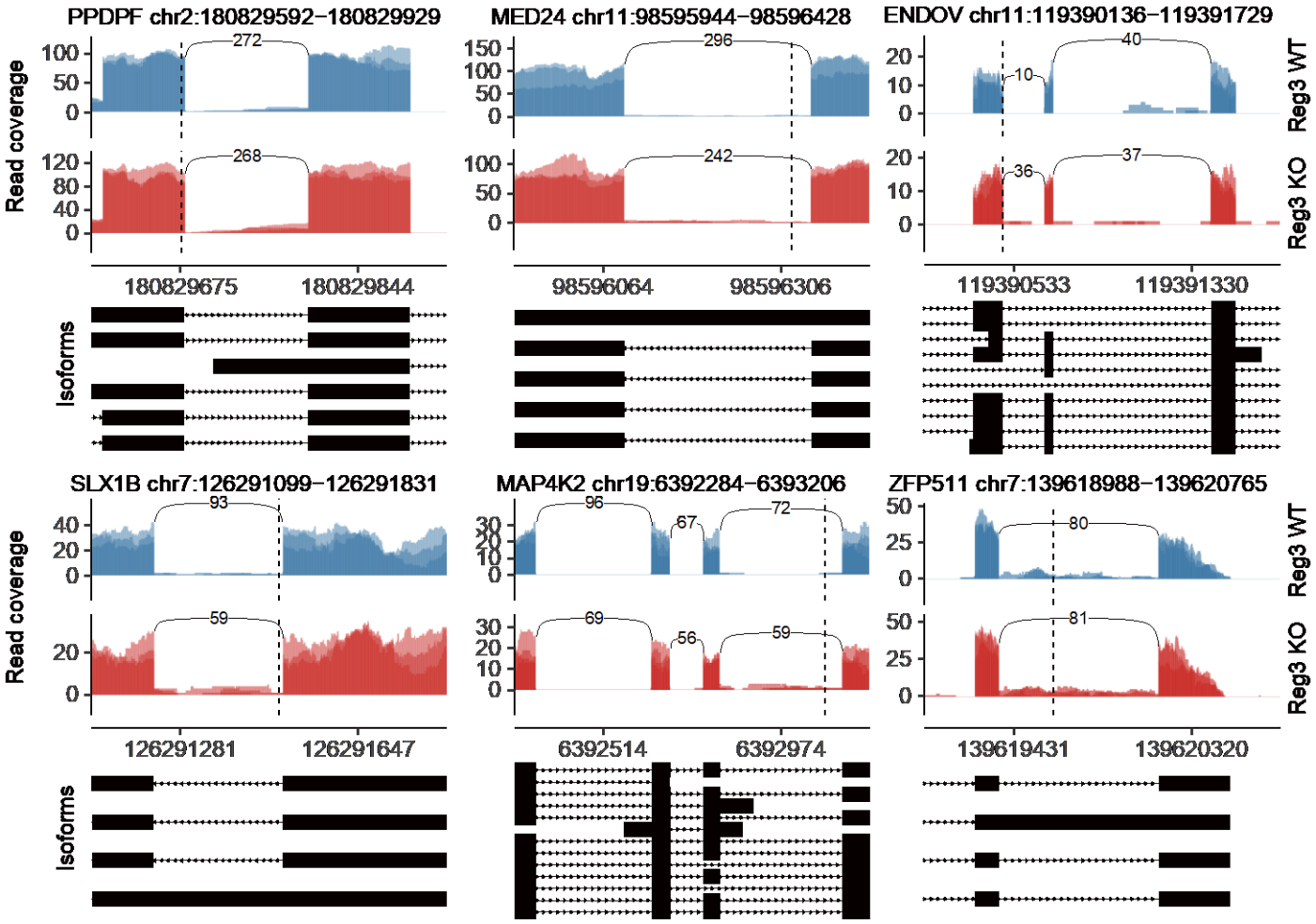

Figure 72. Sashimi plot for the examples of Regnase3 motif related retained intron. Rank-Regnase3cKO condition is shown in red plots, while the wildtype condition is depicted in blue. The X-axis shows the genomic locations, while the Y-axis indicates the transcription intensity. The plots show a "sashimi-like" region, which is a heavily transcribed region of exon, and the blank intronic regions between exons. The line crossing exonic regions represent the reads of junction and the count number is indicated on it. The exonic isoform structure for corresponding gene is displayed below Sashimi plot. The vertical dotted line represents the Regnase3 motif targeted junction which located on the junction of the exon-intron of the retained intron.

In order to further understand the mechanism by which Regnase3 regulates alternative splicing, we examined the locations at which the Regnase3 primary motif was most likely to match. Our findings indicate that the Regnase3 motif is more likely to match the location of the junction of the exon-intron of the retained intron (Figure 71C, Figure 72), and the junction of the exon-intron of upstream exon for AS (Figure 71D, Figure 73). Moreover, Regnase3 motif is also likely to match the exon-intron junction (Figure 71D, Figure 74) and

downstream exon's exon-intron junction of one skipped exon (Figure 71D). This supports the hypothesis that Regnase3 specifically targets pre-RNA and regulates AS by increasing the proportion of targeted skipped exon events and decreasing the probability of targeted retained intron events. Overall, these finding provide new insight into the Regnase3 functions that regulating alternative splicing.

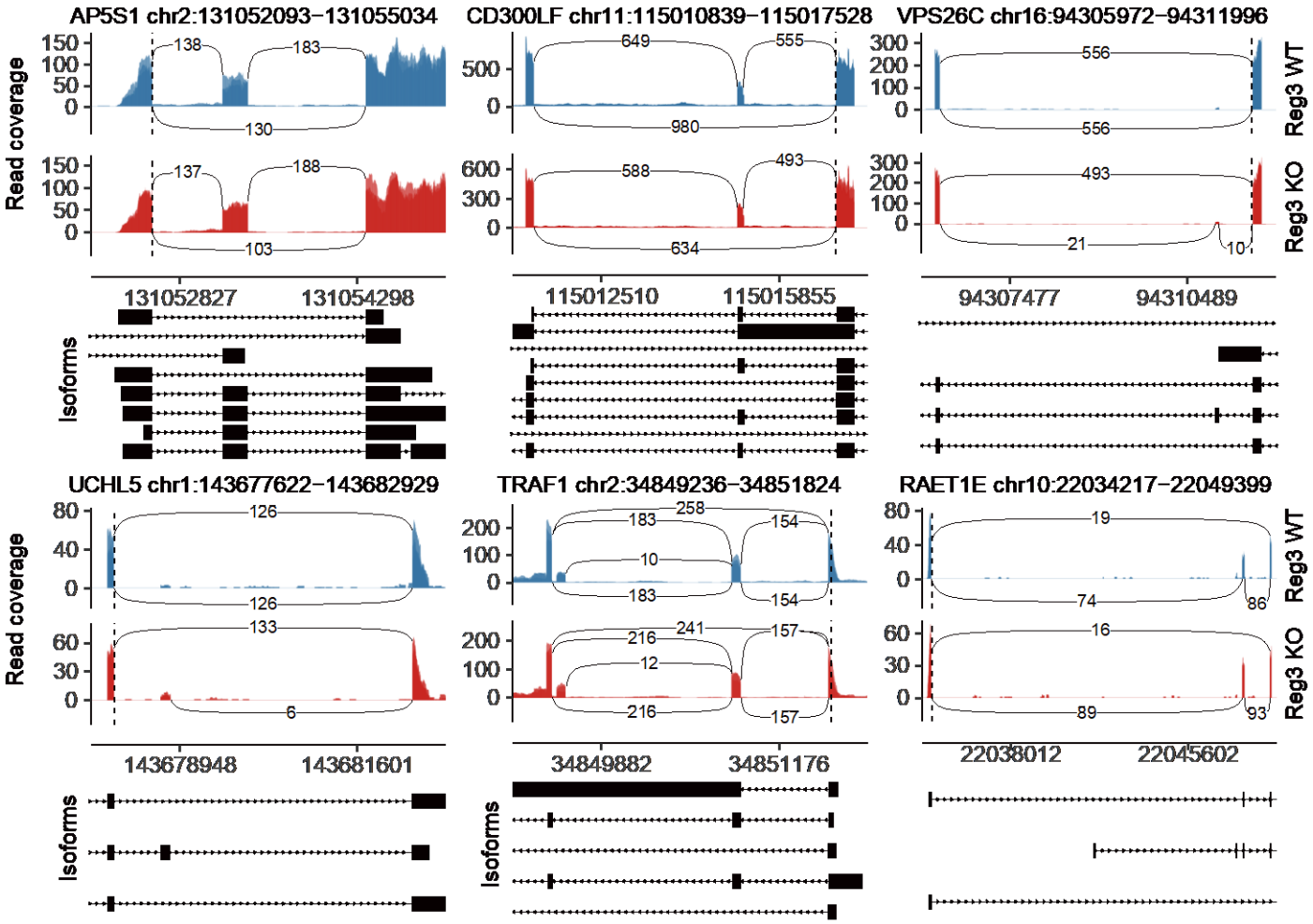

Figure 73. Sashimi plot for the examples of Regnase3 motif related downstream skipped exon. Rank-Regnase3cKO condition is shown in red plots, while the wildtype condition is depicted in blue. The X-axis shows the genomic locations, while the Y-axis indicates the transcription intensity. The plots show a "sashimi-like" region, which is a heavily transcribed region of exon, and the blank intronic regions between exons. The line crossing exonic regions represent the reads of junction and the count number is indicated on it. The exonic isoform structure for corresponding gene is displayed below Sashimi plot. The vertical dotted line represents the Regnase3 motif targeted junction which located on junction of the exon-intron of upstream exon for skipped exon.

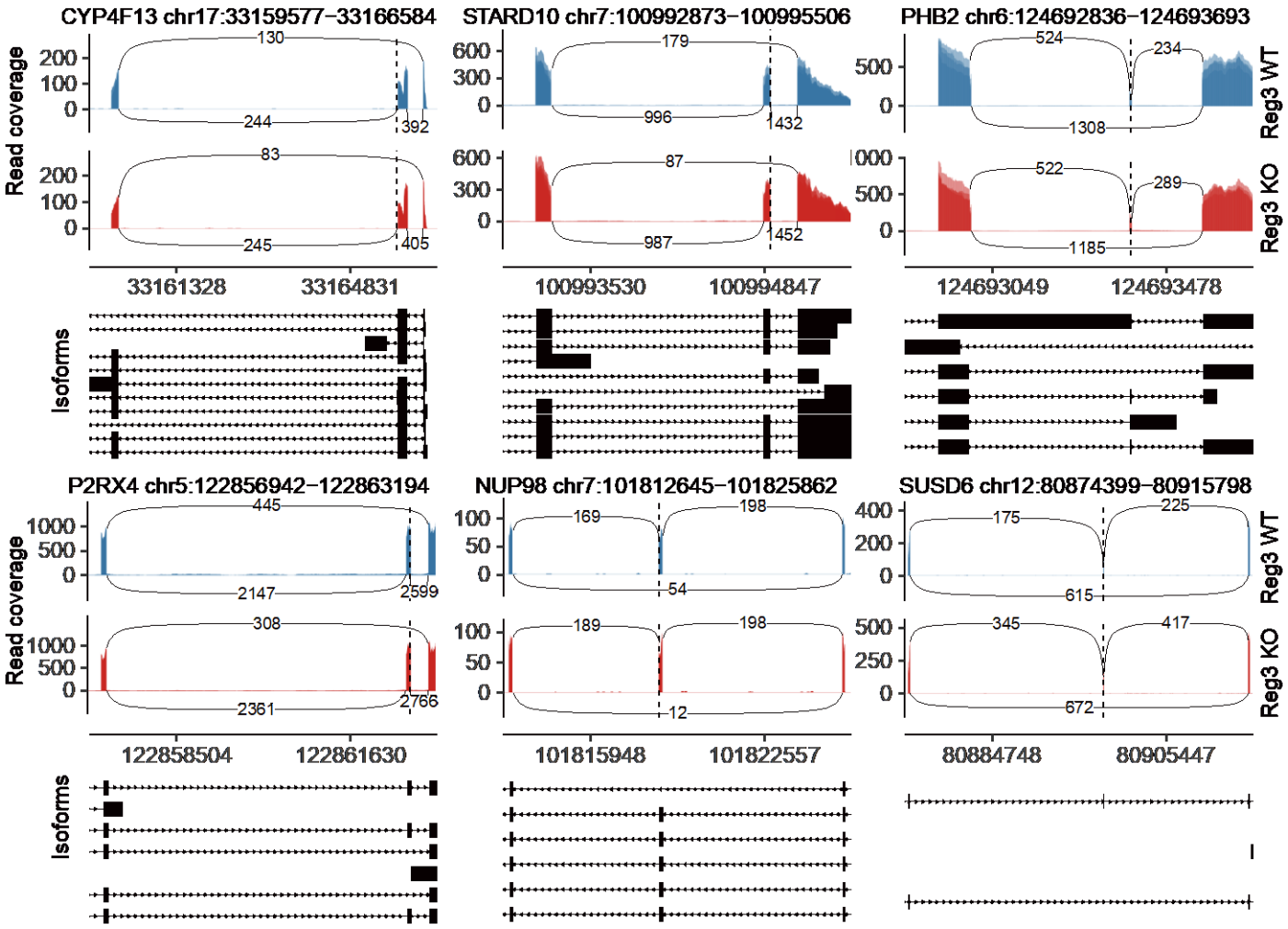

Figure 74. Sashimi plot for the examples of Regnase3 motif related skipped exon. Rank-Regnase3cKO condition is shown in red plots, while the wildtype condition is depicted in blue. The X-axis shows the genomic locations, while the Y-axis indicates the transcription intensity. The plots show a "sashimi-like" region, which is a heavily transcribed region of exon, and the blank intronic regions between exons. The line crossing exonic regions represent the reads of junction and the count number is indicated on it. The exonic isoform structure for corresponding gene is displayed below Sashimi plot. The vertical dotted line represents the Regnase3 motif targeted junction which located on the junction of exon/intron of skipped exon.

5. Discussion

In this thesis, we aimed to study the function of Regnase3 in AKI and nephrocalcinosis-related kidney injury. To do this, we utilized conditional knockout mice, in which the deletion of Regnase3 was targeted to either Rank-Cre macrophages or Pax8-Cre tubular epithelial cells. Our findings revealed that 1) the deletion of Regnase3 in Rank-Cre macrophages exacerbated kidney injury in the postischemic phase, thus contributing to the early injury phase of AKI and the transition to AKI-CKD. Additionally, we discovered that 2) Regnase3 associated with modulating the immune response in AKI and AKI-CKD transition, acting as a regulator of macrophage polarization towards an M1 and M2 phenotype and the capacity of cell migration. Furthermore, we found that 3) TEC-derived Regnase3 contributes to kidney injury, and that the deletion of Regnase3 provides protection against ischemic AKI. Additionally, our results indicate that 4) Regnase3 affects

proliferation and wound healing capability of tubular epithelial cells following injury. Furthermore, our data suggest that 5) Regnase3 specifically targets pre-RNA and regulates alternative splicing by increasing the proportion of targeted skipped exon events and decreasing the probability of targeted retained intron events. This study focused on the Regnase3 on macrophage and renal proximal tubular cells, and evaluated the association between Regnase3 and AKI, which could contribute to the understand of function of Regnase3 that might be a new potential therapy target for the AKI.

The kidneys host diverse populations of tissue-resident macrophages, which have the ability to both cause and prevent kidney injury[193-195]. These macrophages originate from embryonic progenitors during the development of the kidney and continue to proliferate and renew in situ throughout adulthood[196]. Tissue-resident macrophages are very heterogeneous and have tissue-specific properties and functions, such as osteoclast's bone resorption. The Rank plays a critical role in the formation of osteoclasts and the development of certain medical conditions, including autosomal-recessive osteopetrosis and familial expansile osteolysis. This emphasizes the significance of the signaling pathway between the Rank ligand and Rank in distinguishing macrophages that originate from embryos[197]. Studies have shown that Rank is a highly specific marker that efficiently labels yolk sac-derived tissue-resident macrophages, but not fetal liver hematopoietic stem cells and their progeny[158, 197]. Additionally, a subpopulation of dermal $CD11b^{+}MHCII^{+}F4/80^{+}$ cells have been found to be labeled with the Rank, as confirmed by studies using Rank-positive cells from bone marrow and peripheral blood[198]. However, it has been previously reported that the Cre under the promoter of the Rank receptor is active within a small percentage of B and T cells but is also highly active in a large proportion of tissue-resident macrophages[199]. The scRNA-seq data revealed that while Rank mRNA is expressed in the majority of MPCs in AKI within the kidney, some MPCs also express high levels of Rank mRNA in the blood. Rank has been found to be positively correlated with phagocytosis, chemokines, and monocyte maturation. Our own data has shown that Rank is absent in the bone marrow but is upregulated during BMDM maturation. Immunofluorescence results suggest that Rank is co-expressed with F4/80 in macrophages of the kidney interstitium. Additionally, our findings indicate that the Rank-Regnase3cKO BMDM, alveolar and peritoneal macrophage also express low levels of Regnase3, demonstrating that the Rank-Cre is effective for both tissue-resident macrophages and BM-derived maturated macrophages.

To date, there have been several studies that have employed genetic modified mice to investigate the function of Regnase3. All these studies have utilized a global knockout approach for Regnase3 and two of them have

used lysozyme (LysM)-Cre mice to generate Regnase3 deletion specifically in myeloid cells[155, 188, 200]. These studies revealed that mice deficient in Regnase3 develop without any major phenotype abnormalities, except for hypertrophic lymph nodes and an increased systemic IFN signaling. This leads to an increase in immature B cells and innate immune cells, and suppression of follicle and germinal center formation. The use of conditional knockout mice, specifically targeting Regnase3 in myeloid cells, resulted in the development of the same phenotype of lymphadenopathy which appeared on the global Regnase3 deficiency mice[188], but with the reduction of TNF secretion[155]. However, the current knowledge on the function of Regnase3 in disease models is inadequate and conflicting. In disease models, Regnase3 deficiency did not impact skin inflammation in an imiquimod-induced psoriasis model[200], but myeloid cell Regnase3 deficiency did protect from psoriasiform lesions[155]. The reason for these discrepancies in phenotype may be due to differences in the targeted deletion sites of Regnase3. This also could be attributed to the broad range of targets for the LysM-Cre approach, which leads to widespread influence on immunoregulation. The LysM-Cre approach leads to the deletion of floxed alleles in all myeloid-derived infiltration macrophages as well as tissue-resident macrophages, with 40% deletion in splenic macrophages, but a strong deletion of 60~80% in neutrophils and only 10% or less in other myeloid cells such as dendritic cell subsets, eosinophils, basophils, natural killer cells and mast cells[201]. In contrast, in our study, the use of Rank-Cre, which specifically targets tissue-resident macrophages, does not result in any significant differences in lymph size or immune conditions at the steady state (not shown in the thesis). This suggests that the use of tissue-specific Cre recombinase may provide a more precise understanding of the role of Regnase3 in disease models.

Research has revealed a potential interdependence between the function of Regnase1 and Regnase3, as they appear to have complementary and compensatory roles in their respective functions. This is highlighted by the distinct patterns of mRNA expression within the Regnase family, with high expression of Regnase1 in the spleen, lymph nodes, and thymus[188, 202], while Regnase2 exclusively expressed in the [188] and brain tissue[149]. Regnase4 shows similar expression patterns as Regnase1 in the spleen and lymph nodes[188, 202]. In contrast, Regnase3 is lowly expressed in the thymus, bone marrow, and intestine, but has a relatively high expression in such as the heart, lung, brain, liver, and particularly in non-lymphoid tissues like the kidney, which is higher than its expression in the spleen or lymph nodes[188]. The high expression of Regnase3 in non-lymphoid tissues and particularly in the kidney, may be related to the tissue-resident macrophages. Our finding suggests that Regnase3 is highly expressed in immune cells, particularly in matured macrophages. Regnase1 and Regnase3 are also found to be active in response to M1 and M2 polarizing stimuli such as LPS, IFNg, IL4, and IL10.

The expression of Regnase2 and Regnase4, however, only changes in M2 polarizing stimuli and also not to LPS and IFNg. Notably, the knockout of Regnase3 leads to the compensatory upregulation of the other three members of the Regnase family, particularly Regnase1, which is the highest in Regnase3 knockout cells. This phenomenon may be due to the direct decay of Regnase1 mRNA by the Regnase3 protein, which is dependent on the functional RNase PIN domain[188]. This implies that Regnase3 has evolved as an evolutionary counterpart to Regnase1 and acts in macrophage in response to various signaling stimuli and shares similar functions to a certain extent.

Regnase3 as one of the numbers of the Regnase family, has been found to exhibit distinct characteristics in terms of its role in immunoregulation compared to other members. Liu et al. conducted comprehensive research on the effects of Regnase3 on inflammation, using both global Regnase3 knockout and conditional knockout on myeloid cells created with CRISPR-Cas9[155]. The results of their study suggest that Regnase3 contributes to inflammation by enhancing TNF in macrophages and reducing IL6 in plasmacytoid dendritic cells. The impact of Regnase3 differs depending on the specific type of cell involved. In this thesis, we found that Regnase3 does not greatly influence the classic M1 polarization induced by IFNg and M2 polarization induced by IL4 and IL10 in macrophages, which is consistent with Liu's results from the global and conditional knockouts of Regnase3 in myeloid cells. However, using a combination of IFNg (20 ng/ml) and LPS to induce polarization provided more evidence of the effects of Regnase3 on M1 macrophages, as it was found that Regnase3 knockout macrophages are less sensitive to this combination, leading to a significant decrease in the proportion of M1 macrophages but increase TNF. However, when it comes to M2 polarization, IL4 and IL10 have minimal impact on Regnase3 knockout macrophages in comparison to wild type macrophages. Research conducted by the Glasmacher group[188] revealed that the secretion of IL6, TNF, and IP-10 in Regnase3$^{+/+}$ and Regnase3$^{-/-}$ BMDMs remained unchanged upon stimulation with LPS and other stimuli, which has been reported to be the target of Regnase1[134] It should be noted that Regnase1 is important to regulat the decay of inflammatory mRNAs during different stages of the inflammatory response, particularly by controlling the inflammation at early phase through the mRNA cleavage and degradation [203]. In contrast, the mechanism by which Regnase3 regulates inflammation appears to be more complex and may involve indirect signaling pathways or transcription factors rather than direct degradation of cytokines. Overall, the global and conditional deficiency of Regnase3 in myeloid cells highlights the importance of its expression within macrophages for maintaining a balanced immune system.

The full extent of the role played by Regnase3 in non-lymphoid tissues remains largely unknown. Research conducted by Liu et al. provided that Regnase3 in human umbilical vein endothelial cells participate with reduce TNF and chemokines, thereby regulating monocyte infiltration[204]. Furthermore, an in vitro study utilizing U251-MG cells that were transfected with Regnase3 overexpression vector and TNF 3'UTRs luciferase vector, found that Regnase3 negatively regulates TNF, both in terms of luciferase activity and mRNA level[205]. Additionally, using scRNA-seq, we observed that Regnase3 is highly expressed in both kidney tissue-resident macrophages and renal tubular cells. Following an ischemic injury, the expression of Regnase3 in the renal tissue decreases, but increases during the recovery phase at 2 days post-injury. This suggests that Regnase3 may be participated in the maintenance of homeostasis and repair processes in renal tubular cells following injury. Additionally, the correlation between the kidney disease and lymphadenopathy, which was observed in Regnase3 global knockout mice[188], was not clear. To further study the functions of Regnase3 in the kidney, we established an inducible conditional knockout of Regnase3 mice specifically in tubular epithelial cells. This allowed us to study Regnase3 in the kidney without confounding factors. Through our research, we have not observed any cases of lymphadenopathy. Moreover, we have found that the deficiency of Regnase3 in proximal tubular cells provides protection against kidney injury by preserving kidney function, reducing inflammation and macrophage accumulation. Regnase3 knockout tubular cells are better able to tolerate injury by directly reducing cell death, apoptosis and preserving more cellular functions, which may be linked to the inhibition of early apoptosis. The specific mechanism behind the kidney protective effect of Regnase3 remains unknown, but it may be like the complex regulatory activation pathway involved in Regnase3's immunoregulation.

The roles of Regnase1 in apoptosis and cell death have been extensively studied, with evidence supporting its role as a proapoptotic and antiproliferative agent[206]. Regnase1 regulates cell apoptosis in multiple ways, both directly and indirectly[207]. The indirect mechanism of Regnase1 on apoptosis is linked to the formation of stress granules, which are completely blocked by overexpression of Regnase1 and as a result, promotes apoptosis in conditions of stress including hypoxic injury[208]. Additionally, its deficiency has been found to facilitate the formation of granules aggregates and display apoptosis resistance[207]. Moreover, Regnase1 selectively enhances the decay of antiapoptotic gene mRNA transcripts, such as Bcl2 like 1, Bcl2 like a1, NF-KB Subunit, Baculoviral IAP Repeat Containing 3, and Bcl3[209]. We also observed the that the deficiency of Regnase3 in kidney injury reduces the apoptosis of both macrophages and tubular cells. Similarly, resistance to apoptosis, our data showed that Regnase3 can regulate the cell proliferation capacity, and deficiency of Regnase3

promotes cell proliferation and repair after injury, which may be influenced by the number of viable cells that survive after injury. To further investigate this, we seeded cells at low densities and counted the number of cells present by time lapse imaging. Our results showed that Regnase3 deficiency led to an increase of cells number, but the size of these cells was smaller. This is similar to the known effects of Regnase1 on cell proliferation[210], where overexpression of the Regnase1 has been shown to decrease cell viability and proliferation in both in vivo and in vitro models[209, 211], while depletion or inhibition of Regnase1 led to the opposite effect[210, 212]. Additionally, it has been reported that Regnase3 expression decreases significantly with tumor development, and its expression levels vary depending on the tumor grade and metastasis. The tubule progenitors are important for tubule regeneration and repair, but they may also drive ischemic table cells to become tumor stem cells and trigger papillary renal cell adenoma-carcinoma[213-216]. Therefore, it is important to further explore whether Regnase3 deficiency, which leads to better regeneration after AKI, may also lead to tumorigenesis and to understand the underlying mechanism.

There are several limitations of this study.

1) This work only employed male mice to subject to the disease model, which may not account for the potential impact of other factors such as genetics and comorbidities on the development and progression of AKI in the mice. [217, 218]. The AKI is a complex etiology disease, while the models were only applied to the young, healthy, and inbred mice, which is an ideal setting, while in humans AKI preferentially occurs in critically ill patients with other complications. The study's short-term (21 days) follow-up period may not fully capture the long-term effects of the injury on kidney function and recovery. Moreover, The IRI duration for the models of uIRI without the NX is longer than it with NX, as the long ischemic time is lethal when the mice only have one kidney. Although we made the similar conclusions from these models, the underlying damage and repair process may be different. Additionally, the study's focus on specific types of AKI may not be generalizable to other forms of kidney injury.

2) The study also relies on a specific type of experimental methodologies, which may not explore the full range of molecular and cellular mechanisms of Regnase3. For example, the RNA target of the Regnase3 motif need to be confirmed by other approach like the RNA decay assay. Another limitation of this thesis is that it may not account for the potential impact of other factors such as post-transcriptional modifications, protein interactions and microenvironment on the Regnase3 function. In this case, we speculate that the Regnase3 needs to be assisted by other proteins to exert biological function, thus further study on it is needed.

Furthermore, the study may not have fully considered the potential impact of other upstream signaling pathways or transcriptional regulators on Regnase3.

3) The study presented in this thesis focuses on Regnase3 and may not have exhaustively evaluated the functional interplay or specificity among other members of the Regnase family. There may be an unexplored potential for functional overlap or uniqueness between Regnase3 and other members such as Regnase1, 2 and 4, as well as potential interactions and cooperation between these members. Additionally, the study may not have fully addressed the possibility of each Regnase family member having unique or shared motifs and therefore being modulated differently. These limitations may hinder a comprehensive understanding of the functional relationship among the members of the Regnase family and their potential implications in both medicine and biology.

4) Finally, while we investigated the function of Regnase3, we did not embark into the potential for modulating Regnase3 as a target for therapeutic intervention, nor evaluated the effects of its overexpression. Additionally, the study may have overlooked the potential for using Regnase3 modulation as a diagnostic or prognostic marker for certain diseases. Moreover, the study may not have considered the potential clinical implications of its findings, and how they may be translated into developing drugs or other therapies to treat diseases related to Regnase3 regulation.

Conclusions

Our findings indicate that Regnase3 plays a significant role in postischemic kidneys injury, making it a potential therapeutic target for kidney IRI. However, the impact of Regnase3 on kidney injury is contingent upon the specific cell lineage in question. Our research demonstrates that the deletion of Rank-Regnase3 leads to an exacerbation of kidney injury by increasing macrophage recruitment, whereas the deletion of Pax8-Regnase3 leads to an improvement in kidney injury through its effects on cell death and wound healing capability of tubular epithelial cells, providing protection against ischemic AKI. Hence, the function of Regnase3 in kidney damage heavily relies on the type of cell lineage it affects, which ultimately decides whether it has a harmful or helpful effect on kidney injury (Figure 75).

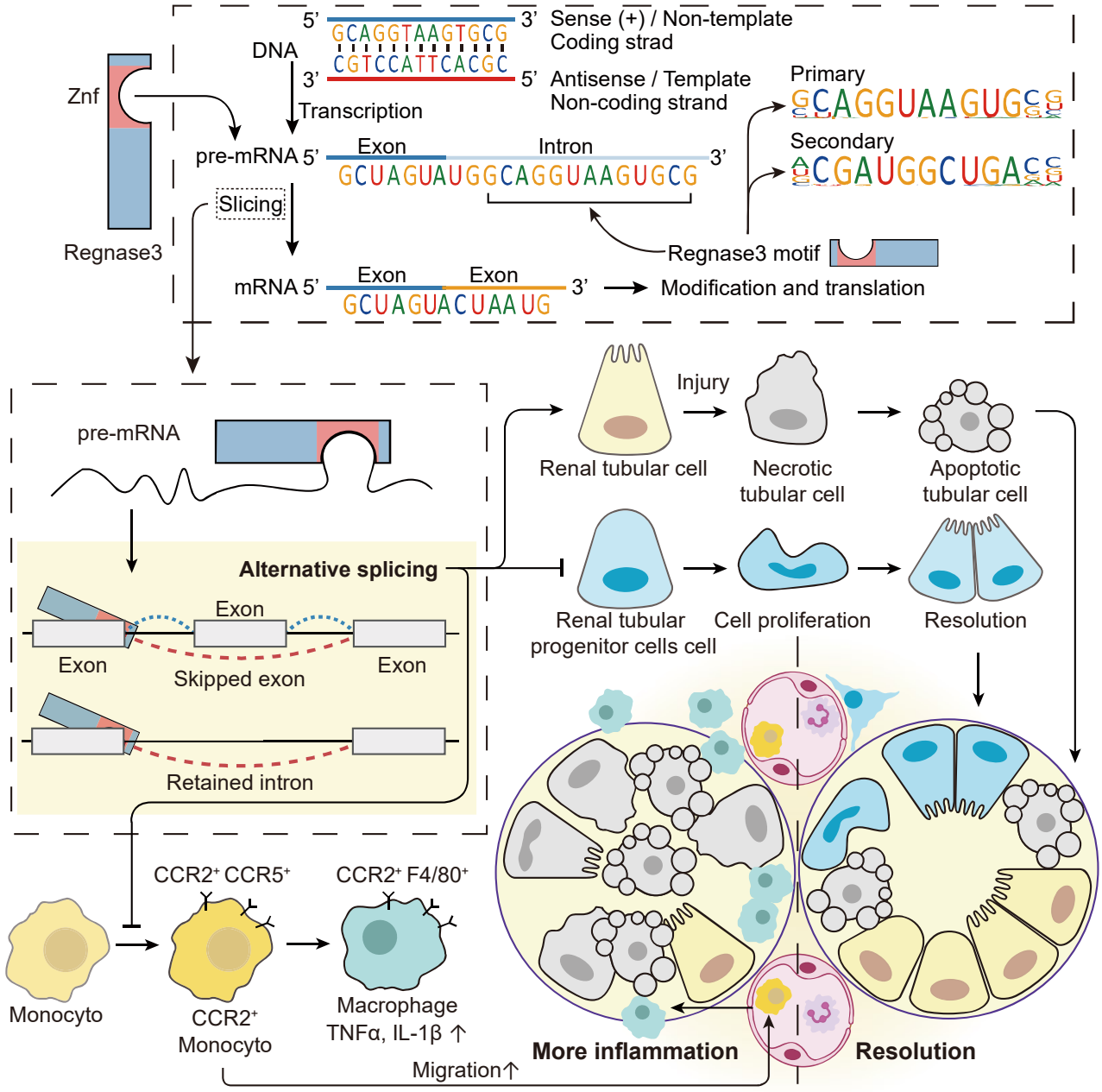

Figure 75. Different roles of Regnase3 in resident macrophages and tubular epithelial cells in kidney disease. Regnase3 primarily targets intron, in particular its primary motif targeting the exon-intron-junction, which is a location for pre-RNA splicing. Regnase3 regulates alternative splicing by increasing the occurrence of targeted skipped exon events upon cell activation while reducing the number of targeted retained intron events. The Regnase3 deletion in $Rank^+$ positive cells result in an exacerbation of kidney injury by increasing $CCR2^+$ monocyte recruitment, increased the expression of pro-inflammation gene TNFα and IL1β in $CCR2^+$ macrophage. The deletion of Regnase3 in tubular cells leads to an improvement in kidney injury through its effects on cell death and wound healing capability of tubular epithelial cells, providing protection against ischemic AKI.

6. References

1. Kellum JA, Romagnani P, Ashuntantang G, Ronco C, Zarbock A and Anders HJ. Acute kidney injury. *Nat Rev Dis Primers*. 2021; 7: 52.
2. Chawla LS, Bellomo R, Bihorac A, et al. Acute kidney disease and renal recovery: consensus report of the Acute Disease Quality Initiative (ADQI) 16 Workgroup. *Nat Rev Nephrol*. 2017; 13: 241-57.
3. Coca SG, Singanamala S and Parikh CR. Chronic kidney disease after acute kidney injury: a systematic review and meta-analysis. *Kidney Int*. 2012; 81: 442-8.
4. Greenberg JH, Coca S and Parikh CR. Long-term risk of chronic kidney disease and mortality in children after acute kidney injury: a systematic review. *BMC Nephrol*. 2014; 15: 184.
5. Thakar CV, Christianson A, Himmelfarb J and Leonard AC. Acute kidney injury episodes and chronic kidney disease risk in diabetes mellitus. *Clin J Am Soc Nephrol*. 2011; 6: 2567-72.
6. Chawla LS, Eggers PW, Star RA and Kimmel PL. Acute kidney injury and chronic kidney disease as interconnected syndromes. *N Engl J Med*. 2014; 371: 58-66.
7. Romagnani P, Remuzzi G, Glassock R, et al. Chronic kidney disease. *Nat Rev Dis Primers*. 2017; 3: 17088.
8. Zhang L, Wang F, Wang L, et al. Prevalence of chronic kidney disease in China: a cross-sectional survey. *Lancet*. 2012; 379: 815-22.
9. Beall D, Bywaters EG, Belsey RH and Miles JA. Crush Injury with Renal Failure. *Br Med J*. 1941; 1: 432-4.
10. Lucke B. Lower nephron nephrosis; the renal lesions of the crush syndrome, of burns, transfusions, and other conditions affecting the lower segments of the nephrons. *Mil Surg*. 1946; 99: 371-96.
11. Strauss MB. Acute renal insufficiency due to lower-nephron nephrosis. *N Engl J Med*. 1948; 239: 693-700.
12. Bywaters EG and Joekes AM. The artificial kidney; its clinical application in the treatment of traumatic anuria. *Proc R Soc Med*. 1948; 41: 420-6.
13. Bellomo R, Ronco C, Kellum JA, Mehta RL, Palevsky P and Acute Dialysis Quality Initiative w. Acute renal failure - definition, outcome measures, animal models, fluid therapy and information technology needs: the Second International Consensus Conference of the Acute Dialysis Quality Initiative (ADQI) Group. *Crit Care*. 2004; 8: R204-12.
14. Hoste EA, Clermont G, Kersten A, et al. RIFLE criteria for acute kidney injury are associated with hospital mortality in critically ill patients: a cohort analysis. *Crit Care*. 2006; 10: R73.
15. Cruz DN, Bolgan I, Perazella MA, et al. North East Italian Prospective Hospital Renal Outcome Survey on Acute Kidney Injury (NEiPHROS-AKI): targeting the problem with the RIFLE Criteria. *Clin J Am Soc Nephrol*. 2007; 2: 418-25.
16. Jenq CC, Tsai MH, Tian YC, et al. RIFLE classification can predict short-term prognosis in critically ill cirrhotic patients. *Intensive Care Med*. 2007; 33: 1921-30.
17. Lopes JA, Jorge S, Neves FC, et al. An assessment of the RIFLE criteria for acute renal failure in severely burned patients. *Nephrol Dial Transplant*. 2007; 22: 285.
18. Lopes JA and Jorge S. The RIFLE and AKIN classifications for acute kidney injury: a critical and comprehensive review. *Clin Kidney J*. 2013; 6: 8-14.
19. Mehta RL, Kellum JA, Shah SV, et al. Acute Kidney Injury Network: report of an initiative to improve outcomes in acute kidney injury. *Crit Care*. 2007; 11: R31.
20. Group KAW. KDIGO clinical practice guidelines for acute kidney injury. *Kidney Int Suppl*. 2012; 2: 1-138.
21. Palevsky PM, Liu KD, Brophy PD, et al. KDOQI US commentary on the 2012 KDIGO clinical practice guideline for acute kidney injury. *Am J Kidney Dis*. 2013; 61: 649-72.
22. Levi TM, de Souza SP, de Magalhaes JG, et al. Comparison of the RIFLE, AKIN and KDIGO criteria to

predict mortality in critically ill patients. *Rev Bras Ter Intensiva*. 2013; 25: 290-6.
23. Rossaint J and Zarbock A. Acute kidney injury: definition, diagnosis and epidemiology. *Minerva Urol Nefrol*. 2016; 68: 49-57.
24. Levey AS and James MT. Acute Kidney Injury. *Ann Intern Med*. 2017; 167: ITC66-ITC80.
25. Susantitaphong P, Cruz DN, Cerda J, et al. World incidence of AKI: a meta-analysis. *Clin J Am Soc Nephrol*. 2013; 8: 1482-93.
26. Mehta RL, Cerda J, Burdmann EA, et al. International Society of Nephrology's 0by25 initiative for acute kidney injury (zero preventable deaths by 2025): a human rights case for nephrology. *Lancet*. 2015; 385: 2616-43.
27. Hoste EAJ, Kellum JA, Selby NM, et al. Global epidemiology and outcomes of acute kidney injury. *Nat Rev Nephrol*. 2018; 14: 607-25.
28. Newsome BB, Warnock DG, McClellan WM, et al. Long-term risk of mortality and end-stage renal disease among the elderly after small increases in serum creatinine level during hospitalization for acute myocardial infarction. *Arch Intern Med*. 2008; 168: 609-16.
29. Goldstein SL, Jaber BL, Faubel S, Chawla LS and Acute Kidney Injury Advisory Group of American Society of N. AKI transition of care: a potential opportunity to detect and prevent CKD. *Clin J Am Soc Nephrol*. 2013; 8: 476-83.
30. Mammen C, Al Abbas A, Skippen P, et al. Long-term risk of CKD in children surviving episodes of acute kidney injury in the intensive care unit: a prospective cohort study. *Am J Kidney Dis*. 2012; 59: 523-30.
31. Lo LJ, Go AS, Chertow GM, et al. Dialysis-requiring acute renal failure increases the risk of progressive chronic kidney disease. *Kidney Int*. 2009; 76: 893-9.
32. See EJ, Jayasinghe K, Glassford N, et al. Long-term risk of adverse outcomes after acute kidney injury: a systematic review and meta-analysis of cohort studies using consensus definitions of exposure. *Kidney Int*. 2019; 95: 160-72.
33. Silver SA, Harel Z, McArthur E, et al. Causes of Death after a Hospitalization with AKI. *J Am Soc Nephrol*. 2018; 29: 1001-10.
34. Zhou X, Xiao F, Sugimoto H, Li B, McAndrews KM and Kalluri R. Acute Kidney Injury Instigates Malignant Renal Cell Carcinoma via CXCR2 in Mice with Inactivated Trp53 and Pten in Proximal Tubular Kidney Epithelial Cells. *Cancer Res*. 2021; 81: 2690-702.
35. Verine J, Varna M, Ratajczak P, et al. Human de novo papillary renal-cell carcinomas in a kidney graft: evidence of recipient origin with adenoma-carcinoma sequence. *Am J Transplant*. 2013; 13: 984-92.
36. Peired AJ, Antonelli G, Angelotti ML, et al. Acute kidney injury promotes development of papillary renal cell adenoma and carcinoma from renal progenitor cells. *Sci Transl Med*. 2020; 12.
37. Sharfuddin AA and Molitoris BA. Pathophysiology of ischemic acute kidney injury. *Nat Rev Nephrol*. 2011; 7: 189-200.
38. Santos WJ, Zanetta DM, Pires AC, Lobo SM, Lima EQ and Burdmann EA. Patients with ischaemic, mixed and nephrotoxic acute tubular necrosis in the intensive care unit--a homogeneous population? *Crit Care*. 2006; 10: R68.
39. Weisberg LS, Allgren RL, Genter FC and Kurnik BR. Cause of acute tubular necrosis affects its prognosis. The Auriculin Anaritide Acute Renal Failure Study Group. *Arch Intern Med*. 1997; 157: 1833-8.
40. Ehrmann S, Helms J, Joret A, et al. Nephrotoxic drug burden among 1001 critically ill patients: impact on acute kidney injury. *Ann Intensive Care*. 2019; 9: 106.
41. Costa e Silva VT, Marcal LJ and Burdmann EA. Risk factors for vancomycin nephrotoxicity: still a matter of debate*. *Crit Care Med*. 2014; 42: 2635-6.
42. Joyce EL, Kane-Gill SL, Priyanka P, Fuhrman DY and Kellum JA. Piperacillin/Tazobactam and Antibiotic-Associated Acute Kidney Injury in Critically Ill Children. *J Am Soc Nephrol*. 2019; 30: 2243-51.

43. Fu EL, Trevisan M, Clase CM, et al. Association of Acute Increases in Plasma Creatinine after Renin-Angiotensin Blockade with Subsequent Outcomes. *Clin J Am Soc Nephrol*. 2019; 14: 1336-45.
44. Brezis M and Rosen S. Hypoxia of the renal medulla--its implications for disease. *N Engl J Med*. 1995; 332: 647-55.
45. Ferenbach DA and Bonventre JV. Mechanisms of maladaptive repair after AKI leading to accelerated kidney ageing and CKD. *Nat Rev Nephrol*. 2015; 11: 264-76.
46. Linkermann A, Brasen JH, Darding M, et al. Two independent pathways of regulated necrosis mediate ischemia-reperfusion injury. *Proc Natl Acad Sci U S A*. 2013; 110: 12024-9.
47. Linkermann A, De Zen F, Weinberg J, Kunzendorf U and Krautwald S. Programmed necrosis in acute kidney injury. *Nephrol Dial Transplant*. 2012; 27: 3412-9.
48. Humphreys BD, Valerius MT, Kobayashi A, et al. Intrinsic epithelial cells repair the kidney after injury. *Cell Stem Cell*. 2008; 2: 284-91.
49. De Chiara L, Conte C, Antonelli G and Lazzeri E. Tubular Cell Cycle Response upon AKI: Revising Old and New Paradigms to Identify Novel Targets for CKD Prevention. *Int J Mol Sci*. 2021; 22.
50. Linkermann A, Skouta R, Himmerkus N, et al. Synchronized renal tubular cell death involves ferroptosis. *Proc Natl Acad Sci U S A*. 2014; 111: 16836-41.
51. Kers J, Leemans JC and Linkermann A. An Overview of Pathways of Regulated Necrosis in Acute Kidney Injury. *Semin Nephrol*. 2016; 36: 139-52.
52. Yang L, Besschetnova TY, Brooks CR, Shah JV and Bonventre JV. Epithelial cell cycle arrest in G2/M mediates kidney fibrosis after injury. *Nat Med*. 2010; 16: 535-43, 1p following 143.
53. Kumar S, Liu J, Pang P, et al. Sox9 Activation Highlights a Cellular Pathway of Renal Repair in the Acutely Injured Mammalian Kidney. *Cell Rep*. 2015; 12: 1325-38.
54. Kusaba T, Lalli M, Kramann R, Kobayashi A and Humphreys BD. Differentiated kidney epithelial cells repair injured proximal tubule. *Proc Natl Acad Sci U S A*. 2014; 111: 1527-32.
55. Humphreys BD, Czerniak S, DiRocco DP, Hasnain W, Cheema R and Bonventre JV. Repair of injured proximal tubule does not involve specialized progenitors. *Proc Natl Acad Sci U S A*. 2011; 108: 9226-31.
56. Berger K, Bangen JM, Hammerich L, et al. Origin of regenerating tubular cells after acute kidney injury. *Proc Natl Acad Sci U S A*. 2014; 111: 1533-8.
57. Lazzeri E, Angelotti ML, Peired A, et al. Endocycle-related tubular cell hypertrophy and progenitor proliferation recover renal function after acute kidney injury. *Nat Commun*. 2018; 9: 1344.
58. Kang HM, Huang S, Reidy K, Han SH, Chinga F and Susztak K. Sox9-Positive Progenitor Cells Play a Key Role in Renal Tubule Epithelial Regeneration in Mice. *Cell Rep*. 2016; 14: 861-71.
59. Rinkevich Y, Montoro DT, Contreras-Trujillo H, et al. In vivo clonal analysis reveals lineage-restricted progenitor characteristics in mammalian kidney development, maintenance, and regeneration. *Cell Rep*. 2014; 7: 1270-83.
60. Kellum JA, Sileanu FE, Bihorac A, Hoste EA and Chawla LS. Recovery after Acute Kidney Injury. *Am J Respir Crit Care Med*. 2017; 195: 784-91.
61. Lazzeri E, Angelotti ML, Conte C, Anders HJ and Romagnani P. Surviving Acute Organ Failure: Cell Polyploidization and Progenitor Proliferation. *Trends Mol Med*. 2019; 25: 366-81.
62. Cao Q, Harris DC and Wang Y. Macrophages in kidney injury, inflammation, and fibrosis. *Physiology (Bethesda)*. 2015; 30: 183-94.
63. Kelly KJ, Williams WW, Jr., Colvin RB, et al. Intercellular adhesion molecule-1-deficient mice are protected against ischemic renal injury. *J Clin Invest*. 1996; 97: 1056-63.
64. Bolisetty S and Agarwal A. Neutrophils in acute kidney injury: not neutral any more. *Kidney Int*. 2009; 75: 674-6.
65. Kinsey GR, Li L and Okusa MD. Inflammation in acute kidney injury. *Nephron Exp Nephrol*. 2008; 109: e102-7.

66. Nakazawa D, Marschner JA, Platen L and Anders HJ. Extracellular traps in kidney disease. *Kidney Int*. 2018; 94: 1087-98.
67. Nakazawa D, Kumar SV, Marschner J, et al. Histones and Neutrophil Extracellular Traps Enhance Tubular Necrosis and Remote Organ Injury in Ischemic AKI. *J Am Soc Nephrol*. 2017; 28: 1753-68.
68. Chaturvedi S, Yuen DA, Bajwa A, et al. Slit2 prevents neutrophil recruitment and renal ischemia-reperfusion injury. *J Am Soc Nephrol*. 2013; 24: 1274-87.
69. Awad AS, Rouse M, Huang L, et al. Compartmentalization of neutrophils in the kidney and lung following acute ischemic kidney injury. *Kidney Int*. 2009; 75: 689-98.
70. Melnikov VY, Faubel S, Siegmund B, Lucia MS, Ljubanovic D and Edelstein CL. Neutrophil-independent mechanisms of caspase-1- and IL18-mediated ischemic acute tubular necrosis in mice. *J Clin Invest*. 2002; 110: 1083-91.
71. Thornton MA, Winn R, Alpers CE and Zager RA. An evaluation of the neutrophil as a mediator of in vivo renal ischemic-reperfusion injury. *Am J Pathol*. 1989; 135: 509-15.
72. Gentek R, Molawi K and Sieweke MH. Tissue macrophage identity and self-renewal. *Immunol Rev*. 2014; 262: 56-73.
73. Molawi K, Wolf Y, Kandalla PK, et al. Progressive replacement of embryo-derived cardiac macrophages with age. *J Exp Med*. 2014; 211: 2151-8.
74. Meng X, Jin J and Lan HY. Driving role of macrophages in transition from acute kidney injury to chronic kidney disease. *Chin Med J (Engl)*. 2022; 135: 757-66.
75. Perdiguero EG and Geissmann F. The development and maintenance of resident macrophages. *Nat Immunol*. 2016; 17: 2-8.
76. Lee S, Huen S, Nishio H, et al. Distinct macrophage phenotypes contribute to kidney injury and repair. *J Am Soc Nephrol*. 2011; 22: 317-26.
77. Lin SL, Li B, Rao S, et al. Macrophage Wnt7b is critical for kidney repair and regeneration. *Proc Natl Acad Sci U S A*. 2010; 107: 4194-9.
78. Huen SC, Huynh L, Marlier A, Lee Y, Moeckel GW and Cantley LG. GM-CSF Promotes Macrophage Alternative Activation after Renal Ischemia/Reperfusion Injury. *J Am Soc Nephrol*. 2015; 26: 1334-45.
79. Meng XM, Mak TS and Lan HY. Macrophages in Renal Fibrosis. *Adv Exp Med Biol*. 2019; 1165: 285-303.
80. Henderson NC, Mackinnon AC, Farnworth SL, et al. Galectin-3 expression and secretion links macrophages to the promotion of renal fibrosis. *Am J Pathol*. 2008; 172: 288-98.
81. Venkatachalam MA, Griffin KA, Lan R, Geng H, Saikumar P and Bidani AK. Acute kidney injury: a springboard for progression in chronic kidney disease. *Am J Physiol Renal Physiol*. 2010; 298: F1078-94.
82. Furuichi K, Gao JL and Murphy PM. Chemokine receptor CX3CR1 regulates renal interstitial fibrosis after ischemia-reperfusion injury. *Am J Pathol*. 2006; 169: 372-87.
83. Ko GJ, Boo CS, Jo SK, Cho WY and Kim HK. Macrophages contribute to the development of renal fibrosis following ischaemia/reperfusion-induced acute kidney injury. *Nephrol Dial Transplant*. 2008; 23: 842-52.
84. Williams TM, Little MH and Ricardo SD. Macrophages in renal development, injury, and repair. *Semin Nephrol*. 2010; 30: 255-67.
85. Vernon MA, Mylonas KJ and Hughes J. Macrophages and renal fibrosis. *Semin Nephrol*. 2010; 30: 302-17.
86. Linfert D, Chowdhry T and Rabb H. Lymphocytes and ischemia-reperfusion injury. *Transplant Rev (Orlando)*. 2009; 23: 1-10.
87. Burne MJ, Daniels F, El Ghandour A, et al. Identification of the CD4(+) T cell as a major pathogenic factor in ischemic acute renal failure. *J Clin Invest*. 2001; 108: 1283-90.
88. Park P, Haas M, Cunningham PN, Bao L, Alexander JJ and Quigg RJ. Injury in renal ischemia-reperfusion

is independent from immunoglobulins and T lymphocytes. *Am J Physiol Renal Physiol*. 2002; 282: F352-7.
89. Rabb H, Daniels F, O'Donnell M, et al. Pathophysiological role of T lymphocytes in renal ischemia-reperfusion injury in mice. *Am J Physiol Renal Physiol*. 2000; 279: F525-31.
90. Burne-Taney MJ, Yokota-Ikeda N and Rabb H. Effects of combined T- and B-cell deficiency on murine ischemia reperfusion injury. *Am J Transplant*. 2005; 5: 1186-93.
91. Kinsey GR, Sharma R, Huang L, et al. Regulatory T cells suppress innate immunity in kidney ischemia-reperfusion injury. *J Am Soc Nephrol*. 2009; 20: 1744-53.
92. Jang HR, Gandolfo MT, Ko GJ, Satpute SR, Racusen L and Rabb H. B cells limit repair after ischemic acute kidney injury. *J Am Soc Nephrol*. 2010; 21: 654-65.
93. Burne-Taney MJ, Liu M, Ascon D, Molls RR, Racusen L and Rabb H. Transfer of lymphocytes from mice with renal ischemia can induce albuminuria in naive mice: a possible mechanism linking early injury and progressive renal disease? *Am J Physiol Renal Physiol*. 2006; 291: F981-6.
94. Kapeli K, Martinez FJ and Yeo GW. Genetic mutations in RNA-binding proteins and their roles in ALS. *Hum Genet*. 2017; 136: 1193-214.
95. Lukong KE, Chang KW, Khandjian EW and Richard S. RNA-binding proteins in human genetic disease. *Trends Genet*. 2008; 24: 416-25.
96. Gebauer F, Schwarzl T, Valcarcel J and Hentze MW. RNA-binding proteins in human genetic disease. *Nat Rev Genet*. 2021; 22: 185-98.
97. Seufert L, Benzing T, Ignarski M and Muller RU. RNA-binding proteins and their role in kidney disease. *Nat Rev Nephrol*. 2022; 18: 153-70.
98. Gerstberger S, Hafner M and Tuschl T. A census of human RNA-binding proteins. *Nat Rev Genet*. 2014; 15: 829-45.
99. Hentze MW, Castello A, Schwarzl T and Preiss T. A brave new world of RNA-binding proteins. *Nat Rev Mol Cell Biol*. 2018; 19: 327-41.
100. Castello A, Fischer B, Eichelbaum K, et al. Insights into RNA biology from an atlas of mammalian mRNA-binding proteins. *Cell*. 2012; 149: 1393-406.
101. Baltz AG, Munschauer M, Schwanhausser B, et al. The mRNA-bound proteome and its global occupancy profile on protein-coding transcripts. *Mol Cell*. 2012; 46: 674-90.
102. Castello A, Fischer B, Frese CK, et al. Comprehensive Identification of RNA-Binding Domains in Human Cells. *Mol Cell*. 2016; 63: 696-710.
103. Hammerle M, Gutschner T, Uckelmann H, et al. Posttranscriptional destabilization of the liver-specific long noncoding RNA HULC by the IGF2 mRNA-binding protein 1 (IGF2BP1). *Hepatology*. 2013; 58: 1703-12.
104. Wang IK, Palanisamy K, Sun KT, et al. The functional interplay of lncRNA EGOT and HuR regulates hypoxia-induced autophagy in renal tubular cells. *J Cell Biochem*. 2020; 121: 4522-34.
105. Fasolo F, Patrucco L, Volpe M, et al. The RNA-binding protein ILF3 binds to transposable element sequences in SINEUP lncRNAs. *FASEB J*. 2019; 33: 13572-89.
106. Sutherland JM, Siddall NA, Hime GR and McLaughlin EA. RNA binding proteins in spermatogenesis: an in depth focus on the Musashi family. *Asian J Androl*. 2015; 17: 529-36.
107. Wahl MC, Will CL and Luhrmann R. The spliceosome: design principles of a dynamic RNP machine. *Cell*. 2009; 136: 701-18.
108. Wende W, Friedhoff P and Strasser K. Mechanism and Regulation of Co-transcriptional mRNP Assembly and Nuclear mRNA Export. *Adv Exp Med Biol*. 2019; 1203: 1-31.
109. Rissland OS. The organization and regulation of mRNA-protein complexes. *Wiley Interdiscip Rev RNA*. 2017; 8.
110. Copsey AC, Cooper S, Parker R, et al. The helicase, DDX3X, interacts with poly(A)-binding protein 1

(PABP1) and caprin-1 at the leading edge of migrating fibroblasts and is required for efficient cell spreading. *Biochem J*. 2017; 474: 3109-20.
111. Dassi E. Handshakes and Fights: The Regulatory Interplay of RNA-Binding Proteins. *Front Mol Biosci*. 2017; 4: 67.
112. Poganik JR, Long MJC, Disare MT, et al. Post-transcriptional regulation of Nrf2-mRNA by the mRNA-binding proteins HuR and AUF1. *FASEB J*. 2019; 33: 14636-52.
113. Wang J, Hjelmeland AB, Nabors LB and King PH. Anti-cancer effects of the HuR inhibitor, MS-444, in malignant glioma cells. *Cancer Biol Ther*. 2019; 20: 979-88.
114. Garcia-Maurino SM, Rivero-Rodriguez F, Velazquez-Cruz A, et al. RNA Binding Protein Regulation and Cross-Talk in the Control of AU-rich mRNA Fate. *Front Mol Biosci*. 2017; 4: 71.
115. Conrad T, Albrecht AS, de Melo Costa VR, Sauer S, Meierhofer D and Orom UA. Serial interactome capture of the human cell nucleus. *Nat Commun*. 2016; 7: 11212.
116. Esmaillie R, Ignarski M, Bohl K, et al. Activation of Hypoxia-Inducible Factor Signaling Modulates the RNA Protein Interactome in Caenorhabditis elegans. *iScience*. 2019; 22: 466-76.
117. Ignarski M, Rill C, Kaiser RWJ, et al. The RNA-Protein Interactome of Differentiated Kidney Tubular Epithelial Cells. *J Am Soc Nephrol*. 2019; 30: 564-76.
118. McGinn J, Zhang F, Aziz M, et al. The Protective Effect of A Short Peptide Derived From Cold-Inducible RNA-Binding Protein in Renal Ischemia-Reperfusion Injury. *Shock*. 2018; 49: 269-76.
119. Li S, Qiu B, Lu H, et al. Hyperhomocysteinemia Accelerates Acute Kidney Injury to Chronic Kidney Disease Progression by Downregulating Heme Oxygenase-1 Expression. *Antioxid Redox Signal*. 2019; 30: 1635-50.
120. Singh M, Martinez AR, Govindaraju S and Lee BS. HuR inhibits apoptosis by amplifying Akt signaling through a positive feedback loop. *J Cell Physiol*. 2013; 228: 182-9.
121. Zuo Z, Jing K, Wu H, et al. Mechanisms and Functions of Mitophagy and Potential Roles in Renal Disease. *Front Physiol*. 2020; 11: 935.
122. Dong W, Wang H, Shahzad K, et al. Activated Protein C Ameliorates Renal Ischemia-Reperfusion Injury by Restricting Y-Box Binding Protein-1 Ubiquitination. *J Am Soc Nephrol*. 2015; 26: 2789-99.
123. Grammatikakis I, Abdelmohsen K and Gorospe M. Posttranslational control of HuR function. *Wiley Interdiscip Rev RNA*. 2017; 8.
124. Ayupova DA, Singh M, Leonard EC, Basile DP and Lee BS. Expression of the RNA-stabilizing protein HuR in ischemia-reperfusion injury of rat kidney. *Am J Physiol Renal Physiol*. 2009; 297: F95-F105.
125. Cen C, Yang WL, Yen HT, Nicastro JM, Coppa GF and Wang P. Deficiency of cold-inducible ribonucleic acid-binding protein reduces renal injury after ischemia-reperfusion. *Surgery*. 2016; 160: 473-83.
126. McGinn JT, Aziz M, Zhang F, et al. Cold-inducible RNA-binding protein-derived peptide C23 attenuates inflammation and tissue injury in a murine model of intestinal ischemia-reperfusion. *Surgery*. 2018; 164: 1191-7.
127. Zhang F, Brenner M, Yang WL and Wang P. A cold-inducible RNA-binding protein (CIRP)-derived peptide attenuates inflammation and organ injury in septic mice. *Sci Rep*. 2018; 8: 3052.
128. Fischer M, Weinberger T and Schulz C. The immunomodulatory role of Regnase family RNA-binding proteins. *RNA Biol*. 2020; 17: 1721-6.
129. Akira S. Regnase1, a ribonuclease involved in the regulation of immune responses. *Cold Spring Harb Symp Quant Biol*. 2013; 78: 51-60.
130. Jura J, Skalniak L and Koj A. Monocyte chemotactic protein-1-induced protein-1 (MCPIP1) is a novel multifunctional modulator of inflammatory reactions. *Biochim Biophys Acta*. 2012; 1823: 1905-13.
131. Liang J, Wang J, Azfer A, et al. A novel CCCH-zinc finger protein family regulates proinflammatory activation of macrophages. *J Biol Chem*. 2008; 283: 6337-46.
132. Cui X, Mino T, Yoshinaga M, et al. Regnase1 and Roquin Nonredundantly Regulate Th1 Differentiation

Causing Cardiac Inflammation and Fibrosis. *J Immunol*. 2017; 199: 4066-77.
133. King KR, Aguirre AD, Ye YX, et al. IRF3 and type I interferons fuel a fatal response to myocardial infarction. *Nat Med*. 2017; 23: 1481-7.
134. Matsushita K, Takeuchi O, Standley DM, et al. Zc3h12a is an RNase essential for controlling immune responses by regulating mRNA decay. *Nature*. 2009; 458: 1185-90.
135. Kotlinowski J, Hutsch T, Czyzynska-Cichon I, et al. Deletion of Mcpip1 in Mcpip1(fl/fl)Alb(Cre) mice recapitulates the phenotype of human primary biliary cholangitis. *Biochim Biophys Acta Mol Basis Dis*. 2021; 1867: 166086.
136. Dobosz E, Wadowska M, Kaminska M, et al. MCPIP-1 Restricts Inflammation via Promoting Apoptosis of Neutrophils. *Front Immunol*. 2021; 12: 627922.
137. Dobosz E, Lorenz G, Ribeiro A, et al. Murine myeloid cell MCPIP1 suppresses autoimmunity by regulating B-cell expansion and differentiation. *Dis Model Mech*. 2021; 14.
138. Dobosz E, Wilamowski M, Lech M, et al. MCPIP-1, Alias Regnase1, Controls Epithelial Inflammation by Posttranscriptional Regulation of IL8 Production. *J Innate Immun*. 2016; 8: 564-78.
139. Lin RJ, Chu JS, Chien HL, et al. MCPIP1 suppresses hepatitis C virus replication and negatively regulates virus-induced proinflammatory cytokine responses. *J Immunol*. 2014; 193: 4159-68.
140. Lin RJ, Chien HL, Lin SY, et al. MCPIP1 ribonuclease exhibits broad-spectrum antiviral effects through viral RNA binding and degradation. *Nucleic Acids Res*. 2013; 41: 3314-26.
141. Tanaka H, Arima Y, Kamimura D, et al. Phosphorylation-dependent Regnase1 release from endoplasmic reticulum is critical in IL17 response. *J Exp Med*. 2019; 216: 1431-49.
142. Matsushita K, Tanaka H, Yasuda K, et al. Regnase1 degradation is crucial for IL33- and IL25-mediated ILC2 activation. *JCI Insight*. 2020; 5.
143. Niu J, Shi Y, Xue J, et al. USP10 inhibits genotoxic NF-kappaB activation by MCPIP1-facilitated deubiquitination of NEMO. *EMBO J*. 2013; 32: 3206-19.
144. Ribeiro A, Dobosz E, Krill M, et al. Macrophage-Specific MCPIP1/Regnase1 Attenuates Kidney Ischemia-Reperfusion Injury by Shaping the Local Inflammatory Response and Tissue Regeneration. *Cells*. 2022; 11.
145. Xiaoming A, Wenbo J, Jinyi W, et al. Macrophage Regnase1 Deletion Deteriorates Liver Ischemia/Reperfusion Injury Through Regulation of Macrophage Polarization. *Front Physiol*. 2020; 11: 582347.
146. Moschovaki-Filippidou F, Steiger S, Lorenz G, et al. Growth Differentiation Factor 15 Ameliorates Anti-Glomerular Basement Membrane Glomerulonephritis in Mice. *Int J Mol Sci*. 2020; 21.
147. Steiger S, Kumar SV, Honarpisheh M, et al. Immunomodulatory Molecule IRAK-M Balances Macrophage Polarization and Determines Macrophage Responses during Renal Fibrosis. *J Immunol*. 2017; 199: 1440-52.
148. Gunthner R, Kumar VR, Lorenz G, Anders HJ and Lech M. Pattern-recognition receptor signaling regulator mRNA expression in humans and mice, and in transient inflammation or progressive fibrosis. *Int J Mol Sci*. 2013; 14: 18124-47.
149. Wawro M, Wawro K, Kochan J, et al. ZC3H12B/MCPIP2, a new active member of the ZC3H12 family. *RNA*. 2019; 25: 840-56.
150. Huang S, Qi D, Liang J, et al. The putative tumor suppressor Zc3h12d modulates toll-like receptor signaling in macrophages. *Cell Signal*. 2012; 24: 569-76.
151. Minagawa K, Wakahashi K, Kawano H, et al. Posttranscriptional modulation of cytokine production in T cells for the regulation of excessive inflammation by TFL. *J Immunol*. 2014; 192: 1512-24.
152. Zhang H, Wang WC, Chen JK, et al. ZC3H12D attenuated inflammation responses by reducing mRNA stability of proinflammatory genes. *Mol Immunol*. 2015; 67: 206-12.
153. Huang S, Liu S, Fu JJ, et al. Monocyte Chemotactic Protein-induced Protein 1 and 4 Form a Complex but

Act Independently in Regulation of Interleukin-6 mRNA Degradation. *J Biol Chem*. 2015; 290: 20782-92.
154. Suk FM, Chang CC, Lin RJ, Lin SY, Chen YT and Liang YC. MCPIP3 as a Potential Metastasis Suppressor Gene in Human Colorectal Cancer. *Int J Mol Sci*. 2018; 19.
155. Liu B, Huang J, Ashraf A, et al. The RNase MCPIP3 promotes skin inflammation by orchestrating myeloid cytokine response. *Nat Commun*. 2021; 12: 4105.
156. Berres ML, Koenen RR, Rueland A, et al. Antagonism of the chemokine Ccl5 ameliorates experimental liver fibrosis in mice. *J Clin Invest*. 2010; 120: 4129-40.
157. Miura K, Yang L, van Rooijen N, Ohnishi H and Seki E. Hepatic recruitment of macrophages promotes nonalcoholic steatohepatitis through CCR2. *Am J Physiol Gastrointest Liver Physiol*. 2012; 302: G1310-21.
158. Weinberger T, Esfandyari D, Messerer D, et al. Ontogeny of arterial macrophages defines their functions in homeostasis and inflammation. *Nat Commun*. 2020; 11: 4549.
159. Maeda K, Kobayashi Y, Udagawa N, et al. Wnt5a-Ror2 signaling between osteoblast-lineage cells and osteoclast precursors enhances osteoclastogenesis. *Nat Med*. 2012; 18: 405-12.
160. Marschner JA, Schafer H, Holderied A and Anders HJ. Optimizing Mouse Surgery with Online Rectal Temperature Monitoring and Preoperative Heat Supply. Effects on Post-Ischemic Acute Kidney Injury. *PLoS One*. 2016; 11: e0149489.
161. Mulay SR, Eberhard JN, Pfann V, et al. Oxalate-induced chronic kidney disease with its uremic and cardiovascular complications in C57BL/6 mice. *Am J Physiol Renal Physiol*. 2016; 310: F785-F95.
162. Ma Q, Steiger S and Anders HJ. Sodium glucose transporter-2 inhibition has no renoprotective effects on non-diabetic chronic kidney disease. *Physiol Rep*. 2017; 5.
163. Scarfe L, Schock-Kusch D, Ressel L, et al. Transdermal Measurement of Glomerular Filtration Rate in Mice. *J Vis Exp*. 2018.
164. Bradski G. The OpenCV Library. *Dr Dobb's Journal of Software Tools*. 2000.
165. Tonnus W, Maremonti F, Belavgeni A, et al. Gasdermin D-deficient mice are hypersensitive to acute kidney injury. *Cell Death Dis*. 2022; 13: 792.
166. Berzaghi R, Ahktar MA, Islam A, Pedersen BD, Hellevik T and Martinez-Zubiaurre I. Fibroblast-Mediated Immunoregulation of Macrophage Function Is Maintained after Irradiation. *Cancers (Basel)*. 2019; 11.
167. Triboulet S, Aude-Garcia C, Carriere M, et al. Molecular responses of mouse macrophages to copper and copper oxide nanoparticles inferred from proteomic analyses. *Mol Cell Proteomics*. 2013; 12: 3108-22.
168. Pireaux V, Sauvage A, Bihin B, et al. Myeloperoxidase-Oxidized LDLs Enhance an Anti-Inflammatory M2 and Antioxidant Phenotype in Murine Macrophages. *Mediators Inflamm*. 2016; 2016: 8249476.
169. Stringer C, Wang T, Michaelos M and Pachitariu M. Cellpose: a generalist algorithm for cellular segmentation. *Nat Methods*. 2021; 18: 100-6.
170. Jaggi U, Yang M, Matundan HH, et al. Increased phagocytosis in the presence of enhanced M2-like macrophage responses correlates with increased primary and latent HSV-1 infection. *PLoS Pathog*. 2020; 16: e1008971.
171. Iwakura T, Marschner JA, Zhao ZB, Swiderska MK and Anders HJ. Electric cell-substrate impedance sensing in kidney research. *Nephrol Dial Transplant*. 2021; 36: 216-23.
172. Guerra MH, Yumnamcha T, Ebrahim AS, Berger EA, Singh LP and Ibrahim AS. Real-Time Monitoring the Effect of Cytopathic Hypoxia on Retinal Pigment Epithelial Barrier Functionality Using Electric Cell-Substrate Impedance Sensing (ECIS) Biosensor Technology. *Int J Mol Sci*. 2021; 22.
173. Wolf FA, Angerer P and Theis FJ. SCANPY: large-scale single-cell gene expression data analysis. *Genome Biol*. 2018; 19: 15.
174. Lun AT, McCarthy DJ and Marioni JC. A step-by-step workflow for low-level analysis of single-cell

RNA-seq data with Bioconductor. *F1000Res*. 2016; 5: 2122.
175. Korsunsky I, Millard N, Fan J, et al. Fast, sensitive and accurate integration of single-cell data with Harmony. *Nat Methods*. 2019; 16: 1289-96.
176. Satija R, Farrell JA, Gennert D, Schier AF and Regev A. Spatial reconstruction of single-cell gene expression data. *Nat Biotechnol*. 2015; 33: 495-502.
177. Yao W, Chen Y, Li Z, et al. Single Cell RNA Sequencing Identifies a Unique Inflammatory Macrophage Subset as a Druggable Target for Alleviating Acute Kidney Injury. *Adv Sci (Weinh)*. 2022; 9: e2103675.
178. Cheung MD, Erman EN, Moore KH, et al. Resident macrophage subpopulations occupy distinct microenvironments in the kidney. *JCI Insight*. 2022.
179. Kirita Y, Wu H, Uchimura K, Wilson PC and Humphreys BD. Cell profiling of mouse acute kidney injury reveals conserved cellular responses to injury. *Proc Natl Acad Sci U S A*. 2020; 117: 15874-83.
180. Klocke J, Kim SJ, Skopnik CM, et al. Urinary single-cell sequencing captures kidney injury and repair processes in human acute kidney injury. *Kidney Int*. 2022.
181. Nitta KR, Jolma A, Yin Y, et al. Conservation of transcription factor binding specificities across 600 million years of bilateria evolution. *Elife*. 2015; 4.
182. Grant CE, Bailey TL and Noble WS. FIMO: scanning for occurrences of a given motif. *Bioinformatics*. 2011; 27: 1017-8.
183. Jolma A, Zhang J, Mondragon E, et al. Binding specificities of human RNA-binding proteins toward structured and linear RNA sequences. *Genome Res*. 2020; 30: 962-73.
184. Kim D, Paggi JM, Park C, Bennett C and Salzberg SL. Graph-based genome alignment and genotyping with HISAT2 and HISAT-genotype. *Nat Biotechnol*. 2019; 37: 907-15.
185. Li H, Handsaker B, Wysoker A, et al. The Sequence Alignment/Map format and SAMtools. *Bioinformatics*. 2009; 25: 2078-9.
186. Gaidatzis D, Burger L, Florescu M and Stadler MB. Analysis of intronic and exonic reads in RNA-seq data characterizes transcriptional and post-transcriptional regulation. *Nat Biotechnol*. 2015; 33: 722-9.
187. Love MI, Huber W and Anders S. Moderated estimation of fold change and dispersion for RNA-seq data with DESeq2. *Genome Biol*. 2014; 15: 550.
188. von Gamm M, Schaub A, Jones AN, et al. Immune homeostasis and regulation of the interferon pathway require myeloid-derived Regnase3. *J Exp Med*. 2019; 216: 1700-23.
189. Liu J, Kumar S, Dolzhenko E, et al. Molecular characterization of the transition from acute to chronic kidney injury following ischemia/reperfusion. *JCI Insight*. 2017; 2.
190. Liu J, Krautzberger AM, Sui SH, et al. Cell-specific translational profiling in acute kidney injury. *J Clin Invest*. 2014; 124: 1242-54.
191. Liao Y, Smyth GK and Shi W. featureCounts: an efficient general purpose program for assigning sequence reads to genomic features. *Bioinformatics*. 2014; 30: 923-30.
192. Yu G, Wang LG, Han Y and He QY. clusterProfiler: an R package for comparing biological themes among gene clusters. *OMICS*. 2012; 16: 284-7.
193. Salei N, Rambichler S, Salvermoser J, et al. The Kidney Contains Ontogenetically Distinct Dendritic Cell and Macrophage Subtypes throughout Development That Differ in Their Inflammatory Properties. *J Am Soc Nephrol*. 2020; 31: 257-78.
194. Li N, Steiger S, Fei L, et al. IRF8-Dependent Type I Conventional Dendritic Cells (cDC1s) Control Post-Ischemic Inflammation and Mildly Protect Against Post-Ischemic Acute Kidney Injury and Disease. *Front Immunol*. 2021; 12: 685559.
195. Salei N, Ji X, Pakalniskyte D, et al. Selective depletion of a CD64-expressing phagocyte subset mediates protection against toxic kidney injury and failure. *Proc Natl Acad Sci U S A*. 2021; 118.
196. Munro DAD and Hughes J. The Origins and Functions of Tissue-Resident Macrophages in Kidney Development. *Front Physiol*. 2017; 8: 837.

197. Percin GI, Eitler J, Kranz A, et al. CSF1R regulates the dendritic cell pool size in adult mice via embryo-derived tissue-resident macrophages. *Nat Commun*. 2018; 9: 5279.
198. Muto A, Mizoguchi T, Udagawa N, et al. Lineage-committed osteoclast precursors circulate in blood and settle down into bone. *J Bone Miner Res*. 2011; 26: 2978-90.
199. Mass E, Ballesteros I, Farlik M, et al. Specification of tissue-resident macrophages during organogenesis. *Science*. 2016; 353.
200. Clayer E, Frank D, Anderton H, et al. ZC3H12C expression in dendritic cells is necessary to prevent lymphadenopathy of skin-draining lymph nodes. *Immunol Cell Biol*. 2022; 100: 160-73.
201. Abram CL, Roberge GL, Hu Y and Lowell CA. Comparative analysis of the efficiency and specificity of myeloid-Cre deleting strains using ROSA-EYFP reporter mice. *J Immunol Methods*. 2014; 408: 89-100.
202. Iwasaki H, Takeuchi O, Teraguchi S, et al. The IkappaB kinase complex regulates the stability of cytokine-encoding mRNA induced by TLR-IL-1R by controlling degradation of Regnase1. *Nat Immunol*. 2011; 12: 1167-75.
203. Mino T, Murakawa Y, Fukao A, et al. Regnase1 and Roquin Regulate a Common Element in Inflammatory mRNAs by Spatiotemporally Distinct Mechanisms. *Cell*. 2015; 161: 1058-73.
204. Liu L, Zhou Z, Huang S, et al. Zc3h12c inhibits vascular inflammation by repressing NF-kappaB activation and pro-inflammatory gene expression in endothelial cells. *Biochem J*. 2013; 451: 55-60.
205. Wawro M, Kochan J, Sowinska W, et al. Molecular Mechanisms of ZC3H12C/Reg-3 Biological Activity and Its Involvement in Psoriasis Pathology. *Int J Mol Sci*. 2021; 22.
206. Miekus K, Kotlinowski J, Lichawska-Cieslar A, Rys J and Jura J. Activity of MCPIP1 RNase in tumor associated processes. *J Exp Clin Cancer Res*. 2019; 38: 421.
207. Zhou L, Azfer A, Niu J, et al. Monocyte chemoattractant protein-1 induces a novel transcription factor that causes cardiac myocyte apoptosis and ventricular dysfunction. *Circ Res*. 2006; 98: 1177-85.
208. Qi D, Huang S, Miao R, et al. Monocyte chemotactic protein-induced protein 1 (MCPIP1) suppresses stress granule formation and determines apoptosis under stress. *J Biol Chem*. 2011; 286: 41692-700.
209. Lu W, Ning H, Gu L, et al. MCPIP1 Selectively Destabilizes Transcripts Associated with an Antiapoptotic Gene Expression Program in Breast Cancer Cells That Can Elicit Complete Tumor Regression. *Cancer Res*. 2016; 76: 1429-40.
210. Marona P, Gorka J, Mazurek Z, et al. MCPIP1 Downregulation in Clear Cell Renal Cell Carcinoma Promotes Vascularization and Metastatic Progression. *Cancer Res*. 2017; 77: 4905-20.
211. Skalniak A, Boratyn E, Tyrkalska SD, et al. Expression of the monocyte chemotactic protein-1-induced protein 1 decreases human neuroblastoma cell survival. *Oncol Rep*. 2014; 31: 2385-92.
212. Lichawska-Cieslar A, Pietrzycka R, Ligeza J, et al. RNA sequencing reveals widespread transcriptome changes in a renal carcinoma cell line. *Oncotarget*. 2018; 9: 8597-613.
213. Yao Y, Liu K, Wu Y, et al. Comprehensive landscape of the functions and prognostic value of RNA binding proteins in uterine corpus endometrial carcinoma. *Front Mol Biosci*. 2022; 9: 962412.
214. Yue Y, Wu Y, Zhao D, et al. Pan-Cancer Analysis Predicts the Immunological and Prognostic Role of ZC3H12C in KIRC. *Biomed Res Int*. 2022; 2022: 4541571.
215. Yang L, Zhang R, Guo G, et al. Development and validation of a prediction model for lung adenocarcinoma based on RNA-binding protein. *Ann Transl Med*. 2021; 9: 474.
216. Li W, Gao LN, Song PP and You CG. Development and validation of a RNA binding protein-associated prognostic model for lung adenocarcinoma. *Aging (Albany NY)*. 2020; 12: 3558-73.
217. James MT, Grams ME, Woodward M, et al. A Meta-analysis of the Association of Estimated GFR, Albuminuria, Diabetes Mellitus, and Hypertension With Acute Kidney Injury. *Am J Kidney Dis*. 2015; 66: 602-12.
218. Grams ME, Sang Y, Ballew SH, et al. A Meta-analysis of the Association of Estimated GFR, Albuminuria, Age, Race, and Sex With Acute Kidney Injury. *Am J Kidney Dis*. 2015; 66: 591-601.

Appendix 1 Instruments and equipment

Instruments	Equipment	Company
Cell incubators	Type B5060 EC-CO2	Heraeus Sepatech, Germany
Fluorescence Microscopes	Leica DMi8	Leica Microsystems, UK
	Nikon Eclipse Ti2	NIKON corporation, Japan
	Nikon DS-Qi2 camera	NIKON corporation, Japan
	Leica DM IL	Leica Microsystems, Germany
ELISA-Reader	Tecan, GENios Plus	Tecan, Crailsheim, Germany
Microscopes	Leica DMRBE	Leica Microsystems, Germany
	Carl Camera	Zeiss Digital Göttingen, DE
Spectrophotometer	Beckman DU® 530	Beckman Coulter, Fullerton, USA
Flow cytometry	FACS Canto II	BD, USA
	FACS Calibur	BD, USA
Centrifuge	Heraeus, Biofuge primo	Kendro Laboratory Products GmbH, Germany
	Heraeus, Minifuge T	VWR International, Germany
	Heraeus, Biofuge A	Sepatech Heraeus Sepatech, Germany
Miniaturized imager device	For GFR measurement	Mannheim Pharma & Diagnostics GmbH
Miniaturized battery	For GFR imager device	Mannheim Pharma & Diagnostics GmbH
PCR cycler	Light Cycler480	Roche Mannheim, Gremany
	PCR cycler	Eppendorf, Germany
Other Equipment	Cryostat CM 3000	Leica Microsystems, Bensheim, Germany
	Microtome HM 340E	Microm, Heidelberg, Germany
	Nanodrop	PEQLAB Biotechnology GMBH
	Homogenizer ULTRA-TURRAX	IKA GmbH, Staufen, Germany

Appendix 2 Chemicals and reagents

Chemicals and reagents	company	Cat. number
10X PBS	Sigma-Aldrich Chemie GmbH	D1408
1X PBS	PAN-Biotech GmbH	P04-36500
2-Mercaptoethanol	Sigma-Aldrich Chemie GmbH	M6250
96 Well Lightcycler Platte	Sarstedt AG & Co. KG	72.1982.202
Agarose	Invitrogen Ltd.	15510-500
Bovine Serum Albumin	Roche Diagnostics GmbH	10735086001
CD45 microbeads	Miltenyibiotec, Germany	130-052-301
Collagenase D	Sigma-Aldrich, Germany	11088866001
Corning® Costar® Transwell® cell culture inserts	Corning	CLS3464-48EA
Creatinine kit	Diasys Diagnositic Systems	117119910026
Cytochalasin D	Sigma-Aldrich, Germany	C8273
D(+)-Saccharose	ROTH	200-334-9
Dextran	Sigma Aldrich, Germany	31392
DirectPCR® Lysis Reagent Tail	PEQLAB Biotechnologie GmbH	VIAG102-T
DMEM medium	Gibco/Thermofisher, UK	21885-025
Doxycycline Hyclate USP	Fagron	803781
EDTA	Carl Roth GmbH & Co. KG	8043.2
Epithelial growth factor	Sigma Aldrich, Germany	SRP3196
Ethibond Excel 5-0	Ethicon Deutschland	EH7260H
Ethyl pyruvate	Sigma-Aldrich, Germany	E47808
Fc block	Biolegend, Inc.	101302
Fetal bovine serum	Biochrom KG, Berlin, Germany	L6113
FITC-sinistrin	Medi Beacon	13109910021
Glycyrrhizic Acid	Sigma-Aldrich, Germany	PHR1516
Helix NPTM Green	Biolegend, Inc.	425303
HEPES	Sigma Life Science, Germany	H3375
Hexanucleotide Mix	Sigma-Aldrich, Germany	11277081001
Human ZC3H12A protein	Euprotein	EP8931790
Human ZC3H12C protein	Euprotein	EP8366170
Hydrocortisone	Sigma Aldrich, Germany	H0888
Hydrogen peroxide solution	Sigma-Aldrich, Germany	H1009
Insulin-Transferrin-Natrimselenit-Zusatz	Sigma-Aldrich, Germany	11074547001
Isofluran CP®	CP-Pharma Handelsgesellschaft GmbH	798-932
Latex beads, carboxylate-modified polystyrene, fluorescent yellow-green	sigma	L4655-1ML
LDH reagent	Roche	4744926001
Leukoplast® hospital	BSN medical GmbH	01757-00
Lipopolysaccharides from Escherichia coli O111:B4	Sigma	L2630-25MG
Low MW DNA Ladder	New England Biolabs® Inc.	N3233S
LS column	MACS Miltenyibiotec, Germany	130-042-401
MACS® SmartStrainers (70 µm)	Miltenyi biotec	130-110-916
MgCl2 25mM	Thermo Fisher Scientific Inc.	R0971

MTT labeling reagent	Sigma-Aldrich, Germany	11465007001
NIC-Kidney Patches 3x3cm	MediBeacon GmbH	003
peqGREEN DNA/ RNA dye	PEQLAB Biotechnologie GmbH	37-5000
Percoll	Sigma-Aldrich, Germany	P1644
Phagocytosis Assay Kit (IgG FITC)	cayman	cay500290
Pierce™ ECL Western Blotting Substrate	ThermoFisher Scientific, Germany	#1610374
Potassium chloride	Merck KGaA, Darmstadt, Germany	7447-40-7
Pre-Seperation Filters (70 µm)	MIltenyi Biotec GmbH	130-095-823
Propidium Iodide Solution	Biolegend, Inc	421301
Protease and phosphatase	Thermo Scientific, Germany inhibitors	A32959
Proteinase K	Qiagen GmbH	1019499
PureLink™ PCR Purification Kit	Thermofisher	K310001
Rechargable batteries for NIC-Kidney devices	MediBeacon GmbH	004
Recombinant mouse GM-CSF	Biolegend, Inc.	576304
Recombinant mouse M-CSF	Biolegend, Inc.	576404
RIPA buffer	Sigma-Aldrich, Germany	R0278
rm CCL2	immunotools	12343383
rm IFN-gamma (Interferon gamma)	Immunotools	12343534
rm IL10 (Interleukin-10)	Immunotools	12340103
rm IL4 (Interleukin-4)	Immunotools	12340043
RNA isolation kit	Invitrogen by ThermoFisher Scientific	12183018A
RNAlater	Ambion, Inc.	AM7021
Rnasin and ribonuclease inhibitor	Promega, Germany	N2515
Strainer (70 µm)	MACS Miltenyibiotec, Germany	130-098-462
SuperscriptTM II Reverse Transcriptase	Invitrogen	18064071
SYBR R Green I nucleic acid gel stain	Sigma-Aldrich Chemie GmbH	86205
Taq DNA Polymerase	Biolabs Inc, New England	M0273E
TranscriptAid T7 High Yield Transcription Kit	Thermofisher	K0441
VicrylTM 5-0	Ethicon Deutschland	V493H
Yasargil Aneurysm Clip	Medicon eG	58.54.10
ZC3H12C Polyclonal Antibody	Thermofisher	PA5-20928
Zinc sulfate solution	Sigma	83265-250ML-F

Appendix 3 Oligonucleotide primers

Gene	Forward	Reverse
18s	GCAATTATTCCCCATGAACG	AGGGCCTCACTAAACCATCC
αSMA	CCTTCGTGACTACTGCCGAG	ATAGGTGGTTTCGTGGATGC
Fibronectin	GCCACCATTACTGGTCTGGA	GGTTGGTGATGAAGGGGGTC
TGFβ	CAACCCAGGTCCTTCCTAAA	GGAGAGCCCTGGATACCAAC
E-cadherin	CCCAGAGACTGGTGCCATTT	TGGCAATGGGTGAACCATCA
SMAD4	CAGCCATAGTGAAGGACTGTTGC	CCTACTTCCAGTCCAGGTGGTA
SMAD5	CAGGAGTTTGCTCAGCTTCTGG	ACGTCCTGTCGGTGGTACTCTG
KIM-1	TCAGCTCGGGAATGCACAA	TGGTTGCCTTCCGTGTCTCT
NGAL	ATGTCACCTCCATCCTGG	GCCACTTGCACATTGTAG
IL18	AGAAAGCCGCCTCAAACCTT	TGTCTGATTCCAGGTCTCCATTT
iNOS	AAACCCCTTGTGCTGTTCTCA	GAACATTCTGTGCTGTCCCAG
TNF	AGCCTCTTCTCATTCCTGCT	TAGACAAGGTACAACCCATC
TIMP2	GCAACAGGCGTTTTGCAATG	AGGTCCTTTGAACATCTTTATCTG
CCL2	CCTGCTGTTCACAGTTGCC	ATTGGGATCATCTTGCTGGT
CXCL1	CCGAAGTCATAGCCACACTCA	CTCCCACACATGTCCTCACC
CXCL2	CCCAGACAGAAGTCATAGCCAC	CTTCCGTTGAGGGACAGCAG
CXCL12	TCAGATTGTTGCACGGCTGA	GTTACAAAGCGCCAGAGCAG
CCR2	GCTGTGTTTGCCTCTCTACCAG	CAAGTAGAGGCAGGATCAGGCT
CCR5	GTCTACTTTCTCTTCTGGACTCC	CCAAGAGTCTCTGTTGCCTGCA
VCAM1	GCTATGAGGATGGAAGACTCTGG	ACTTGTGCAGCCACCTGAGATC
ICAM1	AAACCAGACCCTGGAACTGCAC	GCCTGGCATTTCAGAGTCTGCT
Il1b	TGGACCTTCCAGGATGAGGACA	GTTCATCTCGGAGCCTGTAGTG
IL6	TACCACTTCACAAGTCGGAGGC	CTGCAAGTGCATCATCGTTGTTC
FPR2	GCCTTTTGGCTGGTTCCTGTGT	CAAATGCAGCGGTCCAAGGCAA
CD38	GGTCCAAGTGATGCTCAATGGG	AGCTCCTTCGATGTCGTGCATC
ARG1	GTGAAGAACCCACGGTCTGT	ATCGGCCTTTTCTTCCTTCCC
YM2	GTGACCCTACTGTTAGTGCTGG	GGTACTTCCTGGGTGGCATCAA
IL1a	ACGGCTGAGTTTCAGTGAGACC	CACTCTGGTAGGTGTAAGGTGC
Notch1	GCTGCCTCTTTGATGGCTTCGA	CACATTCGGCACTGTTACAGCC
Notch2	CCACCTGCAATGACTTCATCGG	TCGATGCAGGTGCCTCCATTCT
MAPK8	CGCCTTATGTGGTGACTCGCTA	TCCTGGAAAGAGGATTTTGTGGC
Reg1	AACTGGTTTCTGGAGCGAGG	CGAAGGATGTGCTGGTCTGT
Reg2	ACCTGCAGAACGAAAACCCA	CATCAGGAGGCATGAACCTGT
Reg3	GAACAGTCCCGCCCTGAC	CATCATAGCACACCACTCGC
Reg4	CCTCGTGGGCCCAGCTCCAG	TCCCATGGCTCATTGCCACATTACT
Rank	GGACAACGGAATCAGTGGTC	CCACAGAGATGAAGAGGAGCAG
nephrin	CTGGGGGACAGTGGATTGAC	GGTCTGTGTCTTCAGGAGCC
Synaptopodin	AGGAGCCCAGGCCTTCTCT	GCCAGGGACCAGCCAGATA
CDK2	TCATGGATGCCTCTGCTCTCAC	TGAAGGACACGGTGAGAATGGC
CDK5	GTACTCCACGTCCATCGACATG	GCCATTGTTCCTCAGTCGGTGT
MYC	TCGCTGCTGTCCTCCGAGTCC	GGTTTGCCTCTTCTCCACAGAC
Mki67	GAGGAGAAACGCCAACCAAGAG	TTTGTCCTCGGTGGCGTTATCC
IL1ra	CTGTTGGTGAGGAATGTGGCTG	GGCTCAGGATAACAGGTCTGTC

Appendix 4 Session information for Python and R

Packages	Ver.	Packages	Ver.	Packages	Ver.	Packages	Ver.
Python 3.9.7 session information							
cellpose	0.72	nd2	0.1.6	scanpy	1.8.2	skimage	0.18.3
cv2	4.5.4	numpy	1.20.3	scipy	1.7.3		
harmonypy	0.0.5	pandas	1.3.5	seaborn	0.11.2		
matplotlib	3.5.0	session_info	1.0.0	rpy2	3.4.5		
Python modules imported as dependencies							
PIL	8.4.0	grpc	1.42.0	numexpr	2.8.1	sniffio	1.2.0
anndata	0.7.8	h5py	3.2.1	opt_einsum	v3.3.0	socks	1.7.1
attr	21.2.0	idna	3.2	packaging	21.3	statsmodels	0.13.0
babel	2.9.1	igraph	0.9.8	parso	0.8.2	tables	3.6.1
backcall	0.2.0	imageio	2.9.0	pickleshare	0.7.5	tblib	1.7.0
bcrypt	3.2.0	prompt_toolkit	3.0.20	ipykernel	6.4.1	texttable	1.6.4
bottleneck	1.3.2	ipython_genutils	0.2.0	psutil	5.8.0	threadpoolctl	2.2.0
cachetools	5.2.0	ipywidgets	7.6.5	pyarrow	7.0.0	tlz	0.11.0
cffi	1.14.6	pytz	2021.3	pycparser	2.2	toolz	0.11.1
chardet	4.0.0	torch_optimizer	0.3.0	pydevd	2.4.1	torch	1.13.0
joblib	1.1.0	charset_normalizer	2.0.4	pygments	2.10.0	jinja2	2.11.3
cloudpickle	2.0.0	pynndescent	0.5.5	jsonschema	4.2.1	tornado	6.1
colorama	0.4.4	jupyter_server	1.4.1	pyparsing	3.0.4	tqdm	4.62.3
kiwisolver	1.3.1	jupyterlab_server	2.8.2	leidenalg	0.8.8	traitlets	5.3.0
cycler	0.10.0	cryptography	3.4.8	jedi	0.18.0	umap	0.5.3
cytoolz	0.11.0	pytorch_ranger	0.1.1	pywt	1.1.1	urllib3	1.26.7
dateutil	2.8.2	llvmlite	0.39.1	requests	2.26.0	wcwidth	0.2.5
debugpy	1.4.1	louvain	0.7.1	setuptools	65.6.3	yaml	6
decorator	5.1.0	markupsafe	1.1.1	simplejson	3.17.6	zipp	3.6.0
defusedxml	0.7.1	natsort	7.1.1	sinfo	0.3.4	zmq	22.2.1
entrypoints	0.3	nbformat	5.1.3	six	1.16.0		
fastremap	1.12.2	numba	0.56.4	sklearn	1.0.1		
R 4.1.1 session information							
usethis	2.1.6	AnnotationDbi	1.54.1	stringr	1.4.0	BiocGenerics	0.38.0
QuasR	1.32.0	GenomeInfoDb	1.28.4	Rbowtie	1.32.0	DESeq2	1.32.0
eisaR	1.4.0	SummarizedExp	1.22.0	Rsamtools	2.8.0	Biobase	2.52.0
Biostrings	2.60.2	MatrixGenerics	1.4.3	XVector	0.32.0	matrixStats	0.62.0
IRanges	2.26.0	GenomicRanges	1.44.0	devtools	2.4.4	clusterProfiler	4.0.5
DOSE	3.18.3	RColorBrewer	1.1-3	pheatmap	1.0.12	S4Vectors	0.30.2
enrichplot	1.12.3	org.Mm.eg.db	3.13.0	ggrepel	0.9.1	knitr	1.39
ggpubr	0.4.0	GenomicFeatures	1.44.2	ggplot2	3.3.6		
R modules imported as dependencies							
utf8	1.2.2	VariantAnnotation	1.38.0	pkgload	1.3.0	processx	3.7.0
RSQLite	2.2.15	tidytree	0.3.9	patchwork	1.1.1	genefilter	1.74.1
scatterpie	0.1.7	curl	4.3.2	XML	3.99	rstatix	0.7.0

lifecycle	1.0.1	miniUI	0.1.1.1	compiler	4.1.1	BiocManager	1.30
colorspace	2.0-3	carData	3.0-5	crayon	1.5.1	abind	1.4-5
highr	0.9	BSgenome	1.60.0	later	1.3.0	qvalue	2.24.0
repr	1.1.4	lattice	0.20	geneplotter	1.70.0	ellipsis	0.3.2
polyclip	1.10-0	fastmap	1.1.0	tweenr	1.0.2	plyr	1.8.7
downloader	0.4	GO.db	3.13.0	rappdirs	0.3.3	zlibbioc	1.38.0
generics	0.1.3	png	0.1-7	car	3.1-0	ps	1.7.1
R6	2.5.1	ggforce	0.3.3	pkgconfig	2.0.3	viridis	0.6.2
bitops	1.0-7	latticeExtra	0.6-30	xml2	1.3.3	GenomicFiles	1.28.0
dplyr	1.0.9	gridGraphics	0.5-1	yulab.utils	0.0.5	data.table	1.14.2
tidyselect	1.1.2	promises	1.2.0.1	digest	0.6.29	mime	0.12
ggraph	2.0.5	grid	4.1.1	edgeR	3.34.1	evaluate	0.15
tidygraph	1.2.1	munsell	0.5.0	shiny	1.7.2	jpeg	0.1-9
splines	4.1.1	nlme	3.1-158	pbdZMQ	0.3-7	biomaRt	2.48.3
lazyeval	0.2.2	GOSemSim	2.18.1	viridisLite	0.4.0	shadowtext	0.1.2
yaml	2.3.5	uuid	1.1-0	fansi	1.0.3	ggfun	0.0.6
backports	1.4.1	GenomeInfoDbData	1.2.6	pkgbuild	1.3.1	aplot	0.1.6
tools	4.1.1	bit64	4.0.5	httr	1.4.3	dbplyr	2.2.1
sessioninfo	1.2.2	vctrs	0.4.1	remotes	2.4.2	ShortRead	1.50.0
base64enc	0.1-3	xfun	0.31	bit	4.0.4	cli	3.3.0
purrr	0.3.4	GenomicAlignments	1.28.0	stringi	1.7.6	graphlayouts	0.8.0
prettyunits	1.1.1	cachem	1.0.6	memoise	2.0.1	ggtree	3.0.4
urlchecker	1.0.1	DelayedArray	0.18.0	ape	5.6-2	callr	3.7.1
fs	1.5.2	BiocIO	1.2.0	htmlwidgets	1.5.4	fastmatch	1.1-3
DO.db	2.9	gtable	0.3.0	BiocParallel	1.26.2	restfulr	0.0.15
hms	1.1.1	rlang	1.0.4	interp	1.1-3	rjson	0.2.21
xtable	1.8-4	rtracklayer	1.52.1	withr	2.5.0	jsonlite	1.8.0
gridExtra	2.3	broom	1.0.0	filelock	1.0.2	limma	3.48.3
tibble	3.1.8	reshape2	1.4.4	ggsignif	0.6.3	pillar	1.8.0
htmltools	0.5.3	hwriter	1.3.2.1	httpuv	1.6.5	KEGGREST	1.32.0
tidyr	1.2.0	ggplotify	0.1.0	farver	2.1.1	survival	3.3-1
DBI	1.1.3	Rcpp	1.0.9	treeio	1.16.2	glue	1.6.2
MASS	7.3-58	BiocFileCache	2.0.0	progress	1.2.2	profvis	0.3.7
Matrix	1.4-1	RCurl	1.98	locfit	1.5	blob	1.2.3
igraph	1.3.4	deldir	1.0-6	fgsea	1.18.0	IRkernel	1.3
IRdisplay	1.1	cowplot	1.1.1	assertthat	0.2.1		
annotate	1.70.0	magrittr	2.0.3	scales	1.2.0		

Others

IPython	7.29.0	jupyter_core	4.8.1	notebook	6.4.6		
jupyterlab	3.2.1	jupyter_client	6.1.12				

Appendix 5 List of genes and proteins mentioned in the text

Gene	Symbol	Mouse Entrez id	Human Entrez id	Alias
Abcc1	ATP-binding cassette, sub-family C (CFTR/MRP), member 1	17250	4363	Abcc, Abcc1a, Abcc1b, M, MRP, Md, Mdrap, Mr, Mrp1, Abcc1
Acta2	actin, alpha 2, smooth muscle, aorta	11475	59	SMAalpha, SMalphaA, a-, a-SMA,
Adgre1	adhesion G protein-coupled receptor E1	13733	2015	Emr1, F4/80, Gpf480, Ly7, Ly71,
Ap5S1	adaptor-related protein 5 complex, sigma 1 subunit	69596	55317	0610038L13Rik, 2310035K24Rik, AW060727, sigma5
Arg1	arginase	11846	383	AI, AI256583, Arg, Arg-1, PG,
Bcl2	B cell leukemia/lymphoma 2	12043	596	AW986256, Bcl-, Bcl-2,
Ccdc84	coiled-coil domain containing 84	382073		Cenatac, D630044F24Rik, Gm1114
Ccl2	chemokine (C-C motif) ligand 2	20296	6347	MCA, MCAF, MCP, MCP-, MCP-1
Ccr2	chemokine (C-C motif) receptor 2	12772	729230	CKR, Cc-ckr-2, Ccr2a, Ccr2b, Ckr2,
Ccr5	chemokine (C-C motif) receptor 5	12774	1234	AM4-7, CD195, Cmkbr, Cmkbr5
Cd19	CD19 antigen	12478	930	AW495831
Cd209A	CD209a antigen	170786		CD209, CDSIGN, CI, CIRE, DC-S
Cd300Lf	CD300 molecule like family member F	246746	146722	CLIM1, CLM-1, CLM1, DIg, Digr2,
Cd38	CD38 antigen	12494	952	ADPRC 1, Cd38-r, Cd38-rs1, I-19
Cd4	CD4 antigen	12504	920	L3T, L3T4, Ly-, Ly-4
Cd68	CD68 antigen	12514	968	La, Lamp4, Sca, Scard1, gp11,
Cd8A	CD8 antigen, alpha chain	12525	925	BB154331, Ly-, Ly-2, Ly-3, Ly-35
Cdca2	cell division cycle associated 2	108912	157313	2610311M19Rik, AI586158
Cdh1	cadherin 1	12550	999	AA960649, ARC-1, E-ca, E-cad
Cdk2	cyclin-dependent kinase 2	12566	1017	A630093N05Rik
Cdk5	cyclin-dependent kinase 5	12568	1020	AW048668, Crk, Crk6
Chil4	chitinase-like 4	104183		Chi3, Chi3l4, Ym2
Cirbp	cold inducible RNA binding protein	12696	1153	C, Cirp, R74941
Clec9A	C-type lectin domain family 9, member a	232414	283420	9830005G06Rik, DNGR, DNGR-1
Cubn	Cubilin	65969	8029	AA408369, AL022750, D2Wsu88
Cx3Cr1	chemokine (C-X3-C motif) receptor 1	13051	1524	Cx3cr1
Cxcl1	chemokine (C-X-C motif) ligand 1	14825	2919	F, Fsp, Gr, Gro1, KC, Mg, Mgsa, N5
Cxcl12	chemokine (C-X-C motif) ligand 12	20315	6387	PB, PBSF/SD, Pbsf, SDF-, Scyb1
Cxcl2	chemokine (C-X-C motif) ligand 2	20310	2920	CINC, CINC-2a, GROb, Gr, Gro2,
Cyp4f13	cytochrome P450, family 4, subfamily f, polypeptide 13	170716		0610030I10Rik, Cypf13
E2F5	E2F transcription factor 5	13559	1875	AU024671, E2F-5
Egf	epidermal growth factor	13645	1950	AI790464
Elavl1	ELAV (embryonic lethal, abnormal vision)-like 1 (Hu antigen R)	15568	1994	2410055N02Rik, HUR, Hu, Hua, W91709
Endov	endonuclease V	338371	284131	A730011L01Rik
Fn1	fibronectin 1	14268	2335	E330027I09, F, Fn, Fn-, Fn-1
Fpr2	formyl peptide receptor 2	14289	2358	E330010I07Rik, Fpr, Fpr-rs2
Grb10	growth factor receptor bound protein 10	14783	2887	5730571D09Rik, AI325020, Meg1

Havcr1	hepatitis A virus cellular receptor 1	171283	26762	AI503787, KIM-, KIM-1, TIM-,
Hmox1	heme oxygenase 1	15368	3162	HO, HO-, HO-1, HO1, ,
Hnrnpm	heterogeneous nuclear ribonucleoprotein M	76936	4670	2610023M21Rik, AA409009, Hn
Hspa1B	heat shock protein 1B	15511	3304	HSP70B1, Hsp70, Hsp70-1,
Icam1	intercellular adhesion molecule 1	15894	3383	CD54, Icam, Icam-1, Ly-4, Ly-47,
Ifng	interferon gamma	15978	3458	IFN-g, If, If2f, Ifg, Ifng
Il10	interleukin 10	16153	3586	CSIF, IL, If2a, IL10, Il10
Il18	interleukin 18	16173	3606	Ig, Igif, IL, IL18, Il18
Il1A	interleukin 1 alpha	16175	3552	Il, IL1a, Il1a
Il1B	interleukin 1 beta	16176	3553	IL-, IL1beta, IL1b, Il1b
Il1Rn	interleukin 1 receptor antagonist	16181	3557	F630041P17Rik, IL, IL1ra, Il1rn
Il2Ra	interleukin 2 receptor, alpha chain	16184	3559	CD25, I, Il2r, Ly-4, Ly-43, Il2ra
Il6	interleukin 6	16193	3569	Il, IL6, Il6
Irf3	interferon regulatory factor 3	54131	3661	C920001K05Rik, IRF, IRF-3, Irf3
Irf7	interferon regulatory factor 7	54123	3665	Irf7
Itgam	integrin alpha M	16409	3684	CD11b/CD18, CR, CR3, Cd11b,
Itgax	integrin alpha X	16411	3687	AI449405, Cd11c, Cr4, N418, Itgax
Lcn2	lipocalin 2	16819	3934	24p, 24p3, AW212229, N, NRL,
Lrp2	low density lipoprotein receptor-related protein 2	14725	4036	AI315343, AW536255, D230004K18Rik, Gp33, Gp330,
Map4K2	mitogen-activated protein kinase kinase kinase kinase 2	26412	5871	AI385662, BL4, BL44, GCK, Ra, Rab8ip
Mapk8	mitogen-activated protein kinase 8	26419	5599	JNK, Prk, Prkm8, SAPK1, Mapk8
Med24	mediator complex subunit 24	23989	9862	100kD, 911GSE, AU040102
Mki67	antigen identified by monoclonal antibody Ki 67	17345	4288	D630048A14Rik, Ki-6, Ki-67, Ki6, Ki67, Mki67
Mmp7	matrix metallopeptidase 7	17393	4316	MA, MAT, MMP-7, Mmp7
Myc	myelocytomatosis oncogene	17869	4609	AU016757, Myc2, N, Niard, Nird
Ly6g	lymphocyte antigen 6 complex, locus G	546644	NA	Gr, Gr-, Gr-1, Gr1, Ly-6, Ly-6G,
Nfkb1	nuclear factor of kappa light polypeptide gene enhancer in B cells 1, p105	18033	4790	NF-KB1, NF-k, NF-kappaB, NF-kappaB1, p105, p5, p50, p50/p1
Nos2	nitric oxide synthase 2, inducible	18126	4843	NOS-II, Nos-2, i-NOS, iNOS, Nos2
Notch1	notch 1	18128	4851	9930111A19Rik, Mi, Mis6, N, N1,
Notch2	notch 2	18129	4853	N, N2, Notch2
Nqo1	NAD(P)H dehydrogenase, quinone 1	18104	1728	Dia4, Dtd, NM, NQ, Nmo-1, Nmo1,
Nup98	nucleoporin 98	269966	4928	4732457F17, AI849286, Nup,
P2Rx4	purinergic receptor P2X, ligand-gated ion channel 4	18438	5025	AI504491, AW555605, D5Ertd444, D5Ertd444e, P2X, P2X4, P2rx4
Pax2	paired box 2	18504	5076	Op, Opdc, Pax, Pax-2, Pax2
Pax8	paired box 8	18510	7849	Pax, Pax-8, Pax8
Pecam1	platelet/endothelial cell adhesion molecule 1	18613	5175	C85791, Cd31, PECAM-1, Pecam,
Phb2	prohibitin 2	12034	11331	AU044498, BAP, Bap37, Bcap,
Ppdpf	pancreatic progenitor cell differentiation and proliferation factor	66496	79144	0610012G23Rik, 2610317A05Rik, 2700038C09Rik, 3110053G12Rik,

Ptprc	protein tyrosine phosphatase, receptor type, C	19264	5788	B220, CD45R, Cd45, L-CA, Ly-, Ly-5, Lyt-, Lyt-4, T200, loc, Ptprc
Raet1E	retinoic acid early transcript 1E	379043	135250	Raet1e
Rbfox2	RNA binding protein, fox-1 homolog 2	93686	23543	Fbm2, Fxh, Hrnbp2, Rbm, Rbm9,
Rn18S	18S ribosomal RNA	19791		18s
Slc13A3	solute carrier family 13, member 3	114644	64849	NaD, NaDC, NaDC-3, NaDC3,
Slc5A12	solute carrier family 5, member 12	241612	159963	AI315119, D630015G19, SMCT,
Slc7A11	solute carrier family 7, member 11	26570	23657	9930009M05Rik, AI451155, su, sut,
Slx1B	SLX1 structure-specific endonuclease subunit homolog B (S. cerevisiae)	75764	79008	1110030E23Rik, 2410170E21Rik, 4833422P03Rik, AI853643, Giyd,
Smad4	SMAD family member 4	17128	4089	AW743858, D18Wsu70, D18Wsu70e
Smad5	SMAD family member 5	17129	4090	1110051M15Rik, AI451355, Dwf-C
Srxn1	sulfiredoxin 1 homolog (S. cerevisiae)	76650	140809	1700127B04Rik, AI854065,
Stard10	START domain containing 10	56018	10809	AV048538, CGI-5, CGI-52,
Susd6	sushi domain containing 6	217684	9766	4933426M11Rik, mKIAA0247,
Tac1	tachykinin 1	21333	6863	4930528L02Rik, N, NK, NK-,
Tcrb	T cell receptor beta chain	21577		TCRbeta, Tib
Teto	Tetracycline resistance protein			
TGF-β	transforming growth factor, beta 1	21803	7040	TGF-beta, TGF-beta1, TGF-βeta
TIMP2	tissue inhibitor of metalloproteinase 2	21858	7077	D11Bwg1104e, TIMP, Timp-2,
Tlr2	toll-like receptor 2	24088	7097	Ly10, Ly105, Tlr2
Tlr3	toll-like receptor 3	142980	7098	AI957183, Tlr3
Tlr4	toll-like receptor 4	21898	7099	Lps, Ly87, Ran/M1, Ras, Rasl2-8,
Tnf	tumor necrosis factor	21926	7124	DI, DIF, TNF-, TNF-a, TNF-alpha
Tnfrsf11a	tumor necrosis factor receptor superfamily, member 11a, NFKB activator	21934	8792	Ly109, ODFR, OFE, Rank, TRANCE-R, mRANK, Tnfrsf11a
Traf1	TNF receptor-associated factor 1	22029	7185	4732496E14Rik, Traf1
Txnrd1	thioredoxin reductase 1	50493	7296	T, TR, TR1, Trx, TrxR1, Txnrd1
Uchl5	ubiquitin carboxyl-terminal esterase L5	56207	51377	5830413B11Rik, Uch37, Uchl5
Umod	uromodulin	22242	7369	THP, Urehd, Urehd1, ureh, urehr4
Vcam1	vascular cell adhesion molecule 1	22329	7412	CD106, Vcam, Vcam-1, Vcam1
Vps26C	VPS26 endosomal protein sorting factor C	13185	10311	AW538125, Dc, Dcra, Dsc, Dscr3
Zc3h12a	zinc finger CCCH type containing 12A	230738	80149	MCPIP-1, Mcpip1, Reg1, Regnase1
Zc3h12b	zinc finger CCCH-type containing 12B	547176	340554	MCPIP-2, Mcpip2, Reg2, Regnase2
Zc3h12c	zinc finger CCCH type containing 12C	244871	85463	MCPIP-3, Mcpip3, Reg3, Regnase3
Zc3h12d	zinc finger CCCH type containing 12D	237256	340152	MCPIP-4, Mcpip4, Reg4, Regnase4
Zfp511	zinc finger protein 511	69752		2410004P19Rik, C86579, Znf511,

Appendix 6 Abbreviation

Abbreviation	Full name	Abbreviation	Full name
ADQI	Acute Dialysis Quality Initiative	LPS	Lipopolysaccharide
AKD	Acute kidney disease	LTL	Lotus tetragonolobus lectin
AKI	Acute kidney injury	LysM	lysozyme
AKIN	AKI network	M	Monocyte
ANOVA	Analysis of variance	M1	Pro-inflammatory type macrophages
ARF	Acute renal failure	M2	Anti-inflammatory type macrophages
ATL	thin ascending limb of loop of Henle	MA plot	plot of log-intensity ratios (M-values) versus log-intensity averages (A-values)
ATN	Acute tubular necrosis	Mo	macrophage
ATP	Adenosine triphosphate	MPC	Mononuclear phagocytic cell
BMDM	Bone marrow derived macrophage	MPCs	mononuclear phagocytic cells
BUN	Blood urea nitrogen	mRNA	Messenger Ribonucleic acid
CaOx	Calcium oxalate	MT	metallothionein
CCCH	Cys–Cys–Cys–His	MTAL	thick ascending limb of loop of Henle in medulla
CKD	Chronic kidney disease	MTT	3-(4,5-Dimethylthiazol-2-yl)-2,5-Diphenyltetrazolium Bromide
CNT	connecting tubule	NETs	Neutrophil extracellular traps
Co2	Carbon dioxide	NK	natural killer cell.
CPC	principle cells of collecting duct in cortex	NTD	N-terminal domain
CTAL	thick ascending limb of loop of Henle in cortex	NX	Nephrectomy
CTD	C-terminal domain	p.o.	oral administration
DAPI	4’,6-diamidino-2-phenylindole	PAS	Periodic acid Schiff
DC	dendritic cells	PBS	Phosphate-buffered saline
DCT	distal convoluted tubule	PC	parietal epithelial cells
DEAD	Asp-Glu-Ala-Asp box	PCA	Principal component analysis
DEG	Differentially expressed genes	PDCs	podocytes
DMEM	Dulbecco's Modified Eagle Medium	PH	potential of hydrogen
DNase	Deoxyribonuclease	PIN	Pilt-N-terminus
DTL	descending limb of loop of Henle	Pod	podocytes
EC	endothelial cells	prg	progenitor-like
ECIS	Cell-substrate impedance sensor	prlf	proliferating
eGFR	Estimated glomerular filtration rate	PS	Penicillin-streptomycin
ELISA	Enzyme-Linked Immunosorbent Assay	PT	proximal tubule
ESRD	Ed-stage renal disease	PTCs	proximal tubular cells
FACS	Fluorescence-activated cell sorting	PTS1	S1 segment of proximal tubule
FC	flod change	PTS2	S2 segment of proximal tubule
FCS	Fetal calf serum	PTS3	S3 segment of proximal tubule
FDR	false discovery rate	RBDs	Ribonucleic acid binding domains
Fib	fibroblasts	RBPs	Ribonucleic acid binding proteins

FITC	Fluorescein-isothiocyanate	RIFLE	Risk, Injury, Failure, Loss and End Stage Renal Disease
GCLM	glutamate-cysteine ligase modifier subunit	RNA	Ribonucleic acid
GFR	Glomerular filtration rate	RNA-seq	RNA-seq
GM-CSF	Granulocyte-macrophage colony-stimulating factor	RTEC	renal tubular epithelial cells
GSEA	Gene Set Enrichment Analysis	rtTA	reverse tetracycline transactivator
H_2O_2	Hydrogen peroxide	s.c.	subcutaneous
HR	Hazard ratio	Scr	serum creatinine
i.p.	Intraperitoneal injection	scRNA-seq	single cell RNA-seq
ICA	type A intercalated cells of collecting duct	SD	standard deviation
ICU	Intensive Care Unit	SPP1	osteopontin
IFTA	Interstitial Fibrosis and Tubular Atrophy	TAL	thick ascending limb
IM	infiltrating monocytes	TEC_cnn	Canonical renal cells
IRI	Ischemia-reperfusion injury	UMAP	Uniform Manifold Approximation and Projection
KDIGO	Kidney Disease: Improving Global Outcomes	uIRI	Unilateral ischemia-reperfusion injury
KH	KH-like domain	Uro	urothelium
KRM	kidney resident macrophage	WT	wild type
lacZ	β-galactosidase	ZF	CCCH-type zinc finger domain
LDH	Lactate dehydrogenase		

Acknowledgement

I would like to express my deepest gratitude to my supervisor Prof. Hans-Joachim Anders for his invaluable guidance and support throughout this project. I am extremely grateful for the effort and dedication that he put into helping me understand the complexities of the research process. Without his unwavering support and encouragement, this project would not have been possible. Thank you for believing in me and for all the hard work you have put in.

I am also utmost grateful to Dr. Julian Marschner who pushed me out of my comfort zone and inspired me to pursue my goals. I would like to express my gratitude to Prof. Dr. Maciej Lech and PD Dr. Stefanie Steiger for their excellent organization and management of our lab that provided me with the opportunity to develop this research project and the knowledge and skills necessary to make it a success. Thank Janina Mandelbaum, Anna Anfimiadou and Yvonne Minor for their technical support. Thank Prof. Martha Merrow and Dr. Francesca Sartor for generously providing the access to the Nikon Eclipse Ti2 microscope system. Thank Prof. Yan Xu and Dr. Chen Guan for performing the immunofluorescence staining on Regnase3 and Rank.

I would also like to thank Dr. Yoshihiro Kusunoki, Qiubo Li and Wenkai Xia for the nice teamwork and the help that improve my skills and knowledge in a collaborative environment. I am also thankful to Dr. Zhibo Zhao, Dr. Qiuyue Ma, Dr. Yutian Lei, Dr. Na Li and Dr. Chongxu Shi who provided valuable feedback and input on my work. Their insights have helped me gain a better understanding of the research process, and I am immensely grateful for their support. I am forever thankful to Zhihui Zhu and Khuram Shehzad whose constant encouragement and enthusiasm pushed me to strive to find innovative solutions. Your kind words and unwavering faith in me did wonders to motivate me and keep me going.

Additionally, I am grateful to all those who contributed financially to this project. I thank the funding agencies China Scholarship Council and Deutsche Forschungsgemeinschaft for their generous support, without which none of this work would have been possible.

Finally, I would like to extend my gratitude to animals that have been sacrificed for the betterment of human beings. Their contributions and sacrifices have resulted in tremendous advances in medical research, biotechnology, and other fields, greatly improving the lives of many people. I hope that we as the society can continue to use their contributions responsibly and ethically.

Declaration of academic honesty

Hereby, I declare that all of the present work embodied in this thesis was carried out by myself from 09/2019 until 07/2023 under the supervision of Prof. Dr. Hans Joachim Anders, Nephrologisches Zentrum, Medizinische Klinik und Poliklinik IV, Innenstadt Klinikum der Universität München. This work has not been submitted in part or full to any other university or institute for any degree or diploma.

Part of the work used public datasets from GEO and EBI database, which are all summarized in Table 11

Part of the work has been accepted as an abstract at the ASN Kidney Week 2022.

Part of the work has been accepted as an abstract at the Joint Meeting of DGfI & ÖGAI 2022.

Date: 27.07.2023 Signature: Chenyu Li

Place: Munich, Germany

Affidavit

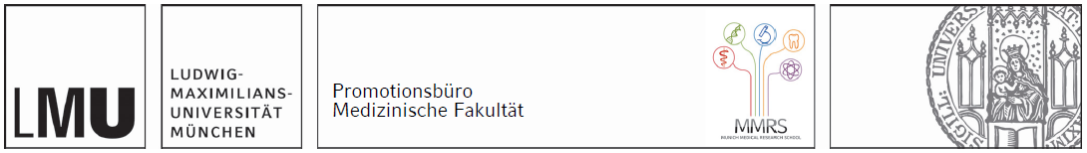

Affidavit

Li, Chenyu
Surname, first name

I hereby declare, that the submitted thesis entitled:

Different roles of Regnase3 in resident macrophages and tubular epithelial cells in kidney disease

is my own work. I have only used the sources indicated and have not made unauthorized use of services of a third party. Where the work of others has been quoted or reproduced, the source is always given.
I further declare that the dissertation presented here has not been submitted in the same or similar form to any other institution for the purpose of obtaining an academic degree.

Munich, 27.07.2023
Place, date

Chenyu Li
Signature doctoral candidate